



**UNIVERSITÀ DEGLI STUDI CATANIA**

**INTERNATIONAL PhD IN CHEMICAL SCIENCES**

**XXX CYCLE**

***Roberto Fiorenza***

***Modified TiO<sub>2</sub>-based catalysts for energy production  
and environmental protection***

Laboratory of Environmental and Industrial Catalysis

Department of Chemical Sciences

Università degli studi di Catania

*PhD COORDINATOR*: Prof. S. Sortino

*TUTOR*: Prof. S. Scirè

---

PhD Thesis

# CONTENTS

|  |               |
|--|---------------|
| <b>INTRODUCTION</b> .....  | <b>- 3 -</b>  |
| - <i>Energy in Europe: The 20-20-20 goal</i> .....   | - 3 -         |
| - <i>New technologies for the environmental protection and the energy production</i> .....                           | - 5 -         |
| <b>References</b> .....  | - 7 -         |
| <b>Chapter 1: Heterogeneous Photocatalysis</b> .....   | <b>- 8 -</b>  |
| 1.1 <i>Principles of photocatalysis</i> .....  | - 8 -         |
| 1.2 <i>Photo-oxidation of organic contaminants in air</i> .....  | - 12 -        |
| 1.3 <i>Photo-oxidation of organic contaminants in water</i> .....  | - 16 -        |
| 1.4 <i>Photocatalytic water splitting</i> .....  | - 19 -        |
| References .....   | - 25 -        |
| <b>Chapter 2: TiO<sub>2</sub>-based materials</b> .....  | <b>- 28 -</b> |
| 2.1 <i>Titanium dioxide</i> .....  | - 28 -        |
| 2.2 <i>Strategy to enhance the TiO<sub>2</sub> photoefficiency: Chemical modifications</i> .....                     | - 31 -        |
| 2.3 <i>Strategy to enhance the TiO<sub>2</sub> photoefficiency: Structural modification of TiO<sub>2</sub></i> ..... | - 37 -        |
| 2.3.1 <i>Reduced TiO<sub>2</sub></i> .....   | - 37 -        |
| 2.3.2 <i>Morphological change of TiO<sub>2</sub></i> .....   | - 39 -        |
| References .....   | - 43 -        |
| <b>Chapter 3: Chemical modifications of TiO<sub>2</sub></b> .....  | <b>- 46 -</b> |
| 3.1 <i>TiO<sub>2</sub>-CeO<sub>2</sub> based composites</i> .....  | - 46 -        |
| 3.2 <i>Au/TiO<sub>2</sub> catalysts</i> .....  | - 47 -        |
| 3.3 <i>Au/TiO<sub>2</sub>-CeO<sub>2</sub> catalysts: Samples preparation and experimental setup</i> .....            | - 49 -        |
| 3.3.1 <i>Results and discussion</i> .....  | - 50 -        |
| 3.3.2 <i>Conclusions and future perspectives</i> .....   | - 59 -        |
| References .....   | - 62 -        |
| <b>Chapter 4: Structural modifications of TiO<sub>2</sub>: Reduced TiO<sub>2</sub></b> .....                         | <b>- 64 -</b> |
| 4.1 <i>Laser irradiated TiO<sub>2</sub></i> .....  | - 64 -        |
| 4.2 <i>Samples preparation and experimental setup</i> .....  | - 64 -        |
| 4.3 <i>Results and discussion</i> .....  | - 65 -        |
| 4.4 <i>Conclusions and future perspectives</i> .....   | - 76 -        |
| References .....   | - 79 -        |
| <b>Chapter 5: Structural and chemical modifications of TiO<sub>2</sub>: Inverse Opal TiO<sub>2</sub></b> .....       | <b>- 80 -</b> |
| 5.1 <i>Photonic crystals</i> .....   | - 80 -        |
| 5.2 <i>Opal and Inverse Opal materials</i> .....   | - 82 -        |

|   |                |
|---|----------------|
| 5.3 Inverse Opal TiO <sub>2</sub> .....   | - 83 -         |
| 5.4 Inverse Opal TiO <sub>2</sub> based materials: Samples preparation and experimental setup ..... | - 84 -         |
| 5.5 Results and discussion.....   | - 90 -         |
| 5.6 Conclusions and future perspectives .....   | - 128 -        |
| References .....  | - 130 -        |
| <b>CONCLUSIONS.....</b>   | <b>- 133 -</b> |
| Appendix A: Characterization techniques used in this work .....                                     | - 136 -        |
| Appendix B: Gas Chromatography .....  | - 142 -        |
| Appendix C: Hydrogen Economy .....  | - 145 -        |
| <b>Curriculum vitae .....</b>   | <b>- 153 -</b> |
| <b>List of publications .....</b>   | <b>- 154 -</b> |
| <b>List of Communications:.....</b>   | <b>- 156 -</b> |
| <b>Courses and Schools.....</b>   | <b>- 158 -</b> |
| <b>Acknowledgements.....</b>  | <b>- 159 -</b> |

## INTRODUCTION

### - Energy in Europe: The 20-20-20 goal

Air pollution and the increase of energy demand are among the most serious problems of the present days. As a central objective of the Europe 2020 strategy, the European Union (EU) has set the goal to cut greenhouse gas (GHG) emissions by 20%, improve energy efficiency by 20% and increase the use of renewable energy to 20% by the year 2020. This is known as the 20-20-20 goal.

The EU framework on climate and energy for 2030 proposed by the European Commission in January 2014 presents targets that are more ambitious and aims at reducing greenhouse gas emissions by 40% and increasing the use of renewable to at least 27% by 2030 [1].

The European Commission and EU governments agreed on the target of cutting greenhouse gases (GHG) by at least 20% by 2020, compared with 1990 levels (Fig.1).

In market based economies like the Europeans it is a general problem to get the cost of externalities like GHG and climate change imbedded into the market so that these cost will influence decisions about production, consumption and investment. As highlighted in various climate change assessment studies the future society costs of climate change and global warming are quite high although not evenly

geographical and sector distributed. To better reflect these costs for producers, consumers and investors and make up for part of the market imperfection a European Union Emission Trading System (EU ETS) was designed back in 2003. By putting a price on carbon and thereby giving a financial value to each tone of emissions saved, the EU ETS has placed climate change on the agenda of company boards across Europe. A sufficiently high carbon price also promotes investment in clean, low-carbon and energy efficient technologies. The EU ETS scheme covers the most GHG intensive sector in Europe including the power sector and a number of industrial sectors like cement and steel production, etc. [2]. These sectors accounts for more than 40% of the total GHG emission in Europe. The 2020 climate and energy package includes a



Fig.1 EU greenhouse gas emission in 2014.  
(Source: EU Parliament, 2014)

comprehensive revision and strengthening of the legislation which underpins the EU ETS, the Emissions Trading Directive. Energy efficiency is the second important point of the 20-20-20 goal. Substantial steps have been taken towards the objective of increasing energy efficiency, notably in the appliances and buildings markets. The new Energy Efficiency Plan [3] aims at responding to the call of the European Council of 4 February 2011 to take determined action to tap the considerable potential for higher energy savings of buildings, transport, products and processes [4]. The energy efficiency measures will be implemented as part of the EU's wider resource efficiency goal, encompassing efficient use of all natural resources and ensuring high standards of environmental protection. The greatest energy saving potential lies in buildings whilst transport has the second largest potential. Energy efficiency in industry will be tackled through energy efficiency requirements for industrial equipment and measures to introduce energy audits and energy management systems. Improvements to the efficiency of power and heat generation are also proposed, ensuring that the plan includes energy efficiency measures across the whole energy supply chain. A

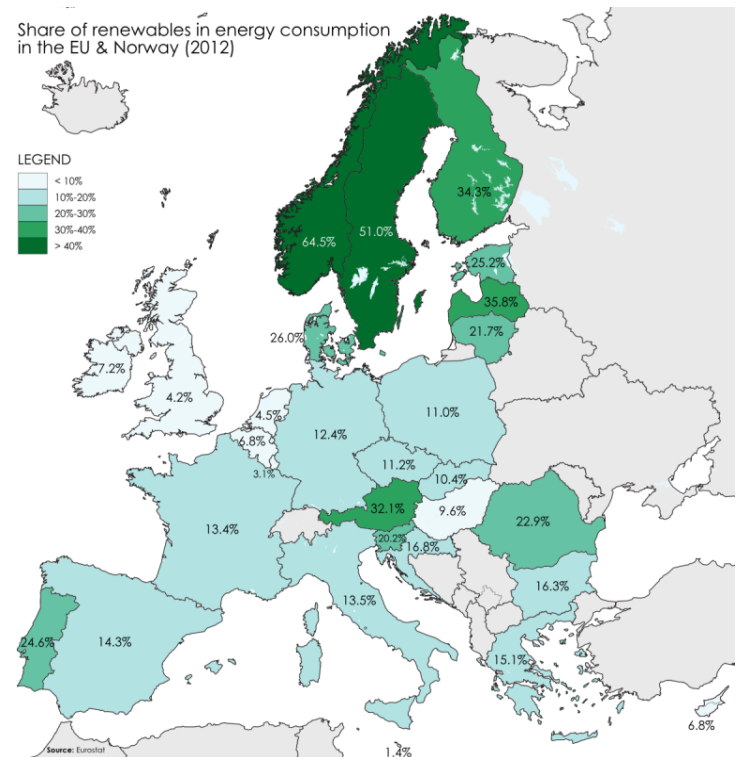


**Fig.2: Renewable energy in the European Union**  
(Source: Eurostat, 2012)

wide range of technologies and methods exist to improve energy efficiency, turn renewables into viable energy sources and reduce emissions.

The EU's Renewable energy directive sets a binding target of 20% final energy consumption from renewable sources by 2020. To achieve this, EU countries have committed to reaching their own national renewables targets ranging from 10% in Malta to 49% in Sweden (Fig.2).

They are also each required to have at least 10% of their transport fuels come from renewable sources by 2020.

All EU countries have adopted national renewable energy action plans showing what actions they intend to take to meet their renewables targets. These plans include: sectorial targets for electricity, heating, cooling and transport; planned policy measures and the different mix of renewables technologies that they expect to employ.

*- New technologies for the environmental protection and the energy production*

Gases that trap heat in the atmosphere are called greenhouse gases and the main are: CO<sub>2</sub>, CH<sub>4</sub>, N<sub>2</sub>O and the fluorinated gases. The greenhouse effect increases the temperature of the earth by trapping heat in our atmosphere. This keeps the temperature of the earth higher than it would be if direct heating by the sun was the only source of warming. When sunlight reaches the surface of the earth, some of it is absorbed which warms the ground and some bounces back to space as heat. Greenhouse gases that are in the atmosphere absorb and then redirect some of this heat back towards the earth. The earth's atmosphere consists mainly of oxygen and nitrogen, neither plays a significant role in enhancing the greenhouse effect because both are essentially transparent to terrestrial radiation. The greenhouse effect is primarily a function of the concentration of water vapor, carbon dioxide (CO<sub>2</sub>), methane (CH<sub>4</sub>), nitrous oxide (N<sub>2</sub>O), and other trace gases in the atmosphere that absorb the terrestrial radiation leaving the surface of the earth. Changes in the atmospheric concentrations of these greenhouse gases can alter the balance of energy transfers between the atmosphere, space, land, and the oceans. Human activities are continuing to affect the earth's energy budget by changing the emissions and resulting atmospheric concentrations of radiatively important gases and aerosols and by changing land surface properties. There are also several gases that, although they do not have a commonly agreed upon direct radiative forcing effect, do influence the global radiation budget. These tropospheric gases include carbon monoxide (CO), nitrogen dioxide (NO<sub>2</sub>), sulfur dioxide (SO<sub>2</sub>), and tropospheric (ground level) ozone (O<sub>3</sub>). Tropospheric ozone is formed by two precursor pollutants, volatile organic compounds (VOCs) and nitrogen oxides (NO<sub>x</sub>) in the presence of ultraviolet light (sunlight).

The term VOCs encompasses many compounds including non-methane hydrocarbons, alcohols, aldehydes and organic acids. Exposure to VOCs may trigger many serious health problems, such as eye, nose, skin, and throat irritation, coughing, headaches, and cancer, even at very low concentrations [5, 6]. Therefore; it is highly desirable to efficiently and cost-effectively abate VOCs. Many practical methods, such as adsorption, thermal combustion, catalytic oxidation, and biofiltration, have been adopted to remove hazardous VOCs [7]. Amongst these technologies, catalytic oxidation is believed to be very promising as it is a highly efficient and relatively inexpensive route to reducing VOCs at low concentrations. More importantly, it decomposes VOCs to non-toxic final products, i.e., CO<sub>2</sub> and H<sub>2</sub>O, with high performance and good durability at lower temperatures (< 600 °C) [8].

Recently, especially applied for the wastewater treatment, the Advanced Oxidation Processes (AOPs) constitute a family of similar but not identical technologies that are based predominantly

(but not exclusively) on the production of very reactive hydroxyl radicals [9]. AOPs include heterogeneous and homogeneous photocatalysis, Fenton and Fenton-like processes, ozonation, the use of ultrasound, microwaves and  $\gamma$ -irradiation, electrochemical processes and wet oxidation processes. One of their main advantages compared to conventional technologies is that they effectively degrade recalcitrant components without generating a secondary waste stream as is the case for example of the membrane processes. Moreover, in most cases the formation of hazardous species in the effluent is limited. This is a specifically important benefit over competing technologies such as for instance chlorine oxidation of organics, during which a considerable amount of organo-chlorinated species is formed [10]. From the turn of the century till now, the number of processes has increased drastically with the development of hybrid synergistic technologies based on the combination of various AOPs.

These combinations have helped to overcome the occurrence of refractory species and also to improve significantly the performance of AOPs, to meet the practical requests in accordance with the green policy of European Union.

Among these new processes, photocatalysis is one of the most attractive advanced oxidation technologies for the decompositions of organic pollutions in water or air [11]. Furthermore in the contest of the other tasks of Europe 20-20-20 (improvement of the energy efficiency by 20% and increasing of the use of renewable energy to 20% by the year 2020) the photocatalytic process can be applied to produce hydrogen or for the CO<sub>2</sub> reduction [12].

Hydrogen would play an important role because it is an ultimate clean energy and it can be used in fuel cells. Moreover, hydrogen is used in chemical industries. For example, a large amount of hydrogen is consumed in industrial ammonia synthesis. At present, hydrogen is mainly produced from fossil fuels such as natural gas by steam reforming. In this process, fossil fuels are consumed and CO<sub>2</sub> is emitted. Hydrogen has to be produced from water using natural energies such as sunlight if one thinks of energy and environmental issues. Therefore, the solar hydrogen production from water is one of the most important topics of current research.

On these bases, this work has the aim to investigate the photocatalytic performance of modified TiO<sub>2</sub>-based materials in some important reactions applied to environment protection and energy production. In particular much effort has been focused in the photo-oxidation of VOCs in gas phase, in the photodegradation of harmful compounds in water and in the hydrogen evolution by photocatalytic water splitting.

## **References**

- [1] G. Liobikien, M. Butkus, *Renew. Energ.* 106 (2017) 298-309.
- [2] Energy and Climate Policies beyond 2020 in Europe- Overall and selected countries Danish Energy Agency; [https://ens.dk/sites/ens.dk/files/Globalcooperation/eu\\_energy\\_and\\_climate\\_policy\\_overview.pdf](https://ens.dk/sites/ens.dk/files/Globalcooperation/eu_energy_and_climate_policy_overview.pdf)
- [3] M. Carvalho, *Energy* 40 (2012) 19-22.
- [4] K. Knoop, S. Lechtenböhmer, *Renew. Sust. Energ. Rev.* 68 (2017) 1097-1105.
- [5] A.P. Jones, *Atmos Environ*, 33 (1999) 4535-4564.
- [6] P. Wolkoff, G.D. Nielse, *Atmos Environ* 35 (2001) 4407-4417.
- [7] G. Leson, A.M. Winer, *J. Air Waste Manage* 41 (1991) 1045-1054.
- [8] J.J. Spivey, *IndEngChem Res*, 26 (1987) 2165-2180.
- [9] C. Cominellis, A. Kapalka, S. Malato, S.A. Parsons, L. Poullos, D. Mantzavinos, *J. Chem. Technol. Biotechnol.* 83 (2008) 769-776.
- [10] C. Pablos, J. Marugan., R. van Grieken, E. Serrano, *Water Res.* 47 (2013) 1237-1245.
- [11] X.B. Chen, S.S. Mao, *Chem. Rev.* 107 (2007) 2891-2959.
- [12] Y. Izum, *Coord. Chem. Rev.* 257 (2013) 171-186.



## Chapter 1: Heterogeneous Photocatalysis

### 1.1 Principles of photocatalysis

Heterogeneous photocatalysis is a discipline which includes a large variety of reactions: mild or total oxidations, dehydrogenation, hydrogen transfer, metal deposition, water detoxification, gaseous pollutant removal, bactericidal action, hydrogen production, etc. Heterogeneous photocatalysis can be carried out in various media: gas phase, pure organic liquid phases or aqueous solutions. As for classical heterogeneous catalysis, the overall process can be decomposed into five independent steps [1-3]:

- Transfer of the reactants in the fluid phase to the surface.
- Adsorption of at least one of the reactants.
- Reaction in the adsorbed phase.
- Desorption of the product(s).
- Removal of the products from the interface region.

The only difference with conventional catalysis is the mode of activation of the catalyst in which the thermal activation is replaced by a photonic activation (Fig. 1.1).

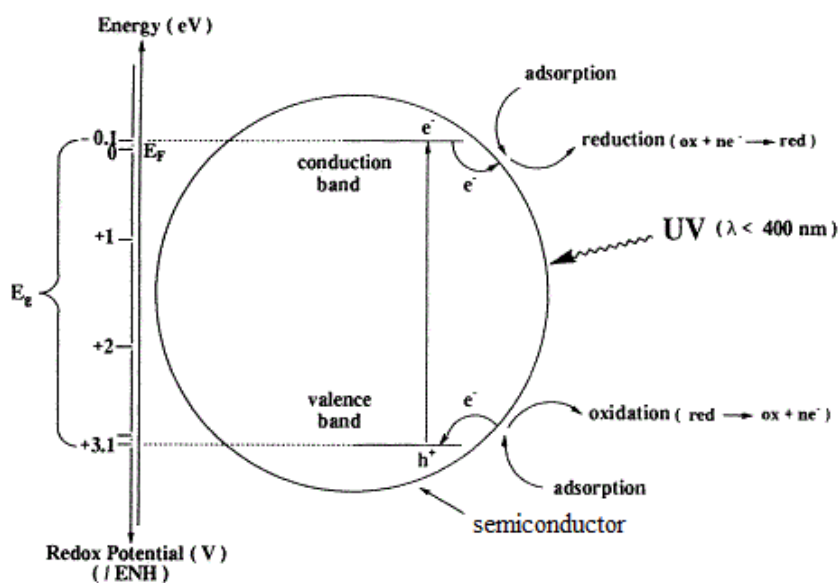
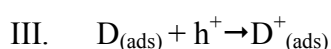
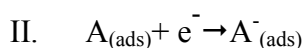


Fig. 1.1 Scheme of photocatalytic processes over semiconductor particles.

When a semiconductor (SC) as  $\text{TiO}_2$ ,  $\text{ZnO}$ ,  $\text{ZrO}_2$ ,  $\text{CeO}_2$  is illuminated with photons whose energy is equal or greater than their band-gap energy  $E_g$  ( $h\nu \geq E_g$ ), there is absorption of these

photons and creation of electron( $e^-$ )/hole( $h^+$ ) pairs (reaction I), which dissociate into free photoelectrons in the conduction band and photoholes in the valence band. Simultaneously, in the presence of a fluid phase (gas or liquid), a spontaneous adsorption occurs and according to the redox potential (or energy level) of each adsorbate, an electron transfer proceeds towards acceptor (A) molecules (reaction II), whereas a positive photohole is transferred to a donor (D) molecule (reaction III, actually the hole transfer corresponds to the cession of an electron by the donor to the solid).



Each ion formed subsequently reacts to form the intermediates and the final products.

The photocatalytic activity can be reduced by the electron-hole recombination, described in Fig.1.2, which corresponds to the conversion of the photoelectronic energy into heat.

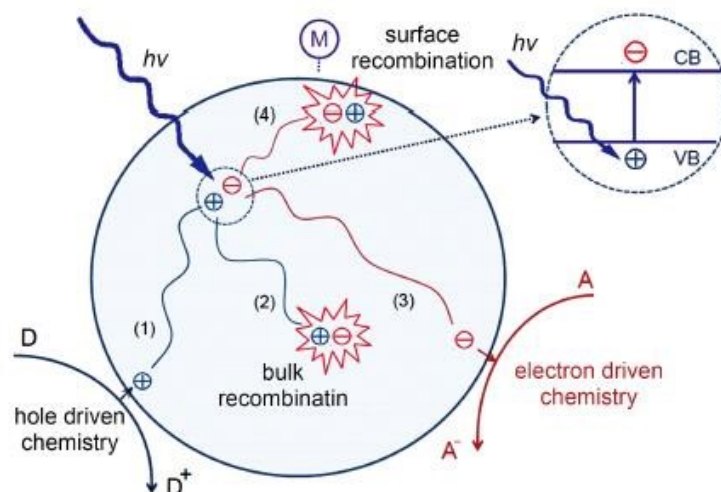


Fig. 1.2 Processes of photoelectron-hole recombination in the semiconductor particles.

A schematic view of the time scale of the different charge carrier-related phenomena just discussed is included in Fig. 1.3.

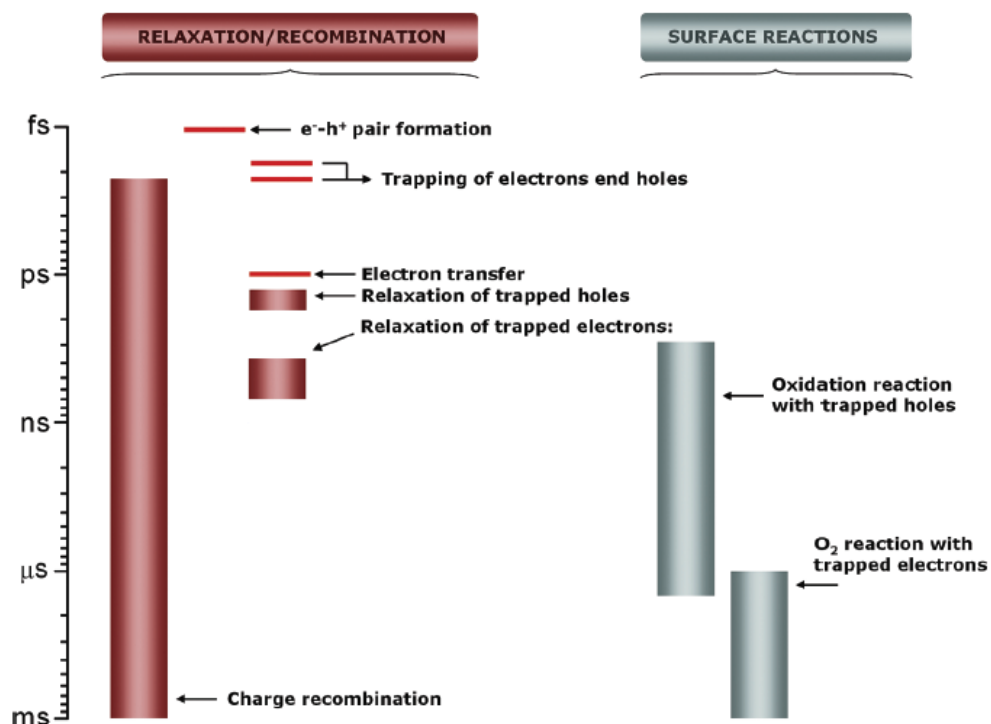
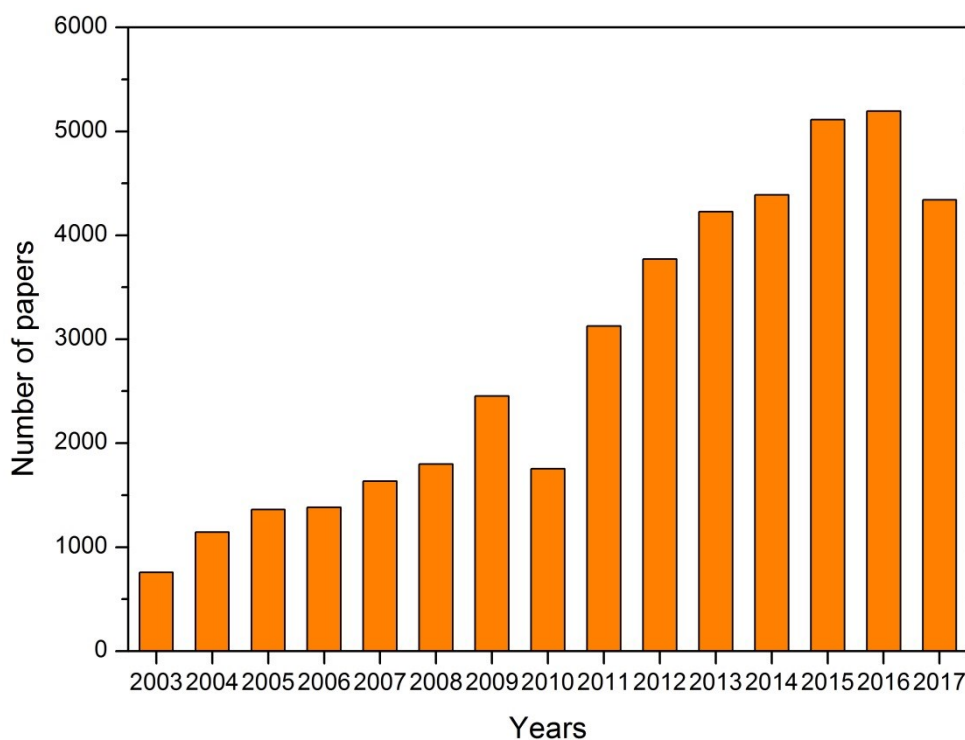


Fig. 1.3 Time scales of “elemental steps” occurring in a typical photocatalytic process.

Both the above surface photoreactions can be exploited for some important environment applications as the degradation of dangerous organic compounds both in air or in water (photo-oxidation reactions) or as the hydrogen production by water splitting (photoreduction reaction). For these reasons, photocatalysis can be regarded as a new and interesting hot subject of the modern research. The increasing interest for this topic is expressed by the continuous increase of number of papers (Fig.1.4) in the last decade.



**Fig. 1.4** Number of publications concerning photocatalysis over the years 2003- 2017( September) based on database Scopus with keyword “photocatalysis”.

Many semiconductors have been used as photocatalysts:  $\text{TiO}_2$ ,  $\text{ZnO}$ ,  $\text{WO}_3$ ,  $\text{CdS}$  and  $\text{NiO}$  can be found among the best performing ones. Each photocatalyst is characterized by a different band gap energy and oxidizing power. The thermodynamic driving forces in photocatalytic processes are strongly dependent on the relative relationships between the conduction band (CB) and valence band (VB) potentials of the semiconductor photocatalysts used and to the redox potentials of reversible target reactions [4, 5]. Thus, the more negative CB positions of semiconductors are beneficial for reduction reactions, while the more positive VB positions of semiconductors are favorable for oxidation reactions. The band positions (at  $\text{pH}=7$  in aqueous solution) for some important semiconductor photocatalysts and their potential applications are listed in Fig. 1.5.

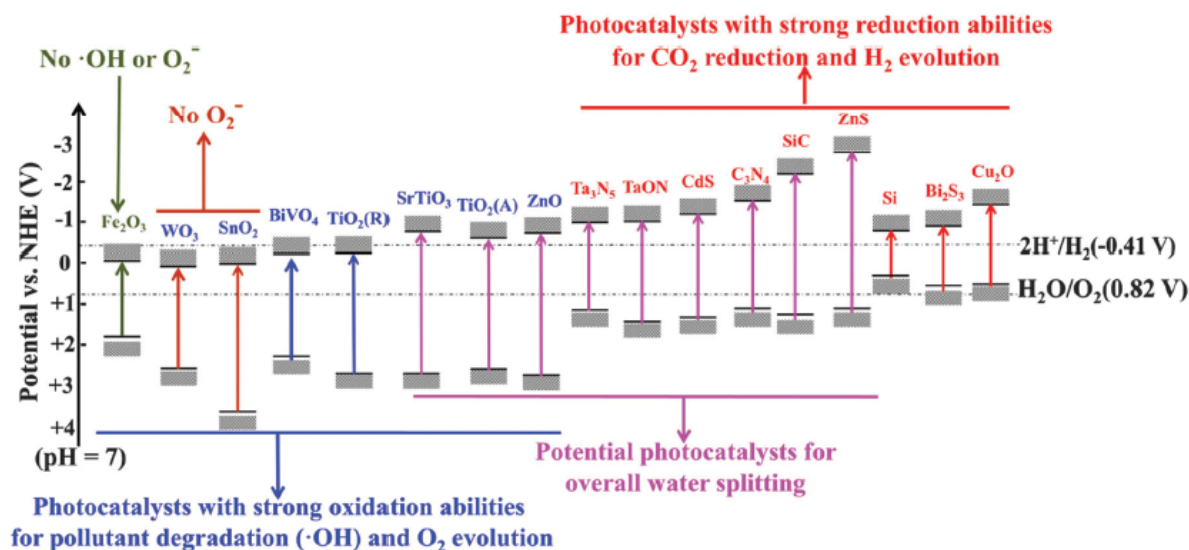


Fig. 1.5 Band positions and potential applications of some typical photocatalysts [4].

Titanium dioxide ( $\text{TiO}_2$ ) has emerged as a leading photocatalyst for environment purifications due to its strong oxidizing power under ultraviolet irradiation, high chemical stability, low cost, and environment friendly [6-10]. However, the photo-catalytic efficiency of  $\text{TiO}_2$  nanomaterials is still not up to the mark to meet out the practical needs under direct sunlight irradiation because the large intrinsic band gap (3.2eV) of  $\text{TiO}_2$  severely restricts its utilization of the visible light and the fast electron-hole recombination in  $\text{TiO}_2$  often results in a low quantum yield and poor photocatalytic activity [11-13]. To efficiently utilize abundant and green sunlight, therefore, a series of strategies, such as metal/non-metal elements doping and coupling with other functional materials have been adopted to increase the  $\text{TiO}_2$ -based photocatalysts activity, by introducing an extrinsic band gap with lower energy, suppressing electron-hole recombination rate, and increasing the surface charge carrier transfer rate of  $\text{TiO}_2$  [14-16]. A detail description of the strategies to improve the  $\text{TiO}_2$  performances and the methodologies used in this work, will be discussed in next chapters.

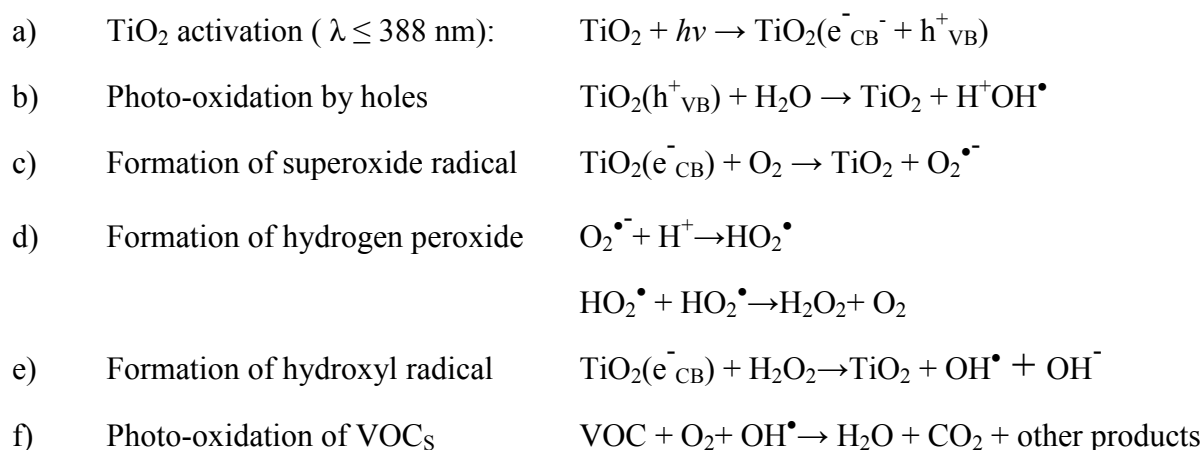
## 1.2 Photo-oxidation of organic contaminants in air

The photocatalytic mechanism can be successful applied in the air purification and in particular one of the most important reactions investigated is the photo-oxidation of VOCs [17-19]. Nowadays people spend most of their time (more than 90% [20]) in an indoor environment; consequently the indoor air quality (IAQ) has a significant impact on human health, comfort and productivity [21]. A long-term exposure to indoor air pollutants can be detrimental to human health and lead to sick building syndrome, building related illnesses and in extreme cases cancer [22]. VOCs, nitrogen oxides ( $\text{NO}_x$ ), carbon monoxide (CO), and particulate matter are among the

main indoor air pollutants. Levels of pollutants in indoor environment can be higher than those of outdoor air due to the contribution of indoor sources such as combustion by-products, building materials, office equipment (e.g. printers and computers), and consumer products [22, 23]. Recently, photocatalysis technology has attracted great attention for removal of gaseous pollutants at low concentrations (i.e. part per billion (ppb) level), owed to its superior features compared to other methods (i.e. adsorption or ozonation) such as room temperature operation, activity towards various contaminants, and benign final products (CO<sub>2</sub> and H<sub>2</sub>O) [21, 22, 24].

After the activation of the semiconductor particles by an opportune light radiation, the photogenerated charge carriers participate in a series of reactions with other molecules such as oxygen and water and produce highly reactive radicals (such as hydroxyl or superoxide radicals). In gas phase, mass transfer of the VOC compounds from the gas phase (i.e. air stream) to the solid phase plays an important role and greatly affects the reaction rate and removal efficiency. After the external (from bulk to exterior surface) and internal diffusions (from exterior surface to internal catalytic surface) and adsorption onto the surface, pollutant molecules come into contact with the produced reactive species and break down to lower molecular weight products and eventually to CO<sub>2</sub>, water and other by products [21,25].

The basic reaction mechanism using a photocatalyst as TiO<sub>2</sub> can be depicted as follows [17, 18, 26]:



Apart from their beneficial participation in oxidation and reduction reactions, electrons and holes also go, as described before, through recombination process where they neutralize one another. Moreover many parameters can influence the photoactivity as the adsorption properties of the photocatalyst, the type and the concentration of VOCs and the type and the intensity of the light source used for the irradiation.

Adsorption of pollutant onto the surface of photocatalyst is a crucial step that greatly affects the reaction rate and removal efficiency. Adsorption of challenge compounds on photocatalyst

brings about better contact between photocatalyst and reactant molecules, which in turn leads to higher oxidation rate. The role of adsorption step is more critical when dealing with gas streams with high humidity level (typical condition in the mechanical ventilation system of buildings) due to the competition between VOCs and water molecules for adsorption sites. Depending on the type of active site available on the surface of photocatalyst and target VOCs, different adsorption mechanisms may exist. *Nimlos et al.* [27] suggested that alcohols and organic acids can be adsorbed over the surface of TiO<sub>2</sub> via both dissociative adsorption at oxygen bridging sites and hydrogen bond to the OH groups while aldehydes can only be adsorbed via hydrogen bond to the surface OH groups. *Alberici and Jardim* [28] reported that the adsorption of VOCs on TiO<sub>2</sub>P25 (80% anatase, 20% rutile) follows the order: methanol > isopropanol > MEK > acetone > toluene > i-octane, indicating higher adsorption of alcohols than aromatics over TiO<sub>2</sub>. Consequently the type and the concentration of VOCs is a key aspect. For various classes of VOCs and broad ranges of concentration, there is general agreement that higher concentration of VOCs results in an improved reaction kinetics (until rate reaches its plateau), lower removal efficiency, and poorer mineralization of pollutants to CO<sub>2</sub> [29-32]. The impact of higher VOCs concentration on photo-oxidation reactions can be analyzed from different aspects: (i) the number of VOCs molecules that can be adsorbed and oxidized on photocatalyst surface increases which boosts the reaction kinetics [33]; (ii) the ratio of reactive species plus active sites to pollutant molecules decreases and consequently, more VOCs can leave the reactor without undergoing degradation [30]; (iii) high amount of by-products/intermediates generated during the reactions can reduce the mineralization and/or occupy part of the active sites, impeding the oxidation progress. The effect of pollutant concentration and type on photocatalytic degradation kinetics has been investigated by many researchers [34-37]. *Jafarikojour et al.* [38] observed that by increasing the inlet concentration of toluene from 20 to 100 ppm at 30% Relative Humidity (RH), the conversion decreased from 37% to ca. 27%. Similarly, *Mo et al.* [24] found that decomposition efficiency of toluene dropped ca. 30% by increasing toluene concentration from 1 to 4 ppm.

*Palmisano et al.* found that the presence of oxygen was essential for the occurrence of the photo-oxidation of toluene while water played an important role in order to maintain the catalyst activity [36, 39]. In another study, *Vildoza et al.* [40] showed that increasing the inlet concentration of 2-propanol from 100 to 700 ppb significantly lowered the mineralization rate from ca. 90% to 63%. Interestingly, it was found a positive linear relationship between K<sub>OH</sub> and photo-oxidation reaction rate constant [41, 42] that is however different towards the various organic compounds. *Jeong et al.* [43] obtained higher removal efficiency for toluene (82.6-

99.9%) compared to benzene (67.1-94.2%), and ascribed this behavior to the higher reaction rate of toluene with hydroxyl radicals in the gas phase and on TiO<sub>2</sub>P25. Considering the principles of catalytic reactions, at low pollutant concentration (number of VOCs molecules ~ number of photocatalyst active sites), the reaction rate increases with pollutant concentration until it reaches a region (i.e. intermediate VOCs concentration) where the reaction rate becomes independent of concentration [44]. Most of the researchers believe that any further increment in the concentration of pollutant neither improves or deteriorates the reaction rate since photocatalyst is working at its maximum capacity [44-47]. On the contrary, investigations on the photo-oxidation of benzene [48] and toluene [49] showed that at higher concentration due to the deposition of refractory reaction intermediates on photocatalyst surface and loss of active sites the reaction rate dramatically drops. Similarly, *Monteiro et al.* [33] observed that under low light intensity, conversion and reaction rate of Perchloroethylene (PCE) firstly increases with concentration and then decreases. The noted downward trend for reaction rate was attributed to the lack of photogenerated  $e^-$ - $h^+$  and surface flooding due to an excessive PCE load.

Light is one of the main pillars of photocatalysis; therefore, light source wavelength (WL) and light intensity (I) can affect the reaction rate and removal efficiency. Theoretically, UV light with wavelength less than 380 nm can excite the electrons in the valence band of TiO<sub>2</sub> (the most used photocatalyst). Germicidal lamp (UVC, 254 nm) and fluorescent black-light lamp (300-400 nm) are the most utilized light sources in the photocatalytic oxidation (PCO) of indoor air pollutants. Some studies employed UV light emitting diode (wavelength usually centered at 365 nm) due to long lifetime and high efficiency. For the same photon energy distribution, i.e. light wavelength, increasing the light intensity leads to generation of a larger number of photons and consequently  $e^-$ - $h^+$  pairs. It is proposed that the impact of UV intensity on the reaction rate can be divided into two regimes: (i) a first-order regime at lowlight intensity and high VOCs concentration where  $e^-$ - $h^+$  pairs are consumed faster by chemical reactions than by recombination and (ii) a half-order regime at high light intensity and low VOCs concentration in which the rate of recombination exceeds the rate of oxidation reactions [50, 51].

In this thesis work the photo-oxidation of 2-propanol and ethanol was investigated over different TiO<sub>2</sub>-based materials under UV irradiation (UV mercury lamp, 100 W, 365 nm), the state of art and the reaction mechanism for the degradation of these alcohols will be discussed in detail in the next chapters.



### 1.3 Photo-oxidation of organic contaminants in water

The discharge of refractory organic contaminants through wastewaters into the environment causes all over the world dangerous environmental pollution. Furthermore the gap between the clean water and its availability is expected to continue to increase with respect to growing contamination, owing to the overwhelming discharge of contaminants and pollutants into the natural water cycle. As far as the environment is concerned, the reuse and recycling of wastewater effluents is thus necessary to augment the limited fresh water supply and to offset more possible water resources in the long run [52]. During the past few decades, a variety of practical strategies have been implemented to develop viable wastewater treatment technologies [53-55]. For instance, conventionally, biological treatments were designed to effectively eliminate assorted types of contaminants from wastewater in the short term; however, these techniques also normally lead to the production of secondary pollution [56] some of which even involves the presence of health-threatening bacteria and soluble refractory organic compounds that are hard to remove [57].

Photocatalysis has been considered as one of the most appealing options for wastewater treatment, due to its great potential and high efficiency by using sunlight to remove organic pollutants and harmful bacteria with the aid of a solid photocatalyst [58, 59].

The general mechanism of photo-oxidation in water is the same described above for the photodegradation of VOCs (pag. 13, reactions a-f). The photogenerated  $h^+$  is widely considered as an oxidant for directly degrading organic contaminants, the capacity of which depends on the catalyst type and oxidation conditions [60]. To design a photocatalyst capable of utilizing safe and sustainable solar energy effectively, several critical requirements need to be satisfied. First, the semiconductor material should have a smaller band-gap to allow it to absorb solar energy across a broad range of spectrum. Simultaneously, the semiconductor should have a relatively positive enough valence band for the ample production of  $h^+$  and  $\bullet OH$  radicals [61]. Second, the catalyst should possess a particular platform/system for the efficient charge separation and transportation [62, 63]. Moreover, the semiconductor materials should have good photoelectrochemical stability in the electrochemical reactions [64].

In most cases, different types of dyes are studied as model compounds for the photocatalytic degradation of large organic molecules in water treatment. Organic dyes are often used in textile, printing, and photographic industries, but a sizable fraction of dyes is wasted in the dyeing process and is released into effluent water streams. In general, the presence of even low concentrations of dyes in effluent streams seriously affects the nature of water, and is difficult to be biodegraded or oxidized with the aid of chemicals.

Pharmaceutical and personal care products (PPCPs) have recently been considered as emerging contaminants, and are an extraordinarily diverse group of chemicals used in prescription and non-prescription drugs, human health and cosmetic care, veterinary medicine, and agricultural practice [65, 66]. Specific PPCPs may cause ecological harm, such as endocrine disruption and antimicrobial resistance, thus some of PPCPs have been classified as “priority pollutants” by both the US Environmental Protection Agency and the European Union Water Framework Directive. PPCPs have frequently been studied with respect to environmental protection because of their toxicity and non-biodegradability.

Phenolic compounds can cause various diseases, including cancer, angiocardopathy, gastroenterology etc., even at very low concentrations, and represent a typical family of organic pollutants widely present in wastewater from petrol, coal, and other chemical industries [67-70]. Most phenolic compounds are usually difficult to be mineralized by a biodegradation method, due to the stable benzene ring and its recalcitrant nature. However, such compounds have been reported to be effectively degraded by TiO<sub>2</sub> and other visible light-responsive photocatalysts [71-74].

Other organic pollutants, such as benzylalcohol, methanol, benzyl amine, hydroxytyrosol, and benzene, in aqueous solutions have also been reported to be efficiently degraded by visible light induced photocatalytic processes [75-77].

The presence of inorganic impurities, such as residual ions and acids, in the water matrix has distinctive effects toward a water system’s ecological environment. Some of them are highly toxic to most of living organisms when their concentration levels are higher than a certain value. For instance, hexavalent chromium (Cr(VI)) is a carcinogenic and mutagenic pollutant, which is frequently found in wastewater, possibly stemming from pigment production, metal plating, leather tanning, etc. The visible light induced photocatalytic reduction of aqueous Cr(VI) has received much attention recently, due to its low cost and high efficiency without secondary pollution [78, 79].

The different types of microbes (bacteria, viruses, fungi, algae, plankton, etc.) present in wastewater are harmful to health and can cause various diseases [80]. Also for this type of pollutants over the past few decades, the visible light activated photocatalytic disinfection of water was intensively studied, with research focus moving from laboratory analysis to potential applications [81, 82]. For example, a dye-sensitized TiO<sub>2</sub> thin film was used in the photocatalytic disinfection of phytopathogenic bacteria under visible light irradiation. The inhibition rates of *Erwiniacarotovora subsp. carotovora 3*, *Enterobacter cloacae SMI*, and *E. carotovora subsp. carotovora 7* that could induce severe soft/basal rot disease in vegetable crops were higher

than 90%. These results indicated that the visible light-responsive dye-sensitized TiO<sub>2</sub> thin film had the potential for direct application to plant protection in water systems [81]. A visible light-activated palladium-modified nitrogen-doped titanium oxide (TiON/PdO) photocatalyst has been demonstrated with good visible light adsorption and a superior efficient photocatalytic disinfection effect on *Fungi Fusarium graminearum macroconidia*.

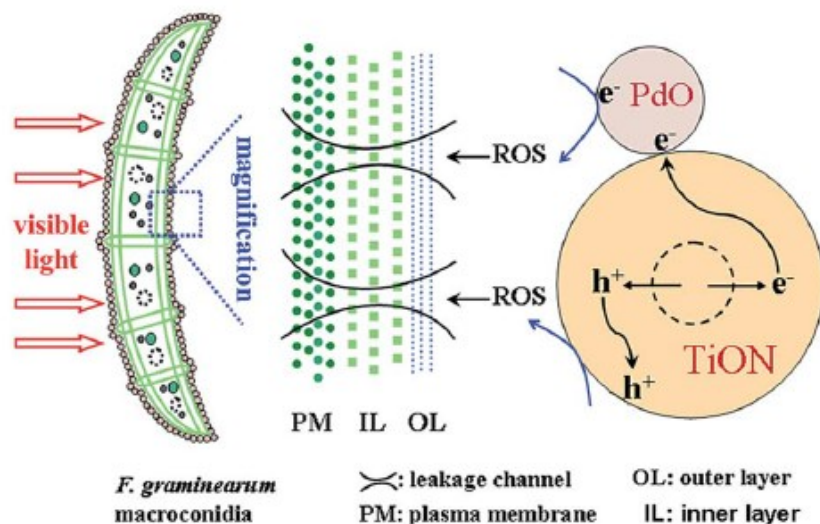


**Fig.1.6** Photocatalytic disinfection mechanism of TiON/PdO photocatalyst on *Fusarium graminearum* macroconidia under visible light irradiation [82].

The disinfection effect benefitted from the strong adsorption of the TiON/PdO photocatalyst onto the *Fusarium graminearum* macroconidia surface due to their opposite surface charges. The photocatalytic disinfection mechanism of the TiON/PdO photocatalyst on the *Fusarium graminearum* macroconidia is displayed in Fig. 1.6, and it is attributed to their cell wall/membrane damage caused by the attack from the reactive oxygen species (ROSs), while a breakage of their cell structure was not necessary for their loss of viability [82].

In this thesis the degradation in water of some dyes, as the Methylene Blue and the Rhodamine B under visible light irradiation was investigated over TiO<sub>2</sub>-based photocatalysts, the results and the mechanisms of these reaction will be discussed in the following chapters.

### 1.4 Photocatalytic water splitting

Hydrogen is considered as an ideal fuel for the future. It can be produced from clean and renewable energy sources and, thus, its life cycle is clean and renewable. Solar and wind are the two major sources of renewable energy and they are also the promising sources for renewable hydrogen production. However, presently, renewable energy contributes only about 5% of the commercial hydrogen production primarily via water electrolysis, while other 95% hydrogen is mainly derived from fossil fuels [83]. Renewable hydrogen production is not popular yet because the cost is still high. Photovoltaic water electrolysis may become more competitive as the cost continues to decrease with the technology advancement; however, the considerable use of small band-gap semiconducting materials may cause serious life cycle environmental impacts. Alternatively, photocatalytic water splitting using TiO<sub>2</sub> for hydrogen production offers promising way for clean, low-cost and environmental friendly production of hydrogen by solar energy.

Concerning the thermodynamics of the reaction:  $2\text{H}_2\text{O} \leftrightarrow 2\text{H}_2 + \text{O}_2$  is an extremely difficult reaction since it is endergonic by  $\sim 240 \text{ kJ mol}^{-1}$  [84, 85] and the dissociation of water can be obtained with reasonable equilibrium yields but with very high thermal input at high temperature. The alternative is to provide the thermodynamic energy with light, in which case we need light of  $\sim 500 \text{ nm}$  wavelength. Such light is abundant on earth, but the kinetic barrier to split off the first hydrogen atom from water is much more energy demanding, needing  $\sim 500 \text{ kJ mol}^{-1}$ , or light at maximum wavelength of  $250 \text{ nm}$ . Hence water is stable at the earth's surface such wavelengths are cut out in the stratosphere before reaching ground level. Hence it is necessary a strategy to get round the kinetic problem, thus involves the use of photocatalysis to lower that barrier [86]. In a typical process the photon energy is converted to chemical energy accompanied with a largely positive change in the Gibbs free energy through water splitting as shown in Fig. 1.7. This reaction is similar to photosynthesis by green plants because these are uphill reactions.

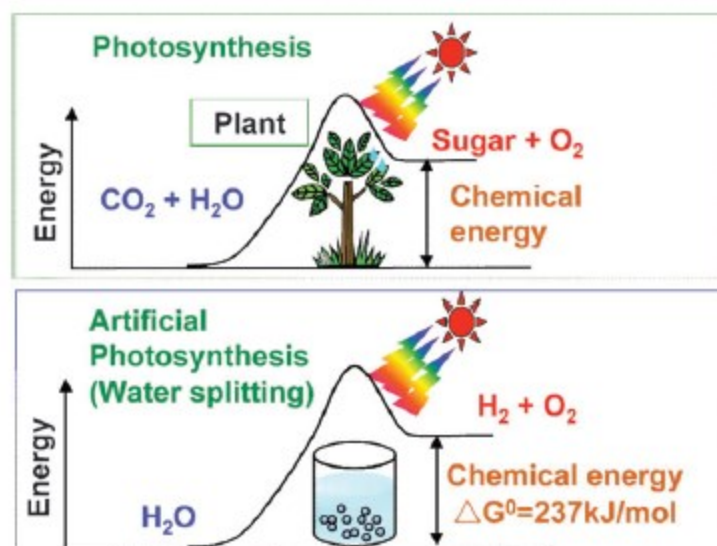


Fig. 1.7 Photosynthesis by green plants and photocatalytic water splitting as an artificial photosynthesis [88].

Therefore, photocatalytic water splitting is regarded as an artificial photosynthesis and is an attractive and challenging theme in chemistry. From the viewpoint of the Gibbs free energy change, photocatalytic water splitting is distinguished from photocatalytic degradation reactions such as photo-oxidation of organic compounds using oxygen molecules that are generally downhill reactions. The Honda-Fujishima effect of water splitting using a TiO<sub>2</sub> electrode is illustrated in Fig. 1.8:

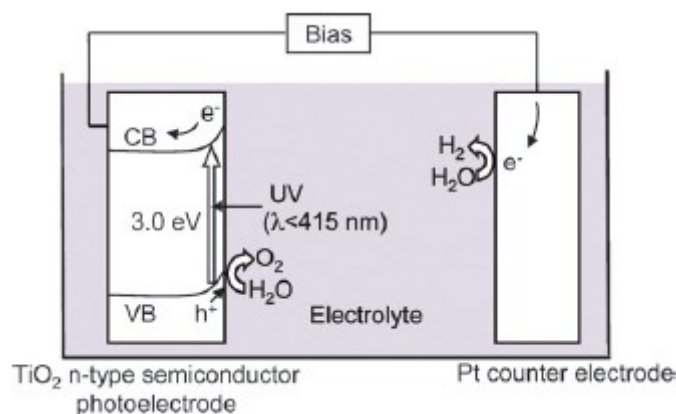


Fig. 1.8 Honda-Fujishima effect-water splitting using a TiO<sub>2</sub> photoelectrode [88].

When TiO<sub>2</sub> is irradiated with UV light electrons and holes are generated and the photogenerated electrons reduce water to form H<sub>2</sub> on a Pt counter electrode while holes oxidize water to form O<sub>2</sub> on the TiO<sub>2</sub> electrode with some external bias by power supply or pH difference between a catholyte and an anolyte.

The characteristic feature of water splitting using a powdered photocatalyst is the simplicity; the opportune light radiation shines the photocatalyst powders dispersed in water, and then hydrogen

is readily obtained. Moreover, powdered photocatalyst systems will be advantageous for large-scale application of solar water splitting because of the simplicity.

The Photocatalytic reactions proceed on semiconductor materials as schematically shown in Fig. 1.9.

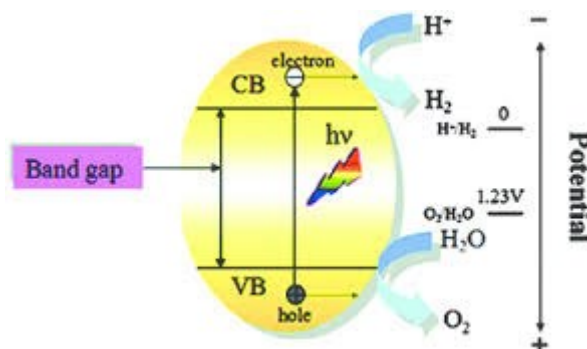
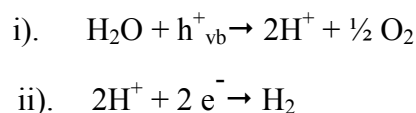


Fig. 1.9 Principle of water splitting using semiconductor photocatalysts.



Water molecules are reduced by the electrons to form H<sub>2</sub> and are oxidized by the holes to form O<sub>2</sub> for overall water splitting. Important points in the semiconductor photocatalyst materials are the width of the band gap and levels of the conduction and valence bands. The bottom level of the conduction band has to be more negative than the redox potential of H<sup>+</sup>/H<sub>2</sub> (0 V vs. Normal Hydrogen Electrode NHE), while the top level of the valence band be more positive than the redox potential of O<sub>2</sub>/H<sub>2</sub>O (1.23 V) [87, 88]. Therefore, the theoretical minimum band gap for water splitting is 1.23 eV that corresponds to light of about 1100 nm.

Presently, the energy conversion efficiency from solar to hydrogen by TiO<sub>2</sub> (the main semiconductor used) is still low. The main reasons are: (1) Recombination of photo-generated electron/hole pairs: CB electrons can recombine with VB holes very quickly and release energy in the form of unproductive heat or photons; (2) Fast backward reaction: Decomposition of water into hydrogen and oxygen is an energy increasing process, thus backward reaction (recombination of hydrogen and oxygen into water) easily proceeds;

(3) Inability to utilize visible light: The band gap of TiO<sub>2</sub> is about 3.2 eV and only UV light can be utilized for hydrogen production. Since the UV light only accounts for about 5% of the solar radiation energy while the visible light contributes about 50%, the inability to utilize visible light limits the efficiency of solar photocatalytic hydrogen production.

In order to resolve the above listed problems and make solar photocatalytic hydrogen production feasible, continuous efforts have been made to promote the photocatalytic activity and enhance the visible light response.

Co-catalysts such as Pt, NiO and RuO<sub>2</sub> are usually loaded to introduce active sites for H<sub>2</sub> evolution because the conduction band levels of many oxide photocatalysts are not high enough to reduce water to produce H<sub>2</sub> without co-catalytic assistance. Active sites for electron oxidation of water are required for O<sub>2</sub> evolution. Co-catalysts are usually unnecessary for oxide photocatalysts because the valence band is deep enough to oxidize water to form O<sub>2</sub>. This is the characteristic point of heterogeneous photocatalysts being different from homogeneous photocatalysts for which O<sub>2</sub> evolution with electron oxidation of H<sub>2</sub>O is a challenging reaction.

Another approach is to apply a two-step excitation mechanism using two different photocatalysts [89] (Fig. 1.10).

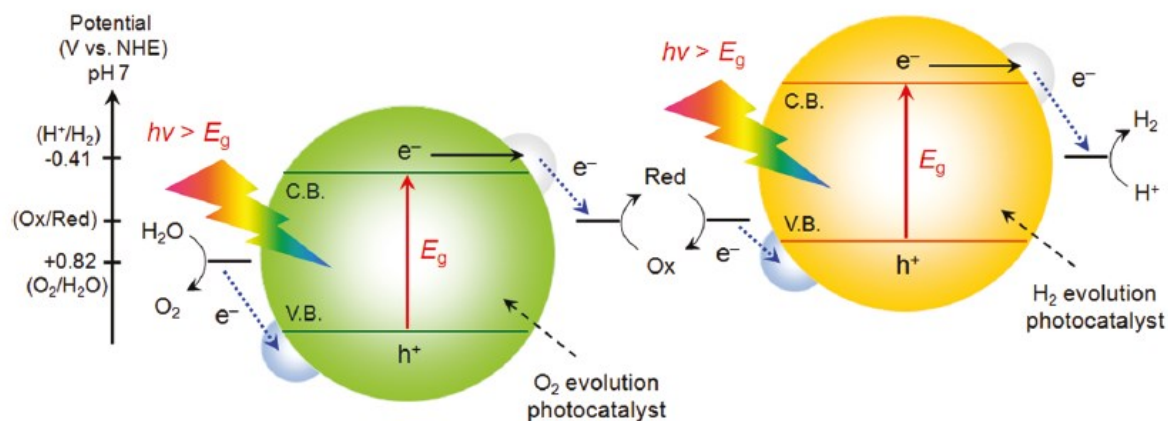


Fig. 1.10 Z-Scheme for the photocatalytic water splitting [89].

This was inspired by natural photosynthesis in green plants and is called the Z-scheme. The advantages of a Z-scheme water splitting system are that a wider range of visible light is available because a change in Gibbs free energy required to drive each photocatalyst can be reduced as compared to the one-step water splitting system and that the separation of evolved H<sub>2</sub> and O<sub>2</sub> is possible. It is also possible to use a semiconductor that has either a water reduction or oxidation potential for one side of the system. For example, some metal oxides (e.g., WO<sub>3</sub> and BiVO<sub>4</sub>) function as a good O<sub>2</sub> evolution photocatalyst in a two-step water splitting system using a proper redox mediator, although they are unable to reduce water [90, 91].

Sacrificial reagents are often employed to evaluate the photocatalytic activity for water splitting because overall water splitting is a tough reaction. When the photocatalytic reaction is carried out in an aqueous solution including a reducing reagent, in other words, electron donors or hole scavengers, such as alcohol and a sulfide ion, photogenerated holes irreversibly oxidize the

reducing reagent instead of water. It enriches electrons in a photocatalyst and an H<sub>2</sub> evolution reaction is enhanced. This reaction will be meaningful for realistic hydrogen production if biomass and abundant compounds in nature and industries are used as the reducing reagents [92, 93].

Organic compounds (hydrocarbons) are widely used as electron donors for photocatalytic hydrogen production as they can be oxidized by VB holes. EDTA, methanol, ethanol, lactic acid and formaldehyde have been tested and proved to be effective to enhance hydrogen production [94-96]. *Nada et al.* [94] carried out a qualitative investigation to study the effects of different electron donors on hydrogen production. The rankings in terms of the degree of hydrogen production enhancement capability were found to be: EDTA > methanol > ethanol > lactic acid. It should be noted that the decomposition of these hydrocarbons could also contribute to a higher hydrogen yield since hydrogen is one of their decomposed products.

In accordance, *Puangpetch et al.* [97] found that over mesoporous-assembled SrTiO<sub>3</sub> photocatalyst the enhancement of the activity by adding different hole scavengers was found in the following order: MeOH > EtOH > d-glucose > 2-PrOH > Na<sub>2</sub>SO<sub>3</sub>. The use of MeOH provided the highest photocatalytic enhancement ability (the ability to increase the photocatalytic hydrogen production activity), as compared to the other studied hole scavengers, possibly because it has the highest ability to donate electrons, to scavenge the valence band holes to preventing photo-generated charge recombination [98, 99]. In a comparison among alcohols, the photocatalytic activity tended to increase with increasing alcohol concentration. For MeOH as the hole scavenger, the hydrogen production rate significantly increased in the MeOH concentration range of 0-20 vol.%; beyond this range, it only slightly increased.

Other inorganic ions, such as S<sub>2</sub><sup>2-</sup>/SO<sub>2</sub><sup>3-</sup>, Ce<sup>4+</sup>/Ce<sup>3+</sup> and IO<sub>3</sub><sup>-</sup>/I<sup>-</sup> were used as sacrificial reagents for hydrogen production [100-102].

*Sayama et al.* [103] reported that addition of carbonate salts could significantly enhance hydrogen and oxygen production stoichiometrically. Addition of Na<sub>2</sub>CO<sub>3</sub> was found to be effective for enhancement of hydrogen and oxygen production using Pt loaded TiO<sub>2</sub> (Pt-TiO<sub>2</sub>). Later, various semiconductor photocatalysts including TiO<sub>2</sub>, Ta<sub>2</sub>O<sub>5</sub> and ZrO<sub>2</sub> were tested and it was found that the presence of Na<sub>2</sub>CO<sub>3</sub> was very beneficial for hydrogen and oxygen production for all the photocatalysts tested [104]. The Infrared (IR) study revealed that the surface of Pt-TiO<sub>2</sub> catalyst was covered by many types of carbonates species, such as HCO<sub>3</sub><sup>-</sup>, CO<sub>3</sub><sup>2-</sup>, HCO<sub>3</sub><sup>•</sup> and C<sub>2</sub>O<sub>6</sub><sup>2-</sup>. Therefore, photo-generated holes were consumed by reacting with carbonate species to form carbonate radicals, which is beneficial for photo-excited electron/hole separation.



In this work thesis the H<sub>2</sub> production by photocatalytic water splitting was tested over modified TiO<sub>2</sub>-based materials both under UV and solar light irradiation. The effect of a sacrificial agent as ethanol was furthermore investigated.

## References

- [1] J.M. Herrmann, *Top. Catal.* 34 (2005) 49-65.
- [2] G. Palmisano, E. García-López, G. Marci, V. Loddo, S. Yurdakal, V. Augugliaro, L. Palmisano, *Chem. Commun.* 46 (2010) 7074–7089.
- [3] Y. Quab, X. Duan, *Chem. Soc. Rev.* 42 (2013) 2568-2580.
- [4] X. Li, J. Yu, M. Jaroniec, *Chem. Soc. Rev.* 45(2016) 2603-2636.
- [5] A. Di Paola, E. García-López, G. Marci, L. Palmisano, *J. Hazard. Mater.* 211-212 (2012) 3-69.
- [6] J. Chen, F. Qiu, W. Xu, S. Cao, H. Zhu, *Appl. Catal. A: Gen.* 495 (2015) 131-140.
- [7] P. Yap, T. Lim, *Appl. Catal. B: Environ.* 101 (2011) 709-717.
- [8] S. Oros-Ruiz, R. Zanella, B. Prado, *J. Hazard. Mater.* 263 (2013) 28-35.
- [9] C. Lin, Y. Song, L. Cao, S. Chen, *J. Chin. Adv. Mater. Soc.* 1 (2013) 188-199.
- [10] M. Addamo, V. Augugliaro, A. Di Paola, E. García-López, V. Loddo, G. Marci, R. Molinari, L. Palmisano, M. Schiavello, *J. Phys. Chem. B* 108 (10) (2004) 3303–3310.
- [11] L. Liu, H. Bai, J. Liu, D.D. Sun, *J. Hazard. Mater.* 261 (2013) 214-223.
- [12] J. Fang, L. Xu, Z. Zhang, Y. Yuan, S. Cao, Z. Wang, L. Yin, Y. Liao, C. Xue, *ACS Appl. Mater. Interfaces*, 5 (2013), 8088-8092
- [13] R. Asahi, T. Morikawa, T. Ohwaki, K. Aoki, Y. Taga, *Science*, 293 (2001), 269-271.
- [14] T. Kamegawa, S. Matsuura, H. Seto, H. Yamashita, *Angew. Chem. Int. Ed.* 52 (2013) 916-919.
- [15] S. Hoang, S.P. Berglund, N.T. Hahn, A.J. Bard, C.B. Mullins, *J. Am. Chem. Soc.*, 134 (2012), 3659-3662.
- [16] Z. Wang, C. Yang, T. Lin, H. Yin, P. Chen, D. Wan, F. Xu, F. Huang, J. Lin, X. Xie, M. Jiang, *Adv. Funct. Mater.*, 23 (2013), 5444-5450.
- [17] A. H. Mamaghani, F. Haghghat, C.-S. Lee, *Appl. Catal. B: Environ.* 203 (2017) 247-269.
- [18] Y. Boyjoo, H. Sun, J. Liu, V. K. Pareek, S. Wang, *Chem. Eng. J.* 310 (2017) 537-559.
- [19] M.A. Aramendia, J.C. Colmenares, S. Lopez-Fernandez, A. Marinas, J.M. Marinas, F.J. Urbano, *Catal. Today* 129 (2007) 102-109.
- [20] N.E. Klepeis, W.C. Nelson, W.R. Ott, J.P. Robinson, A.M. Tsang, P. Switzer, J.V. Behar, S.C. Hern, W.H. Engelmann, *Anal. Environ. Epidemiol.* 11 (2001) 231–252.
- [21] L. Zhong, F. Haghghat, *Build. Environ.* 91 (2015) 191–203.
- [22] S. Wang, H.M. Ang, M.O. Tade, *Environ. Int.* 33 (2007) 694-705.
- [23] S.W. Verbruggen, *J. Photochem. Photobiol. C: Photochem. Rev.* 24 (2015) 64-82.
- [24] J.H. Mo, Y.P. Zhang, Q.J. Xu, J.J. Lamson, R.Y. Zhao, *Atmos. Environ.* 43 (2009) 2229-2246.
- [25] K. Nakata, A. Fujishima, *J. Photochem. Photobiol. C: Photochem. Rev.* 13 (2012) 169-189.
- [26] V. Augugliaro, M. Bellardita, V. Loddo, G. Palmisano, L. Palmisano, S. Yurdakal, *J. Photochem. Photobiol. C: Photochem. Rev.* 13 (2012) 224-245.
- [27] M.R. Nimlos, E.J. Wolfrum, M.L. Brewer, J.A. Fennell, G. Bintner, *Environ. Sci. Technol.* 30 (1996) 3102-3110.
- [28] R.M. Alberici, W.F. Jardim, *Appl. Catal. B: Environ.* 14 (1997) 55–68.
- [29] J. Mo, Y. Zhang, Q. Xu, R. Yang, *J. Hazard. Mater.* 168(2009) 276–281.
- [30] F.V.S. Lopes, R.A.R. Monteiro, A.M.T. Silva, G.V. Silva, J.L. Faria, A.M. Mendes, V.J.P. Vilar, R.A.R. Boaventura, *Chem. Eng. J.* 204-206 (2012) 244-257.
- [31] P.-A. Deveau, F. Arzac, P.-X. Thivel, C. Ferronato, F. Delpech, J.-M. Chovelon, P. Kaluzny, C. Monnet, *J. Hazard. Mater.* 144 (2007) 692–697.
- [32] A. Bouzaza, C. Vallet, A. Laplanche, *J. Photochem. Photobiol. A: Chem.* 177 (2006) 212–217.
- [33] R.A.R. Monteiro, S.M. Miranda, C. Rodrigues-Silva, J.L. Faria, A.M.T. Silva, R.A.R. Boaventura, V.J.P. Vilar, *Appl. Catal. B: Environ.* 165 (2015) 306–315.
- [34] L. Zhong, F. Haghghat, C.-S. Lee, *Build. Environ.* 62 (2013) 155-166.
- [35] D. Farhanian, F. Haghghat, *Build. Environ.* 72 (2014) 34-43.
- [36] V. Augugliaro, S. Colucci, V. Loddo, L. Marchese, G. Martra, L. Palmisano, M. Schiavello, *Appl. Catal. B: Environ.* 20 (1999) 15-27.
- [37] A.K. Boulamanti, C.J. Philippopoulos, *Atmos. Environ.* 43 (2009) 3168-3174.
- [38] M. Jafarikoju, M. Sohrabi, S.J. Royae, A. Hassanvand, *Clean Soil Air Water* 43 (2015) 662–670.

- [39] G. Marci, M. Addamo, V. Augugliaro, S. Coluccia, E. Garcia-López, V. Loddo, G. Martra, L. Palmisano, M. Schiavello *J. Photochem. Photobiol. A* 160 (2003) 105-114.
- [40] D. Vildoza, C. Ferronato, M. Sleiman, J.-M. Chovelon, *Appl. Catal. B: Environ.* 94 (2010) 303-310.
- [41] A.K. Boulamanti, C.A. Korologos, C.J. Philippopoulos, *Atmos. Environ.* 42 (2008) 7844-7850.
- [42] K.-P. Yu, G.W.M. Lee, W.-M. Huang, C. Wu, S. Yang, *Atmos. Environ.* 40 (2006) 375-385.
- [43] J. Jeong, K. Sekiguchi, W. Lee, K. Sakamoto, *J. Photochem. Photobiol. A: Chem.* 169 (2005) 279-287.
- [44] W. Wang, Y. Ku, *J. Photochem. Photobiol. A: Chem.* 159 (2003) 47-59.
- [45] M. Sleiman, P. Conchon, C. Ferronato, J.-M. Chovelon, *Appl. Catal. B: Environ.* 86 (2009) 159-165.
- [46] L. Cao, F.-J. Spiess, A. Huang, S.L. Suib, T.N. Obee, S.O. Hay, J.D. Freihaut, *J. Phys. Chem. B* 103 (1999) 2912-2917.
- [47] T.N. Obee, S.O. Hay, *Environ. Sci. Technol.* 31 (1997) 2034-2038.
- [48] H. Einaga, T. Ibusuki, S. Futamura, *J. Solar Energy Eng.* 126 (2004) 789-793.
- [49] F. Tang, X. Yang, *Build. Environ.* 56 (2012) 329-334.
- [50] D.H. Chen, X. Ye, K. Li, *Chem. Eng. Technol.* 28 (2005) 95-97.
- [51] J.-M. Herrmann, *Catal. Today* 53 (1999) 115-129.
- [52] J. Qu, M. Fan, *Crit. Rev. Environ. Sci. Technol.*, 40 (2010) 519-560.
- [53] X. Zhou, Y. Li, Y. Zhao, *RSC Adv.* 30 (2014) 15620-15629.
- [54] V. K. Gupta, I. Ali, T. A. Saleh, A. Nayak, S. Agarwal, *RSC Adv.* 2 (2012) 6380-6388.
- [55] S. Sun, C. Li, J. Sun, S. Shi, M. Fan, Q. Zhou, *J. Hazard. Mater.* 161 (2009) 1052-1057.
- [56] O. Ganzenko, D. Huguenot, E. D. van Hullebusch, G. Esposito and M. A. Oturan, *Environ. Sci. Pollut. Res.*, 21 (2014) 8493-8524.
- [57] S. Ray, M. Takafuj, H. Ihara, *RSC Adv.*, 3 (2013) 23664-23672.
- [58] S. Dong, J. Feng, M. Fan, Y. Pi, L. Hu, X. Han, M. Liu, J. Sun, *J. Sun RSC Adv.* 5 (2015) 14610-14630.
- [59] P.A.K. Reddy, P.V.L. Reddy, E. Kwon, K.H. Kim, T. Akter, S. Kalagara *Environ. Int.* 91 (2016) 94-103.
- [60] M. N. Chong, B. Jin, C. W. K. Chow, C. Saint, *Water Res.* 44 (2010) 2997-3027.
- [61] E. Casbeer, V. K. Sharma, X. Z. Li, *Sep. Purif. Technol.*, 87 (2012) 1-14.
- [62] Y. Qu, X. Duan, *Chem. Soc. Rev.*, 42 (2013) 2568-2580.
- [63] C. Chen, W. Ma, J. Zhao, *Chem. Soc. Rev.*, 39 (2010) 4206-4219.
- [64] R. Abe, *J. Photochem. Photobiol.*, C 11 (2010) 179-209.
- [65] S. T. Gadge, B. M. Bhanage, *RSC Adv.* (4) 2014 10367-10389.
- [66] R. Molinari, F. Pirillo, V. Loddo, L. Palmisano, *Catal. Today* 118 (2006) 205-2113.
- [67] G. Li, Y. Zhang, L. Wu, F. Wu, R. Wang, D. Zhang, J. Zhuang, H. Li, *RSC Adv.* 2 (2012) 4822-4828.
- [68] G. Mele, R. Del Sole, G. Vasapollo, E.G.-López, L. Palmisano, M. Schiavello, *J. Catal.* 217 (2003) 334-342.
- [69] G. Palmisano, M. Addamo, V. Augugliaro, T. Caronna, E. G. Lopez, V. Loddo, L. Palmisano, *Chem. Commun.*, 9 (2006) 1012-1014.
- [70] M. Bellardita, H.A. ElNazer, V. Loddo, F. Parrino, A.M. Venezia, L. Palmisano, *Catal. Today* 284 (2017) 92-99.
- [71] A. Di Paola, G. Marci, L. Palmisano, M. Schiavello, K. Uosaki, S. Ikeda, B. Ohtani, *J. Phys. Chem. B* 106 (2002) 637-645.
- [72] A. Di Paola, E.G. López, S. Ikeda, G. Marci, B. Ohtani, L. Palmisano, *Catal. Today* 75 (2002) 87-93.
- [73] J. Sheng, X. Li, Y. Xu, *ACS Catal.* 4 (2014) 732-737.
- [74] Y. Chen, S. Liang, L. Wen, W. Wu, R. Yuan, X. Wang and L. Wu, *Phys. Chem. Chem. Phys.*, 15 (2013) 12742-12747,
- [75] S. Higashimoto, R. Shirai, Y. Osano, M. Azuma, H. Ohue, Y. Sakata, H. Kobayashi, *J. Catal.* 311 (2014) 137-143.
- [76] R. M. Mohamed, E. Aazam, *Desalin. Water Treat.*, 51 (2013) 6082-6090.
- [77] A. A. Ismail, L. Robben, D. W. Bahnemann, *ChemPhysChem*, 12 (2011) 982-991.
- [78] L. Wang, X. Li, W. Teng, Q. Zhao, Y. Shi, R. Yue, Y. Chen, *J. Hazard. Mater.* 244-245 (2013) 681-688.
- [79] J. Yang, J. Dai, J. Li, *Environ. Sci. Pollut. Res.* 20 (2012) 2435-2447.
- [80] H. Chen, X. Zheng, Y. Chen, H. Mu, *RSC Adv.*, 3 (2013) 9835-9842.
- [81] K. S. Yao, D. Y. Wang, C. Y. Chang, K. W. Weng, L. Y. Yang, S. J. Lee, T. C. Cheng, C. C. Hwang, *Surf. Coat. Technol.*, 202 (2007) 1329-1332.
- [82] J. Zhang, Y. Liu, Q. Li, X. Zhang, J. K. Shang, *ACS Appl. Mater. Interfaces* 5 (2013) 10953-10959.
- [83] M. Ni, M.K.H. Leung, D.Y.C. Leung, K. Sumathy, *Renew. Sust. Energ. Rev.* 11 (2007) 401-425.

- [84] M. Bowker, *Catal. Lett.* 142 (2012) 923-929.
- [85] M Bowker, *Green Chem.* 13 (2011) 2235-2246.
- [86] M. Bowker, H. Bahruji, J. Kennedy, W. Jones, G. Hartley, C. Morton, *Catal Lett* 145 (2015) 214–219.
- [87] T.Hisatomi, K.Takanabe, K. Domen, *Catal. Lett.* (2015) 145, 95-108.
- [88] A. Kudo, Y.Miseki, *Chem. Soc. Rev.* 38 (2009), 253-278.
- [89] K. Maeda, K.Domen, *J. Phys. Chem. Lett.* 1 (2010) 2655–2661.
- [90] K. Sayama, K. Mukasa, R. Abe, Y. Abe, H.Arakawa, *Chem. Commun* (2001) 2416-2417.
- [91] H.Kato,M.Hori, R.Konta, Y.Shimodaira,A.Kudo, *Chem. Lett.* 33 (2004), 1348-1349.
- [92] T. Kawai, T. Sakata, *Nature* (1980) 286, 474-476.
- [93] GR. Bamwenda, S. Tsubota, T.Nakamura, M. Haruta, *J Photochem.Photobiol. A: Chem* 89(2) (1995) 177–89.
- [94] AA. Nada, MH. Barakat, HA. Hamed, NR. Mohamed, TN.Veziroglu, *Int J Hydrogen Energy* 30(7) (2005) 687-691.
- [95] SQ Peng, YX Li, FY Jiang, GX Lu, SB Li,*ChemPhys Lett* 398 (2004), 1–3, 235-239.
- [96] T Kida, GQ Guan, N Yamada, T Ma, K Kimura, A.Yoshida,*Int J Hydrogen Energy* 29(3) (2004)269-274.
- [97] T. Puangpetch, T. Sreethawong, S. Yoshikawa, S. Chavadej, *J. Mol. Catal. A: Chem.* 312 (2009) 97-106.
- [98] T. Sreethawong, T. Puangpetch, S. Chavadej, S. Yoshikawa, *J. Power Sources* 165 (2007) 861-869.
- [99] A. Hameed, M.A. Gondal, *J. Mol. Catal. A: Chem.* 233 (2005) 35-41.
- [100] A.Koca, M.Sahin *Int J of Hydrogen Energy* 27 (2002) 363–367.
- [101] GR Bamwenda, H.Arakawa, *Sol Energy Mater Sol Cells* 70 (2001) 1-14.
- [102] R. Abe, K.Sayama, K.Domen, H.Arakawa. *Chem Phys Lett* 344 (2001) 339–44.
- [103] K Sayama, K Yase, H Arakawa, K Asakura, A Tanaka, K Domen, et al. *J PhotochemPhotobiol A: Chem* 114 (1998) 125-135.
- [104] K Sayama, H Arakawa. *J PhotochemPhotobiol A: Chem* 77 (1994) (2–3) 243–247.

## Chapter 2: TiO<sub>2</sub>-based materials

### 2.1 Titanium dioxide

Titanium dioxide (TiO<sub>2</sub>) has attracted considerable attention for various applications such as pigments, photocatalysis, dye-sensitized solar cells, sensor devices, cosmetics and protective coatings. In particular, TiO<sub>2</sub> is the most studied photocatalyst because of its high efficiency, non-toxicity, chemical and biological stability, and low cost.

There are four common crystalline phases of TiO<sub>2</sub>: anatase, rutile, brookite, and TiO<sub>2</sub>(B) [1].

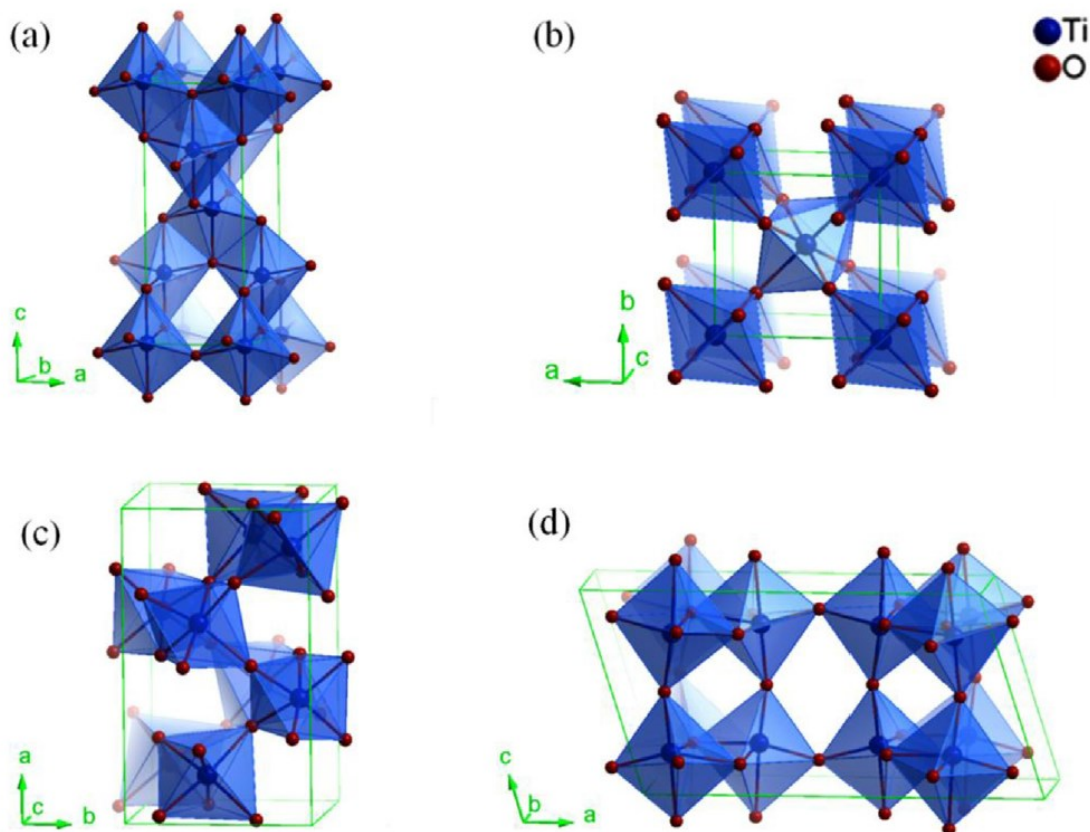


**Fig. 2.1** Crystalline structures of TiO<sub>2</sub> in different phases: (a) anatase, (b) rutile, (c) brookite, and (d) TiO<sub>2</sub>(B) [1].

As shown in Fig. 2.1, all of these phases consist of TiO<sub>6</sub> octahedra, but differ in both the distortion of their octahedra units and the manner in which they share edges and corners [2]. For anatase, four of the eight neighbors of each octahedral share edges; the subsequent others share corners. The corner-sharing octahedron forms the (0 0 1) planes and their edges connect with the plane of the octahedron below [3]. In rutile, the octahedral structure shares two edges and eight corners. The corner-sharing is along the [1 1 0] direction and stacks with their long axis alternation by 90° [3]. The Ti-O bond lengths are 1.937 and 1.966 Å for anatase and 1.946 and

1.983 Å for rutile in the equatorial and axial directions, respectively [3]. The different structural arrangements result in different space groups. For brookite, both corners and edges are connected [4, 5]. TiO<sub>2</sub>(B) is mainly derived from the layered titanates. The structure of TiO<sub>2</sub>(B) is composed of corrugated sheets consisting of both edges and corners shared by the TiO<sub>6</sub> octahedra [6].

Rutile is the stable phase at high temperatures, but anatase and brookite are common in fine grained (nanoscale) natural and synthetic samples. On heating concomitant with coarsening, the following transformations are all seen: anatase to brookite to rutile, brookite to anatase to rutile, anatase to rutile, and brookite to rutile. These transformation sequences are very closely balanced in energetic as a function of particle size. The surface enthalpies of the three polymorphs are sufficiently different that crossover in thermodynamic stability can occur under conditions that preclude coarsening, with anatase and/or brookite stable at small particle size [7]. The electronic structure of TiO<sub>2</sub> has been extensively studied using ab initio methodology [8]. Considering rutile and anatase phases, their differences in lattice structures cause different densities and electronic band structures, leading to different band gaps. For bulk materials, the band gap for anatase TiO<sub>2</sub> is approximately 3.20 eV (corresponding to 384 nm) and the band gap of rutile is 3.02 eV (corresponding to 410 nm). The electronic structure of both phases of TiO<sub>2</sub> can be understood with molecular band theory [8]. At the top of the valence band maximum (VBM) is the nonbonding O p orbital (out of the Ti<sub>3</sub>O cluster plane), where at the bottom of the conduction band maximum (CBM) are the nonbonding Ti d<sub>xy</sub> states. For rutile, the Ti d<sub>xy</sub> orbitals at CBM are relatively isolated, while the t<sub>2g</sub> orbitals of the CBM provide the metal-metal interaction with a smaller distance of 2.96 Å. The conductive band width of anatase is thus smaller than that of rutile, resulting in a slightly wider band gap of 3.2 eV as compared to 3.0 eV for rutile [9, 10].

Theoretical and experimental works report band gap values for brookite both smaller and larger than that of anatase. Experimental band gap energies ranging from 3.1 to 3.4 eV have been reported for brookite, but there is disagreement on whether the optical response is attributable to direct or indirect transitions [4]. The band gap was usually determined by diffuse reflectance measurements, from the tangent lines to the plots of the modified Kubelka-Munk function,  $[F(R'_{\infty})/hv]^{1/2}$ , versus the energy of the exciting light [11] considering brookite as an indirect semiconductor. Direct band gap values have been also obtained [12-14].

The precise value of E<sub>g</sub> is currently unknown since the experimental results often refer to samples not well crystallized.

The flat band potential, (E<sub>FB</sub>), of a semiconductor is a fundamental property for the thermodynamics of the interfacial electron transfer steps. For an n-type semiconductor as TiO<sub>2</sub> it

can be assumed that the positions of the flat band potential and the quasi-Fermi level ( $*E_f$ ) are the same and very close to the lower edge of the conduction band [15]. Di Paola *et al.* [16] determined the flat band potentials of anatase, brookite, and rutile by a slurry method [17], measuring the photovoltage of the corresponding suspensions in the presence of methyl viologen dichloride as a function of pH. As shown in Fig. 2.2, the values obtained at pH 7 were -0.45 V for anatase, -0.46 V for brookite, and -0.37 V for rutile.

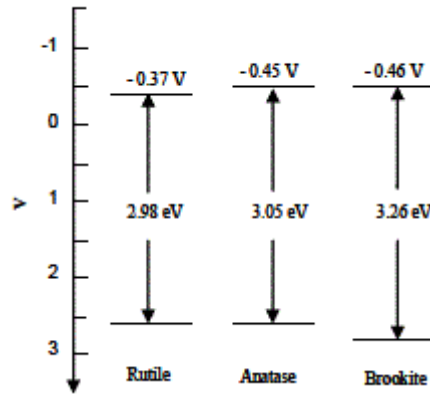
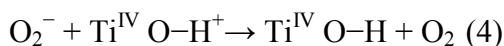
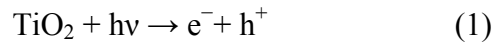


Fig. 2.2 Electrochemical potentials of the band edges of anatase, brookite, and rutile at pH = 7 [16].

The few experimental values of flat band potential of brookite reported in literature and the uncertainty on its band gap do not allow to exactly locate the position of the conduction and valence band edges of the three oxides of titanium. Anyway, the most probable hypothesis is that the flat band of brookite is shifted negatively with respect to that of anatase.

The electronic band structure influences the photon absorption process and redox reaction ability for photocatalysis. As explained in the chapter one, only photons with energy pertaining to that of the TiO<sub>2</sub> band gap can be absorbed. Upon exposure to the required photon energy, electrons in the valence band will be excited to the conduction band while leaving positively charged holes in the valence band. An electron-hole pair will therefore be generated, as expressed in followed equation typical for the TiO<sub>2</sub>-based materials:



These charge carriers have three possible fates: (i) be captured and trapped by defect sites within or on the surface of the material, (ii) recombine and release energy in the form of heat or light, or (iii) migrate to the surface and generate radical species in equations (2)-(4) [18]. Electron paramagnetic resonance studies have found that electrons are trapped by Ti atoms, forming two

Ti<sup>III</sup> centers, while holes are trapped as O centered radicals covalently linked to surface Ti atoms and localized differently at defect sites in TiO<sub>2</sub> nanoparticles [19]. Consequently, the reactions (1) and (2) are known as ‘deactivation processes’ since these electron-hole pairs do not play any part in photocatalysis. Therefore, the photocatalytic efficiency is determined by inhibiting process (1) and (2), while enhancing process (3) at optimized conditions.

As described before, the photocatalytic efficiency of TiO<sub>2</sub> photocatalyst is still low [20].

A variety of effective strategies have been adopted to enhance the photocatalytic efficiency of TiO<sub>2</sub> materials. In general, they can be summarized as either morphological change, such as tailoring the surface complexity, crystalline phase, pore and size of these materials, or as chemical modification by incorporation of additional components in the TiO<sub>2</sub> structure.

### *2.2 Strategy to enhance the TiO<sub>2</sub> photoefficiency: Chemical modifications*

It is possible to increase the photocatalytic activity of TiO<sub>2</sub> photocatalyst towards the development of supported TiO<sub>2</sub> materials to decrease their aggregation, designing the TiO<sub>2</sub> photocatalytic performance in the visible light range by doping with metallic or non-metallic elements or synthesizing TiO<sub>2</sub>-based composites.

Because of relatively small size (5-50 nm), TiO<sub>2</sub> is subjected to rapid aggregation in a suspension, considerably decreasing its effective surface area and catalytic efficiency. Another main limitation of pure TiO<sub>2</sub> is very poor adsorptive power, especially for non-polar dyes and organic pollutants due to its intrinsic surface characteristics, which restrict the photocatalytic oxidation reaction [21]. Therefore, photocatalysts in the form of nanoparticles, single atoms, molecules, and clusters should be anchored on various bulky support materials such as activated carbon [22], clay [23] and silica [24, 25] due to the small size of powder, leaking problems in aqueous media, and difficult handling in practical engineering applications [26]. Clearly, the support materials affect not only the adsorption of organic substrates, due to their nature, but also the crystallinity of TiO<sub>2</sub> photocatalyst [26].

In order to fully utilize the solar energy, considerable endeavor has been devoted to enhancing the TiO<sub>2</sub> photocatalytic performance in the visible light range [27, 28]. Doping with metallic or non-metallic elements has been widely used to improve photoactivity under visible light irradiation, in which non-metal or metal ions are either incorporated into the bulk of TiO<sub>2</sub> (Figs 2.3, 2.4) [29, 30].



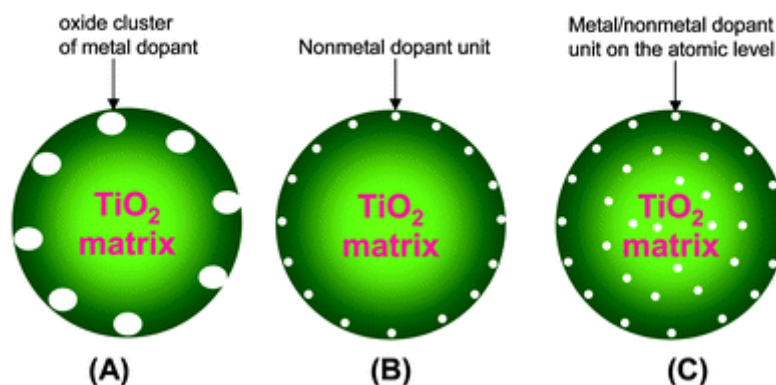


**Fig. 2.3** Scheme of modified  $\text{TiO}_2$ : (A) with transition metal oxide clusters, (B) with surface non-metal dopants and (C) bulk metal/non-metal dopants [30].

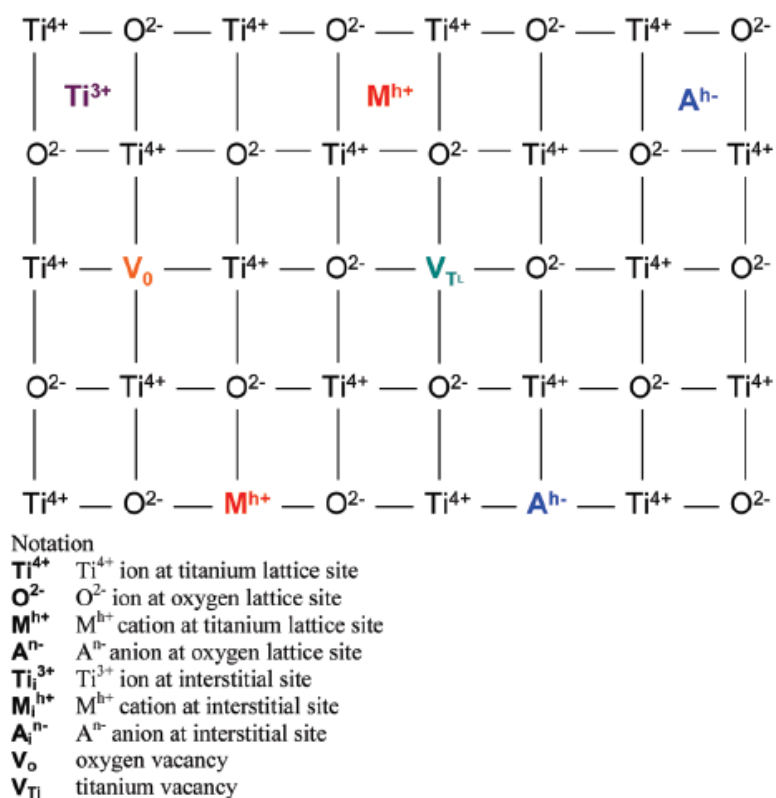


**Fig. 2.4** Schematic representation of the possible point defects present at the  $\text{TiO}_2$  lattice [31]

Non-metal doping is far more successful than metal decorating because it can create a mid-gap state acting as an electron donor or acceptor in the band gap of  $\text{TiO}_2$ , which introduces lower band gap and shifts the optical absorption of  $\text{TiO}_2$  into the visible-light region [31, 32]. In particular, carbon doping exhibits greatly potential advantages over other types of non-metal doping because of the several outstanding properties [33, 34]. For instance, carbon presents

metallic conductivity as one of the many possible electronic materials [35]. It has a large electron-storage capacity and can accept the photon-excited electrons to improve the separation of photo-generated carries [36]. Moreover, carbon absorbs a wide range of visible light absorption and show a high adsorption of organic pollutants, facilitating the interface reaction of photocatalysis [33, 34]. In the process of carbon doping, the C elements implied permeating to the lattice of TiO<sub>2</sub> substituting a lattice O atom and form O-Ti-C bond, which produces a hybrid orbital just above the valence band of TiO<sub>2</sub> resulting in an enhanced visible light absorbance [37].

N-doped TiO<sub>2</sub> seems to be promising dopant because of its comparable atomic size with oxygen, small ionization energy and high stability [38-40]. In the process of nitrogen doping, the N element is suggested permeating to the lattice of TiO<sub>2</sub> substituting a lattice oxygen atom and form nitride (Ti-N) or oxynitride (O-Ti-N) arrangements, introducing energy states above the valence band of titania due to N 2p, mixing of the N 2p with O 2p states, or introducing a new mid-gap state created by N incorporation [38-40].

Electron-hole charge separation is a key factor in achieving high quantum photocatalytic efficiency [41]. Noble metal particles such as Ag, Au, Pd and Pt have been introduced in TiO<sub>2</sub> materials to increase the lifetime of e<sup>-</sup>/h<sup>+</sup> pairs due to their plasmon resonance produced by the collective oscillations of surface electrons (Fig. 2.5) [42].

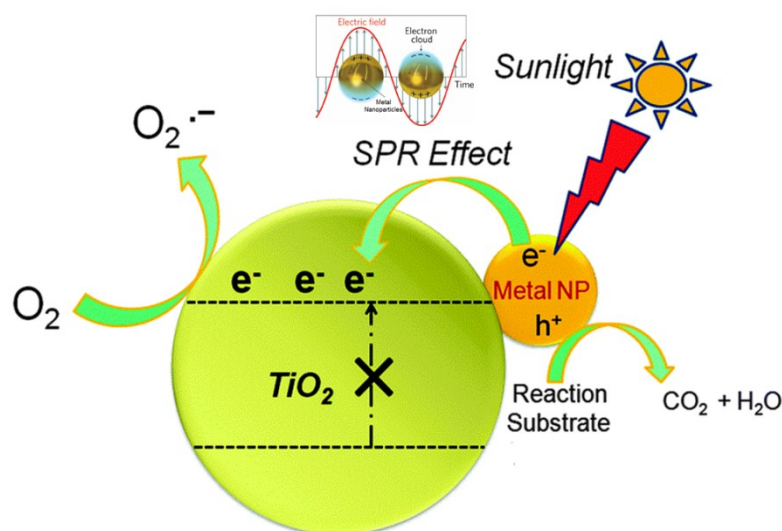
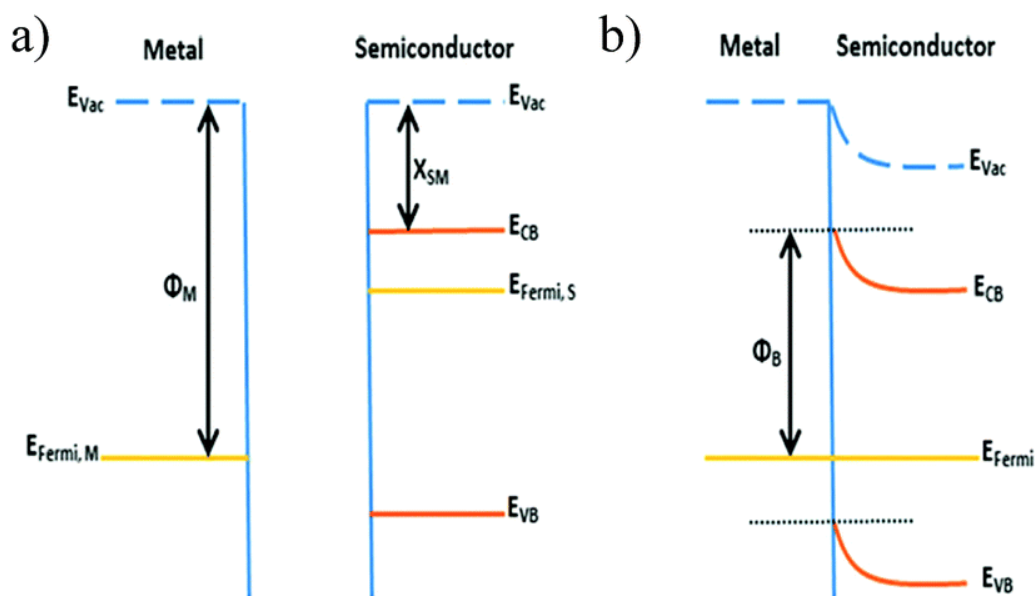


Fig. 2.5 Surface Plasmon Resonance effect on noble metal particles/TiO<sub>2</sub> system.

Here, the metal nanoparticle acts as a mediator in storing and shuttling photo-generated electrons from TiO<sub>2</sub> surface to an acceptor [43]. Decorating noble metal on TiO<sub>2</sub> photocatalyst has some advantages including:

(1) Delay of the electron-hole pair separation due to the Schottky barrier formed at the metal-semiconductor interface.

The formation of the Schottky barrier at noble metal-TiO<sub>2</sub> (semiconductor) interface is highly dependent on the work function of the noble metal ( $\phi_M$ ) and the electron affinity of the TiO<sub>2</sub> ( $X_{SM}$ ). Normally, the value of  $\phi_M$  is larger than that of  $X_{SM}$ , where  $X_{SM}$  is the energy difference between the minimum conduction band (CB) and the vacuum ( $E_{Vac}$ ) energy. Also the Fermi level ( $E_F$ ) of noble metal is typically lower than that of a semiconductor as shown in Fig. 2.6. When the noble metal and the semiconductor come into contact, the electrons in the semiconductor are transferred to the noble metal until they reach equilibrium. This results in the bending of the CB (i.e. Schottky barrier  $\phi_B$ ). More importantly, this charge redistribution leads to a built in electric field at the interface, which inhibits the recombination of photogenerated charges and improves the performance of devices for solar energy related applications [44, 45].



**Fig. 2.6** Formation of the Schottky barrier between a metal and a semiconductor before contact (a) and (b) after contact [44].

(2) Shift of the absorption of semiconductor from UV to visible-light region of the solar spectrum due to the unique surface plasmon resonance absorbance feature;

(3) Modification of the surface properties of the photocatalysts with a higher production of hydroxyl radicals through the reaction with hydrogen peroxide produced by oxygen photoreduction.

However, some disadvantages also exist [46, 47]. For instance, high concentration decorating could lead to formation of metal clusters, blocking the surface of semiconductor, and subsequently reducing light absorption and photocatalytic efficiency. Moreover, negatively charged metal particles can act as recombination centers trapping holes. Therefore, the suitable

amount of metal is vital for noble metal/TiO<sub>2</sub> photocatalysts with enhanced photocatalytic efficiency.

TiO<sub>2</sub> composite structures can create and tune similar properties such as mid-band gap electronic states which can alter charge migration or can produce a red shift in the absorption spectrum. Further, the formation of heterojunctions between TiO<sub>2</sub> and other materials can enhance visible light absorption by facilitating the charge separation of TiO<sub>2</sub>. When the TiO<sub>2</sub>-host oxide species is exclusively at the surface of the material, the result is the formation of composite systems. The TiO<sub>2</sub>-containing host phase may be present as patches of reduced dimensionality or completely encompassing the surface.

These systems consist of various useful systems as for example: host oxide-TiO<sub>2</sub>, phosphate-TiO<sub>2</sub>, and chalcogenide-TiO<sub>2</sub> materials. Archetypical examples are the rutile-anatase (TiO<sub>2</sub>-TiO<sub>2</sub>), TiO<sub>2</sub>-(SnO<sub>2</sub>; ZnO; ZrO<sub>2</sub>; Bi<sub>2</sub>O<sub>3</sub>; Fe<sub>2</sub>O; Fe<sub>3</sub>O<sub>4</sub>; WO<sub>3</sub>; CeO<sub>2</sub>; Cu<sub>2</sub>O), Bi<sub>2</sub>S<sub>3</sub>-, PbS-, CdS-, and CdSe-TiO<sub>2</sub> materials [31]. However, the list is shortened when limited to active and reasonably stable systems in connection with sunlight-excitation: WO<sub>3</sub>-; Cu<sub>2</sub>O-; BiO<sub>x</sub>Cl<sub>y</sub>- as well as specific geometrical configurations of CdS-; and CdSe-TiO<sub>2</sub> systems. Other useful candidates could be  $\gamma/\alpha$ -Fe<sub>2</sub>O<sub>3</sub>-TiO<sub>2</sub> and CeO<sub>2</sub>-TiO<sub>2</sub>, but these are somewhat limited since apparently there are only a few reports with sunlight although there are several with UV or visible light sources. Recently, some complex oxides such as FeTiO<sub>3</sub> [48] NiTiO<sub>3</sub> [49], LaVO<sub>4</sub> [50] and Bi-based oxides, or oxohalides [51, 52] have been also tested in contact with TiO<sub>2</sub>. Other less explored but yet important systems are the polyoxometalates and heteropolyacid-TiO<sub>2</sub>, [53-55] phosphate-TiO<sub>2</sub> [56], multiwall carbon-nanotube-TiO<sub>2</sub> [57] or polymer-TiO<sub>2</sub> systems [58, 59]. In these latter cases, the non-oxidic component but also the interface plays a capital role in the absorption of visible light photons.

Rutile-anatase (TiO<sub>2</sub>-TiO<sub>2</sub>) is interesting because the ion-doping of any of these phases leads to visible-light active materials and it is subjected to the most intense structural research. In the case of the P25 system (80% anatase, 20% rutile), it is well-known that nanometric (smaller than 20 nm) anatase patches are supported on larger rutile particles (ca. 25-30 nm). The Ti and O surface sites appear to complete their coordination at the interfaces, reaching, respectively, 6- and 3-fold coordinations characteristic of the bulk. This occurs at a narrow interface layer (less than 0.5 nm) with some general disorder with respect to the bulk oxides [60, 61]. In addition, novel punctual defects seem to appear.

**Fig. 2.7** illustrates the solubility of various elements on the TiO<sub>2</sub> anatase. Typically it has been observed a tendency for the surface segregation on TiO<sub>2</sub> for V, Ca, Sr, Ba, Mn, Zn, Sb, Fe, La and In and occasionally detected for Cr, Co, Ni, Mo, Zr, Sn, Ce or Nd, while other cations such

as Ta, Nb or W do not show any appreciable tendency to accumulate at the surface layer [31]. This is a direct consequence of the corresponding Metal (M) solubility limit into the anatase structure. This is relatively low (below 5 atom % in  $Ti_{1-x}M_xO_{2+\delta}$ ) for V, Fe, Mn, La and In; intermediate (ca. 5-12 atom %) for Mo, Cr, Co, Ni, Sn, Zr, Ce or Nd; very high (near or above 20 atom %) for their main cations mentioned. Ca, Sr and Ba may display high solubility limit(s) but concomitant amorphization of the titania structure occurs above ca. 5 atom % [62].

|                                |                                 |                                 |                                |                                     |                                 |                                 |                                 |                                |                                  |                                |                                  |                                  |                                |                                   |                                 |                                  |                              |                             |  |                             |
|--------------------------------|---------------------------------|---------------------------------|--------------------------------|-------------------------------------|---------------------------------|---------------------------------|---------------------------------|--------------------------------|----------------------------------|--------------------------------|----------------------------------|----------------------------------|--------------------------------|-----------------------------------|---------------------------------|----------------------------------|------------------------------|-----------------------------|--|-----------------------------|
| IA                             |                                 |                                 |                                |                                     |                                 |                                 |                                 |                                |                                  | VIII A                         |                                  |                                  |                                |                                   |                                 |                                  |                              |                             |  |                             |
| 1<br>H<br>Hydrogen<br>1.00797  | IIA                             |                                 |                                |                                     |                                 |                                 |                                 |                                |                                  |                                |                                  |                                  |                                |                                   |                                 |                                  |                              |                             |  | 2<br>He<br>Helium<br>4.0026 |
| 3<br>Li<br>Lithium<br>6.939    | 4<br>Be<br>Beryllium<br>9.0122  |                                 |                                |                                     |                                 |                                 |                                 |                                |                                  |                                |                                  |                                  |                                |                                   |                                 |                                  |                              | 10<br>Ne<br>Neon<br>20.183  |  |                             |
| 11<br>Na<br>Sodium<br>22.9897  | 12<br>Mg<br>Magnesium<br>24.312 |                                 |                                |                                     |                                 |                                 |                                 |                                |                                  |                                |                                  |                                  |                                |                                   |                                 |                                  |                              | 18<br>Ar<br>Argon<br>39.948 |  |                             |
| 19<br>K<br>Potassium<br>39.102 | 20<br>Ca<br>Calcium<br>40.08    | 21<br>Sc<br>Scandium<br>44.956  | 22<br>Ti<br>Titanium<br>47.88  | 23<br>V<br>Vanadium<br>50.942       | 24<br>Cr<br>Chromium<br>51.996  | 25<br>Mn<br>Manganese<br>54.938 | 26<br>Fe<br>Iron<br>55.847      | 27<br>Co<br>Cobalt<br>58.9332  | 28<br>Ni<br>Nickel<br>58.71      | 29<br>Cu<br>Copper<br>63.546   | 30<br>Zn<br>Zinc<br>65.37        | 31<br>Ga<br>Gallium<br>69.72     | 32<br>Ge<br>Germanium<br>72.59 | 33<br>As<br>Arsenic<br>74.9216    | 34<br>Se<br>Selenium<br>78.96   | 35<br>Br<br>Bromine<br>79.904    | 36<br>Kr<br>Krypton<br>83.80 |                             |  |                             |
| 37<br>Rb<br>Rubidium<br>85.47  | 38<br>Sr<br>Strontium<br>87.62  | 39<br>Y<br>Yttrium<br>88.905    | 40<br>Zr<br>Zirconium<br>91.22 | 41<br>Nb<br>Niobium<br>92.906       | 42<br>Mo<br>Molybdenum<br>95.94 | 43<br>Tc<br>Technetium<br>(99)  | 44<br>Ru<br>Ruthenium<br>101.07 | 45<br>Rh<br>Rhodium<br>102.905 | 46<br>Pd<br>Palladium<br>106.4   | 47<br>Ag<br>Silver<br>107.868  | 48<br>Cd<br>Cadmium<br>112.40    | 49<br>In<br>Indium<br>114.82     | 50<br>Sn<br>Tin<br>118.69      | 51<br>Sb<br>Antimony<br>121.75    | 52<br>Te<br>Tellurium<br>127.60 | 53<br>I<br>Iodine<br>126.9044    | 54<br>Xe<br>Xenon<br>131.30  |                             |  |                             |
| 55<br>Cs<br>Cesium<br>132.905  | 56<br>Ba<br>Barium<br>137.34    | 57<br>La<br>Lanthanum<br>138.91 | 72<br>Hf<br>Hafnium<br>178.49  | 73<br>Ta<br>Tantalum<br>180.948     | 74<br>W<br>Tungsten<br>183.85   | 75<br>Re<br>Rhenium<br>186.2    | 76<br>Os<br>Osmium<br>190.2     | 77<br>Ir<br>Iridium<br>192.2   | 78<br>Pt<br>Platinum<br>195.09   | 79<br>Au<br>Gold<br>196.967    | 80<br>Hg<br>Mercury<br>200.59    | 81<br>Tl<br>Thallium<br>204.37   | 82<br>Pb<br>Lead<br>207.19     | 83<br>Bi<br>Bismuth<br>208.980    | 84<br>Po<br>Polonium<br>(210)   | 85<br>At<br>Astatine<br>(210)    | 86<br>Rn<br>Radon<br>(222)   |                             |  |                             |
| 87<br>Fr<br>Francium<br>(223)  | 88<br>Ra<br>Radium<br>(226)     | 89<br>Ac<br>Actinium<br>(227)   |                                |                                     |                                 |                                 |                                 |                                |                                  |                                |                                  |                                  |                                |                                   |                                 |                                  |                              |                             |  |                             |
| Lanthanide Series              |                                 |                                 | 58<br>Ce<br>Cerium<br>140.12   | 59<br>Pr<br>Praseodymium<br>140.907 | 60<br>Nd<br>Neodymium<br>144.24 | 61<br>Pm<br>Promethium<br>(145) | 62<br>Sm<br>Samarium<br>150.35  | 63<br>Eu<br>Europium<br>151.96 | 64<br>Gd<br>Gadolinium<br>157.25 | 65<br>Tb<br>Terbium<br>158.924 | 66<br>Dy<br>Dysprosium<br>162.50 | 67<br>Ho<br>Holmium<br>164.930   | 68<br>Er<br>Erbium<br>167.26   | 69<br>Tm<br>Thulium<br>168.934    | 70<br>Yb<br>Ytterbium<br>173.04 | 71<br>Lu<br>Lutetium<br>174.97   |                              |                             |  |                             |
| Actinide Series                |                                 |                                 | 90<br>Th<br>Thorium<br>232.038 | 91<br>Pa<br>Protactinium<br>(231)   | 92<br>U<br>Uranium<br>238.03    | 93<br>Np<br>Neptunium<br>(237)  | 94<br>Pu<br>Plutonium<br>(242)  | 95<br>Am<br>Americium<br>(243) | 96<br>Cm<br>Curium<br>(247)      | 97<br>Bk<br>Berkelium<br>(247) | 98<br>Cf<br>Californium<br>(251) | 99<br>Es<br>Einsteinium<br>(254) | 100<br>Fm<br>Fermium<br>(257)  | 101<br>Md<br>Mendelevium<br>(258) | 102<br>No<br>Nobelium<br>(259)  | 103<br>Lr<br>Lawrencium<br>(260) |                              |                             |  |                             |

Fig. 2.7 Periodic table highlighting doping elements with small (orange), intermediate (blue) and high (yellow) solubility limit at the anatase structure [31].

M cations can additionally show differences in their location into the anatase lattice as most of the cations tend to occupy substitutional positions. Only a few such as Nd, V and Fe (and the noble metals) can favor partial (as they are additionally present at substitutional positions in most cases) occupation of interstitial positions [63-65]. There is some uncertainty with respect to Ce as well as Ni, Mn, Cr and/or Co on the doping level. These are typically either below or above 5 atom % which is attributable to the range of conditions driven by the multitude of experimental preparation methods. In the case of Ce, this can be related to the presence of additional phases such as  $CeTiO_4$  or the pyrochlore-type  $Ce_2Ti_2O_4$  which because they display limited crystallinity escape detection by conventional techniques. In addition, the presence of such phases would result in photoactivity and hence render the study of these Ce-Ti binary systems much more difficult [66, 67].

## 2.3 Strategy to enhance the TiO<sub>2</sub> photoefficiency: Structural modification of TiO<sub>2</sub>

### 2.3.1 Reduced TiO<sub>2</sub>

Recently, reduced TiO<sub>2</sub> (TiO<sub>2-x</sub>) materials have received much attentions, owing to the high photocatalytic and photoelectro-chemical (PEC) performance [68, 69]. The material was reported to show unique properties such as extended absorption edge of solar light and colorful appearance (ranging from yellow, red, blue, grey to black [70-73] color), along with structural changes on the surface and/or in the bulk: generation of Ti<sup>3+</sup> species and oxygen vacancies, formation of disordered layers on the surface, improvement of Ti-H species or Ti-OH bonds, narrowed band gap of the catalyst and modified electron density.

Regarding the properties of the (TiO<sub>2-x</sub>) materials some authors reported that the disorder lattice generates by the reduction process introduced mid-gap states inside the band gap of bare TiO<sub>2</sub> causing a blue shift of valence band, which was stabilized via the hydrogen incorporation by passivating dangling bonds [74]. The authors demonstrated that the enhanced solar light absorption over black TiO<sub>2</sub> was caused by the disordered surface layers, rather than traditional Ti<sup>3+</sup> doping [75]. Interestingly, other authors reported that the hydrogenated TiO<sub>2</sub> presented the generation of oxygen vacancies and hydroxyl group [76], and no shift of valence band was observed. That is, the hydrogen corporation results into the generation of Ti<sup>3+</sup> species and oxygen vacancies, rather than the formation of disordered layers on the surface of TiO<sub>2</sub>. The interaction between H atoms and oxygen vacancies was confirmed by *Mo et al.* via DFT (Density Function Theory) calculations [77]. Except oxygen vacancies, *Saputera et al.* and *Wang et al.* observed Ti<sup>3+</sup> species in electron paramagnetic resonance (EPR) [78, 79]. Furthermore, *Hu et al.* confirmed both the presence of Ti<sup>3+</sup> in the bulk of TiO<sub>2</sub> and disorders on the surface [80].

In general, reduced TiO<sub>2</sub> catalysts could be considered as the removal of a neutral oxygen atom on the surface or/and in the bulk of TiO<sub>2</sub>, and/or the incorporation of H atoms into the TiO<sub>2</sub> catalysts. The generation of oxygen vacancies induced by the removal of oxygen atoms will cause charge imbalance, promoting the formation of neighboring Ti<sup>3+</sup> species. The subsequent introduction of Ti<sup>3+</sup> will induce localized electronic states below the conduction band minimum (CBM) [81, 82]. The obtained localized states may act as the recombination centers of photogenerated electron-hole pairs and hinder the photocatalytic performance of TiO<sub>2-x</sub> samples. However, with continuous formation of oxygen vacancies, the localized states will enrich and mix with the CBM, narrowing the band gap of TiO<sub>2</sub> [75]. Meanwhile, the up-shifting of valence band maximum (VBM) with a band tail was also observed in the so-called “black” TiO<sub>2</sub> catalysts which were obtained by H<sub>2</sub> thermal treatment or plasma process which provided the active H species [83]. DFT calculation shows that while H atoms are incorporated into TiO<sub>2</sub> materials via

thermal treatment, the H atoms will occupy the location of oxygen vacancies, and attract electrons from the neighboring Ti and O atoms, resulting into high electron density of the H atoms. As a result, a shallow donor state will be introduced into TiO<sub>2</sub>. Besides, the blue-shift of band tail for hydrogenated P25 catalyst was confirmed by *Naldoni et al.* from  $\sim 1.2$  eV below the Fermi level to about  $-0.3$  eV, as shown in Fig. 2.8 [73].

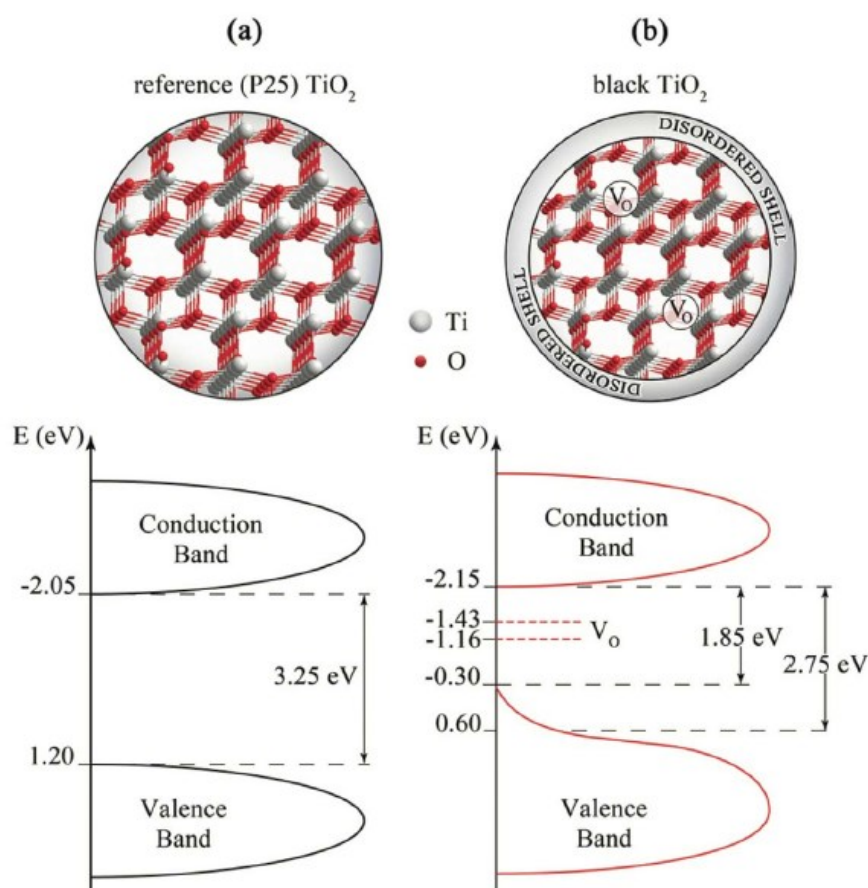


**Fig. 2.8** Schematic illustration of the structure of pure P25 (a) and black hydrogenated P25 (b) samples, respectively. The hydrogenated P25 catalyst showed a band tail above the VBM with a shift from 1.20 eV to  $-0.3$  eV. [73].

To probe the Ti<sup>3+</sup> and oxygen vacancies in reduced TiO<sub>2</sub> samples, XPS, EPR, STM, extended X-ray absorption fine structure (EXAFS) and other characterization techniques are employed. XPS is a common technique to analyze the surface chemical composition and the oxidation states of the elements. However, XPS can only reach few layers of the surface of TiO<sub>2</sub> samples, which limits the detect depth to  $\sim 10$  nm. To probe Ti<sup>3+</sup> in the bulk or subsurface of TiO<sub>2</sub>, XPS analysis combined with an argon sputtering treatment could be used to remove the top layers of TiO<sub>2</sub> under ultra-vacuum [84]. The locations of Ti 2p<sub>3/2</sub> and Ti 2p<sub>1/2</sub> usually show a blue shift because

of the introduction of Ti<sup>3+</sup> species, and oxygen vacancies can also be evidenced in the O1s XPS spectra.

Based on the special physical and chemical properties of TiO<sub>2-x</sub> photocatalyst, TiO<sub>2-x</sub> presents superior photocatalytic and photoelectrochemical performance, including photocatalytic degradation of organic compounds, photocatalytic hydrogen generation from water splitting, and CO<sub>2</sub> photoreduction [73]. TiO<sub>2-x</sub> was reported to show enhanced photocatalytic degradation of methylene blue, rhodamine B, methyl orange, 4-chlorophenol, reactive black 5 and phenol, because of its enhanced solar light absorption, narrowed band gap and improved separation of electron and hole pairs [73]. The photocatalytic H<sub>2</sub> production performance from water splitting is also improved after hydrogenation of TiO<sub>2</sub> catalyst [85, 86] and Ti<sup>3+</sup> doping [87, 88]. Besides, Fang *et al.* reported the CO<sub>2</sub> photoreduction for selective CH<sub>4</sub> evolution of TiO<sub>2-x</sub> materials under solar light irradiation [89]. Except for facilitating the separation of photogenerated electrons and holes, the oxygen vacancies enhance the trapping of CO<sub>2</sub> molecules and promote the formation of CO<sub>2</sub><sup>-</sup> species through a charge-transfer process.

### 2.3.2 Morphological change of TiO<sub>2</sub>

The most used TiO<sub>2</sub> morphology is that of nanoparticles/nanopowders with well-defined size and high crystallinity. It has been documented that TiO<sub>2</sub> nanocatalyst with lower particle size and higher surface area was more efficient at photodegrading substrates through photogenerated holes (h<sup>+</sup>) [90]. In the case of non-adsorbed substrates, however, the most efficient TiO<sub>2</sub> photocatalyst is that with large particle size, high crystallinity and high anatase phase content. However, the lifetime of reactive oxygen species, such as HO<sup>•</sup>, HOO<sup>•</sup> and H<sub>2</sub>O<sub>2</sub>, is insufficient long, particularly under ultraviolet (UV) irradiation, leading to incomplete mineralization of organic pollutants [91]. In addition, due to its low affinity to organic pollutants and the low surface area, the adsorbed amount of organic pollutants on TiO<sub>2</sub> surface is relatively low, yielding slow photocatalytic degradation rates [91]. The introduction of porosity in TiO<sub>2</sub> has been proved to be a promising mean for improving the photocatalytic activity, which is responsible for an enhanced mass transfer due to large pores in comparison to a solid TiO<sub>2</sub> material [92, 93]. Whilst the enhanced surface accessibility and photocatalytic reaction centers within the porous materials result in a higher amount of mass transfer of adsorbed reactants [94, 95]. Until now, the most popular method to develop porous TiO<sub>2</sub> materials has involved the use of various removable or sacrificial templates, including soft templating and hard templating approaches. The former mainly involves the use of low molecular-weight materials, such as



surfactant micelles, vesicles, bi- or tri-block copolymers, ionic liquids, and biomacro-molecules [96, 97], as templates to prepare porous TiO<sub>2</sub> materials.

The use of polymer or copolymer, such as silica, colloidal crystals, and polymeric beads [98, 99] is a simpler and facile approach in tailoring the morphology, structure, and pore size of TiO<sub>2</sub>. The typical fabrication method is shown in Fig. 2.9.

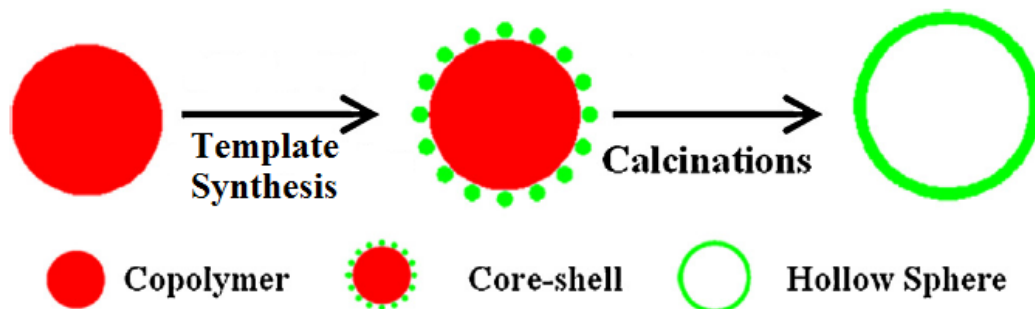


Fig. 2.9 Template strategy for the synthesis of hollow TiO<sub>2</sub>.

Another strategy to obtain a various hierarchically hollow microspheres, including CaCO<sub>3</sub>, TiO<sub>2</sub>, SnO<sub>2</sub>, Al<sub>2</sub>O<sub>3</sub> and WO<sub>3</sub>, is the chemically induced self-transformation method. The mechanism of chemically induced self-transformation (CIST) differs from the in situ template-free assembly, which refers to the spontaneous self-assembly of nanosized building blocks around the primary nuclei, while in CIST the hierarchical nanostructures such as hollow interiors are created via chemical etching of the primary particles. In general, the etching agents such as HF or OH<sup>-</sup> are in situ produced during the synthesis process [100]. The formation mechanism of the self-templated hollow spheres has been proposed based on a stepwise chemically induced self-transformation (CIST) process, as shown in Fig. 2.10 [101].

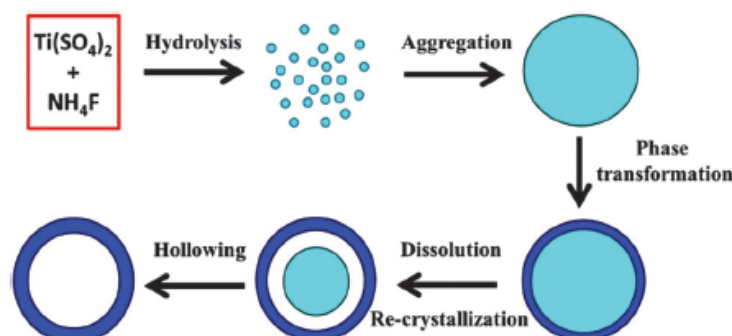
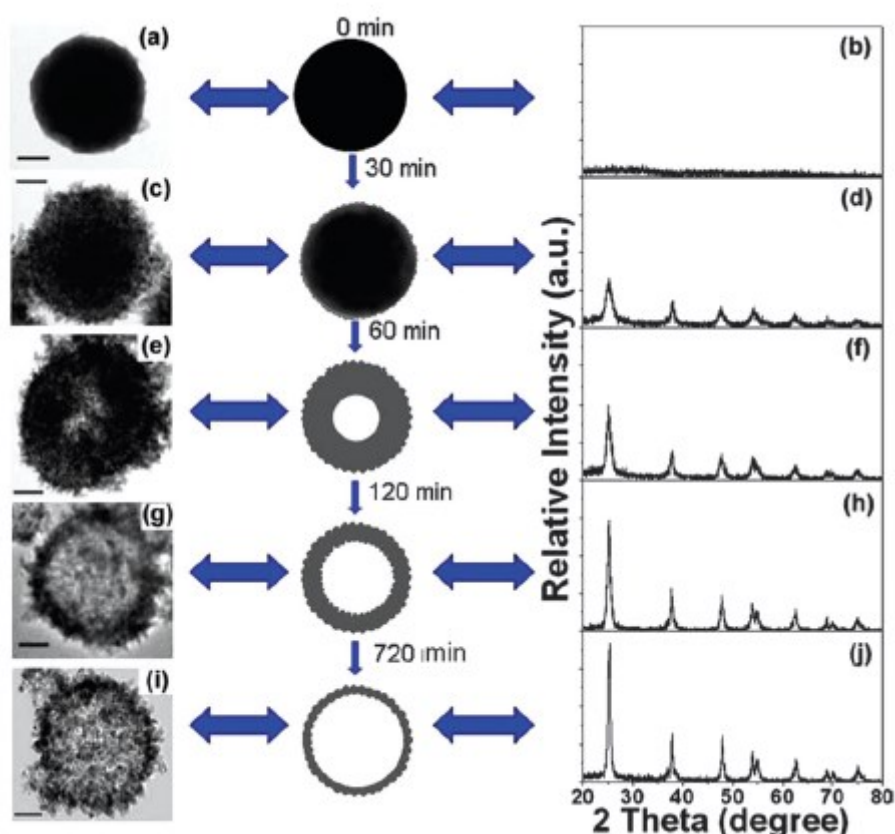


Fig. 2.10 Schematic illustration of the fluoride-induced self-transformation synthesis of hollow TiO<sub>2</sub> anatase microspheres [101].

Clearly, in the fluoride mediated self-transformation process, HF plays an important role in the dissolution of interior of particles and the fabrication of hollow structures. To avoid the strong

etching effect of HF, the well-defined anatase hollow microspheres can be fabricated in the presence of urea [102]. Later, it was suggested that a combined mechanism should be considered to better understand the complex formation process of hierarchical structures.

Photocatalysts with hierarchical structures can be formed through the selective oxidative etching and chemical etching [103, 104]. The surface-protected etching strategy can be further applied for producing hierarchical high-quality semiconductors for photocatalytic applications [105, 106]. Anatase TiO<sub>2</sub> hollow spheres can be easily prepared by self-transformation of amorphous TiO<sub>2</sub> solid spheres in an NH<sub>4</sub>F aqueous solution at 180°C for 12 h (Fig. 2.11) [107].



**Fig. 2.11** Formation mechanism of anatase TiO<sub>2</sub> hollow spheres prepared by hydrothermal treatment of amorphous TiO<sub>2</sub> solid spheres in NH<sub>4</sub>F aqueous solution. The left and right panels respectively show the TEM images and the corresponding XRD patterns of the intermediate products obtained at 180°C for different time periods (scale bar: 100 nm) [107].

It was shown that F<sup>-</sup> plays an important role in the formation of TiO<sub>2</sub> hollow spheres. The F<sup>-</sup> induced hollowing of TiO<sub>2</sub> solid spheres promoted the transformation of amorphous TiO<sub>2</sub> phase to anatase nanocrystals. The formation of TiO<sub>2</sub> hollow spheres is due to localized Ostwald ripening and chemically induced self-transformation.

On the basis of the above considerations, in this thesis three different approaches are used to increase the activity of TiO<sub>2</sub>-based materials:

- a) Chemical modifications; in particular the addition of CeO<sub>2</sub> and noble metals as Au, Ag and Pt at the commercial TiO<sub>2</sub> P25 was studied, investigating specifically the catalytic performance in the photo-oxidation of VOCs in the gas-phase, in the degradation of dyes in water and in the H<sub>2</sub> production by water splitting.
- b) Structural modifications: The influence of laser irradiation on various TiO<sub>2</sub> phases (anatase, rutile, P25) was examined, the changes in the chemico-physical properties were evaluated and correlated to the catalytic activity in the water splitting reaction.
- c) Structural and chemical modifications: The combination of structural (synthesis of Inverse Opal TiO<sub>2</sub>) and chemical (addition of other oxides (CeO<sub>2</sub>, CuO), BiVO<sub>4</sub>, and metals and non-metal (W, Hf, N) on the Inverse Opal TiO<sub>2</sub> ) modifications was studied, the photocatalytic performance in the degradation of dyes in water, in the photo-oxidation of VOCs and in the H<sub>2</sub> production by water splitting was examined.

## References

- [1] Y. Ma, X. Wang, Y. Jia, X. Chen, H. Han, C. Li Chem. Rev. 114 (2014) 9987-10043.
- [2] I.Hwang, M.Baek, K.Yong, ACS Appl. Mater.Interfaces 7 (2015)27863-27870.
- [3] U.Diebold, Surf. Sci. Rep. 48 (2003) 53–229.
- [4] A. Di Paola, M.Bellardita, L. Palmisano, Catalysts 3 (2013) 36.
- [5] Y. Xu, H. Lin, L. Li, X. Huang, G.Li, J. Mater. Chem. A (2015) 3 22361-22368.
- [6] Z.Liu, YG.Andreev, A.R. Armstrong, S.Brutti, Y.Ren, P.G.Bruce,Prog. Nat. Sci. Mater. Int.23 (2013) 235-244.
- [7] X. Chen, SS Mao, Chem. Rev. 107 (2007), 2891-2959.
- [8] R. Asahi, Y. Taga, W.Mannstadt, A.J. Freeman Phys. Rev. B 61 (2000) 7459-7465.
- [9] Y. Liu, Z. Li, M. Green, M. Just, Y.Y. Li, X. Chen, J. Phys. D: Appl. Phys. 50 (2017) 193003.
- [10]A. Fujishima , X. Zhang, D. A. Tryk, Surf. Sci. Rep. 63 (2008) 515-582.
- [11]Y.I Kim, S.J Atherton,E.S Brigham, T.E Mallouk,J. Phys. Chem. 97 (1993) 11802-11810.
- [12]W Hu,L.Li, G.Li,C.Tang,L.Sun, Cryst. Growth Des. 9 (2009) 3676–3682.
- [13]V Štengl, D. Králová, Mater. Chem. Phys. 129 (2011) 794–801.
- [14]T.D.Nguye-Phan, E.J Kim, S.H. Hahn, W.J. Kim, E.W Shin, J. Colloid Interface Sci. 356 (2011) 138–144.
- [15]D.Dung, J.Ramsden, M.Grätzel, J. Am. Chem. Soc. 104 (1982) 2977–2985.
- [16]A. Di Paola, M.Bellardita,R.Ceccato, L.Palmisano, F. Parrino,J. Phys. Chem. C 113 (2009) 15166–15174.
- [17]A.M.Roy, G.C De,N.Sasmal,S.S.Bhattacharyya, Int. J. Hydrogen Energy 20 (1995) 627-630.
- [18]S.H. Szczepankiewicz, A.J.Colussi, M.R. Hoffmann J. Phys. Chem. B 104 (2000) 9842 9850.
- [19]R. F.Howe, M. Gratzel J. Phys. Chem. 91 (1987) 3906-3909.
- [20]J. Chen, F. Qiu, W. Xu, S. Cao, H. Zhu, Appl. Catal. A: Gen: 495 (2015) 131-140.
- [21]J. Mo, Y. Zhang, Q. Xu, R. Yang, J. Hazard. Mater. 168 (2009) 276-281.
- [22]J.W. Shi, H.J. Cui, J.W. Chen, M.L. Fu, B. Xu, H.Y. Luo, Z.L. Ye, J. Colloid InterfaceSci. 388 (2013) 201-208.
- [23]C. Liao, Q. Wu, T. Su, D. Zhang, Q. Wu, Q. Wang, ACS Appl. Mater. Interfaces 6(2014) 1356-1360.
- [24]S.F. Resende, E.H. Nunes, M. Houmard, W.L. Vasconcelos, J. Colloid InterfaceSci. 433 (2014) 211-217.
- [25]M. Bellardita , M. Addamo, A. Di Paola, G. Marci, L. Palmisano, L. Cassar, M. Borsac, J. Colloid InterfaceSci. 174 (2010) 707-713.
- [26]X. Qian, K. Fuku, Y. Kuwahara, T. Kamegawa, K. Mori, H. Yamashita, Chem-SusChem 7 (2014) 1528-1536.
- [27]S. Neatu, J. A. Macia -Agullo, P. Concepcion, H. Garcia, J. Am. Chem. Soc. 2014, 136, 15969-15976.
- [28]D. Ding, K. Liu, S. He, C. Gao, Y. Yin, Nano Lett., 2014, 14 (11), 6731-6736.
- [29]Z. Zhang, X. Wang, J. Long, Q. Gu, Z. Ding, X. Fu, J. Catal. 276 (2010) 201-214.
- [30]G. Liu, L. Wang, H. G. Yang, H.-M. Cheng, G. Q.M. Lu, J. Mater. Chem., 20 (2010) 831-843.
- [31]A. Kubacka, M. Fernandez-García, G. Colon, Chem. Rev. 112 (2012) 1555–1614.
- [32]P. Zhang, C. Shao, Z. Zhang, M. Zhang, J. Mu, Z. Guo, Y. Liu, Nanoscale 3 (2011) 2943–2949.
- [33]S. Lee, Y. Lee, D.H. Kim, J.H. Moon, ACS Appl. Mater. Interfaces 5 (2013)12526-12532.
- [34]Z. He, W. Que, Y. He, RSC Adv. 4 (2014) 3332–3339.
- [35]K. Woan, G. Pyrgiotakis, W. Sigmund, Adv. Mater. 21 (2009) 2233-2239.
- [36]G. Zhang, F. Teng, Y. Wang, P. Zhang, C. Gong, L. Chen, C. Zhao, E. Xie, RSC Adv.3 (2013) 24644-24649.
- [37]Y. Zhang, Z. Zhao, J. Chen, L. Cheng, J. Chang, W. Sheng, C. Hu, S. Cao, Appl.Catal. B: Environ. 165 (2015) 715–722.
- [38]D. Wang, L. Jia, X. Wu, L. Lu, A. Xu, Nanoscale 4 (2012) 576-584.
- [39]F. Spadavecchia, G. Cappelletti, S. Ardizzone, C.L. Bianchi, S. Cappelletti, C. Oliva,P. Scardi, M. Leoni, P. Fermo, Appl. Catal. B: Environ. 96 (2010) 314-322.
- [40]M. Bellardita, M. Addamo, A. Di Paola, L. Palmisano, A. M. Venezia, Phys. Chem. Chem. Phys., 11 (2009) 4084-4093.
- [41]S. Kedem, D. Rozen, Y. Cohen, Y. Paz, J. Phys. Chem. C 113 (2009) 14893–14899.
- [42]H. Fang, C.X. Zhang, L. Liu, Y.M. Zhao, H.J. Xu, Biosens. Bioelectron. 64 (2014)434–441.
- [43]Z. Xiong, J. Ma, W.J. Ng, T.D. Waite, X.S. Zhao, Water Res. 45 (2011) 2095–2103.

- [44]C. Ray, T.PalJ. Mater. Chem. A5 (2017) 9465-9487.
- [45]M. R. Khan, T. W. Chuan, A. Yousuf, M. N. K. Chowdhury and C. K. Cheng, Catal. Sci. Technol. 5 (2015) 2522-2531
- [46]E.P. Melián, O. González Díaz, J.M. Dona Rodríguez, G. Colón, J.A. Navío, M.Maciasb, J. Pérez P`ena, Appl. Catal. B: Environ. 127 (2012) 112-120.
- [47]C. Liu, Z. Lei, Y. Yang, H. Wang, Z. Zhang, Bioresour. Technol. 137 (2013)57-62.
- [48]B. Gao, Y. J. Kim, A. K.Chakraborty,W. I. Lee, Appl. Catal. B: Environ.83 (2008), 202-207.
- [49]D.H. Kim, H.S.Park, S.J. Kim, K.S. Lee, Catal. Lett. 106 (2006) 29-33.
- [50]H.Huang, D.Li,Q.Lin, W. Zhang,Y.Shao,Y. Chen,M.Sun, X.Fu, Environ. Sci. Technol. 43 (2009) 4164-4168.
- [51]Z. Ban, J.Zhu, S.Wang, Y.Cao,X.Quian,H. Li, J. Phys. Chem. C 112 (2008) 6258-6262.
- [52]X.Zhang, L.Zhang, T.Xie,D.Wang, J. Phys. Chem. C 113 (2009)7371-7378.
- [53]N. Fu, G. Lu, Chem. Commun. (2009) 3591-3593.
- [54]G. Marci, E. García-López, V. Vaiano, G. Sarno, D. Sannino, L. Palmisano, Catal. Today 281 (2017) 60-70.
- [55]G. Marci, E. García-López, F. R. Pomilla, L. F Liotta, L. Palmisano, Appl. Catal A:Gen. 528 (2016) 113-122.
- [56]K.Rajeshwar,N. R de Tacconi, C. R. Chenthamarakshan, Chem. Mater. 13 (2001) 2765-2782.
- [57]K.Woan, G.Pyrgiotakis,W.Sigmud, Adv. Mater. 21 (2009) 2233–2239.
- [58]A. Kubacka, C. Serrano, M.L Cerrada, M. Fernandez-García, M. Ferrer, M. J. Fernandez-García, Phys. Chem. C 113 (2009) 9182-9190.
- [59]Y.Wang, M.Zhang, F.Cheng,J. Yang, Appl. Catal., B: Environ. 90 (2009) 249-254.
- [60]Y.Bessekhouad, D.Robert,Jr.Weber, J. Photochem. PhotobiolA 163 (2004) 569-580.
- [61]N.A Deskins, S.Kerisit, K.M. Rosso, M.J Dupuis,Phys. Chem. C 111 (2007) 9290-9298.
- [62]J. Lin, J.C. Yu, D. Lo,S. K. Lam, J. Catal. 183 (1999)368-372.
- [63]M. Fernandez-García, A. Martínez-Arias, A. Fuente; J.C. Conesa, J. Phys. Chem. B 109 (2005) 6075-6083.
- [64]P.Knauth, A.V Chadwick,. P.E.; LippensG. Auer, Phys. Chem. Phys. Chem. 10 (2009) 1238-1246.
- [65]J.A.Wang,. R. Limas-Ballesteros,T. Lopez, A. Moreno, R. Gomez, O. Novaro, X. Bokhimi, J. Phys. Chem. B 105 (2001) 9692-9698.
- [66]Y.Xie,C.Yuan, Appl. Catal., B 2003, 46, 251-259.
- [67]Y.M Otsuka,. S. Omata, T. Yoshimura, M. J. Alloys Compd. 2004, 376, 262-267.
- [68]Z. Wang, B. Wen, Q. Hao, L.M. Liu, C. Zhou, X. Mao, X. Lang, W.J. Yin, D. Dai, A.Selloni, X. Yang, J. Am. Chem. Soc. 137 (2015)9146–9152.
- [69]W. Fang, M. Xing, J. Zhang, Appl. Catal. B:Environ. 160(2014) 240-246.
- [70]Z. Tian, H. Cui, G. Zhu, W. Zhao, J. Xu, F. Shao, J. He, F. Huang, J. Power Sources 325 (2016) 697-705.
- [71]Y. Liu, B. Quan, G. Ji, H. Zhang, Mater. Lett. 162 (2016) 138-141.
- [72]G. Liu, L.-C. Yin, J. Wang, P. Niu, C. Zhen, Y. Xie, H.-M. Cheng, Energ. Environ. Sci. 5 (2012)9603-9610.
- [73]A. Naldoni, M. Allieta, S. Santangelo, M. Marelli, F. Fabbri, S. Cappelli, C.L.Bianchi, R. Psaro, V. Dal Santo, J. Am. Chem. Soc. 134(2012) 7600-7603.
- [74]X. Chen, L. Liu, P.Y. Yu, S.S. Mao, Science 331 (2011) 746-750.
- [75]W. Fang, M. Xing, J. Zhang, J. Photoch. Photobio. C32 (2017) 21-39.
- [76]T. Leshuk, R. Parviz, P. Everett, H. Krishnakumar, R.A. Varin, F. Gu, ACS Appl. Mater. Inter. 5 (2013) 1892-1895.
- [77]L.B. Mo, Y. Wang, Y. Bai, Q.Y. Xiang, Q. Li, W.Q. Yao, J.O. Wang, K. Ibrahim,H.H. Wang, C.H. Wan, J.L. Cao, Sci.Rep. 5 (2015) 17634.
- [78]W.H. Saputera, G. Mul, M.S. Hamdy, Catal. Today 246 (2015) 60–66.
- [79]J. Cai, Y. Wang, Y. Zhu, M. Wu, H. Zhang, X. Li, Z. Jiang, M. Meng, ACS Appl. Mater. Inter. 7(2015) 24987–24992.
- [80]W. Hu, W. Zhou, K. Zhang, X. Zhang, L. Wang, B. Jiang, G. Tian, D. Zhao, H. Fu, J. Mater. Chem. A 4 (2016) 7495-7502.
- [81]F. Zuo, L. Wang, T. Wu, Z. Zhang, D. Borchardt, P. Feng, J. Am.Chem. Soc. 132 (2010) 11856-11857.
- [82]E. Finazzi, C.D. Valentin, G. Pacchioni, A. Selloni, J. Chem. Phys. 129 (2008) 154113.

- [83]G. Panomsuwan, A. Watthanaphanit, T. Ishizaki, N. Saito, *Phys. Chem. Chem. Phys.* 17 (2015)13794–13799.
- [84]Z. Zhang, M.N. Hedhili, H. Zhu, P. Wang, *Phys. Chem. Chem. Phys.* 15 (2013) 15637-15644.
- [85]H. Tan, Z. Zhao, M. Niu, C. Mao, D. Cao, D. Cheng, P. Feng, Z. Sun, *Nanoscale* 6 (2014) 10216-10223.
- [86]A. Sinhamahapatra, J.-P. Jeon, J.-S. Yu, *Energ. Environ. Sci.* 8 (2015) 3539-3544.
- [87]X. Liu, Z. Xing, H. Zhang, W. Wang, Y. Zhang, Z. Li, X. Wu, X. Yu, W. Zhou, *ChemSusChem* 9 (2016) 1118-1124.
- [88]G. Fu, P. Zhou, M. Zhao, W. Zhu, S. Yan, T. Yu, Z. Zou, *Dalton Trans.* 44 (2015) 12812-12817.
- [89]W. Fang, L. Khrouz, Y. Zhou, B. Shen, C. Dong, M. Xing, S. Mishra, S. Daniele, J.Zhang, *Phys. Chem. Chem. Phys.* 19 (2017) 13875-13881
- [90]C. Fernández-Rodríguez, J.M. Dõna-Rodríguez, O. González-Díaz, I. Seck, D.Zerbani, D. Portillo, J. Perez-Pena, *Appl. Catal. B: Environ.* 125 (2012) 383-389.
- [91]Z. Xiong, J. Ma, W.J. Ng, T.D. Waite, X.S. Zhao, *Water Res.* 45 (2011) 2095-2103.
- [92]X. Wang, R.A. Caruso, *J. Mater. Chem.* 21 (2011) 20-28.
- [93]Z. Xing, W. Zhou, F. Du, L. Zhang, Z. Li, H. Zhang, W. Li, *ACS Appl. Mater.Interfaces* 6 (2014) 16653-16660.
- [94]S. Lu, D. Wu, Q. Wang, J. Yan, A.G. Buekens, K. Cen, *Chemosphere* 82 (2011)1215–1224.
- [95]M. Srinivasan, T. White, *Environ. Sci. Technol.* 41 (2007) 4405-4409.
- [96]L.N. Quan, Y.H. Jang, K.A. Stoerzinger, K.J. May, Y.J. Jang, S.T. Kochuveedu, Y. Shao-Horn, D.H. Kim, *Phys. Chem. Chem. Phys.* 16 (2014) 9023-9030.
- [97]H.Y. Chen, T.L. Zhang, J. Fan, D.B. Kuang, C.Y. Su, *ACS Appl. Mater. Interfaces* 5(2013) 9205-9211.
- [98]S. Linley, T. Leshuk, F.X. Gu, *ACS Appl. Mater. Interfaces* 5 (2013) 2540-2548.
- [99]M.C. Orilall, N.M. Abrams, J. Lee, F.J. DiSalvo, U. Wiesner, *J. Am. Chem. Soc.* 130(28) (2008) 8882-8883.
- [100] X. Li, J. Yu, M. Jaroniec, *Chem. Soc. Rev.*45 (2016) 2603-2636.
- [101] K. Lv, B. Cheng, J. Yu and G. Liu, *Phys. Chem. Chem. Phys.*,2012, 14, 5349-5362.
- [102] S. Liu, J. Yu, S. Mann, *Nanotechnology* 20 (2009) 325606.
- [103] S. Sun, X. Song, C. Kong, Z. Yang, *CrystEngComm*, 13 (2011) 6616-6620.
- [104] J. Cao, B. Xu, H. Lin, B. Luo, S. Chen, *Chem. Eng. J.* 185 (2012) 91-99.
- [105] Q. Zhang, T. Zhang, J. Ge, Y. Yin, *Nano Lett.* 8 (2008)2867-2871
- [106] J. H. Pan, X. Z. Wang, Q. Huang, C. Shen, Z. Y. Koh, Q. Wang, A. Engel, D. W. Bahnemann, *Adv. Funct. Mater.* 24 (2014) 95-104.
- [107] J. G. Yu, J. Zhang, *Dalton Trans.*, 39 (2010) 5860-5867.

## Chapter 3: Chemical modifications of TiO<sub>2</sub>

### 3.1 TiO<sub>2</sub>-CeO<sub>2</sub> based composites

Cerium dioxide (ceria, CeO<sub>2</sub>) has been extensively utilized in many practical applications [1] such as polishing materials [2], solar cells [3], ultra-violet light-blocking materials [4] and catalytic and photocatalytic material [5-7]. Ceria has attracted much attention due to its well-controlled morphology, fluorite-type structure [8], remarkable redox properties and prominent oxygen storage [9, 10] and release capacity (OSC) via facile conversion between Ce<sup>4+</sup> and Ce<sup>3+</sup> oxidation states [11, 12]. Recently, the nanocomposites of TiO<sub>2</sub> with CeO<sub>2</sub> have received a great deal of interest because of special f and d electron orbital structures, the unique UV absorbing ability, the high thermal stability, the high electrical conductivity and the large oxygen storage capacity of CeO<sub>2</sub> which significantly improves the photocatalytic efficiency of TiO<sub>2</sub> [13, 14]. The different electronic structures of Ce<sup>3+</sup>(4f<sup>1</sup>5d<sup>0</sup>) and Ce<sup>4+</sup>(4f<sup>0</sup>5d<sup>0</sup>) could result in different optical and catalytic properties [15, 16]. *Li et al.* [15] proposed that the presence of Ce<sup>4+</sup> on the surface of TiO<sub>2</sub> promotes the production of hydroxyl radicals from dissolved oxygen increasing the capture efficiency of photogenerated electrons. Apart from its redox properties, *Li et al.* [16] also proposed that Ce doping would increase on the surface of TiO<sub>2</sub> the proportion of surface oxygen vacancies able to capture photogenerated electrons and limiting therefore the bulk recombination process. Moreover, *Xu et al.* [17] confirmed that rare earth doping of TiO<sub>2</sub> could be efficient for further extension of the light absorption of TiO<sub>2</sub> to the visible region. Moreover, photocatalytic properties of cerium-doped TiO<sub>2</sub> strongly depend on the way with this rare earth element is implemented onto the semiconductor.

Different methods have indeed been applied to introduce cerium element in the structure of TiO<sub>2</sub>, as sol-gel, solvothermal processes or electrospinning techniques [18-20]. In all the above cases, cerium was found to be located at the TiO<sub>2</sub> surface. By contrast with these previous examples, *Gu et al.* [21] synthesized Ce intercalated layered titanates through an ion-exchange process followed by thermal treatment. This process however leads to lattice dislocation strongly affecting negatively the ability for photocatalysis. Only a suitable thermal treatment at T ≥ 400°C led to lattice re-arrangement and improved photocatalytic properties through enhanced electron-hole separation induced by the intercalated cerium ion. Additionally, the impregnation method was also considered [22, 23] due to its easiness of preparation and its ability to better preserve the total amount of introduced dopant in the final material. Using this approach, *Xue et al.* [22] found Ce-doped TiO<sub>2</sub> nanotubes active in the photodegradation of the glyphosate herbicide.

Main results revealed that crystal growth and electron-hole life time are the most important factors to be controlled in order to reach high photocatalytic efficiency. CeO<sub>2</sub>-TiO<sub>2</sub> mixed oxide powders have been prepared with different Ce/Ti ratios, ranging from 0.1 to 0.9. An intermixed solid solution can form when ceria is the predominant component, while separate phases of ceria and titania coexist when CeO<sub>x</sub> is a minor component [24]. *Barrio et al.* [25] prepared CeO<sub>x</sub>-TiO<sub>2</sub> catalysts by wet impregnation methods with 6 and 15 wt % ceria loadings. Depending on the ceria loading, the interaction between the two metal oxides could lead to unusual coordination modes; nanoparticles with a fluorite structure were observed only at the high ceria loadings. Better reducibility was observed for lower ceria loading, indicating stronger interaction of the CeO<sub>x</sub> nanoparticles with the TiO<sub>2</sub> support. *Kundu et al.* [26] investigated the electronic properties and structure of Pt dispersed on ceria-modified TiO<sub>2</sub>. Interestingly, Ce<sup>3+</sup> was identified on the surface and at the CeO<sub>x</sub>-TiO<sub>2</sub> interface drastically enhancing the formation of electron-hole pairs under visible light irradiation. In this system, the Pt not only played the role of an electron-trapping center, prolonging the charge carrier lifetime, but also increased the Ce<sup>3+</sup> concentration, whereby improving performance for photocatalytic water splitting.

### 3.2 Au/TiO<sub>2</sub> catalysts

The excellent catalytic performance of gold nanoparticles in environmental processes such as low temperature CO oxidation, removal of VOCs and Water Gas-Shift (WGS) reactions has been in the last decade largely demonstrated [27-29]. All these processes benefit from the unique catalytic properties of gold nanoparticles finely dispersed on metal oxides supports [27]. Modified Incipient Wetness Impregnation or Deposition-Precipitation are the methods more widely used for the preparation of these catalysts [27, 30]. Apart from the particle size, the morphology of gold aggregates is also considered as a key factor for this singular catalytic behavior [31, 32]. The effect of the support and/or the presence of different kinds of promoters on the catalytic performance of gold have also been investigated, and a general agreement about the advantages of using reducible oxides and, in particular, ceria-based mixed oxides is deduced from a revision of the most recent literature [27, 33]. It is thus recognized that the interaction between gold particles and ceria leads to highly dispersed metal systems with improved properties in terms of both activity and stability under reaction conditions. Changes in the electronic and structural properties of the gold particles as a consequence of the metal-support interactions have also been argued to explain the catalytic response of CeO<sub>2</sub> and ceria based mixed oxides [34, 35].

Gold nanoparticles (NPs) were also used as an efficient doping system of TiO<sub>2</sub> [36, 37]. Au-TiO<sub>2</sub> NPs showed, in fact, a strong absorption of the visible light due to the surface resonance plasmon



(SPR) of gold free electrons [37, 38]. Therefore, the Au-TiO<sub>2</sub> plasmonic photocatalyst exhibited high efficiency in UV or visible light photo-activated reactions such as 2-propanol degradation chemo-selective oxidation of alcohols, CO<sub>2</sub> reduction and water splitting for H<sub>2</sub> and O<sub>2</sub> generation [39-40].

The enhancement of the performance under UV irradiation was ascribed to the more efficient interfacial charge transfer in the presence of metallic NPs whereas the emergence of high activity under visible irradiation was attributed to the occurrence of the SPR effect, which allows the absorption of visible light. To explain the above effects, two different roles of Au nanoparticles have been claimed in the literature: on the one hand, the photo-excited electrons of the gold surface plasmon can be injected into the TiO<sub>2</sub> conduction band, thus creating separated electron-holes and then increasing their lifetime by hindering the recombination process [41]; on the other hand, Au NPs can favor electron transfer from the TiO<sub>2</sub> surface to the adsorbed molecular oxygen. The SPR phenomenon has been reported to be affected by the size, the shape, the content and the neighboring environment of gold NPs (Fig. 3.1)[37, 42].

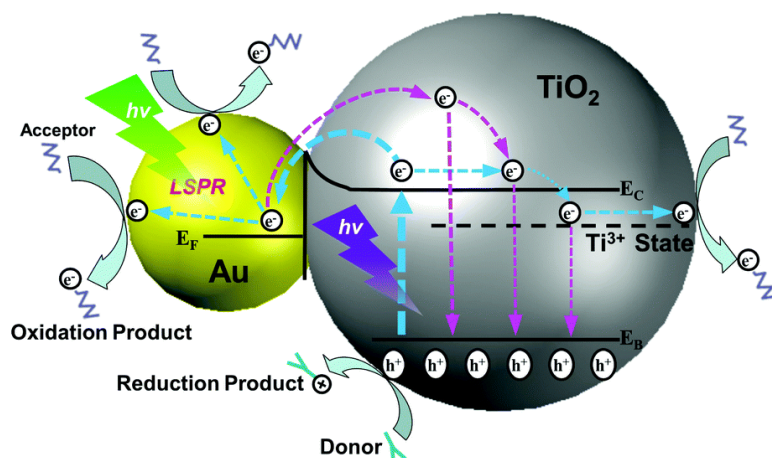


Fig. 3.1 Mechanism of the SPR effect on the photocatalytic activity of Au/TiO<sub>2</sub> [42].

The above features of gold are particularly useful for photocatalytic water splitting, in fact, using excitation wavelengths matching the gold plasmon band, Au NPs absorb photons and inject electrons into the conduction band of the TiO<sub>2</sub>. This latter effect is not common for a metal, but the nanometer size of Au particles and the occurrence of quantum size effects could be responsible for this mechanism and can explain the good activity of the Au/TiO<sub>2</sub> system for this reaction [39, 40].

On the basis of the above considerations, this thesis work investigates the photocatalytic performance of Au/TiO<sub>2</sub>-CeO<sub>2</sub> systems in both photo-oxidation<sup>1</sup> (VOCs photo-oxidation (2-propanol chosen as VOC model), and photoreduction<sup>2</sup> (photocatalytic water splitting) reactions.

### 3.3 Au/TiO<sub>2</sub>-CeO<sub>2</sub> catalysts: Samples preparation and experimental setup

Mixed TiO<sub>2</sub> (Degussa P25)-CeO<sub>2</sub> composites with different weight percentages of CeO<sub>2</sub> (1, 5, 10, 15) were prepared. Different aliquots of TiO<sub>2</sub> were impregnated with a proper amount of Ce(NO<sub>3</sub>)<sub>3</sub>·6H<sub>2</sub>O solution, and the slurries were stirred for 4 h, dried at 120°C and finally calcined in air at 350°C for 4 h. Calcination at 350°C for 4 h was also carried out on the bare TiO<sub>2</sub>.

CeO<sub>2</sub> was prepared by precipitation with KOH (0.1 M) from water solution of Ce(NO<sub>3</sub>)<sub>3</sub>·6H<sub>2</sub>O, and subsequent filtration and calcination in air at 450°C for 4 h of the obtained solid.

Gold (1wt%) was deposited on the bare or mixed TiO<sub>2</sub>-CeO<sub>2</sub> oxides by deposition-precipitation. After the pH of the aqueous solutions of the gold precursor (HAuCl<sub>4</sub>) was adjusted to the value of 8 by using an aqueous solution of KOH (0.1 M), the support was added under vigorous stirring (500 rpm), keeping the slurry at 70°C for 3 h. The obtained slurry was kept digesting for 24 h, filtered and washed several times (until disappearance of chlorides), dried at 110°C and finally ground before use.

The samples were coded as TiCeXX% and Au/TiCeXX%, where XX indicates the wt% of CeO<sub>2</sub>.

The photocatalytic oxidation tests were carried out by using a cylindrical continuous Pyrex photoreactor, operating in gas-solid regime. A porous glass septum in the inlet of the flow allowed to distribute homogeneously the gaseous mixture. The reactivity runs were carried out with 300 mg of solid powder by simply dispersing it as a thin layer inside the photoreactor (the fixed bed height was ca. 0.3 mm). The gas feeding the photoreactor consisted of 2-propanol (0.1mM) and air, the first one fed by means of a B.Braun Perfusor VI infusion pump, the second one by a mass gas-flow controller. The flow rate of the gaseous stream for the photo-assisted runs was 20 cm<sup>3</sup> min<sup>-1</sup>. All runs were carried out at atmospheric pressure. The reactor and the pipes of the set-up to and from the reactor were heated by an electric resistance and K-type thermocouples allowed to monitor the temperature in the whole system. The reactions were carried out at 25°C and 50°C and the temperature inside the photoreactor was maintained constant by means of a refrigeration water jacket surrounding the lamp and filtering the infrared radiations. The set-up was illuminated from the top with a Helios-Italquartz 125 W medium pressure Hg lamp and the irradiance reaching the photoreactor, measured in the range 300-400 nm with a UVX Digital radiometer, was equal to 1.5 mW cm<sup>-2</sup>. The runs lasted 80 minutes and

---

<sup>1</sup>R.Fiorenza, M. Bellardita, L. Palmisano, S. Scirè, J. Mol. Catal. A: Chem. 415 (2016) 56-64.

<sup>2</sup>R. Fiorenza, M. Bellardita, L. D'Urso, G. Compagnini, L. Palmisano, S. Scirè, Catalysts 6 (2016) 121.

samples of the reacting fluid were analyzed by a Shimadzu GC 2010 equipped with a Phenomenex Zebron Wax-Plus (30  $\mu\text{m}$   $\times$  0.32  $\mu\text{m}$   $\times$  0.53  $\mu\text{m}$ ) column and a FID detector using He as carrier gas. CO<sub>2</sub> determination was performed by a HP 6890 Series GC System equipped with a packed GC 60/80 Carboxen<sup>TM</sup>-1000 column and a thermal conductivity detector (TCD). The scheme of the experimental setup used is displayed in Fig. 3.2.

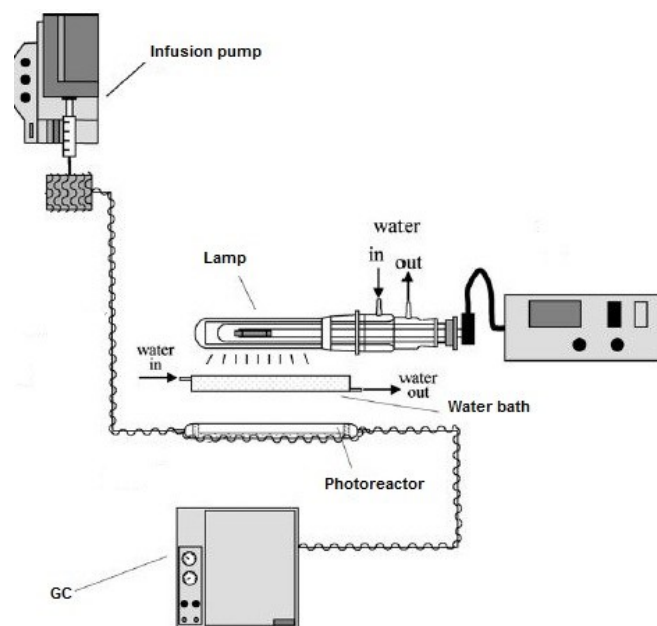


Fig. 3.2 Experimental setup used for the photo-oxidation of 2-propanol.

Hydrogen generation by photocatalytic water splitting was performed in a home-made Pyrex jacketed reactor thermostated at 30°C. The reactor headspace was linked to an inverted buret, filled with water at atmospheric pressure. This allows the quantification of the evolved gas. The evolution of H<sub>2</sub> was confirmed by analyzing the effluent gases with an online gas chromatograph (HP 6890 Series GC System, Agilent Technologies, Santa Clara, CA, US) equipped with a packed column (Carboxen 1000) and thermal conductivity detector. Specifically, the catalyst (50 mg) was placed inside the photo-reactor, with 100 mL of deionized water under stirring. The suspension was purged with a nitrogen flow for at least 30 min before irradiation in order to remove dissolved air. The suspension was then irradiated for 80 minutes using a 100 W UV mercury lamp.

### 3.3.1 Results and discussion

Photocatalytic oxidation data of 2-propanol (time on stream: 80 min) in term of alcohol conversion and selectivity to acetone and CO<sub>2</sub> under UV irradiation at 25°C are depicted in Fig. 3.3A. As far as 2-propanol conversion is concerned, the best results were obtained by using the

Au/TiO<sub>2</sub> catalyst (96%), followed by TiO<sub>2</sub> (70%), TiCe1% (68%) and Au/TiCe10% samples (64%). The enhancement of photocatalytic activity of TiO<sub>2</sub>, due to the presence of gold particles, is attributed to the different Fermi levels of the two species resulting in an increase of the charge separation between the excited electron (e<sup>-</sup>) and hole (h<sup>+</sup>) [43, 44]. The high activity of Degussa P25 could be due to the existence of an interaction between the two phases of TiO<sub>2</sub> (80% anatase, 20% rutile), that enhances the electron-hole separation and increases the total photoefficiency [45, 46].

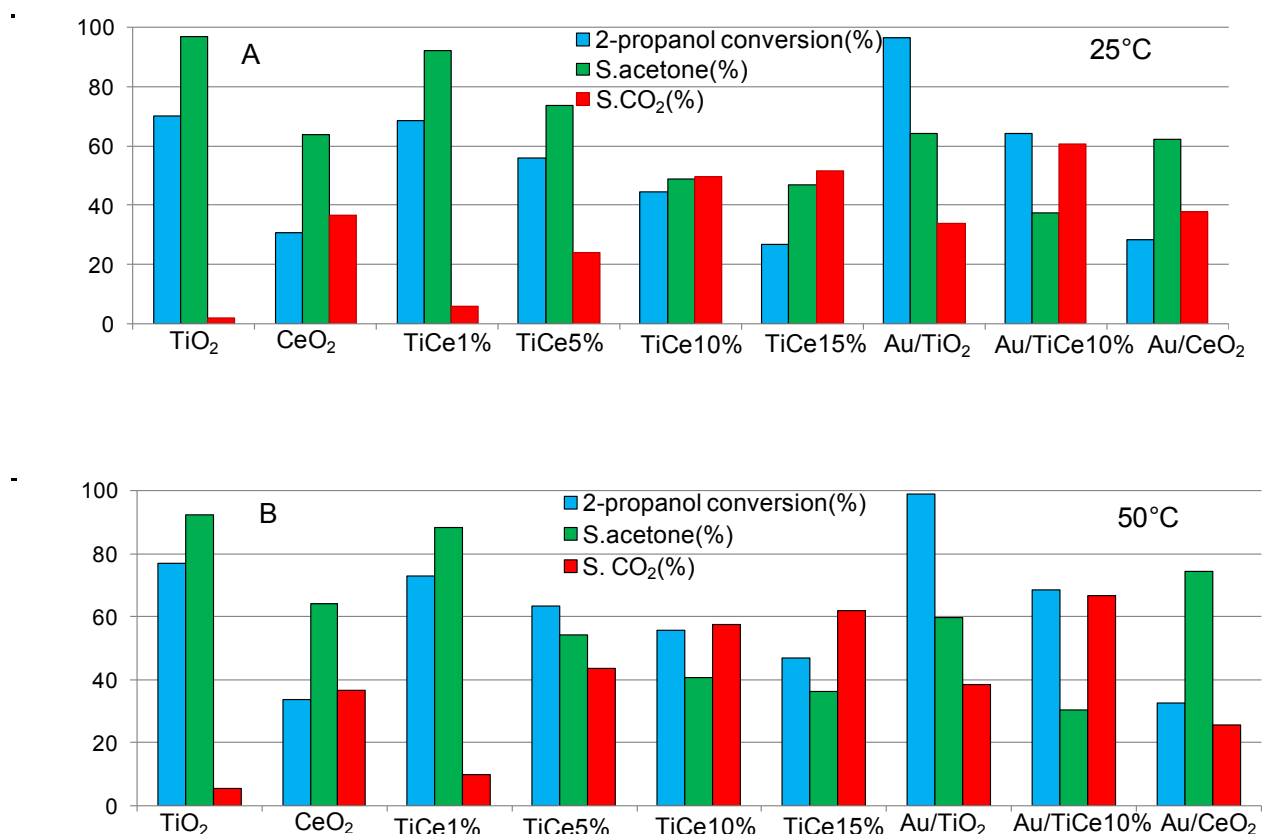


**Fig. 3.3** Results of 2-propanol photocatalytic oxidation under UV irradiation, in terms of conversion, selectivity to acetone and selectivity to CO<sub>2</sub>: (A) 25°C, (B) 50°C.

The bare CeO<sub>2</sub> showed a low activity for the conversion of 2-propanol (31%), while on the TiO<sub>2</sub>-CeO<sub>2</sub> system the values of alcohol conversion decreased by increasing the wt% of CeO<sub>2</sub>, being 68% (similar to bare TiO<sub>2</sub>) for TiCe1%, 56% for TiCe5%, 45% for TiCe10% and 27% for TiCe15% samples.

As regards the selectivity to acetone, the TiO<sub>2</sub> P25 had the highest value (97%) in agreement with the data reported in the literature for this reaction [47-49]. Also in this case the increase of the amount of CeO<sub>2</sub> had a negative effect which caused a decrease of selectivity down to 92%,

74%, 48% and 46% for TiCe1%, TiCe5%, TiCe10% and TiCe15% systems, respectively. The Au/TiO<sub>2</sub> sample was more selective to acetone (64%) compared to the Au/TiCe10% catalyst (37%).

The selectivity to CO<sub>2</sub> had an opposite trend. The Au/TiCe10% system showed the highest selectivity (60%) while for the TiO<sub>2</sub>-CeO<sub>2</sub> mixed oxides it increased with the wt% of CeO<sub>2</sub>, being higher for the TiCe10% and TiCe15% samples (49% and 51% respectively). By considering that the bare CeO<sub>2</sub> showed a considerable value of CO<sub>2</sub> selectivity (33%), these results suggest that the presence of CeO<sub>2</sub> greater affects the total oxidation of 2-propanol to CO<sub>2</sub> rather than the partial oxidation to acetone. In all of the photocatalytic tests with the TiO<sub>2</sub>-based samples, the formation of propene was detected, with very low selectivity (1-3%). As reported in the literature [50, 51] the selective oxidation of 2-propanol can proceed with two reaction routes: the dehydration to propene and water or the oxidative dehydrogenation to acetone and water. In this case the formation of propene (not detected for Au/CeO<sub>2</sub> and CeO<sub>2</sub> catalysts) is due to the more acidic nature of TiO<sub>2</sub> with respect to CeO<sub>2</sub> [50, 51].

The photoactivity at 50°C is reported in Fig. 3.3B. Concerning the 2-propanol conversion, the increase of temperature caused a slight enhancement of alcohol conversion values. Similarly to the results obtained at 25°C the best activity was displayed by Au/TiO<sub>2</sub> (98%), followed by TiO<sub>2</sub> (76%), TiCe1% (73%) and Au/TiCe10% (68%). The TiCe10% and TiCe15% samples, notwithstanding a greater enhancement of the values of 2-propanol conversion with temperature (10% and 20%), still remain the least active. Moreover it is possible to notice an increase of CO<sub>2</sub> selectivity for all of the TiO<sub>2</sub>-CeO<sub>2</sub> samples, the Au/TiCe10% sample being also in this case the most selective catalyst.

The photo-activity of all investigated catalysts in the water splitting reaction  $\text{H}_2\text{O} \rightarrow \text{H}_2 + 1/2 \text{O}_2$ , evaluated in terms of hydrogen evolution versus reaction time, is compared in Fig. 3.4. For all samples, we observed the formation of O<sub>2</sub> in an almost stoichiometric amount (half moles than H<sub>2</sub>), with only a slight defect of oxygen. By taking into account that the experiments were carried out in pure water without sacrificial agents, this confirms the occurrence of the water splitting reaction.

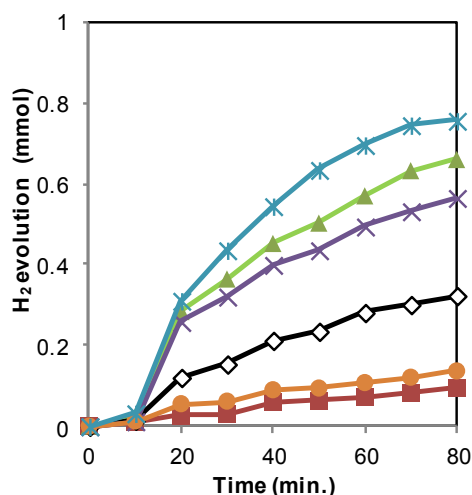


**Fig. 3.4** Photocatalytic H<sub>2</sub> production at 30°C under UV irradiation over: TiO<sub>2</sub> (◇), CeO<sub>2</sub> (■), TiO<sub>2</sub>-10%CeO<sub>2</sub> (▲), Au/TiO<sub>2</sub> (×), Au/CeO<sub>2</sub> (●) and Au/TiO<sub>2</sub>-10%CeO<sub>2</sub> (✱).

For all samples it is possible to note that, after a short induction period (around 10 min), due to the stabilization of lamp irradiation and/or water saturation with evolved gases [52], hydrogen production firstly undergoes an almost linear increment for up to 40 min, followed by a moderate decrease of the production rate. According to the literature [53, 54] this can be the result of two fundamental effects:

- (1) a recombination of charge carriers, namely the photo-generated electron-hole pairs, as electrons of the conduction band can quickly recombine with holes of the valence band, thus releasing energy as unproductive heat or photons;
- (2) A fast backward reaction, namely the recombination of hydrogen and oxygen into water. It is noteworthy that repetitive photocatalytic tests, using the same sample three times in succession, gave the same catalytic profile, with good data reproducibility, thus ruling out that hydrogen might partially arise from the presence of organic residues due to the synthesis, acting as sacrificial agents.

Interestingly, both bare TiO<sub>2</sub> (black line) and CeO<sub>2</sub> (brown line) samples showed some activity in the production of hydrogen which was found to increase in the presence of gold. The coupling of CeO<sub>2</sub> with TiO<sub>2</sub> positively affected the photocatalytic activity with a further increase obtained by the deposition of gold particles in the binary system of TiO<sub>2</sub>-CeO<sub>2</sub>. In fact, both TiO<sub>2</sub>-10%CeO<sub>2</sub> (green line) and Au/TiO<sub>2</sub>-10%CeO<sub>2</sub> (blue line) catalysts showed better performance than bare TiO<sub>2</sub> (H<sub>2</sub> evolution around two times higher) and Au/TiO<sub>2</sub> (H<sub>2</sub> evolution around 25% higher). As reported in the literature, despite the bulk ceria and titania not having a similar crystal structure, cerium ions (Ce<sup>3+</sup> and Ce<sup>4+</sup>) can replace the Ti<sup>4+</sup> ions, modifying the physicochemical properties of TiO<sub>2</sub>. Such an interaction between the CeO<sub>2</sub> and TiO<sub>2</sub> frameworks could be the key factor explaining the enhancement of the photocatalytic activity of this mixed

oxide system towards water splitting [55,56]. The metal atoms, instead, pile up the electrons from the TiO<sub>2</sub> conduction band and transfer them to hydrogen protons, acting as H<sub>2</sub> evolution centers.

The catalytic activity data reported, clearly pointed out that gold and/or CeO<sub>2</sub> affected in a different way the photocatalytic performance of TiO<sub>2</sub>, depending on the reaction taken into consideration. In particular in the photocatalytic water splitting the presence of gold produced an increase of the hydrogen production both on TiO<sub>2</sub> and on CeO<sub>2</sub>. The rate of H<sub>2</sub> production was further enhanced by using ternary Au/TiO<sub>2</sub>-CeO<sub>2</sub> systems, the co-presence of gold and ceria leading to the highest hydrogen evolution.

Also in the photocatalytic oxidation of 2-propanol the presence of gold was necessary to have good performance, being Au/TiO<sub>2</sub> the most active sample for the alcohol conversion and Au/TiO<sub>2</sub>-10%CeO<sub>2</sub> the catalyst showing the best mineralization yield. The effect of CeO<sub>2</sub> addition to TiO<sub>2</sub> was instead negative in terms of 2-propanol conversion, resulting however in a sensible increase in the CO<sub>2</sub> yield (Fig. 3.5).

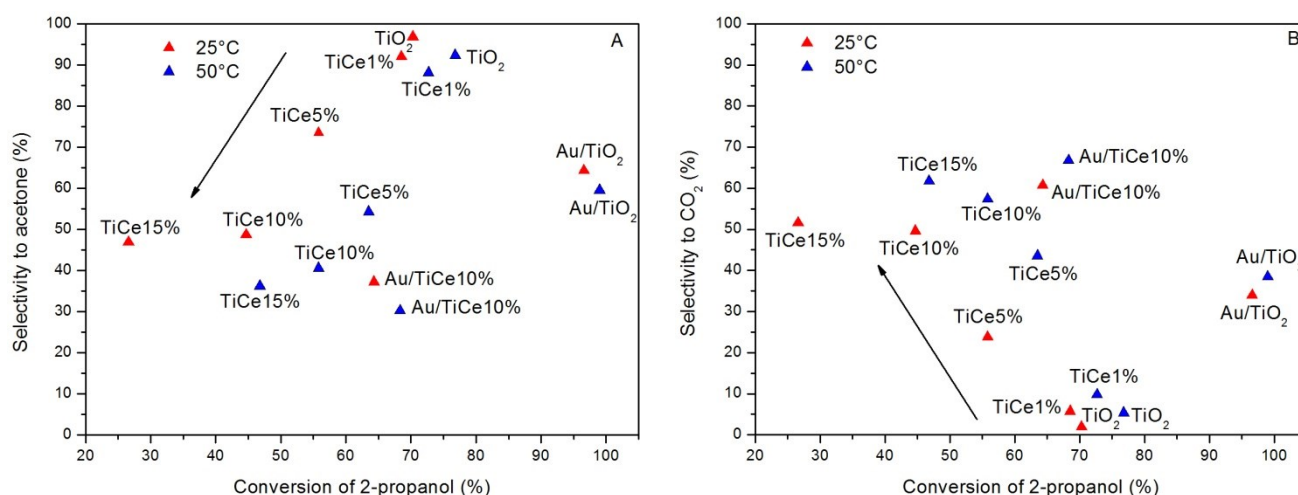


**Fig. 3.5** Dependence of selectivity to acetone (A) and to CO<sub>2</sub> (B) on 2-propanol photocatalytic conversion at 25°C (red triangle) and at 50°C (blue triangle) for the TiO<sub>2</sub>-CeO<sub>2</sub> based catalysts.

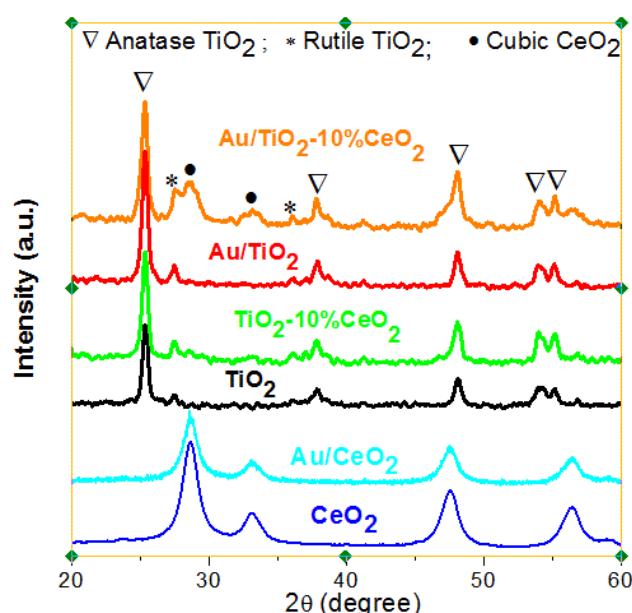
Interestingly in this case a direct correlation between catalysts performance and percentage of CeO<sub>2</sub> was found. It must be underlined that in the photocatalytic oxidation Au acts essentially favouring the total oxidation of the alcohol, increasing the selectivity towards CO<sub>2</sub>.

The chemico-physical characterization of the investigated Au/TiO<sub>2</sub>-CeO<sub>2</sub> catalysts helped to rationalize the above results. The main properties of the catalysts are displayed in Table 3.1. As revealed by XRD measurements (Fig. 3.6), TiO<sub>2</sub> anatase was the main crystal phase for all samples, and the presence of CeO<sub>2</sub> and/or Au induced a slight decrease in the crystallites size.

**Table 3.1.** Chemico-physical properties of Au/TiO<sub>2</sub>-CeO<sub>2</sub> catalysts

| Catalysts           | S <sub>BET</sub> (m <sup>2</sup> g <sup>-1</sup> ) | E <sub>g</sub> (eV) | Crystallite size (nm)* | Crystal phase  |
|---------------------|--|---------------------|------------------------|--|
| CeO <sub>2</sub>    | 111.2  | 2.90                | 10                     | CeO <sub>2</sub> fluorite                                    |
| Au/CeO <sub>2</sub> | 113.8  | 2.95                | 11                     | CeO <sub>2</sub> fluorite                                    |
| TiO <sub>2</sub>    | 44.7   | 2.98                | 24                     | TiO <sub>2</sub> Anatase-Rutile                              |
| Au/TiO <sub>2</sub> | 46.3   | 2.97                | 21                     | TiO <sub>2</sub> Anatase-Rutile                              |
| TiCe10%             | 47.2   | 2.93                | 22                     | TiO <sub>2</sub> Anatase-Rutile                              |
| Au/TiCe10%          | 50.4   | 2.96                | 19                     | TiO <sub>2</sub> Anatase-Rutile<br>CeO <sub>2</sub> fluorite |

\* estimated by XRD measurements.

**Fig. 3.6** XRD patterns of investigated catalysts.

The Raman spectra (Fig. 3.7A), exhibiting bands at around 150 cm<sup>-1</sup>, 403 cm<sup>-1</sup>, 524 cm<sup>-1</sup> and 647 cm<sup>-1</sup>, confirmed that anatase was the main TiO<sub>2</sub> polymorphic phase in these samples [57, 58]. The Au/TiO<sub>2</sub> sample (red line) showed the same bands of bare TiO<sub>2</sub> (black line). In the TiO<sub>2</sub>-10%CeO<sub>2</sub> sample (green line) the signal at 466 cm<sup>-1</sup> was associated to the cubic phase of the CeO<sub>2</sub> fluorite [59] and the small component at 600 cm<sup>-1</sup> assignable to intrinsic O vacancies in ceria due to its non-stoichiometric composition (presence of Ce<sup>3+</sup> in the lattice) [59, 60]. Interestingly over the Au/TiO<sub>2</sub>-10%CeO<sub>2</sub> sample the peak associated to cubic CeO<sub>2</sub> was less intense, broader and shifted to lower frequencies compared to TiO<sub>2</sub>-10%CeO<sub>2</sub> (Fig.3.7B, orange and green line respectively).



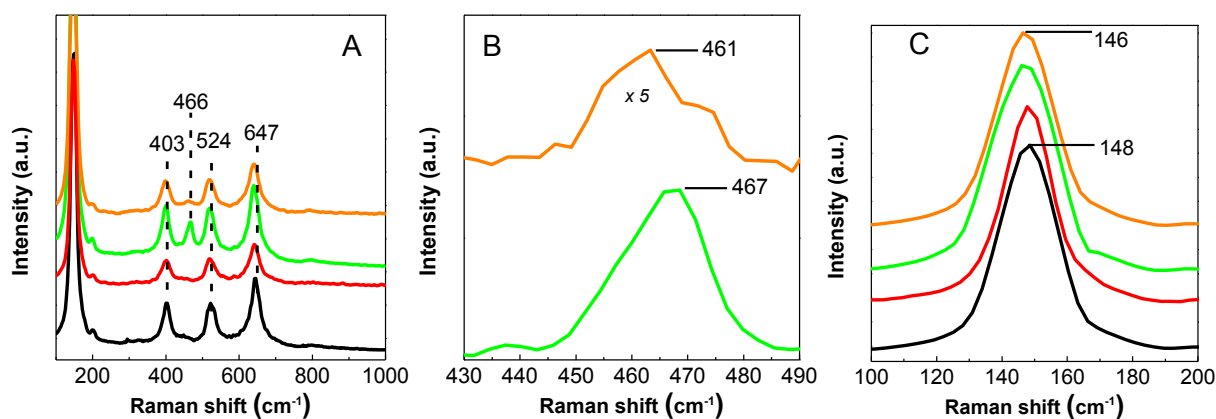


**Fig. 3.7** (A) Vibrational modes of Raman spectra of TiO<sub>2</sub> (—), Au/TiO<sub>2</sub> (—), TiO<sub>2</sub>-10%CeO<sub>2</sub> (—), and Au/TiO<sub>2</sub>-10%CeO<sub>2</sub> (—) samples; (B) Raman shift of the signal of cubic CeO<sub>2</sub> on TiO<sub>2</sub>-10%CeO<sub>2</sub> (—), and Au/TiO<sub>2</sub>-10%CeO<sub>2</sub> (—) samples; (C) Raman shift of the main E<sub>g</sub> vibrational mode of TiO<sub>2</sub> anatase.

This could be due to a less crystalline and more defective structure of ceria in the presence of gold. In fact, Raman has been reported to be sensitive to the degree of crystallinity of samples, with broader less intense Raman peaks in the case of less crystalline materials [61].

To analyze the distribution of cerium oxide on TiO<sub>2</sub> a Raman mapping analysis was performed. This technique allows non-destructive and non-invasive analysis of features such as separation of chemical species in multicomponent samples. Chemical maps of TiO<sub>2</sub> and CeO<sub>2</sub> nanostructures performed on the TiO<sub>2</sub>-10%CeO<sub>2</sub> sample, based on the detailed Raman image (over a 15 μm x 15 μm image scan, with 150 points per line and 150 lines per image) are presented in Fig. 3.8. Representative spectra of two different regions are reported in red and violet color scale. The spectra show almost identical features but with very different intensities. CeO<sub>2</sub> characteristic band (466 cm<sup>-1</sup>) of higher intensity was recorded in the red region while in the violet one TiO<sub>2</sub> peaks (150 cm<sup>-1</sup>, 403 cm<sup>-1</sup>, 524 cm<sup>-1</sup> and 647 cm<sup>-1</sup>) are well visible with ceria band of decreased intensity (according to the 10%), pointing out as ceria was not homogeneously dispersed on TiO<sub>2</sub> bulk.

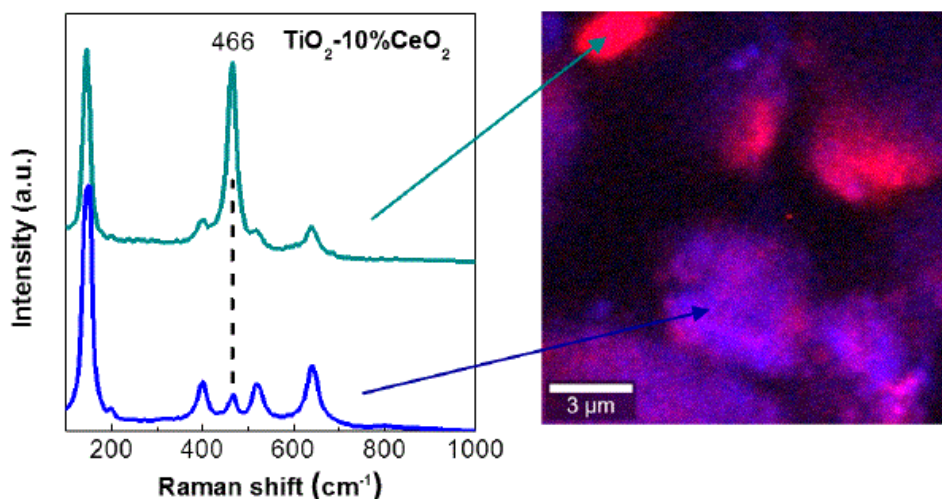


Fig. 3.8 Confocal Raman mapping image of TiO<sub>2</sub>-10%CeO<sub>2</sub> sample.

The band-gap energy values (Table 3.1) estimated by plotting the modified Kubelka-Munk function,  $[F(R_{\infty})/hv]^{1/2}$ , versus the energy of the exciting light [62] showed that the TiO<sub>2</sub>-10%CeO<sub>2</sub> sample has a lower  $E_g$  (2.93 eV) compared to the bare TiO<sub>2</sub> (2.98 eV). This can be related to the substitution of Ti<sup>4+</sup> cations by Ce<sup>4+</sup> or Ce<sup>3+</sup> cations in the TiO<sub>2</sub> network [63, 64]. It must be underlined that no significant variation in the BET surface area of investigated samples was observed by the presence of gold and/or CeO<sub>2</sub>. It must be also noted that the bare TiO<sub>2</sub> showed a surface area of 44.8 m<sup>2</sup>g<sup>-1</sup>, lower than the values reported in the literature for the Degussa P25 (50-54 m<sup>2</sup>g<sup>-1</sup>), reasonably due to pre-treatment conditions of TiO<sub>2</sub> (calcination at 350°C) [65].

EDX analysis of TiCe10% and Au/TiCe10% samples was carried out in order to highlight differences in the surface composition of these mixed oxides. The elemental composition of these catalysts is reported in Table 3.2. For the Au/TiCe10% sample the atomic surface percentage of Ce is about 4 times higher than that of TiCe10% (5.07 and 1.21 respectively), pointing out that the presence of gold on mixed oxides leads to a considerable cerium surface enrichment.

Table 3.2 EDX elemental composition of investigated catalysts.

| Element | TiCe10%    |            | Au/TiCe10% |            |
|---------|------------|------------|------------|------------|
|         | Weight (%) | Atomic (%) | Weight (%) | Atomic (%) |
| C       | 3.58       | 7.37       | 4.19       | 11.40      |
| O       | 43.93      | 67.87      | 26.65      | 54.49      |
| K       | -          | -          | 0.64       | 0.54       |
| Ti      | 45.61      | 23.54      | 40.10      | 27.39      |
| Ce      | 6.88       | 1.21       | 21.70      | 5.07       |
| Au      | -          | -          | 6.72       | 1.12       |

The different role of gold and CeO<sub>2</sub> in affecting the properties and the catalytic behaviour of TiO<sub>2</sub> in the photo-oxidation and the photoreduction reactions here investigated could be rationalized by considering the surface active species involved in these reactions. As for the photocatalytic water/air oxidative purification, the photocatalytic hydrogen production requires essentially photogeneration of hole/electron pairs. However, the role of holes/electrons as well as the surface reactions involved is different. In the photocatalytic oxidations, valence band (VB) holes are the key elements that induce decomposition of contaminants. On the other hand, when photocatalysis is applied to perform water splitting the reducing CB electrons become important as their role is essentially that of reducing protons to hydrogen molecules. The addition of gold to TiO<sub>2</sub> causes an enhancement in the photocatalytic oxidation activity of 2-propanol, due to an increase of the charge separation between the excited electron and the hole of TiO<sub>2</sub> [43, 66]. The proposed scheme of the electron transfer phenomena taking place in the Au/TiO<sub>2</sub>-CeO<sub>2</sub> system is illustrated in Fig. 3.9. We must underline that under the irradiation conditions used in this work (medium pressure Hg lamp, providing UV and to a less extent visible photons) the SPR effect of Au nanoparticles, before discussed and involving an inverse transfer of electron from Au to CB of TiO<sub>2</sub>, should play a minor role, becoming important only when visible light is used as the irradiation source.

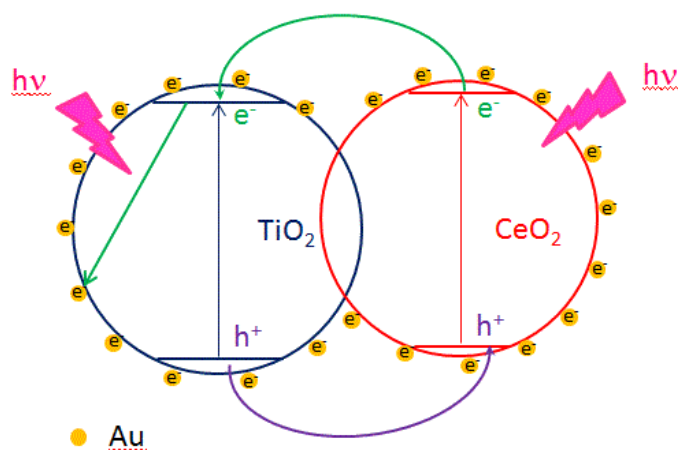


**Fig. 3.9** Scheme of the electron transfer phenomena taking place in the Au/TiO<sub>2</sub>-CeO<sub>2</sub> system by irradiation with UV light.

Interestingly when also the cerium oxide was present, photo-generated active species (superoxide oxygen and hydroxyl radicals) could allow an easier re-oxidation of ceria thus speeding up its redox process [14]. These processes were beneficial for the complete oxidation to CO<sub>2</sub>. Furthermore the basic and redox character of CeO<sub>2</sub> sites with respect to the more acid TiO<sub>2</sub>

ones could facilitate the direct combustion of 2-propanol to CO<sub>2</sub> [67, 68], resulting in the highest CO<sub>2</sub> yield over the Au/TiO<sub>2</sub>-10%CeO<sub>2</sub> system.

The surface mechanisms induced by gold were less efficient for the photocatalytic water splitting. In fact, even if the photogenerated electrons and holes possess thermodynamically adequate potentials for water splitting, they tend to recombine with each other if the number of active sites for the redox reaction is not sufficient. In this case the substitution of cerium ions (Ce<sup>3+</sup> and Ce<sup>4+</sup>) in the TiO<sub>2</sub> framework, as suggested by DRS measurements, was the key factor to have good performance. The cerium defects act, in fact, as holes traps [55, 56, 69], avoiding the recombination of active electrons and holes thus favouring the reduction of water. In this case gold positively affects the photocatalytic performance both increasing the defective structure of ceria, as shown by Raman, and favouring the enrichment of ceria on the surface of TiO<sub>2</sub>, as shown by EDX, thus explaining the highest H<sub>2</sub> production rate of the Au/TiO<sub>2</sub>-10%CeO<sub>2</sub> system.

### 3.3.2 Conclusions and future perspectives

The photocatalytic performance of the Au/TiO<sub>2</sub>-CeO<sub>2</sub> system was studied both in the oxidation of 2-propanol and in the water splitting reaction. Characterization experiments (XRD, EDX, Surface area measurements, DRS and Raman spectroscopy) allowed to suggest that the interaction of gold with TiO<sub>2</sub> causes an increase in the photocatalytic oxidation activity, due to a charge separation enhancement between the excited electron and the hole of TiO<sub>2</sub>. The co-existence of Au and both TiO<sub>2</sub> and CeO<sub>2</sub> oxides favours the mineralization of the alcohol. In the water splitting reaction, the presence of ceria, acting as a hole trap, is essential to have a high hydrogen production rate, while Au conveys the electron transfer from TiO<sub>2</sub> to the H<sup>+</sup> ions.

For the same reactions, the presence of silver added to TiO<sub>2</sub> with the same experimental procedures (deposition-precipitation using AgNO<sub>3</sub> as salt precursor) affected in minor extent the photocatalytic performance of TiO<sub>2</sub> P25 (Fig. 3.10). In particular in the photo-oxidation of 2-propanol (Fig. 3.10A), the Ag/TiO<sub>2</sub> exhibited similar activity of bare TiO<sub>2</sub>, whereas the Ag/TiO<sub>2</sub>-10% CeO<sub>2</sub> sample showed a higher selectivity to acetone compared to the Au/TiO<sub>2</sub>-10% CeO<sub>2</sub>.

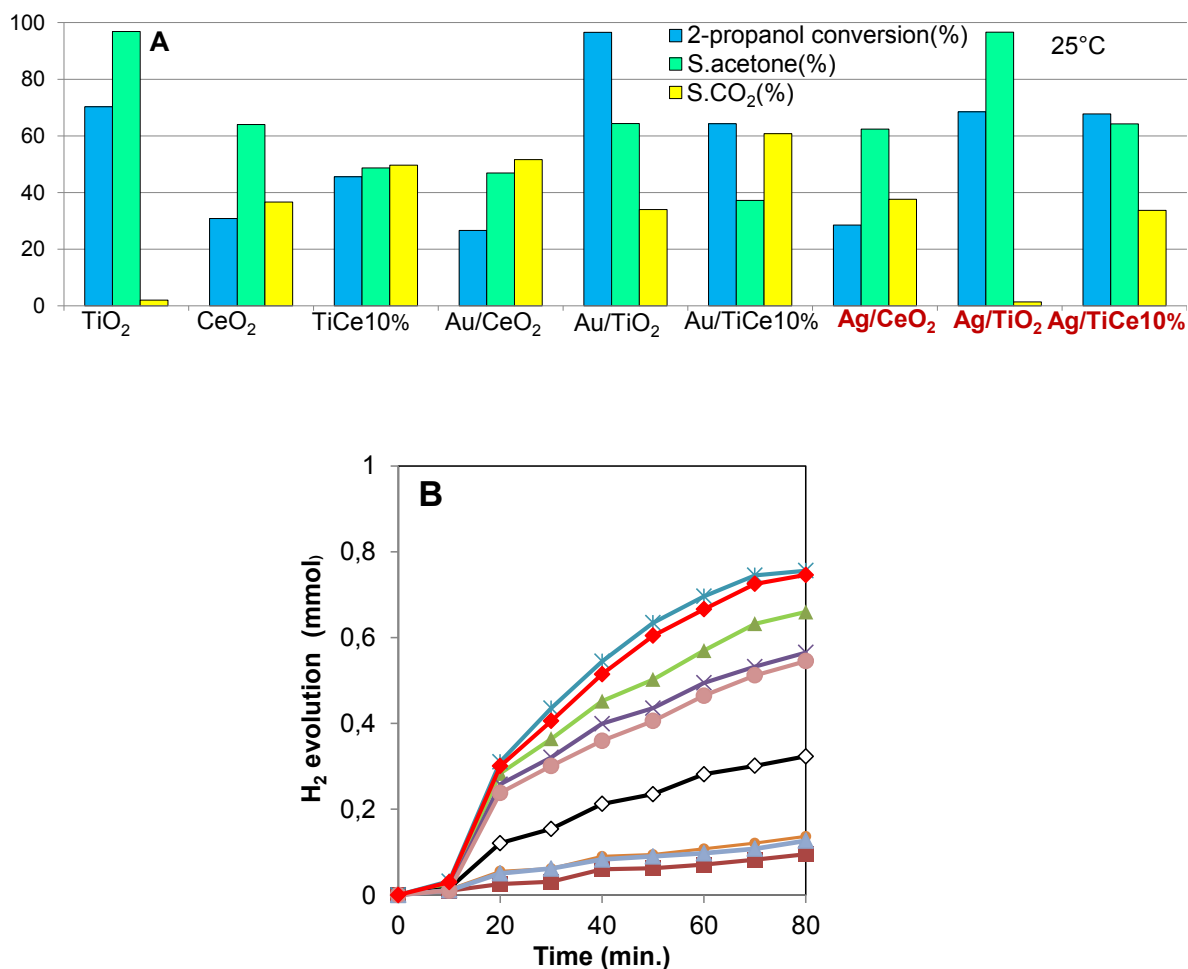


**Fig. 3.10** (A) Results of 2-propanol photocatalytic oxidation at 25°C, in terms of conversion, selectivity to acetone and selectivity to CO<sub>2</sub>; (B) Photocatalytic H<sub>2</sub> production at 30°C under UV irradiation over: TiO<sub>2</sub> (◇), CeO<sub>2</sub> (■), TiO<sub>2</sub>-10%CeO<sub>2</sub> (▲), Au/TiO<sub>2</sub> (×), Au/CeO<sub>2</sub> (●), Au/TiO<sub>2</sub>-10%CeO<sub>2</sub> (\*), Ag/CeO<sub>2</sub> (▲), Ag/TiO<sub>2</sub> (●) and Ag/TiO<sub>2</sub>-10%CeO<sub>2</sub> (◆).

In the photocatalytic water splitting reaction the silver-based catalysts (Fig. 3.10B) showed a similar activity to gold-based catalyst.

To investigate the photoactivity of these samples under solar irradiation, the degradation of a dye (solution of Methylene Blue (MB) in water, 10<sup>-5</sup> M) under simulated solar light irradiation was evaluated (Fig. 3.11).

The Au/TiO<sub>2</sub>-10%CeO<sub>2</sub> catalyst confirmed the good photoactivity also under solar irradiation, whereas the addition of platinum (wetness impregnation, H<sub>2</sub>PtCl<sub>6</sub> used as salt precursor) and silver had a less positive effect.

These results suggest that the strong interaction between gold and titania boosted by the presence of cerium oxide lead to have good results both for photocatalytic oxidation and photocatalytic reduction reactions under UV and solar light irradiation. The Surface Plasmon Resonance effect and the charge separations are more efficient when gold was added to TiO<sub>2</sub> respect to silver or

platinum. Due to the promising photocatalytic performance of the Au/TiO<sub>2</sub>-CeO<sub>2</sub> system this catalyst could be tested for other important reactions as the photoreduction of CO<sub>2</sub>.

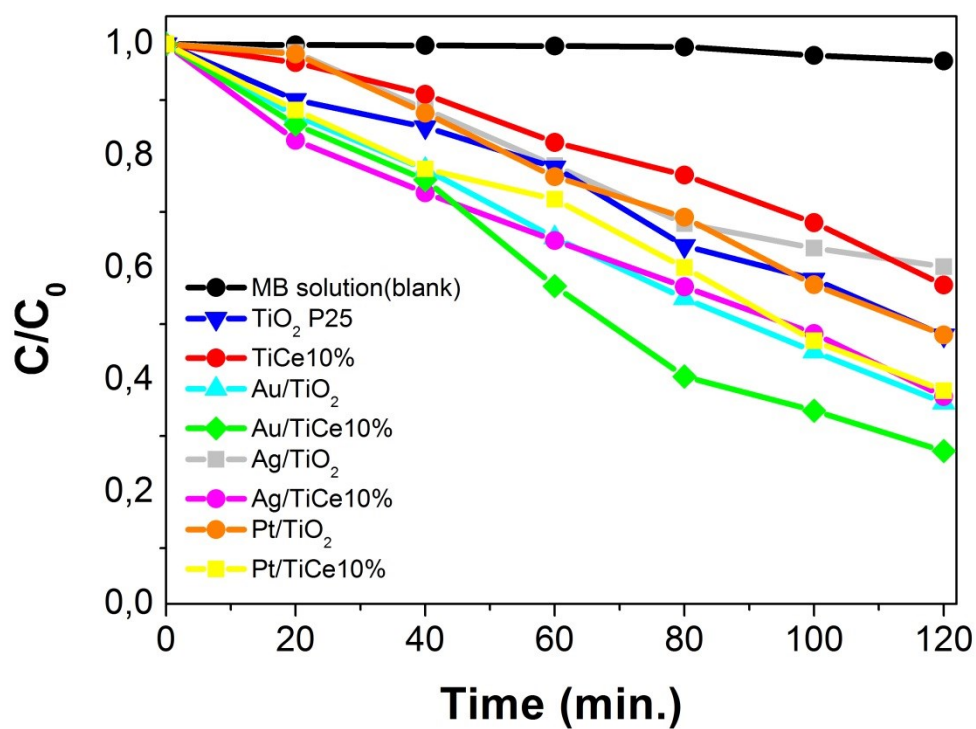


Fig. 3.11 The variation of MB concentrations ( $C/C_0$ ) with irradiation time over TiO<sub>2</sub>-CeO<sub>2</sub> samples.

## References

- [1] A. Trovarelli, P. Fornasiero, *Catalysis by Ceria and Related Materials*, 2nd ed., Imperial College Press, London, 2014.
- [2] C.Y. Cao, Z.M. Cui, C.Q. Chen, W.G. Song, W. Cai, *J. Phys. Chem. C* 114 (2010) 9865-9870.
- [3] H. Imagawa, A. Suda, K. Yamamura, S. Sun, *J. Phys. Chem. C* 115 (2011) 1740-1745.
- [4] G.-R. Li, D.-L. Qu, L. Arurault, Y.-X. Tong, *J. Phys. Chem. C* 113 (2009) 1235-1241.
- [5] S. Scirè, P.M. Riccobene, C. Crisafulli, *Appl. Catal. B: Environ.* 101 (2010) 109-117.
- [6] L.F. Liotta, M. Ousmane, G. Di Carlo, G. Pantaleo, G. Deganello, A. Boreave, A. Giroir-Fendler, *Catal. Lett.* 127 (2009) 270-276.
- [7] L. Li, H.K. Yang, B.K. Moon, Z. Fu, C. Guo, J.H. Jeong, S.S. Yi, K. Jang, H.S. Lee, *J. Phys. Chem. C* 113 (2008) 610-617.
- [8] T. Mokkelbost, I. Kaus, T. Grande, M.-A. Einarsrud, *Chem. Mater.* 16 (2004) 5489-5494.
- [9] S. Scirè, S. Minicò, C. Crisafulli, C. Satriano, A. Pistone, *Appl. Catal. B: Environ.* 40 (2003) 43-49.
- [10] K. Otsuka, Y. Wang, M. Nakamura, *Appl. Catal. A: Gen.* 183 (1999) 317-324.
- [11] M. Boaro, C. De Leitenburg, G. Dolcetti, A. Trovarelli, *J. Catal.* 193(2) (2000) 338-347.
- [12] V. Rico-Pérez, E. Aneggi, A. Bueno-López, A. Trovarelli, *Appl. Catal. B: Environ.* 197 (2016) 95-104.
- [13] M. Meksi, H. Kochkar, G. Berhault, C. Guillard, *J. Mol. Catal. A: Chem.* 409 (2015) 162-170.
- [14] M. Zeng, Y. Li, M. Mao, J. Bai, L. Ren, X. Zhao, *ACS Catal.* 5 (2015) 3278-3286.
- [15] F.B. Li, X.Z. Li, M.F. Hou, K.W. Cheah, W.C.H. Choy, *Appl. Catal. A: Gen.* 285 (2005) 181-189.
- [16] S. Li, Q. Wang, T. Chen, Z. Zhou, Y. Wang, J. Fu, *Nanoscale Res. Lett.* 7 (2012) 227-229.
- [17] A.W. Xu, Y. Gao, H.Q. Liu, *J. Catal.* 207 (2002) 151-157.
- [18] B. Choudhury, B. Borah, A. Choudhury, *Mater. Sci. Eng. B* 178 (2013) 239-247.
- [19] J. Xie, D. Jiang, M. Chen, D. Li, J. Zhu, X. Lu, C. Yan, *Colloids Surf. A* 372 (2010) 107-114.
- [20] M.S. Hassan, T. Amna, O.-B. Yang, H.-C. Kim, M.-S. Khil, *Ceram. Int.* 38 (2012) 5925-5930.
- [21] X. Gu, F. Chen, B. Zhao, J. Zhang, *Superlattice Microstruct.* 50 (2011) 107-118.
- [22] W. Xu, Y. Yu, C. Zhang, H. He, *Catal. Commun.* 9 (2008) 1453-1457.
- [23] W. Xue, G. Zhang, X. Xu, X. Yang, C. Liu, *Chem. Eng. J.* 167 (2011) 397-402.
- [24] S. Luo, T. D. N. Phan, A. C. Johnston-Peck, L. Barrio, S. Sallis, D. A. Arena, S. Kundu, W. Xu, L. F. J. Piper, E. A. Stach, D. E. Polyansky, E. Fujita, J. A. Rodriguez, S. D. Senanayake, *J. Phys. Chem. C* 119 (2015) 2669-2679.
- [25] L. Barrio, G. Zhou, I. D. Gonzalez, M. Estrella, J. Hanson, J. A. Rodriguez, R. M. Navarro, J. L. G. Fierro, *Phys. Chem. Chem Phys.* 14 (2012) 2192-2202.
- [26] S. Kundu, J. Ciston, S. D. Senanayake, D. A. Arena, E. Fujita, D. Stacchiola, L. Barrio, R. M. Navarro, J. L. G. Fierro, J. J. Rodriguez, *Phys. Chem. C* 116 (2012) 14062-14070.
- [27] S. Scirè, L.F. Liotta, *Appl. Catal. B: Environ.* 125 (2012) 222-246.
- [28] H.Y. Kim, H.M. Lee, G. Henkelman, *J. Am. Chem. Soc.* 134 (2012) 1560-1570.
- [29] Q. Fu, H. Saltsburg, M. Flytzani-Stephanopoulos, *Science* 301 (2003) 935-938.
- [30] E. del Río, D. Gaona, J.C. Hernández-Garrido, J.J. Calvino, M.G. Basallote, M.J. Fernández-Trujillo, J. A. Pérez-Omil, *J. Catal.* 318 (2014) 119-127.
- [31] M. Haruta, *Chem. Rec.* 3 (2003) 75-87.
- [32] M. Valden, *Science* 281 (1998) 1647-1650.
- [33] M. Kipnis, *Appl. Catal. B Environ.* 152-153 (2014) 38-45.
- [34] J.A. Hernández, S.A. Gómez, T.A. Zepeda, J.C. Fierro-González, G.A. Fuentes, *ACS Catal.* 5 (2015) 4003-401.
- [35] H.Y. Kim, H.M. Lee, G. Henkelman, *J. Am. Chem. Soc.* 134 (2012) 1560-1570.
- [36] P. Wang, B. Huang, Y. Dai, M.H. Whangbo, *Phys. Chem. Chem Phys.* 149 (2012) 9813-9825.
- [37] E. Kowalska, O.O.P. Mahaney, R. Abe, B. Ohtani, *Phys. Chem. Chem Phys.* 12 (2010) 2344-2355.
- [38] C.J. Orendorff, T.K. Sau, C.J. Murphy, *Small* 2 (2006) 636-639.
- [39] V. Jovic, W.T. Chen, D. Sun-Waterhouse, M.G. Blackford, H. Idriss, G.I.N. Waterhouse, *J. Catal.* 305 (2013) 307-317.
- [40] M. H.-Reyes, A. Hernández-Gordillo, R. Zanella, V. Rodríguez-González, *Catal. Today* 266 (2016) 2-8.
- [41] W. Hou, W.H. Hung, P. Pavaskar, A. Goeppert, M. Aykol, S.B. Cronin, *ACS Catal.* 1 (2011) 929-936.

- [42] Z. Lin, X. Wang, J. Liu, Z. Tian, L. Dai, B. He, C. Han, Y. Wu, Z. Zeng, Z. Hu, *Nanoscale* 7 (2015) 4114-4123.
- [43] E. Kowalska, R. Abe, B. Ohtani, *Chem. Commun.* (2009) 241-243.
- [44] A.A Ismail, D.W. Bahnemann, S.A. Al-Sayari, *Appl. Catal. A: Gen.* 431-432 (2012) 62-68.
- [45] B. Sun, P.G. Smirniotis, *Catal. Today* 88 (2003) 49-59.
- [46] T. Ohno, K. Jarukawa, K. Tokieda, M. Matsumura, *J. Catal.* 203 (2001) 82-86.
- [47] J.C. Colmenares, M.A. Aramendia, A. Marinas, J.M. Marinas, F.J. Urbano, *Appl. Catal. A: Gen.* 306 (2006) 120-127.
- [48] F.J. López-Tenllado, A. Marinas, F.J. Urbano, J.C. Colmenares, M.C. Hidalgo, J.M. Marinas, J.M. Moreno, *Appl. Catal. B: Environ.* 128 (2012) 150-158.
- [49] M.A. Aramendia, J.C. Colmenares, A. Marinas, J.M. Marinas, J.M. Moreno, J.A. Navio, F.J. Urbano, *Catal. Today* (2007) 235-244.
- [50] M.E. Manriquez, T. Lopez, R. Gomez, J. Navarrete, *J. Mol. Catal. A: Chem.* 220 (2004) 229-237.
- [51] T. Mizuno, Y. Matsumura, T. Nakajima, S. Mishima, *Int. J. Hydrogen Energy* 28 (2003) 1393-1399.
- [52] A. Galińska, J. Walendziewski, *Energy Fuels* 19 (2005) 1143-1147.
- [53] M. Ni, M. K. H. Leung, D. Y. C. Leung, K. A. *Renew. Sustain. Energy Rev.* 11 (2007) 401-425.
- [54] K. Maeda, *J. Photochem. Photobiol. C Photochem. Rev.* 12 (2011) 237-268.
- [55] K. Shankhamala, J. Ciston, S.D. Senanayake, D.A. Arena, E. Fujita, D. Stacchiola, L. Barrio, R.M. Navarro, J.L.G. Fierro, J.A. Rodriguez, *J. Phys. Chem. C* 116 (2012) 14062-1407.
- [56] L. Guisheng, Z. Dieqing, C. Y. Jimmy, *Phys. Chem. Chem. Phys.* 11 (2009) 3775-3782.
- [57] M. Hinojosa-Reyes, V. Rodríguez-González, R. Zanella, *RSC Adv.* 4 (2013) 4308-4316.
- [58] B. Choudhury, B. Borah, A. Choudhury, *Mater. Sci. Eng. B* 178 (2013) 239-247.
- [59] L. Ilieva, P. Petrova, G. Pantaleo, R. Zanella, L. F. Liotta, V. Georgiev, S. Boghosian, Z. Kaszukur, J. W. Sobczak, W. Lisowski, A. M. Venezia, T. Tabakova, *Appl. Catal. B Environ.* 188 (2016) 154-168.
- [60] E. Mamontov, T. Egami, R. Brezny, M. Koranne, S. Tyagi, *J. Phys. Chem. B* 104 (2000) 11110-11116.
- [61] F. Vindigni, M. Manzoli, A. Damin, T. Tabakova, A. Zecchina, *Chem. Eur. J.* 17 (2011) 4356-4361.
- [62] Y. I Kim, S. J. Atherton, E. S. Brigham, T. E. Mallouk, *J. Phys. Chem.* 97 (1993) 11802-11810.
- [63] F. Galindo, R. Gómez, M. Aguilar, *J. Mol. Catal. Chem.* 281 (2008) 119-125.
- [64] M. E. Contreras-García, M. L. García-Benjume, V. I. Macías-Andrés, E. Barajas-Ledesma,; A. Medina-Flores, M. I. Espitia-Cabrera, *Mater. Sci. Eng. B* 183 (2014) 78-85.
- [65] J. F. Porter, Y.G. Li, C. K. Chan, *J. Mater. Sci.* 34 (1999) 1523-1531.
- [66] B. Ohtani, *Catalysts* 3 (2013) 942-953.
- [67] S. Y. Liu, S. M. Yang, *Appl. Catal. A: Gen.* 334 (2008) 92-99.
- [68] S. Watanabe, X. Ma, C. Song, *J. Phys. Chem. C* 113 (2009) 14249-14257.
- [69] X. Sun, H. Liu, J. Dong, J. Wei, Y. Zhang, *Catal. Lett.* 135 (2010), 219-225.



## Chapter 4: Structural modifications of TiO<sub>2</sub>: Reduced TiO<sub>2</sub>

### 4.1 Laser irradiated TiO<sub>2</sub>

Recent investigations have demonstrated that the reduced TiO<sub>2</sub>, i.e. presence of a high defective TiO<sub>2</sub> structure, significantly improves the photocatalytic activity in the overall solar spectrum, including visible and UV [1, 2]. In this sample surface defect states are composed by under-coordinated Ti<sup>4+</sup> sites and oxygen vacancies which act [3] as anchoring and charge injection/recombination sites, playing a crucial role in the electron injection and recombination dynamics [4].

Literature presents several methods to reduce TiO<sub>2</sub>. Among them treatment under vacuum [5] or under reducing conditions [6] and treatments by using hydrogen plasmas [7, 8]. These methods inevitably involve high processing temperatures (400-700°C), vacuum systems, long processing times and multistep operations. For these reasons it is exceptionally desirable to explore simple and economic strategies to synthesize stable active Ti<sup>3+</sup> doped TiO<sub>2-x</sub> photocatalysts. Very recently the ‘in liquid’ laser irradiation technique has been demonstrated to be an interesting method to easily increase the photocatalytic activity of TiO<sub>2</sub> [9] and other nanomaterials [10, 11] towards the degradation of organic pollutants. In particular *Chen et al.* [9], reporting the activity of laser treated TiO<sub>2</sub> for the enhanced degradation of rhodamine B.

In the present work, a series of photocatalytic water splitting experiments on several laser modified TiO<sub>2</sub> colloids were performed. A consistent increase of the H<sub>2</sub> production, related to a deep structural modification was verified. In the case of water splitting, this method can be ‘built in’, since laser irradiation and hydrogen production can be performed in the same system at the same site. Indeed in our measurements, laser irradiation is performed on aqueous titania dispersions which can be directly used for the subsequent water splitting process.

### 4.2 Samples preparation and experimental setup

TiO<sub>2</sub> Anatase, Rutile and P25 nanopowders were modified by laser irradiation. Anatase and Rutile nanoparticles have been purchased by Sigma Aldrich, while P25 Areoxide by Acros. All products have nominal particle size well below 100 nm. In a typical experiment<sup>1</sup> 25 mg of titania were added to 40 mL of distilled water and sonicated. The obtained titania dispersion was

---

<sup>1</sup>S. Filice, G. Compagnini, R. Fiorenza, S. Scirè, L. D’Urso, M. E. Fragalà, P. Russo, E. Fazio, S. Scalese. *J. Colloid Interf. Sci.* 489 (2017) 131-137.

irradiated under continuous stirring. For such a process, we used the second harmonic (532 nm) radiation of a Nd:YAG pulsed laser system (Continuum, Surelite II model) operating with a pulse duration of 5 ns and a repetition rate of 10 Hz. The laser beam size was around 28 mm<sup>2</sup>, and it was directed toward the titania solution without any focusing lens. The titania suspension was irradiated homogeneously at a constant laser power up to 1.45W (0.5 J/cm<sup>2</sup>) for 30 min. The highest considered fluences are far below the ablation threshold (around 0.8 J/cm<sup>2</sup>). No plasma emission has been detected during the irradiation. Immediately after the irradiation, the initially white suspension turns towards deep blue.

For a complete characterization of as received and irradiated samples, a drop of titania water suspension was placed into copper grids, on glass and silicon slides. Each deposit was placed in a drier overnight.

Photocatalytic water splitting experiments were performed in a Pyrex jacketed reactor at 30°C (thermostated) under the irradiation of a 100 W mercury lamp (Black-Ray B-100A, 365 nm) or under the irradiation of a Osram Ultra Vitalux 300W E27 lamp, specially designed for sunlight simulation. The headspace of the reactor was connected to an inverted buret, filled with water at atmospheric pressure. This allows the measurement of the evolved gases. The evolution of H<sub>2</sub> was also confirmed by analyzing the effluent gases with an online gas chromatograph equipped with a packed column (Carboxen 1000) and thermal conductivity detector. Generally 25 mg of catalyst were suspended in deionized water under stirring. The suspension was then purged with a nitrogen flow for at least 30 min in order to remove dissolved air and then irradiated.

### 4.3 Results and discussion

The effect of laser irradiation on the three investigated powders has some similarities as well as some differences. Initially, anatase, rutile and P25 exhibit sizes below 50 nm and a random polyhedral shape, as shown in Fig. 4.1A. After the irradiation all the investigated samples show the formation of submicrometric, perfectly spherical particles whose concentration increases by increasing the irradiation fluence or the irradiation time, basically in agreement with the works by the Koshizaki group [12]. These authors have reported that such a phenomenon is governed by melting. This initially generates the particle's fusion and it is followed by a rapid cooling step, responsible for the growth of the spheres (Fig. 4.1B). Negligible differences have been observed for the three investigated samples that exhibited a typical sphere size distribution (Fig. 4.1C). The remaining nanoparticles have been found in a mixed rutile/anatase phase, depending on the initial composition.

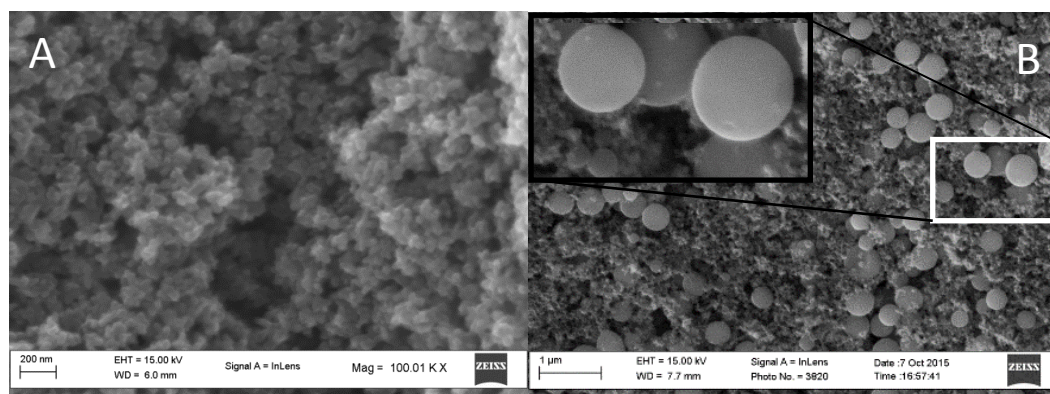


**Fig. 4.1** Typical SEM images for some titania nanoparticles before (A) and after (B) the irradiation (here at  $0.4 \text{ J/cm}^2$ ) showing the changes in size and shape. The variation is similar independently from the initial unirradiated phase; (C) the typical sphere size distribution (as example of the P25 sample) after the irradiation process.

Indeed in Fig. 4.2a a set of well-defined diffraction rings are observed as electron diffraction pattern of the P25 nanomaterial. Characteristic TiO<sub>2</sub> nanocrystal lattice spacing of 0.351 nm, 0.233 nm and 0.189 nm can be assigned to the inter-planar distances of anatase (1 0 1), (1 0 3) and (2 0 0), respectively [13], while the lattice spacing of 0.218 nm corresponds to the interplanar distances of rutile (1 1 1) [14]. After the laser process the nanocrystals are morphologically less regular with respect to the initial well-defined shape, as evidenced by the high resolution image shown in Fig. 4.2b. The morphological change suggests a moderate increase of porosity which can be ascribed to the high pressure conditions during laser irradiation [15, 16] and confirmed by the increase of BET surface area analysis (Fig. 4.3).

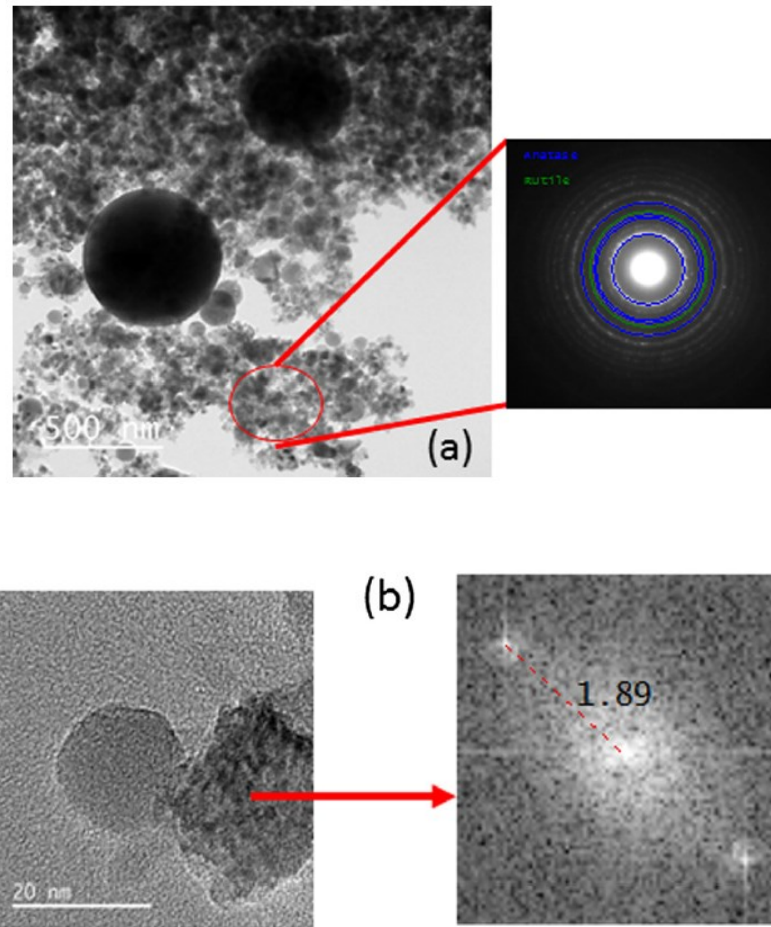


**Fig. 4.2** Detailed TEM images and selected area diffraction analysis of the irradiated samples (a), showing bigger spherical particles within well-defined crystalline materials. Similar analysis has been reported with high resolution images (b).

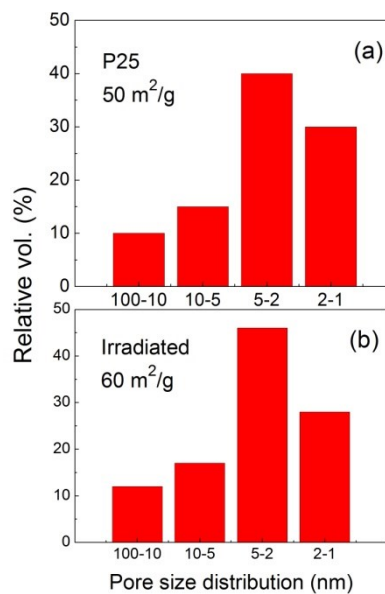


**Fig. 4.3** BET surface area and pore size distribution of P25 sample before (a) and after (b) the irradiation process.

Changes in the crystalline structure and composition have been observed performing Raman analysis. Despite the similarities observed in the morphology between the three sets of samples, laser irradiation partially converts the anatase phase, leaving the rutile and P25 crystalline structure essentially unaltered. Fig. 4.4 reports Raman spectra for rutile, anatase and P25, before and after irradiation at the maximum fluence (0.5 J/cm<sup>2</sup>).

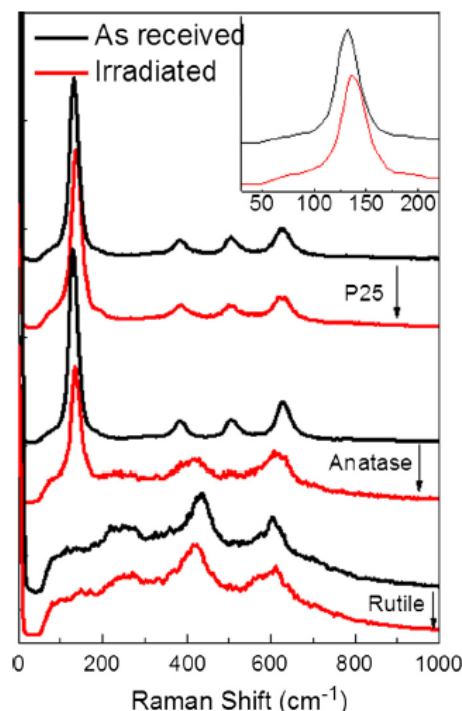


**Fig. 4.4** Typical Raman spectra of as received and irradiated TiO<sub>2</sub> nanoparticles showing a definite change of the crystalline phase for the anatase particles. The inset shows a detailed Raman feature for P25.

The anatase structure is characterized by the tetragonal space group of I4(1)/amd and six Raman transitions (1A<sub>1g</sub>, 2B<sub>1g</sub> and 3E<sub>g</sub>) are allowed according to the factor group analysis. The rutile structure is characterized by the tetragonal space group of P4(2)/mnm and five Raman transitions (B<sub>1g</sub>, multi-photon process, E<sub>g</sub>, A<sub>1g</sub> and B<sub>2g</sub>) are allowed [17]. In the present study, four Raman active modes of E<sub>g</sub> (140 cm<sup>-1</sup>), B<sub>1g</sub> (395 cm<sup>-1</sup>), A<sub>1g</sub> (515 cm<sup>-1</sup>) and E<sub>g</sub> (635 cm<sup>-1</sup>) are observed for anatase TiO<sub>2</sub>. Rutile also gives three signals: multi-photon (230 cm<sup>-1</sup>), E<sub>g</sub> (445 cm<sup>-1</sup>) and A<sub>1g</sub>(610 cm<sup>-1</sup>). E<sub>g</sub>, B<sub>1g</sub> and A<sub>1g</sub> are caused by symmetric stretching, bending and antisymmetric O-Ti-O motion respectively [17]. Since the signal at 140 cm<sup>-1</sup> dominates the anatase Raman pattern and the band at 445 cm<sup>-1</sup> is characteristic for rutile, in the case of a two phase mixture it is thus possible to measure the relative intensity of the lines and estimate the rutile/anatase relative content, once the relative cross section has been calibrated with a mixture with a known composition. In this respect the spectral changes observed after the laser irradiation reveal that a partial phase transformation of anatase into rutile has occurred up to 73%. In Fig. 4.5 is reported

a Raman map of anatase after irradiation. The map has been obtained by using the peaks at 140 cm<sup>-1</sup> and at 445 cm<sup>-1</sup> corresponding respectively to anatase (blue) and rutile (red) phases.

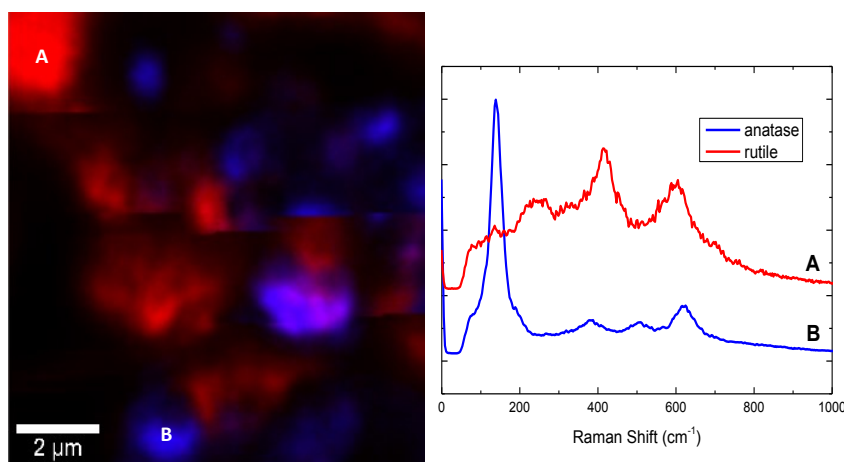


**Fig. 4.5** Raman map of the anatase sample after the irradiation process reporting the signal at 140 cm<sup>-1</sup> for anatase phase (blue) and the signal at 445 cm<sup>-1</sup> for rutile phase (red). The Raman spectra are acquired in correspondence of the maximum signal for both the phase.

Besides, no phase change has been obtained irradiating rutile suspensions, consistently with the fact that rutile is the most thermodynamically stable phase. Raman analysis also reveals that P25 is not modified after irradiation (even at the highest fluence), although it has 80% anatase initial composition. We believe that this observation is consistent with previous studies [18]. In this case, it has been observed that the transformation of P25 into pure rutile under thermal treatments occurs at higher temperatures with respect to anatase. The authors have motivated this anomaly by observing that the phase transformation of titania starts from the interface among the agglomerated anatase particles. If the direct contact between anatase particles is avoided, the phase transformation could be retarded or prohibited. In P25 the presence of rutile zones interacting with the anatase surface could be the reason of a delayed phase transformation [19, 20].

Irradiation also broadens the Raman features and shifts the signals (Table 4.1 and inset in Fig. 4.5). This is generally considered a fingerprint of lattice distortions. According to Ref. [21], there is a correlation between the Raman frequency ( $\nu$ ) and the bond length ( $r$ ) in such a way that:

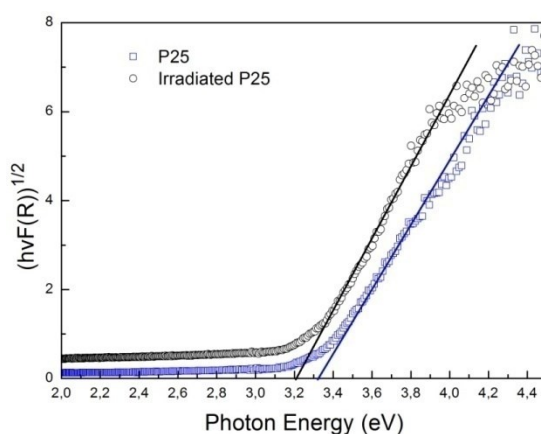
$$\nu = 722 e^{-1.55(r-1.81)}$$

The reported bond lengths for the initial samples are consistent with the known values for anatase and rutile phases [22, 23]. Shifts of the Raman peaks could also be correlated to a nanoparticle size change. In particular, the anatase peak at 140 cm<sup>-1</sup> shows a strong dependence on the sample nanostructure and this has been attributed to quantum confinement effects [24].

**Tab. 4.1** Raman shift, FWHM (Full Width at Half Maximum) values of the characteristic peaks and calculated bond length for the titanium samples after and before the irradiation process.

|                | COMMERCIAL SAMPLE               |                          |                 | LASER IRRADIATED SAMPLES        |                          |                 |
|----------------|---------------------------------|--------------------------|-----------------|---------------------------------|--------------------------|-----------------|
|                | Raman Shift (cm <sup>-1</sup> ) | FWHM (cm <sup>-1</sup> ) | Bond length (Å) | Raman Shift (cm <sup>-1</sup> ) | FWHM (cm <sup>-1</sup> ) | Bond length (Å) |
| <b>RUTILE</b>  | 435                             | 56                       | 2.136           | 423                             | 60                       | 2.154           |
|                | 603                             | 37.4                     | 1.925           | 611                             | 71                       | 1.917           |
| <b>ANATASE</b> | 136.35                          | 24.2                     | 2.885           | 142                             | 24.6                     | 2.858           |
|                | 390                             |                          | 2.206           | 422                             |                          | 2.162           |
|                | 510.55                          |                          | 2.033           | 624                             |                          | 1.903           |
|                | 634                             |                          | 1.893           |                                 |                          |                 |
| <b>P25</b>     | 139.5                           | 25                       | 2.870           | 142                             | 28                       | 2.859           |
|                | 391.7                           | 30                       | 2.204           | 391.7                           | 39                       | 2.204           |
|                | 511                             | 30                       | 3.460           | 511                             | 33                       | 3.460           |
|                | 633                             | 38                       | 1.899           | 633                             | 42                       | 1.899           |

All these results are in agreement with the morphological characterization and reinforce a view in which the formation of highly defective surface states is induced by laser irradiation, with significant changes in the electronic structure of the irradiated materials. As it has been previously mentioned, a first qualitative evidence of the changes induced by laser irradiation is the coloration of the processed nano-powder, consistent with the formation of Ti<sup>3+</sup> vacancies. Quantitatively, an UV-vis reflectance analysis and the calculation of the Tauc plot confirm this hypothesis: the calculated band gap decreases of about 0.2 eV after irradiation (Fig. 4.6).

**Fig. 4.6** Tauc plot for commercial and laser irradiated P25 samples.

The surface and sub-surface states (at a depth up to few nm) of titania was investigated by means of XPS. The results are shown in Fig. 4.7. In the Ti 2p region binding energy values at 458.4 and 464.1 eV are assignable to 2p<sub>3/2</sub> and 2p<sub>1/2</sub> of Ti<sup>4+</sup> in TiO<sub>2</sub> samples [9]. After irradiation, a broader

intensity profile was observed for the blue titania samples. These variations suggest the partial reduction of TiO<sub>2</sub> with the formation of Ti<sup>3+</sup> on the surface of the as-prepared samples.

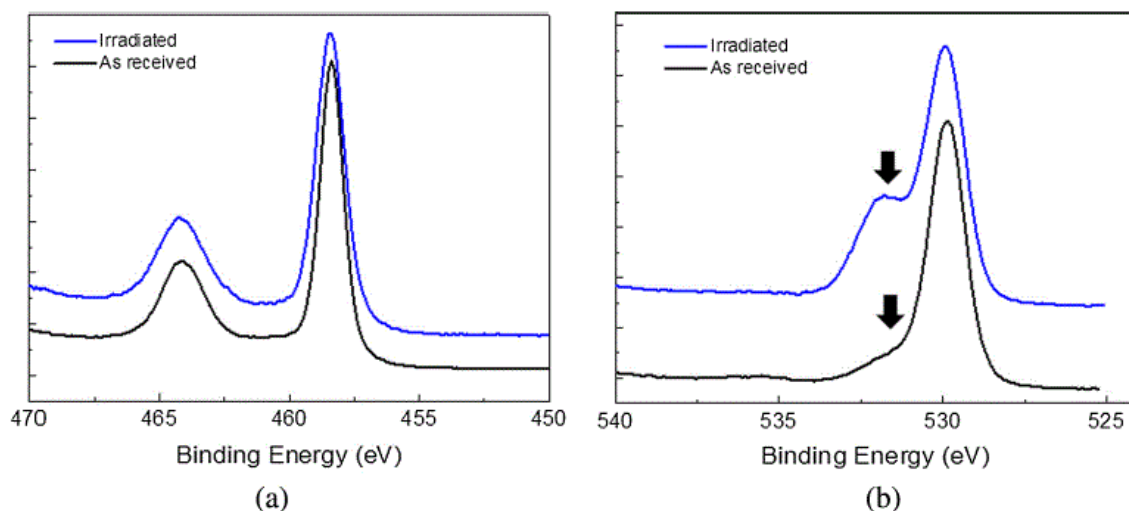


**Fig. 4.7** Typical XPS signals for as received and irradiated samples, showing a moderate variation of the Ti2p signal (a) with the formation of Ti<sup>3+</sup> defects and a consistent increase of the O1s signal (b) at 532 eV, evidencing the formation of strongly bonded hydroxyl groups.

In [Table 4.2](#) the different oxidation states of Ti obtained after the deconvolution of the Ti 2p<sub>3/2</sub> are reported for all the samples before and after the irradiation process. The ratio of Ti<sup>3+</sup>/Ti<sup>4+</sup> is the same for the commercial products and it slightly increases after the irradiation process. In general, the existence of Ti<sup>3+</sup> in TiO<sub>2</sub> indicates that the oxygen vacancies will be generated to maintain electrostatic balance. [Fig.4.7b](#) exhibits the O1s photoelectron signals. O1s electrons, coming from the Ti-O bond, are generally located at 529.5 eV present a more or less pronounced tail at higher binding energies for the nanophase, since surface hydroxyl group are created. Definitely, the irradiation increases the high binding energy tail, leading to the formation of a prominent structure centered at 531.9 eV. Then, while binding energies around 529.6 eV are attributed to crystal lattice oxygen in O-Ti<sup>4+</sup>, the signal at 531.9 eV is consistent with the formation of Ti-OH bonds [9]. It is important to highlight that, since physically absorbed hydroxyl groups on TiO<sub>2</sub> can be easily removed under the ultrahigh vacuum condition of the XPS system, Ti-OH are strongly bound to surface and are characteristically produced by the laser irradiation process.



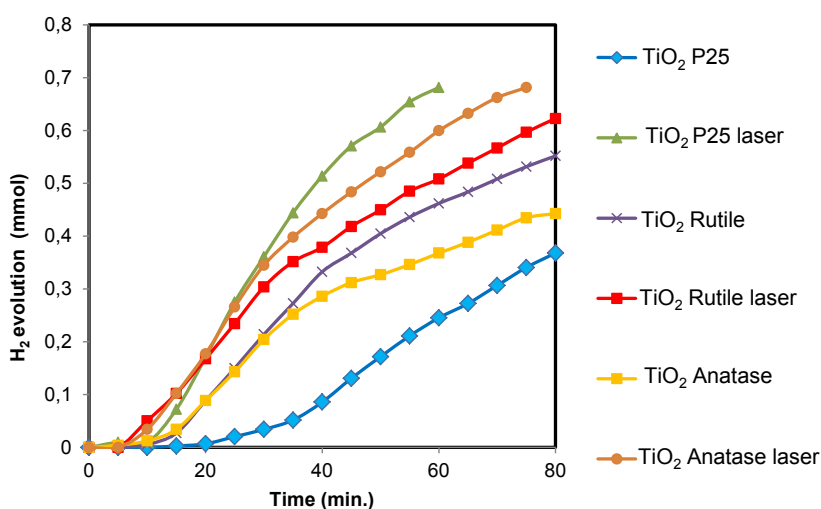
**Tab. 4.2** The percentages and binding energy of different oxidation states of titanium.

|                  | RUTILE |              | IRRADIATED RUTILE |              | ANATASE |              | IRRADIATED ANATASE |              | P25   |              | IRRADIATED P25 |              |
|------------------|--------|--------------|-------------------|--------------|---------|--------------|--------------------|--------------|-------|--------------|----------------|--------------|
|                  | % Ti   | Peak BE (eV) | % Ti              | Peak BE (eV) | % Ti    | Peak BE (eV) | % Ti               | Peak BE (eV) | % Ti  | Peak BE (eV) | % Ti           | Peak BE (eV) |
| Ti <sup>2+</sup> | 0,88   | 455,7        | 0,9               | 455,7        | 0,85    | 455,7        | 0,54               | 455,7        | 0,99  | 455,7        | 1,3            | 455,7        |
| Ti <sup>3+</sup> | 6,5    | 457,19       | 8,78              | 457,3        | 6,32    | 457,3        | 6,38               | 457,16       | 6,34  | 457,2        | 8,62           | 457,08       |
| Ti <sup>4+</sup> | 92,61  | 458,37       | 90,32             | 458,44       | 92,83   | 458,55       | 93,08              | 458,6        | 92,66 | 458,47       | 90,08          | 458,28       |

The most impressive results obtained after laser irradiation is the increased photocatalytic efficiency during water splitting experiments using UV light at 365 nm. Fig. 4.8 shows the hydrogen evolution as a function of time, comparing as received and irradiated samples. All the curves are composed by:

- (1) An initial induction period lasting less than 10 min.
- (2) A linear increment in which there is a maximum in the hydrogen production rate.
- (3) A moderate decrease of the production rate after about one hour irradiation.

The induction is certainly due to the stabilization of lamp radiation and the saturation of water with evolved gases [25], while the decrease of the production rate after one hour is consistent with two fundamental effects [26]. The first is related to a recombination of photo-generated electron/hole pairs: conduction band electrons can recombine with valence band holes very quickly and release energy in the form of unproductive heat or photons. The second can be ascribed to a fast backward reaction: decomposition of water into hydrogen and oxygen is an energy increasing process, thus backward reaction (recombination of hydrogen and oxygen into water) easily proceeds.

**Fig. 4.8** Evolution of hydrogen measured as a function of time in a photocatalytic water splitting experiment for irradiated and as received samples.

The laser irradiation strongly enhances the production rate of hydrogen. It is possible to exclude a correlation between the increased activity and the phase change of titania from anatase to rutile. Indeed P25, which is the sample with the largest difference in the activity, does not exhibit any relevant change in the crystalline phase due to irradiation. In agreement with the theoretical studies reported by Zhao and Liu [27] data reported in Fig. 4.8 evidences also a higher rutile activity with respect to anatase.

The increase of fluence has a positive effect on the photocatalytic performance of titania (Fig. 4.9A) which can be correlated to higher concentration of defects (as confirmed by Raman data).

The Fig. 4.9B displayed the hydrogen production yield for irradiated nanoparticles and that obtained after a standard reduction procedure at 500 °C for 1 h in hydrogen atmosphere. It can be seen that the photocatalytic performances in the H<sub>2</sub> reduced sample is lower compared to laser irradiation. This is quite interesting considering that, very recently, hydrogenated blue titania has been found to greatly enhance both solar absorption and photocatalytic methyl orange decomposition compared to the pristine TiO<sub>2</sub> [28]. These results pointed to the higher efficiency of the laser irradiation process compared to the classical method to reduce TiO<sub>2</sub>.

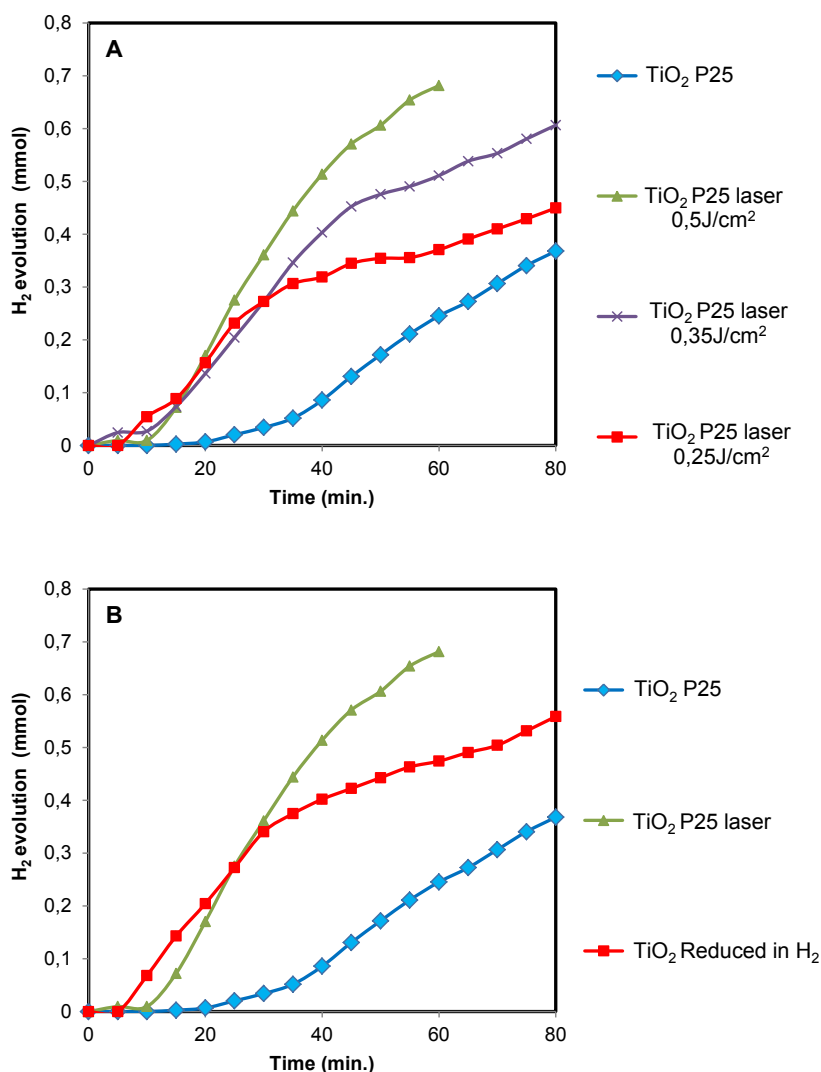


**Fig. 4.9** Overall hydrogen production rate for TiO<sub>2</sub> P25 catalyst tested before and after laser irradiation (A) Rate as a function of the irradiation fluence; (B) A comparison for the P25 sample modified by the laser and by heating treatment in hydrogen atmosphere at 500°C.

The result of consecutive repeated runs are reported in Fig. 4.10. There is a moderate decrease of the maximum rate efficiency and a good data reproducibility which implies negligible deactivation or poisoning of the catalyst. The maximum rate has been always found after 20 min of irradiation. An enhancement of the hydrogen production is also obtained by irradiating the sample using a solar lamp, as shown in Fig. 4.11 for P25.

In this case however it is possible to note that the total amount of hydrogen production with visible light is considerably lower than that found with UV irradiation. This behavior is reasonable, considering the energy band-gap measurements.

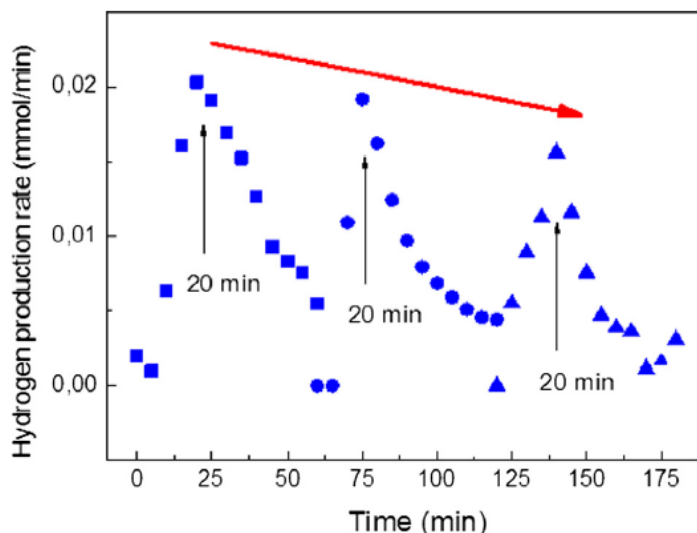


**Fig. 4.10** Hydrogen production rate obtained by using the same irradiated sample three times in succession. The maximum rate is indicated at 20 min under UV irradiation.

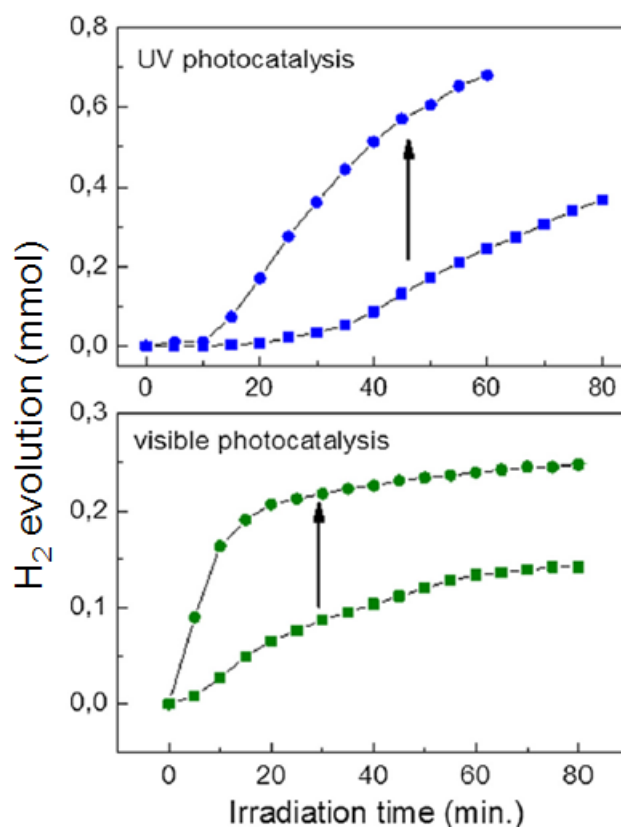


**Fig. 4.11** Comparison of hydrogen evolution measured as function of time for irradiated and as received samples in photocatalytic water splitting experiment under UV or solar light irradiation respectively.

Considering the comparison between the H<sub>2</sub> production rates using UV and solar radiations, it is possible to note that the former has a decrease of the yield more pronounced as time goes by. This effect can be due to a quicker recombination of photo-generated electron/hole pairs.

#### 4.4 Conclusions and future perspectives

The pulsed laser irradiation of several TiO<sub>2</sub> colloidal nanoparticles increases the photocatalytic water splitting performances of the materials under UV and solar actions. The induced magnification is long living and provides a simple and environmental friendly methodology. A detailed structural analysis of the colloids has evidenced that upon irradiation the nanoparticles undergo to a series of modifications, some of which have been demonstrated to be crucial for the enhanced catalytic performances. Among the most significant modifications there are the formation of under-coordinated Ti ions and the induced lattice distortion, which have consequences in the modification of the electronic structure, and a moderate increase of the effective porosity. Laser radiation induced other interesting effects such as the formation of submicrometric spherical particles and a phase change from anatase towards rutile which, however, is inhibited for P25.

In order to further increase the photoactivity also under visible or solar light irradiation and considering that the modifications responsible of increased photocatalytic activity depend on the laser process parameters, preliminary tests changing the laser wavelength and the dispersing solvent of titania colloids were performed. In particular, the third harmonic of Nd:YAG laser (355 nm) instead of the second harmonic (532 nm) was used for the modification of anatase and to investigate the effect of solvent it was dispersed both in water than in ethanol.

**Fig. 4.12** shows the samples after the laser process evidencing the change of the colour of titania colloids to blue, that results more intense in the case of the ethanol sample. The most homogeneous samples were obtained by laser irradiation of titania colloids (3 mg of titania nanoparticles into 10 mL of solvent) for 15 minutes at a constant fluence of 140 mJ/cm<sup>2</sup>.

The changes in the morphology of titania samples by laser irradiation are reported in **Fig. 4.13** showing the SEM images of laser irradiated titania nanoparticles dispersed in bi-distilled water (A) or (B) ethanol. After the irradiation process, both the sample prepared in water and the one prepared in ethanol show the formation of sub-micrometric, perfectly spherical particles with dimension below 200 nm. The conversion of bare (untreated) anatase sample into sub-micrometer spherical particles is not complete in water, as evidenced in **Fig.4.13A** by the presence of brighter particles, having sizes below 25 nm and a random polyhedral shape, due to the bare anatase. The sample prepared in ethanol (**Fig. 4.13B**) shows a quasi totally conversion of initial nanoparticles into sub-micrometer spherical particles of homogeneous size distribution.

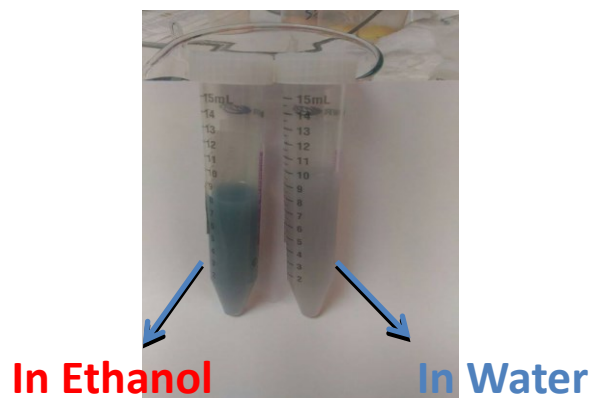


Fig. 4.12 Laser irradiated titania (Anatase) nanoparticles dispersed in bi-distilled water and ethanol.

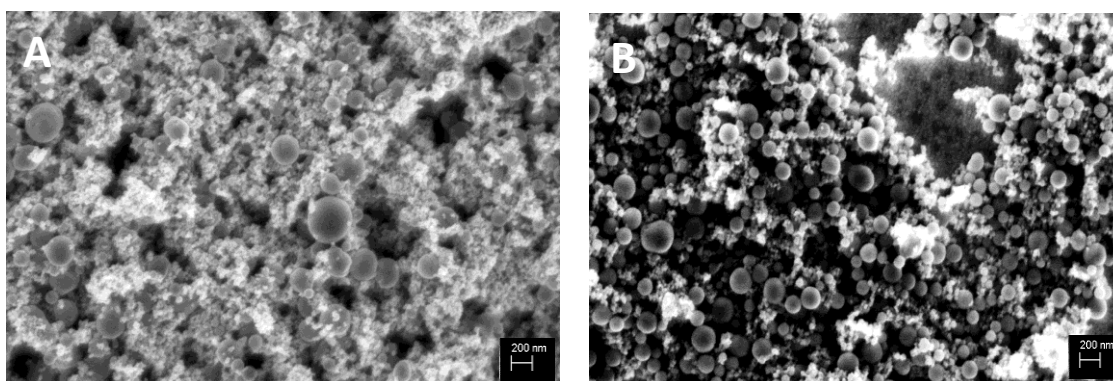
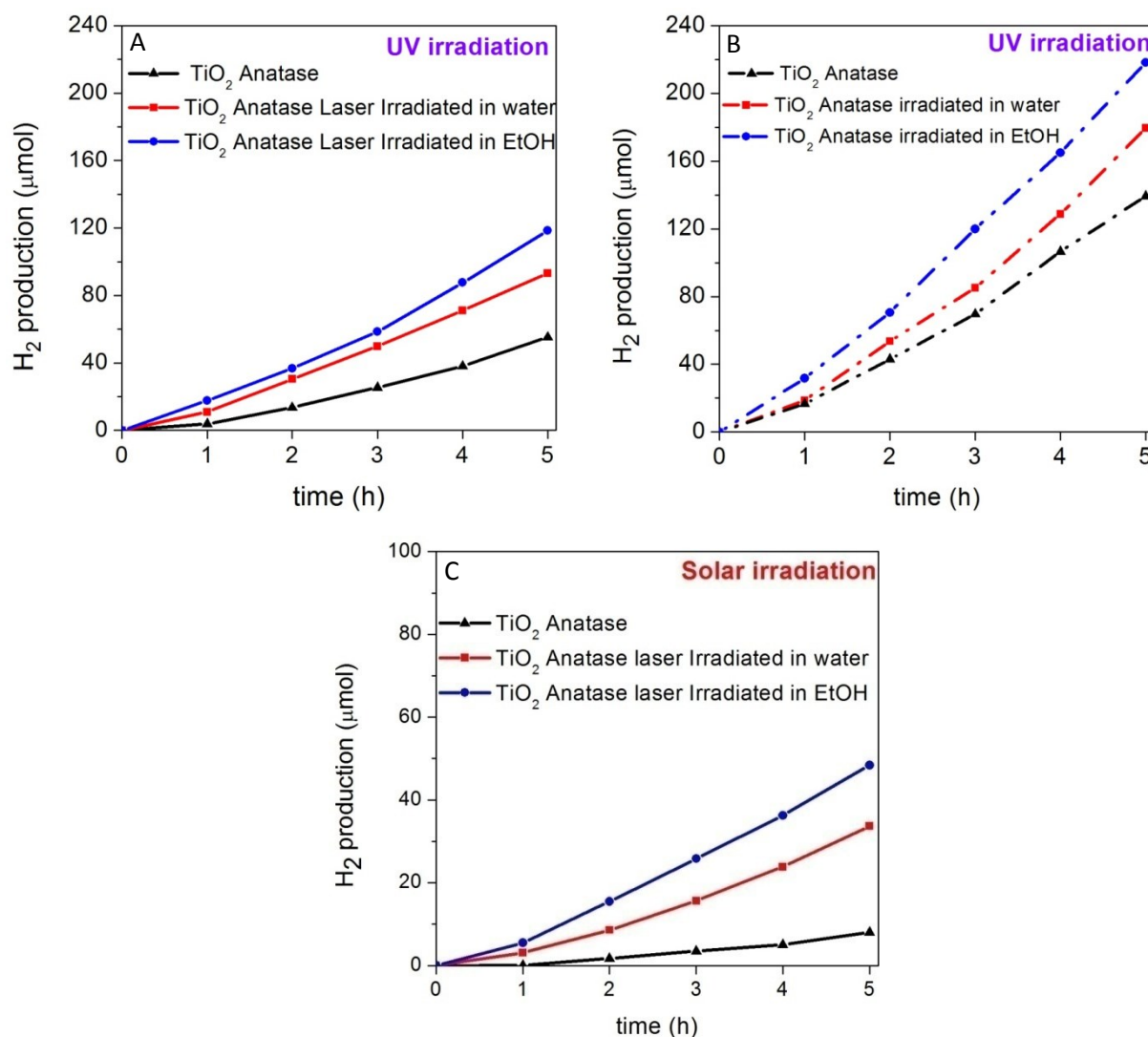


Fig. 4.13 SEM images of laser irradiated titania nanoparticles dispersed in bi-distilled water (A) and (B) ethanol.

The morphological change suggests a moderate increase of porosity which can be ascribed to the high pressure conditions during laser irradiation. This is confirmed by BET Surface area measurements, on the commercial anatase a surface area value of 55 m<sup>2</sup>/g was measured and this value is increased up to 61 m<sup>2</sup>/g and 76 m<sup>2</sup>/g, respectively for laser modified sample in water and ethanol.

Fig. 4.14 shows the hydrogen evolution versus time under UV and Solar light irradiation for the investigated TiO<sub>2</sub> samples. It is interesting to note that the laser modified samples showed a higher activity compared to commercial TiO<sub>2</sub> anatase, the photocatalyst irradiated in ethanol providing the best performance. Under UV irradiation (Fig. 4.14A) the sample irradiated in ethanol exhibits an increased hydrogen production, two times higher compared to commercial TiO<sub>2</sub> anatase. A further increase of hydrogen production was verified using ethanol together with water in the photoreaction mixture (Fig. 4.14B). As reported in the literature [29, 30], ethanol, being a holes scavenger can act as sacrificial agents to avoid the problem of the undesired electrons-holes recombination reaction, which is thermodynamically favored. The role of ethanol as sacrificial agent was further confirmed by the CO<sub>2</sub> peak detected during all the measurements due to the mineralization of organic compound. Interestingly the hydrogen production of TiO<sub>2</sub>

samples modified by laser under solar light irradiation (Fig. 4.14C) displayed a remarkable activity compared to commercial TiO<sub>2</sub> anatase (i.e. 6 and 3 times higher for the sample treated in ethanol and water respectively). The use of ethanol as solvent in the laser processes can be the best choice to improve the activity of TiO<sub>2</sub> sample under visible or solar light irradiation as direct consequence of the better morphology homogeneity. A deep investigation of the chemico-physico properties of the TiO<sub>2</sub>-modified in ethanol could shed light to the effectiveness and of the role of other solvent instead of water in the laser irradiation processes.



**Fig. 4.14** Micromoles of produced hydrogen versus time for the initial sample and the laser modified samples: A) UV irradiation B) effect of ethanol as holes scavenger; C) Solar irradiation (water-ethanol reaction mixture).

## References

- [1] Y. Shiraiishi, H. Sakamoto, Y. Sugano, S. Ichikawa, T. Hirai, *ACS Nano* 7 (2013) 9287-9297.
- [2] J. Tian, X. Hu, H. Yang, Yanli Zhou, H. Cui, H. Liu, *Appl. Surf. Sci.* 360 (2016) 738–743.
- [3] B. Vijayan, N.M. Dimitrijevic, T. Rajh, K.J. Gray, *Phys. Chem. C* 114 (2010) 12994-13002.
- [4] D.C. Hurum, A.G. Agrios, K.A. Gray, T. Rajh, M.C. Thurnauer, *J. Phys. Chem. B* 107 (2003) 4545-4549.
- [5] V.E. Henrich, R.L. Kurtz, *Phys. Rev. B* 23 (1981) 6280–6287.
- [6] Y. Li, X. Li, J. Li, J. Yin, *Mater. Lett.* 59 (2005) 2659–2663.
- [7] B.B. Li, Z.B. Zhao, Q. Zhou, B. Meng, X.T. Meng, J.S. Qiu, *Chem. – Eur. J.* 20 (2014) 14763–14770.
- [8] Z. Wang, C.Y. Yang, T.Q. Lin, H. Yin, P. Chen, D.Y. Wan, F.F. Xu, F.Q. Huang, J.H. Lin, X.M. Xie, M.H. Jiang, *Adv. Funct. Mater.* 23 (2013) 5444-5450.
- [9] X. Chen, D. Zhao, K. Liu, C. Wang, L. Liu, B. Li, Z. Zhang, D. Shen, *ACS Appl. Mater. Interfaces* 7 (2015) 16070-16077.
- [10] P. Russo, L. D’Urso, A. Hu, N. Zhou, G. Compagnini, *Appl. Surf. Sci.* 348 (2015) 85-91.
- [11] M.A. Buccheri, D. D’Angelo, S. Scalese, S.F. Spanò, S. Filice, E. Fazio, G. Compagnini, M. Zimbone, M.V. Brundo, R. Pecoraro, A. Alba, F. Sinatra, G. Rappazzo, V. Privitera, *Nanotechnology* 27 (2016) 245704–245716.
- [12] T. Tsuji, Y. Higashi, M. Tsuji, H. Fujiwara, Y. Shikawa, N. Koshizaki, *J. Laser Micro/Nanoeng.* 8 (3) (2013) 292-295.
- [13] S.K. Das, M.K. Bhunia, A. Bhaumik, *Dalton Trans.* 39 (2010) 4382-4390.
- [14] Q.Y. Zhang, Y. Li, E.A. Ackerman, M. Gajdardziska-Josifovska, H.L. Li, *Appl. Catal. A Gen.* 400 (2011) 195-202.
- [15] L. Li, X. Qin, G. Wang, L. Qi, G. Du, Z. Hu, *Appl. Surf. Sci.* 257 (2011) 8006-8012.
- [16] S. Rather, N. Mehraj-ud-din, R. Zacharia, S. W. Hwang, A. R. Kim, K. S. Nahm, *Int. J. Hydrogen Energy* 34 (2009) 961-996.
- [17] T. Ohsaka, F. Izumi, Y.J. Fujiki, *Raman Spectrosc.* 7 (1978) 321-324.
- [18] H.C. Schniepp, J.L. Li, M.J. McAllister, H. Sai, M.H. Alonso, D.H. Adamson, R.K. Prud’homme, R. Car, D.A. Saville, I.A. Aksay, *J. Phys. Chem. B* 110 (2006) 931.
- [19] R.I. Bickley, T. Gonzalez-Carreno, J.S. Lees, L. Palmisano, R.J.D. Tilley, *J. Sol. Stat. Chem.* 92 (1991) 178-190.
- [20] J.Z. Meijun, L. Zhaochi, F.J. Chen, C. Li, *J. Phys. Chem. B* 110 (2) (2006) 927-935.
- [21] M. Samir, M. Salama, N.K. Allam, *J. Mater. Chem. A* 4 (2016) 9375-9380.
- [22] D.T. Cromer, K. Herrington, *J. Am. Chem. Soc.* 77 (1955) 4708-4709.
- [23] M. Horn, C.F. Schwerdtfeger, E.P. Meagher, *Z. Kristallogr.* 136 (1972) 273-281.
- [24] V. Swamy, A. Kuznetsov, L.S. Dubrovinsky, R.A. Caruso, D.G. Shchukin, B.C. Muddle, *Phys. Rev. B* 71 (2005) 184302.
- [25] A. Galinska, J. Walendziewski, *Energy Fuels* 19 (2005) 1143-1147.
- [26] M. Ni, M.K.H. Leung, D.Y.C. Leung, K. Sumathy, *Renew. Sustain. Energy Rev.* 11 (2007) 401–425.
- [27] W.-N. Zhao, Z.-P. Liu, *Chem. Sci.* 5 (2014) 2256–2264.
- [28] G. Zhu, Y. Shan, T. Lin, W. Zhao, J.Xu, Z. Tian, H. Zhang, C. Zheng, F. Huang, *Nanoscale* 8 (2016) 4705-4712.
- [29] A.Galin’ska, J. Walendziewsk, *Energ. Fuel* 19 (2005) 1143-1147.
- [30] S. Bashir, A.K. Wahab, H. Idriss, *Catal. Today* 240 (2015) 242-245.



## Chapter 5: Structural and chemical modifications of TiO<sub>2</sub>: Inverse Opal TiO<sub>2</sub>

### 5.1 Photonic crystals

Semiconductors technology plays a key role in the modern society involving almost every aspect of our daily lives. The paradigm “ miniaturization = high speed performance ” of integrated electronic circuits has stimulated considerable research effort around the world. One of possibility to reach good results is to turn the light instead of electrons as the information carrier. Light has several advantages over the electron. It can travel in a dielectric material at much greater speeds than an electron in a metallic wire. Light can also carry a larger amount of information per second. Regarding the materials that can be used, in the last few decades a new frontier is opened up with the synthesis and development of *photonic crystals*[1].

A crystal is a periodic arrangement of atoms or molecules. The pattern with which the atoms or molecules are repeated in the space is the crystal lattice. There may be gaps in the energy band structures of the crystal, meaning that electrons are forbidden to propagate with certain energies in certain directions. If the lattice potential is strong enough, the gap can extend to cover all possible propagation directions, resulting in a complete band-gap, as the semiconductors, where there is a complete gap between the valence and the conduction energy bands.

The optical analogue is the *photonic crystal*, in which the atoms or molecules are replaced by macroscopic media with differing dielectric constant the periodic potential is replaced by a periodic dielectric constant (or, equivalently, a periodic index of refraction) [2]. If the dielectric constants of the constituent media are different enough, Bragg scattering off the dielectric interfaces can produce many of the same phenomena for photons as the atomic potential does for electrons [3]. Thus a photonic crystal could be design to possess a *photonic band-gap*: a range of frequencies for which light is forbidden to exist within the interior of the crystal.

In synthesis, the feature of the photonic crystals (PCs) can allow to modulate the light propagation in the structures. In the length scale of the wavelength of light, in fact, light with certain energies is forbidden to propagate in the PCs because of coherent Bragg diffraction. This lead stop-band reflection (photonic band gap, PBG) and the reflected energies (wavelength) depend on the periodic and dielectric contrast of the photonic crystals. At the frequency edges of the stop bands, photons propagate with strongly reduced group velocity in solid matter leading to the *slow photon* appearance. The slow photons can be observed at the edges (red and blue edges) of any stop band. The frequencies of slow photons can be thus varied depending on the edges

frequencies (both at red and blue edges) of the stop bands of the photonic crystal. The location of stop bands and then of the red and blue edges depends on the photonic crystal structures when the chemical composition of two phases forming the photonic crystal structures is defined. This light reflectance and slow photons are generated by a structure effect. With the same chemical composition, by changing the air sphere diameter, the stop band position can be modulated [1-4]. To better understand this phenomenon, it is possible to see a simple example in Fig. 5.1. It is illustrated a material having a photonic band gap at 580 nm. If it is exposed to sunlight, it will appear yellow because it specifically reflects the waves of 580 nm while the others will be transmitted through the material.

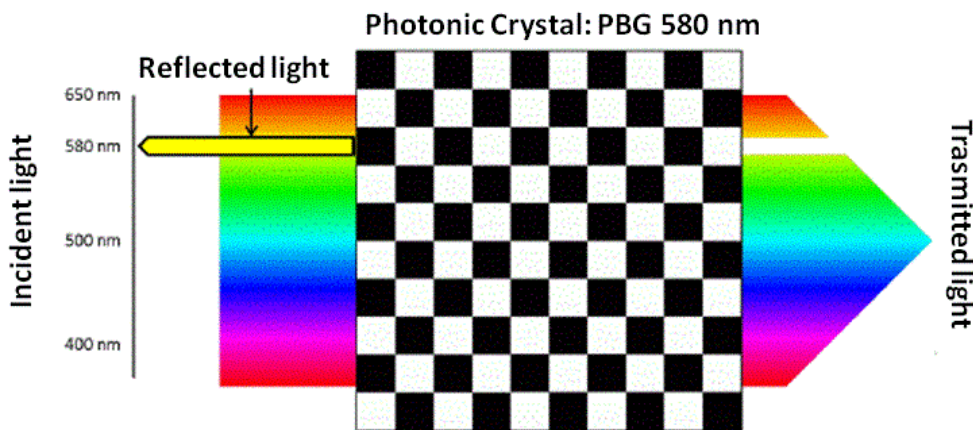
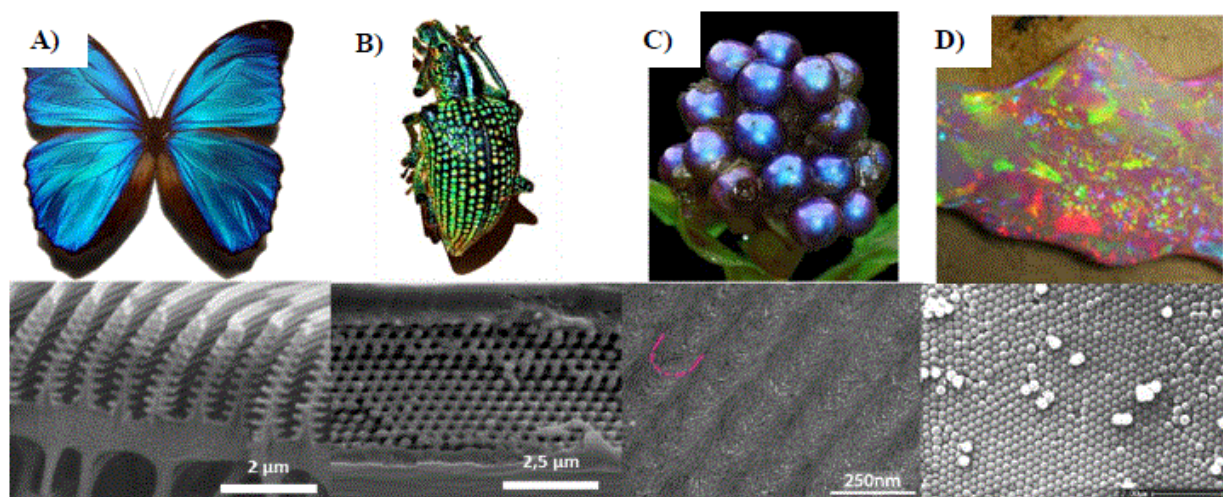


Fig. 5.1 Example of Photonic crystal: Reflection of yellow light.

It is easy to make a parallelism between the couples photonic crystals/photons and semiconductor/electrons. Indeed, the photonic band gap is similar to the electronic band gap and this similarity allows us to imagine a transposition of electronic technologies in photonics technologies for many applications.

In nature for communications, camouflage or protection, many animals and plants have photonic structures. These natural structures provide access to structural colors, obtained by photons/interference structure, as opposed to the pigment colors. Some examples are reported in Fig. 5.2.



**Fig. 5.2** Photos and SEM images of natural crystals photonics: A) “Morpho” butterfly, B) “Entimus Imperialis” beetle, C) plant “Pollia Condensata” and D) Opal stones.

### 5.2 Opal and Inverse Opal materials

The “Opal” material is a hydrated amorphous form of silica ( $\text{SiO}_2 \cdot n\text{H}_2\text{O}$ ); its water content may range from 3 to 21% by weight, but is usually between 6 and 10%. Because of its amorphous character, it is classed as a mineraloid, unlike crystalline forms of silica, which are classed as minerals.

The most important property of opal materials is the diffraction of the light; depending on the conditions in which are formed, in fact, they can take many colours. Precious opal ranges from clear through white, gray, red, orange, yellow, green, blue, magenta, rose, pink, slate, olive, brown, and black. Of these hues, the black opals are the rarest, whereas white and greens are the most common. It varies in optical density from opaque to semitransparent.

Artificial opals are self-assembled face-centred cubic (fcc) structures of spherically shaped beads, which show interesting applications as *photonic band-gap materials* [5].

Convective evaporation is a common method to make artificial opals [6, 7], and has been used to deposit square centimetres of polystyrene or silica beads. Polystyrene (PS) spheres are readily available in a wide range of sizes and can be deposited on a wide range of substrates.

Inverse opals are *photonic crystals* consisting of fcc packed voids embedded in a high refractive index material matrix [8, 9]. Such structures have been used to enhance the efficiency of photocatalytic materials [10, 11], and motivate further studies to improve the deposition process and the quality of the template opals [12, 13].

### 5.3 Inverse Opal TiO<sub>2</sub>

As described in the previous chapters, generally the photocatalytic activity of a semiconductor is mainly determined by three factors:

- a. the light absorption properties;
- b. the light excited charges (electron-hole pairs) transport rate;
- c. The electron-hole recombination rates on the surface

A possible way to reinforce the light absorption property is the increase of the path length of light to improve the photocatalytic efficiency, namely a structure effect other than chemical composition effect. Several studies show that the hierarchically macro-mesoporous TiO<sub>2</sub> structures exhibit an important light harvesting effect of the macrochannels allowing light waves to penetrate deeper inside the photocatalyst [14-16].

Recently, the macroporous inverse opals TiO<sub>2</sub> (I.O. TiO<sub>2</sub>) have been intensively studied in photocatalysis since this kind of structure can provide easy mass transportation and high surface area because of the hierarchical porous structure resulting in enhanced photocatalytic activity [17, 18].

One of the most important properties of macroporous inverse opal materials are in fact, the crystal structures; being *photonic crystals* they have a periodic dielectric contrast and can provide an immense potential to increase the path length of light [19-21]. Moreover it is possible to exploit also the slow photon effect. In particular this effect can be used to enhance the light absorption only if a specific condition is verified: the wavelength of slow photons (at red or blue edge) overlaps with the electronic excitation wavelength (electronic band-gap frequency) of semiconducting materials and the applied irradiation light wavelength.

When these three wavelengths fall at the same wavelength zone, i.e. the condition cited above is satisfied, an enhancement of the light absorption by these slow photons can be expected and these slow photons will excite electrons of semiconducting materials from valence band to conduction band with the generation of a large number of electron-hole pairs resulting in an enhanced photocatalytic activity [19-21]. If the above condition is not satisfied, i.e. only two of three wavelengths coincide no slow photon enhanced light absorption effect can be observed. For example, if the red or blue edge wavelength of stop band coincides with the irradiation wavelength zone, however the electron excitation wavelength (electron excitation band-gap) is located at a different wavelength, no photon at red and blue edges can be used to excite the electron. The occurrence of slow photon effect depends thus also on the irradiation wavelength and electronic band gap of materials. The irradiation wavelength can be easily adjusted

following the position of red and blue edges and electronic band gap of materials. The stop band can be tuned by the variation of materials and also by changing the incident angle [4, 18, 22, 23].

In this work the combination of structural (synthesis of inverse opal TiO<sub>2</sub> with a highly ordered porous framework) and chemical modifications of TiO<sub>2</sub> (addition of different amounts of CeO<sub>2</sub><sup>1</sup>, CuO, BiVO<sub>4</sub> and doping agents as N, W and Hf to the inverse opal TiO<sub>2</sub>) was studied with the aim to investigate how these changes influence the chemico-physical properties of TiO<sub>2</sub> and the photocatalytic performances both in the photo-oxidation (degradation of VOC in gas phase and dye in water) than in the photoreduction<sup>2</sup> (hydrogen generation by photocatalytic water splitting) reactions.

#### 5.4 Inverse Opal TiO<sub>2</sub> based materials: Samples preparation and experimental setup<sup>3</sup>

The Inverse Opal TiO<sub>2</sub> was prepared following three steps:

- 1) Preparation of polystyrene (PS) opal spheres
- 2) Infiltration by sol-gel method using a solution of titanium isopropoxide
- 3) Aging and calcination to obtain an inverse opal structure.

Fig. 5.3 reports the scheme of the synthesis.

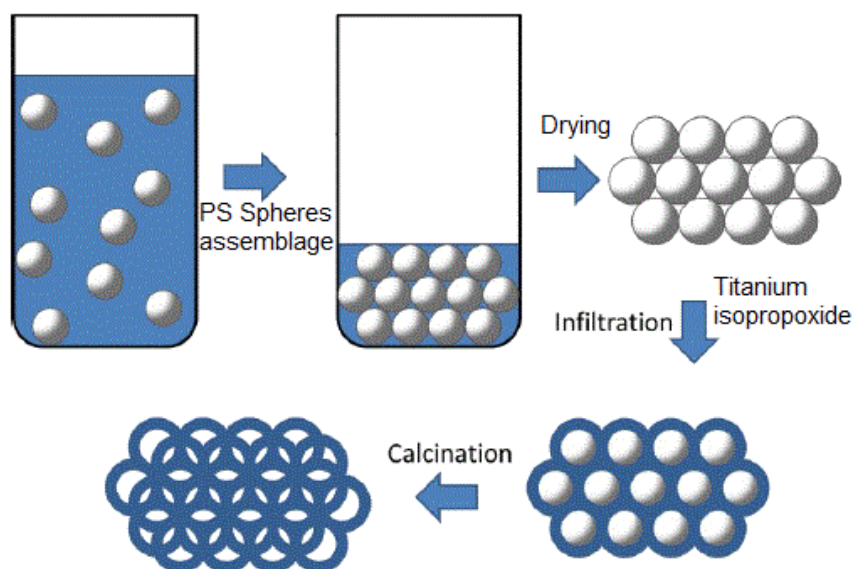


Fig. 5.3 Synthesis of the Inverse Opal TiO<sub>2</sub>.

In particular the Polystyrene spheres were synthesized by an emulsion polymerization method without the addition of a surfactant. Styrene (20 mL) was washed three times with a solution of

<sup>1</sup> R. Fiorenza, M. Bellardita, T. Barakat, S. Scirè, L. Palmisano, J. Photoch. Photobio. A (2017), In press, doi.org/10.1016/j.jphotochem.2017.10.052.

<sup>2</sup> R. Fiorenza, M. Bellardita, S. Scirè, L. Palmisano, Catal. Today (2017), Submitted.

<sup>3</sup> In collaboration with the CMI lab (University of Namur, Belgium) where I spent my period (6 months) as visiting PhD student.

NaOH (1 M) to remove the polymerization inhibitor (4-tert-butylcatechol), and then added to 160 mL of distilled water in a two-neck flask. This solution was stirred at 350 rpm under an inert atmosphere (Ar, to minimize the presence of radical superoxide due to the presence of atmospheric oxygen;  $\text{O}_2 \rightarrow \text{O}_2^{\cdot-}$ ) and heated to  $70^\circ\text{C}$ . After 30 min after the temperature was stabilised at  $70^\circ\text{C}$ , 0.16 g of  $\text{K}_2\text{S}_2\text{O}_8$  was added to initiate the polymerization. After other 30 min, the mixture became cloudy and later 5 hours the polymerization was stopped by cooling and venting the flask. To obtain an opal structured template, the PS beads dispersion was self-assembled by oven-drying at  $40^\circ\text{C}$  or  $60^\circ\text{C}$  for 5 days and characterised by scanning electron microscopy (SEM).

The fabrication of high ordered macroporous titania was achieved via a templating strategy, as reported in the literature [4, 18, 22, 23] in which a thick layer of self-assembled polystyrene spheres (PS) was deposited onto a filter paper in a Buchner funnel under vacuum. The PS assembly was then infiltrated with the precursor solution. The  $\text{TiO}_2$  sol, formed by 5 mL of absolute anhydride ethanol ( $\text{C}_2\text{H}_5\text{OH}$ ), 1 mL of HCl concentrated, 5 mL of titanium isopropoxide and 1 mL of distillate water, was added drop-wise to completely cover the PS spheres whilst under vacuum such that it occupied the voids inside the PS assembly. The precursor-template mixture was then air dried for 24 h and to obtain  $\text{TiO}_2$  photonic crystals (PCs) with an inverse opal structure (IOS), the follow thermal treatment was used (i.e. calcination, Fig. 5.4):

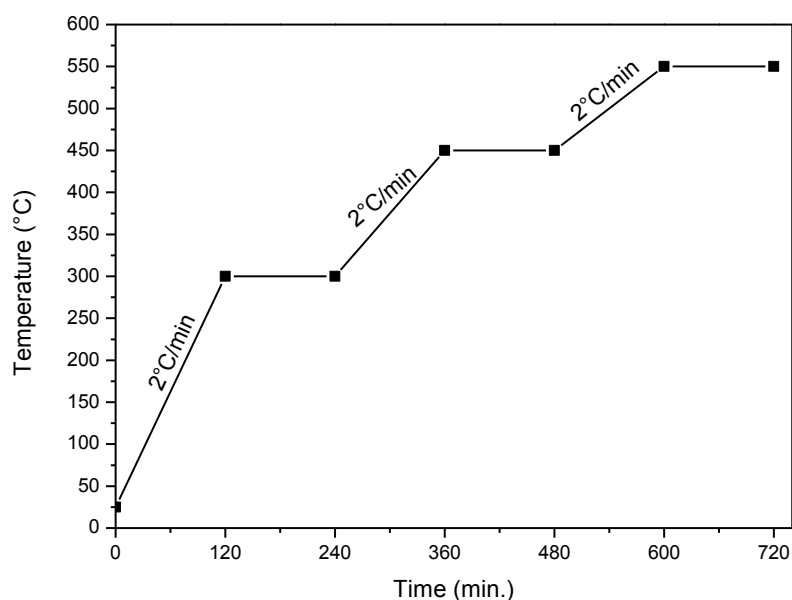


Fig. 5.4 Thermal treatments of the  $\text{TiO}_2$  precursor-template mixture.

1. First ramp ( $2^\circ\text{C}/\text{min}$ ) from room temperature to  $300^\circ\text{C}$  for 2 hours
2. Second ramp ( $2^\circ\text{C}/\text{min}$ ) from  $300^\circ\text{C}$  to  $450^\circ\text{C}$  for 2 hours
3. Third ramp ( $2^\circ\text{C}/\text{min}$ ) from  $450^\circ\text{C}$  to  $550^\circ\text{C}$  for 2 hours
4. Cooling at room temperature ( $2^\circ\text{C}/\text{min}$ )

This treatment was chosen considering the thermogravimetric (TG) analysis reported in Fig. 5.5. Three main zones of weight loss are observed in the analysis. The first mass loss, between 20 and 300 °C, is related to the evaporation of solvents: ethanol, water and 2-propanol (formed during the synthesis of the TiO<sub>2</sub> sol), it is marked by a broad endothermic peak. Between 300 and 350 °C, significant loss of mass is observed, accompanied by a strong exothermic peak corresponding to the degradation of polystyrene coke. The third mass loss, lower, is between 350 and 500°C, characterized by a major exothermic peak. The coke oxidation and condensation of the Ti-O-H hydroxides in Ti-O-Ti take place. Beyond 500°C, the variation in mass becomes negligible and no variations in the TG track are observed.

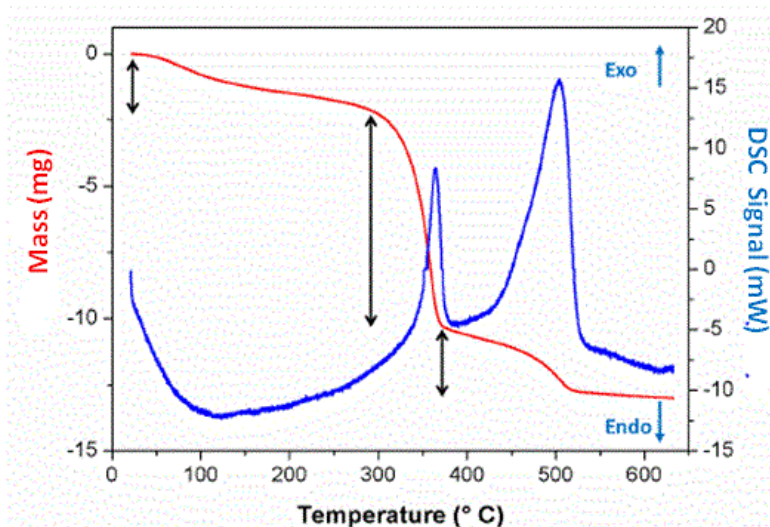


Fig. 5.5 TG-DSC track of the TiO<sub>2</sub> precursor-template mixture.

The modified Inverse Opal TiO<sub>2</sub> systems was prepared with the same procedure adding in the phase of infiltration, together to titanium isopropoxide sol a proper amount of metals salt precursor, in the order: copper (II) chloride (I.O. TiO<sub>2</sub>-CuO catalysts), ammonium chloride, (I.O. TiO<sub>2</sub>-N catalysts), tungsten (VI) chloride (I.O. TiO<sub>2</sub>-W catalysts) and hafnium (IV) n-butoxide (I.O. TiO<sub>2</sub>-Hf system). Co-doped samples were also prepared with an atomic metal/N ratio of 1:2 (TiO<sub>2</sub>-0.5%W-1%N and TiO<sub>2</sub>-0.5%Hf-1%N samples) as to investigate the effects of the co-presence of nitrogen and a metal ion.

The wet-impregnation method was used for the I.O. TiO<sub>2</sub>-CeO<sub>2</sub> samples; different aliquots of cerium nitrate solutions were added to already formed inverse opal TiO<sub>2</sub> material. After drying at 100°C for 24 h the slurry was calcined at 300°C for 3 hours (ramp of 2°C/min).

The I.O. TiO<sub>2</sub>-BiVO<sub>4</sub> systems were prepared using the hydrothermal method. In a typical process, stoichiometric amounts of Bi(NO<sub>3</sub>)<sub>3</sub>·5H<sub>2</sub>O and NH<sub>4</sub>VO<sub>3</sub> were dissolved in a stoichiometric volume of an ethylene glycol-water mixture and stirred for about 10 min until a

clear solution was formed. Then, different amounts of porous TiO<sub>2</sub> were added into the solution and sonicated for 15 min. After 1 h stirring, the obtained yellow-coloured mixture was transferred into a Teflon-sealed autoclave which was maintained at 160°C for 24 h. The solid powders were washed with distilled water several times. Finally, the obtained solid was dried at 100°C for 24 h and then calcined at 300°C for 3 h (ramp of 2°C/min). Bare BiVO<sub>4</sub> oxide was synthesized under the same experimental conditions. The I.O. TiO<sub>2</sub> composites (I.O. TiO<sub>2</sub>-CeO<sub>2</sub>, I.O. TiO<sub>2</sub>-CuO and TiO<sub>2</sub>-I.O. BiVO<sub>4</sub>) were prepared with a nominal concentration of host component varying from 1% to 25% wt, whereas for the I.O. TiO<sub>2</sub> doped systems (I.O. TiO<sub>2</sub>-N, I.O. TiO<sub>2</sub>-W and I.O. TiO<sub>2</sub>-Hf) the nominal concentrations of doping agents ranking from 0.2 to 2% at.

The photodegradation of Rhodamine B (RhB, chosen dye) in water was performed under visible light irradiation (400-800 nm) using 6 neon lamps of 18 W (Osram Lumilux T8). The luminous power of each lamp was 1250 lm and the total luminous power was 7500 lm in the photocatalytic reactor (Fig. 5.6).

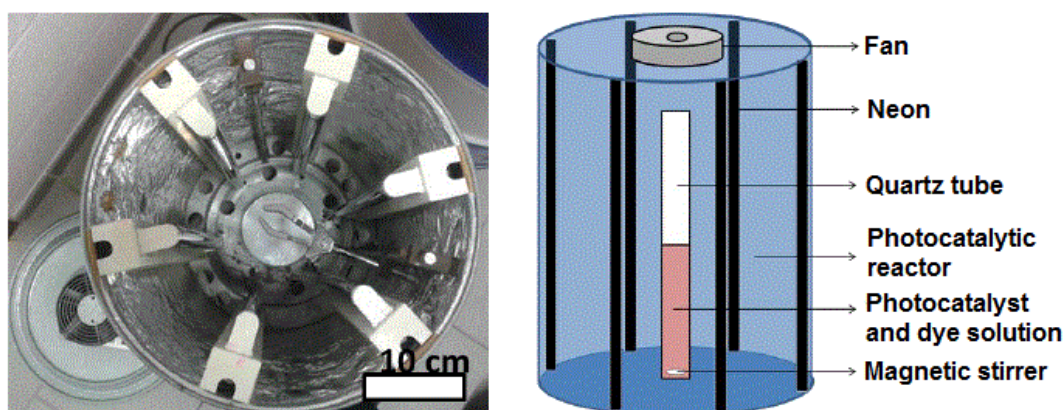


Fig. 5.6 Photocatalytic reactor used.

The intensity of UV light emitted by the neon lamp was very low and can be neglected, and hence no UV filter was used to cut the UV light. The fan located on the surface of the cylindrical reactor maintained the reaction temperature at room temperature. In each experiment 20 mg of the photocatalyst were placed in 50 mL of reactant solution with an initial concentration of 10<sup>-5</sup> M of RhB. The suspension was poured into the quartz tube, inserted into a reactor and stirred in the dark for 120 min to ensure adsorption/desorption equilibrium prior to irradiation. During irradiation, 2 mL of the suspension was removed at a given time interval for subsequent RhB concentration analysis using a UV-vis spectrophotometer.

To compare the photocatalytic performance of the synthesized systems varying the light emission, another photoreactor illustrated in Fig. 5.7 was used.



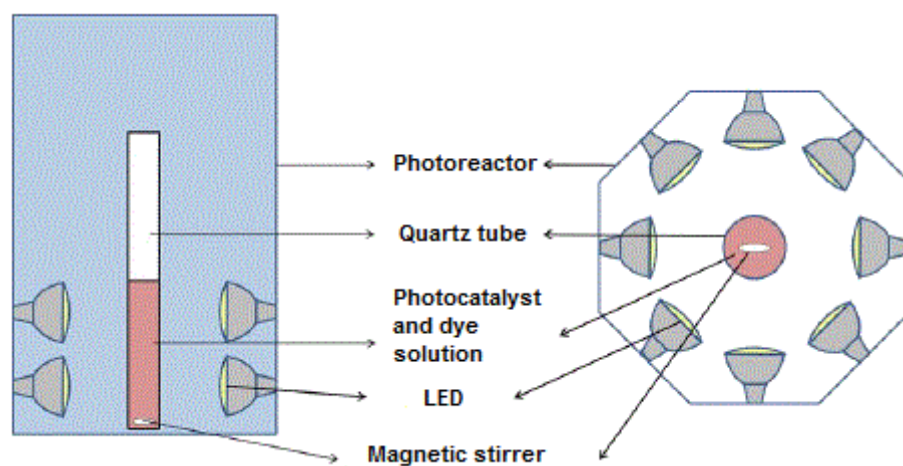
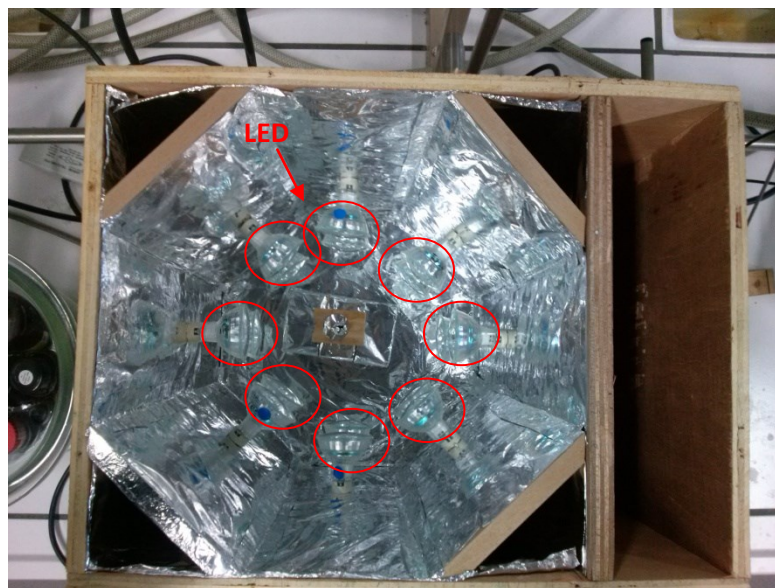


Fig. 5.7 LED Photoreactor.

It was an octahedral reactor with a diameter of 30 cm, with 16 lamp holders allowing to work with Light Emitting Diode (LED) emitting in the blue (Paulmann GU5.3 1W blue 430-470 nm), green (Paulmann 1W GU5.3 green 525-565 nm), yellow (yellow Paulmann GU5.3 1W 585-590 nm) and red (Paulmann GU5.3 1W red 600-620 nm). Two lamp holders are positioned on each side of the reactor, spaced 9 cm from each other. LEDs are distant 8 cm from the center.

To correctly evaluate the dye degradation, it is important select the most appropriate source of excitation light. The dye should not absorb the excitation light to avoid the phenomenon of photolysis. The RhB, i.e. [9-(2-carboxyphenyl)-6-diethylamino-3-xanthenylidene]-diethylammonium chloride (IUPAC name ) exhibits a strong absorbance in the visible region (555 nm green/yellow), as shown in the absorption spectrum of the molecule reported in the Fig. 5.8, for this reason in this work only the blue LEDs (430-470 nm ) were used.

The RhB is a pink dye belonging to the class of xanthene and it also used as food colorant or as a marker in aqueous solution and it is stable in the pH range 5-9.

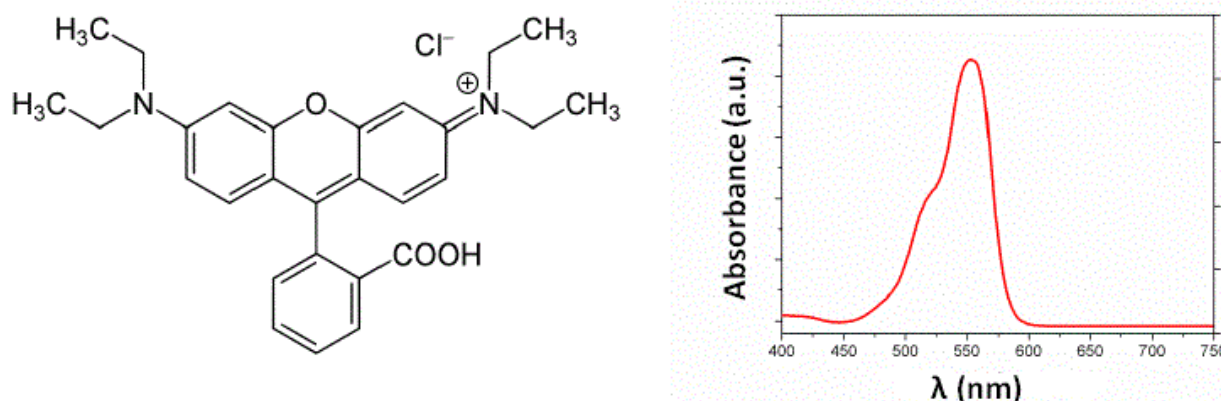


Fig. 5.8 Molecule of Rhodamine B and its absorption spectra.

Hydrogen generation by photocatalytic reforming of aqueous ethanol solution was performed in a home-made Pyrex jacketed reactor thermostated at 30°C (Fig. 5.9). The evolution of H<sub>2</sub> was quantified by analyzing the effluent gases with an online gas chromatograph equipped with a packed column (Carboxen 1000) and thermal conductivity detector using Argon as carrier gas. Specifically, the catalyst (25 mg) was placed inside the photo-reactor with 45 mL of deionized water and 5 ml of ethanol used as sacrificial agent, under stirring. The suspension was purged with an argon flow for at least 1 h before irradiation in order to remove dissolved air. Then it was irradiated for 5 h by using a UV 100 W Hg lamp (Black-Ray B 100A, 365 nm) or a special lamp designed for sunlight simulation (Osram Ultra Vitalux 300W).

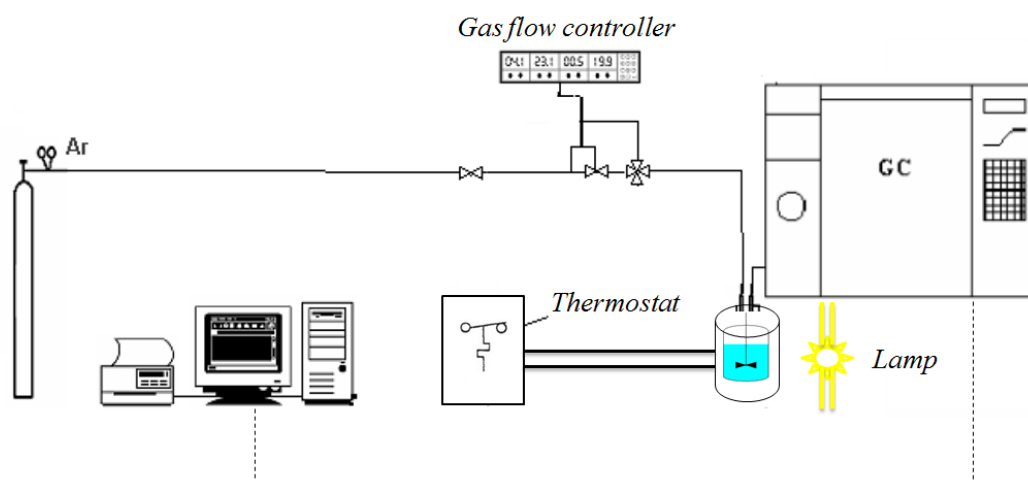


Fig. 5.9 Scheme of the experimental setup used for the photocatalytic water splitting measurements.

The photocatalytic oxidation of ethanol (model VOC) was carried out in the gas phase at atmospheric pressure in a continuous-flow quartz reactor filled with the catalyst (0.2 g). For each experiment, the reactant mixture (0.1 vol.% ethanol 10 vol.% air, balance in helium) was passed over the catalyst for 15 min (to reach a steady-state) before sampling the products for analysis. By using the above procedure, conversion and selectivities were reproducible within 3-5%. Preliminary runs, carried out at different flow-rates, showed the absence of external diffusional limitations. The reactant mixture was fed to the reactor by flowing a part of the He stream through a saturator containing the VOC and then mixing with air and He before reaching the catalyst (Fig. 5.10). A flow rate of the reactant mixture of 20 cm<sup>3</sup> min<sup>-1</sup> with a resulting space velocity (GHSV) of 7.6 x 10<sup>-3</sup> mol<sub>VOC</sub> h<sup>-1</sup> g<sub>cat</sub><sup>-1</sup> was used. The effluent gases were analysed on-line by a gas chromatograph, equipped with a packed column with 10% FFAP on Chromosorb W and FID detector, and by a quadrupole mass spectrometer (VG quadropoles). The carbon balance was always higher than 95%. The reactor was irradiated by a UV mercury lamp (100 W, 365 nm) for 2 hour. The temperature was maintained constant with a fan located near the reactor.

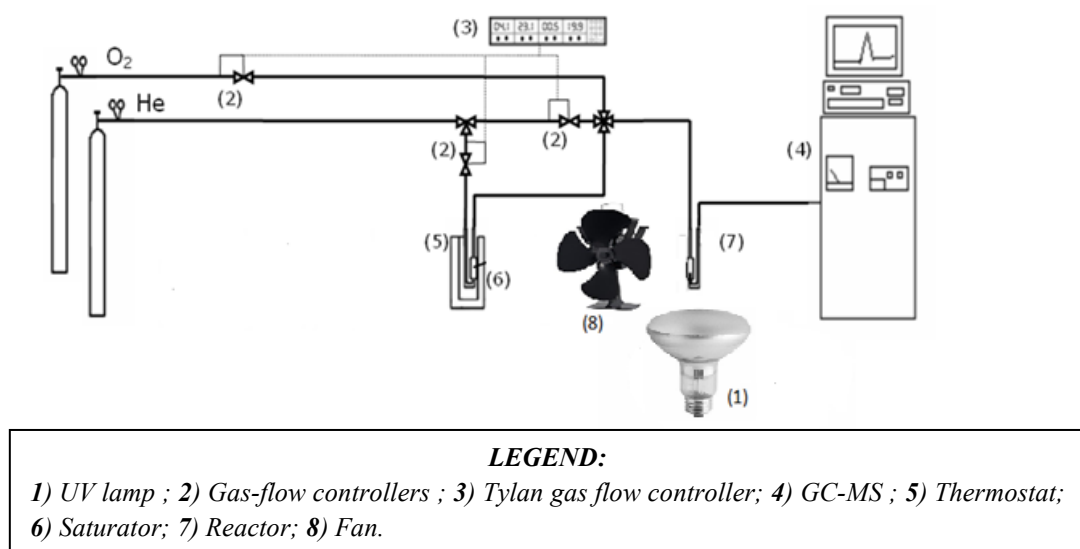


Fig. 5.10 Scheme of the experimental setup used for the photo-oxidation of ethanol.

### 5.5 Results and discussion

Fig. 5.11 shows the SEM images of self-assembled PS spheres, obtained after drying at 40°C for five days. They exhibit a homogeneous close-packed structure. The PS sphere size was around 300 nm, with a low polydispersity (< 5%). It is important to remark that a higher temperature of drying (60°C) the formation of bigger spheres (350-400 nm) with higher polydispersity was detected.

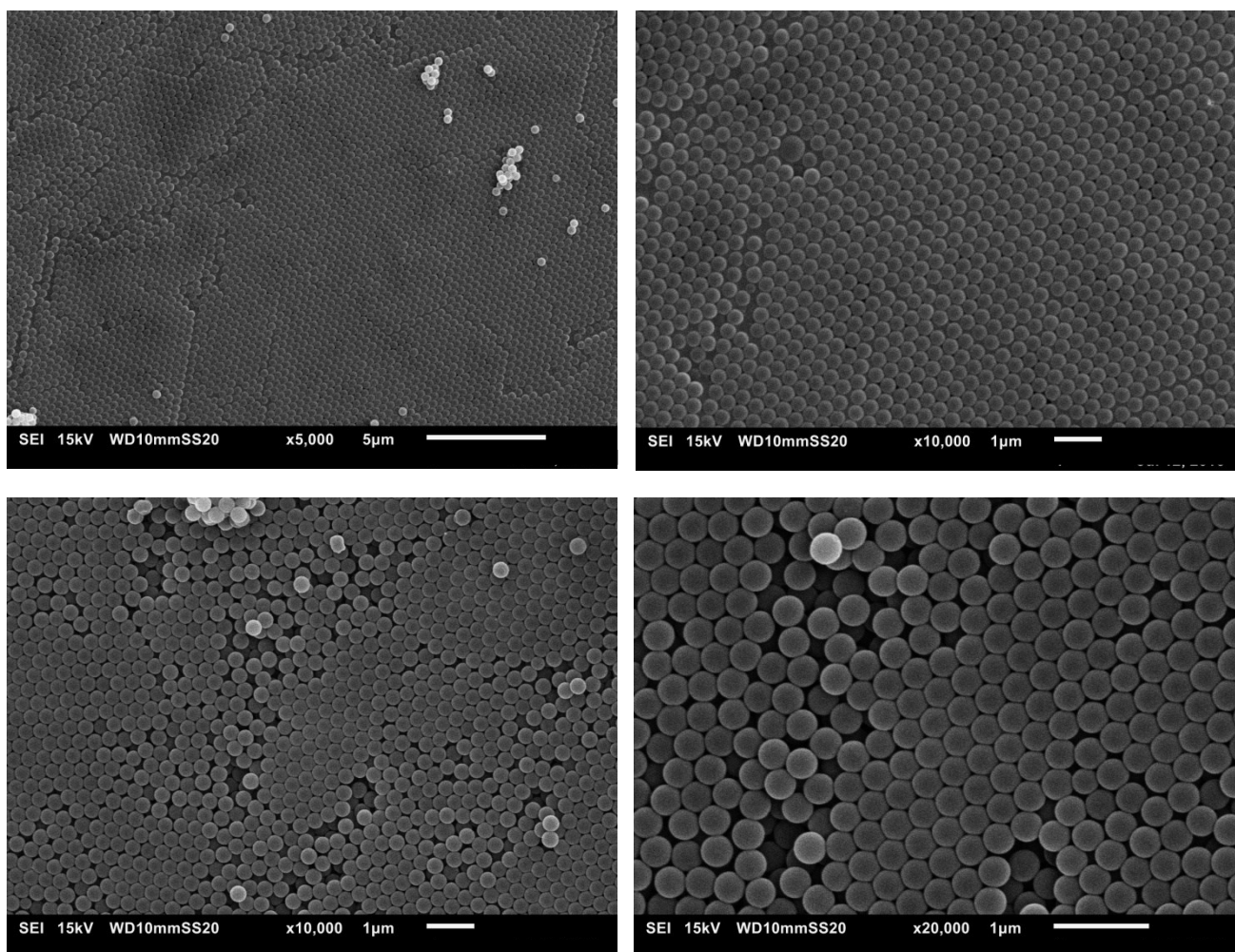
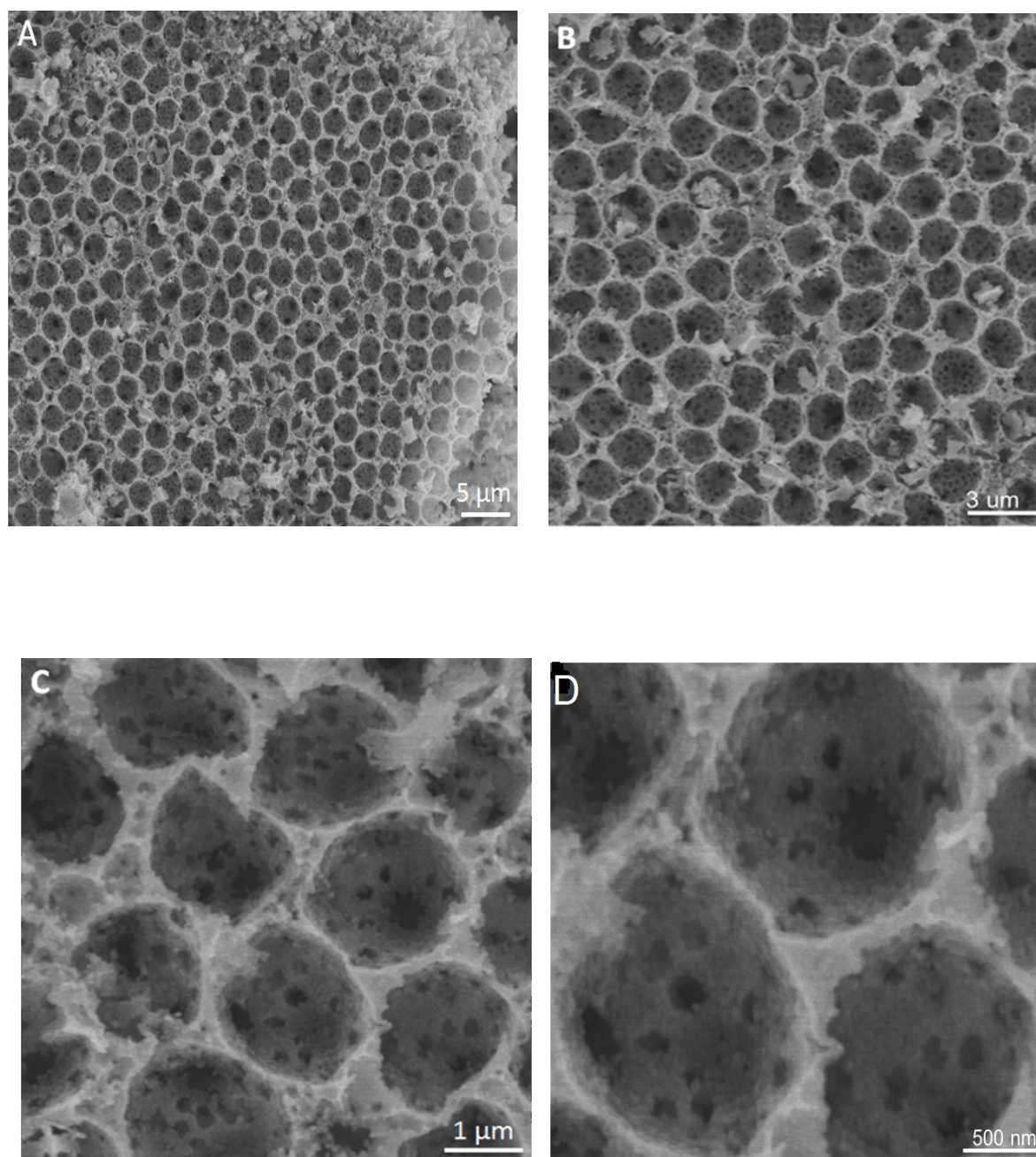


Fig. 5.11 SEM images of PS opal template.

The Inverse Opal  $\text{TiO}_2$  obtained after calcination and consequent removal of PS template had an inverse opal structure with interconnected pores (Fig. 5.12). The macrostructure of the inverse opal  $\text{TiO}_2$  structure was examined by TEM (Fig. 5.13), where the macropores can be clearly identified. The  $\text{TiO}_2$  nanocomposite possessed a highly porous structure which was composed of interconnected macropores within a nanocrystalline skeleton, in good agreement with the SEM observations.

No substantial variation in the morphology of  $\text{TiO}_2$  was observed in the presence of the chemical agents. It is possible to note in the Fig. 5.14 the typical dumbbell-like structure of bare  $\text{BiVO}_4$ .



**Fig. 5.12** SEM images of inverse opal  $\text{TiO}_2$  system at different magnifications.

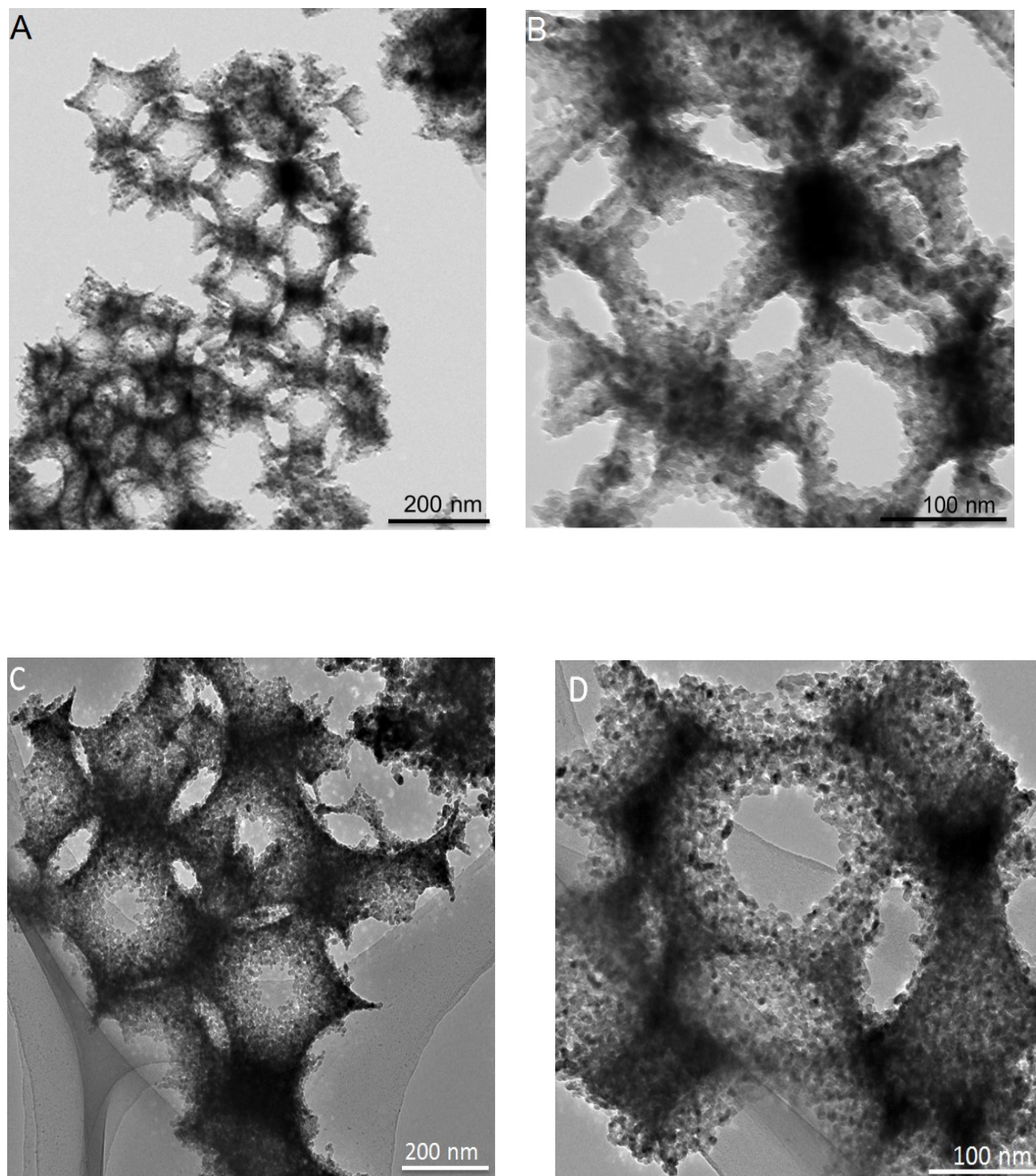


**Fig. 5.13** TEM images of inverse opal  $\text{TiO}_2$  system at different zones and magnifications.

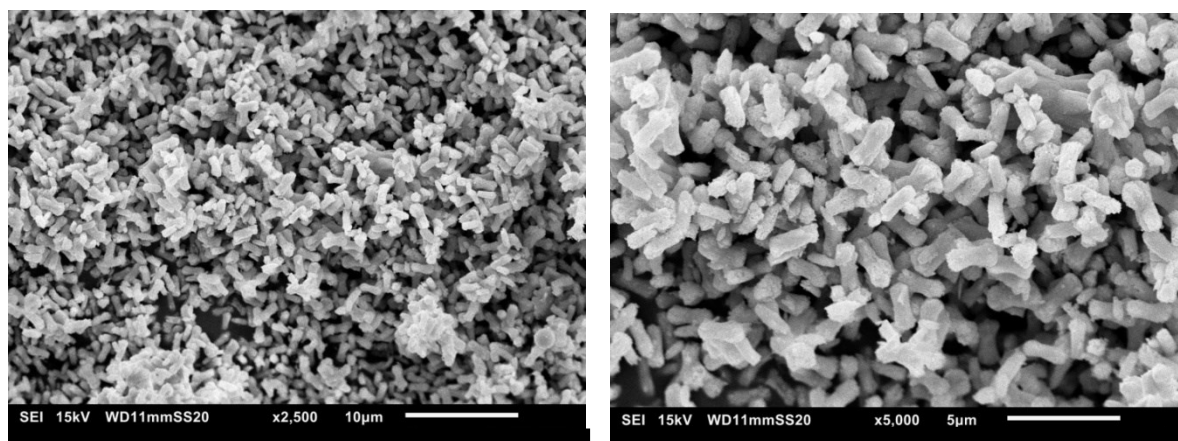


**Fig. 5.14** Typical “Dumbbell-like” morphology of bare BiVO<sub>4</sub>.

XRD patterns of the bare inverse opal TiO<sub>2</sub> and those of modified with the other chemical agents are shown in Fig. 5.15. The bare inverse opal TiO<sub>2</sub> structure shows five peaks at  $2\theta = 25.3^\circ$ ,  $37.8^\circ$ ,  $48.0^\circ$ ,  $54.0^\circ$  and  $55.1^\circ$  indicates that the TiO<sub>2</sub> sample adopts only anatase phase after the calcination at  $550^\circ\text{C}$  [22, 24]. On the TiO<sub>2</sub>-CeO<sub>2</sub> system (Fig. 5.15A, the samples are coded as TiO<sub>2</sub>-XX%MO<sub>x</sub> where XX indicates the wt% of the other component) the XRD peak associated to the CeO<sub>2</sub> phase in the cubic crystal structure of fluorite at  $2\theta = 28.6^\circ$  is well visible only in the sample TiO<sub>2</sub>-25%CeO<sub>2</sub> whereas for a minor amount of cerium oxide the intensity of this signal is very low.

Similarly, also for the I.O. TiO<sub>2</sub>-CuO series (Fig. 5.15B) the catalysts with a high amount of copper oxide (I.O. TiO<sub>2</sub>-10%CuO and I.O. TiO<sub>2</sub>-25%CuO) exhibited both TiO<sub>2</sub> (anatase) and copper(II) oxide (monoclinic CuO at  $2\theta = 35.7^\circ$  and  $38.9^\circ$  [25, 26]) signals. No peak associated to copper(I) oxide was detected, according to the thermal treatment used (calcination at  $550^\circ\text{C}$ ) [26, 27].

The XRD signals of bare BiVO<sub>4</sub> (Fig. 5.15C, red line) nanoparticles correspond to the monoclinic scheelite phase [28, 29]. Also in this case only the doped sample with the 10% (low intensity) and the 25% of bismuth vanadate shows both the signals of TiO<sub>2</sub> and BiVO<sub>4</sub>.

The lack of signals of the TiO<sub>2</sub> host component with an amount lower of 25 wt% is presumably due to a combination of the low content and high dispersion of the other component on I.O. TiO<sub>2</sub> composites.

The average crystallites size of the investigated oxides was determined by applying the Scherrer formula using the (1 0 1) anatase diffraction peak ( $2\theta = 25.3^\circ$ ). The average crystallite sizes of the samples are reported on the Table 5.1.

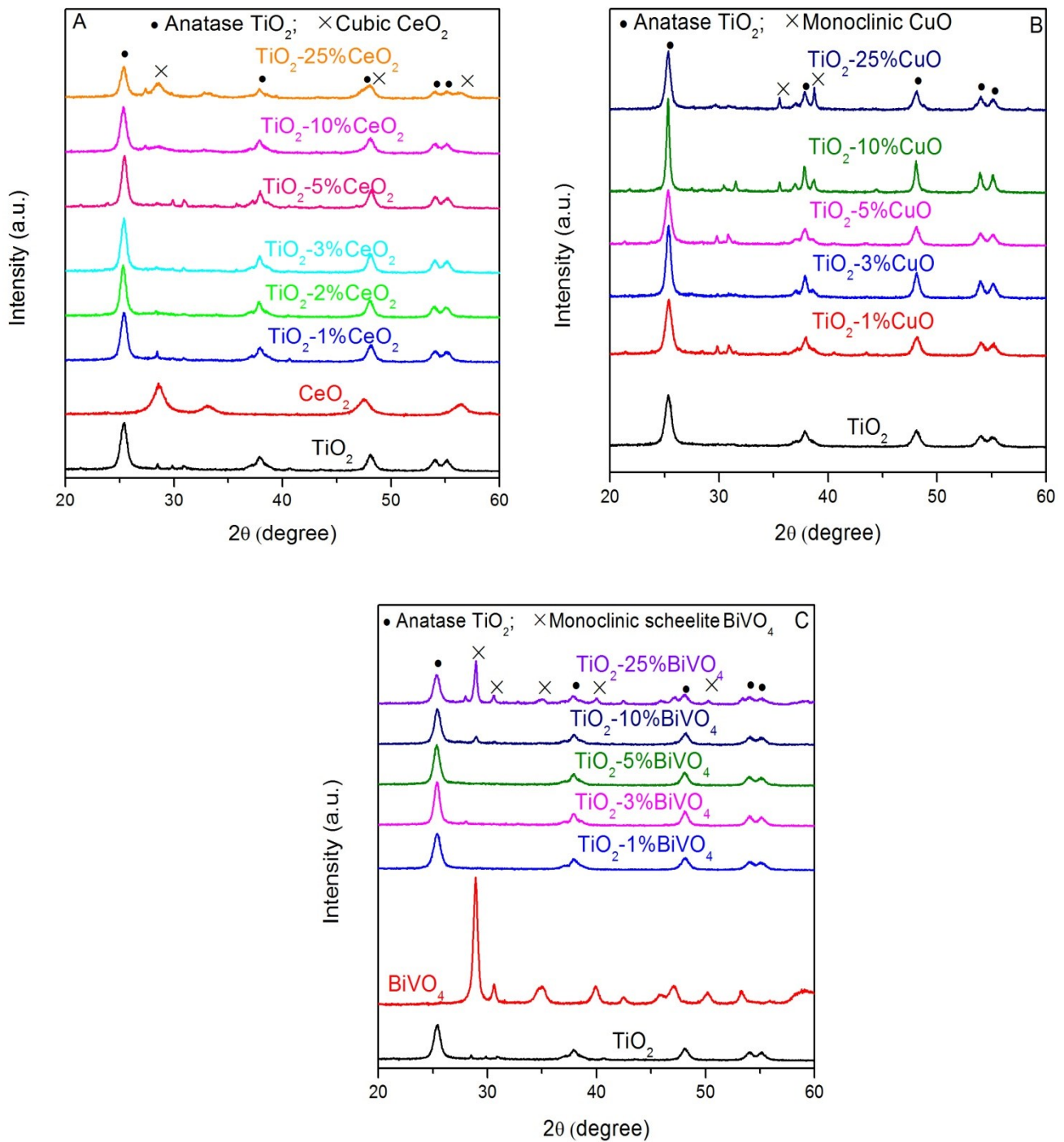


**Fig. 5.15** XRD patterns of inverse opal  $\text{TiO}_2$ - $\text{CeO}_2$  (A); inverse opal  $\text{TiO}_2$ - $\text{CuO}$  (B) and  $\text{TiO}_2$ - $\text{BiVO}_4$  (C) systems.



**Tab. 5.1** Crystallite size calculated by Scherrer equation, BET Surface area, Mean pore diameter ( $d_p$ ), Pore volume and Band-gap energy ( $E_g$ ) for investigated I.O. TiO<sub>2</sub>-based samples.

| Catalysts                              | Crystallite size (nm) | S <sub>BET</sub> (m <sup>2</sup> g <sup>-1</sup> ) | d <sub>p</sub> (nm) (bimodal) | Pore volume (cm <sup>3</sup> g <sup>-1</sup> ) | E <sub>g</sub> (eV) |
|--|-----------------------|--|-------------------------------|--|---------------------|
| TiO <sub>2</sub>                       | 26.9                  | 28.0   | 1.5/-                         | 0.10   | 3.23                |
| TiO <sub>2</sub> -1%CeO <sub>2</sub>   | 27.2                  | 29.8   | 1.4/-                         | 0.08   | 3.23                |
| TiO <sub>2</sub> -2%CeO <sub>2</sub>   | 27.6                  | 29.0   | 1.5/-                         | 0.10   | 3.24                |
| TiO <sub>2</sub> -3%CeO <sub>2</sub>   | 27.8                  | 28.1   | 2.2/-                         | 0.09   | 3.21                |
| TiO <sub>2</sub> -5%CeO <sub>2</sub>   | 28.5                  | 25.5   | 2.7/65.7                      | 0.06   | 3.22                |
| TiO <sub>2</sub> -10%CeO <sub>2</sub>  | 33.1                  | 23.3   | 2.5/69.2                      | 0.06   | 3.18                |
| TiO <sub>2</sub> -25%CeO <sub>2</sub>  | 33.6                  | 13.3   | 2.7/74.4                      | 0.05   | 3.17                |
|  |                       |  |                               |  |                     |
| TiO <sub>2</sub> -1%CuO                | 25.8                  | 28.7   | 1.4/-                         | 0.08   | 3.25                |
| TiO <sub>2</sub> -3%CuO                | 23.9                  | 31.4   | 1.5/-                         | 0.10   | 3.19                |
| TiO <sub>2</sub> -5%CuO                | 20.0                  | 33.0   | 1.4/36                        | 0.09   | 3.16<br>*2.04       |
| TiO <sub>2</sub> -10%CuO               | 17.2                  | 32.2   | 1.2/19                        | 0.06   | 3.18<br>*2.10       |
| TiO <sub>2</sub> -25%CuO               | 16.6                  | 34.5   | 1.5/4                         | 0.06   | 3.14<br>*2.06       |
|  |                       |  |                               |  |                     |
| TiO <sub>2</sub> -1%BiVO <sub>4</sub>  | 25.1                  | 28.3   | 1.4/-                         | 0.08   | 3.19                |
| TiO <sub>2</sub> -3%BiVO <sub>4</sub>  | 25.6                  | 30.3   | 1.5/-                         | 0.10   | 3.18                |
| TiO <sub>2</sub> -5%BiVO <sub>4</sub>  | 26.2                  | 29.7   | 1.4/-                         | 0.09   | 3.17                |
| TiO <sub>2</sub> -10%BiVO <sub>4</sub> | 28.1                  | 28.1   | 1.2/-                         | 0.06   | 3.19                |
| TiO <sub>2</sub> -25%BiVO <sub>4</sub> | 29.3                  | 27.3   | 1.3/-                         | 0.06   | 3.17                |
|  |                       |  |                               |  |                     |
| TiO <sub>2</sub> -0.2%N                | 25.9                  | 28.4   | 1.4/-                         | 0.11   | 3.24                |
| TiO <sub>2</sub> -0.5%N                | 26.5                  | 25.6   | 1.2/-                         | 0.08   | 3.24                |
| TiO <sub>2</sub> -1%N                  | 26.7                  | 26.7   | 1.6/-                         | 0.11   | 3.26                |
| TiO <sub>2</sub> -2%N                  | 25.3                  | 29.0   | 1.7/-                         | 0.11   | 3.27                |
|  |                       |  |                               |  |                     |
| TiO <sub>2</sub> -0.2%W                | 26.8                  | 29.1   | 1.3/-                         | 0.11   | 3.26                |
| TiO <sub>2</sub> -0.5%W                | 26.0                  | 29.2   | 1.4/-                         | 0.08   | 3.26                |
| TiO <sub>2</sub> -1%W                  | 26.6                  | 29.2   | 1.4/-                         | 0.09   | 3.26                |
| TiO <sub>2</sub> -2%W                  | 26.8                  | 31.8   | 1.5/-                         | 0.11   | 3.26                |
| TiO <sub>2</sub> -0.5%W-1%N            | 27.5                  | 25.8   | 1.3/-                         | 0.08   | 3.25                |
|  |                       |  |                               |  |                     |
| TiO <sub>2</sub> -0.2%Hf               | 27.8                  | 30.1   | 1.4/-                         | 0.14   | 3.27                |
| TiO <sub>2</sub> -0.5%Hf               | 28.3                  | 26.6   | 1.6/-                         | 0.12   | 3.29                |
| TiO <sub>2</sub> -0.5%Hf-1%N           | 28.2                  | 30.0   | 1.7/-                         | 0.13   | 3.27                |

\*Mid-gap value

Interestingly it is possible to note different effects depending on the synthesis method used. In general, an increase of the crystallite size is observed in the high temperature treated samples. The presence of CeO<sub>2</sub> (salt precursor added after the formation of the TiO<sub>2</sub> macroporous structure) caused a slight increase of crystallite size from 27 nm of bare TiO<sub>2</sub> to 30-33 nm of the TiO<sub>2</sub>-CeO<sub>2</sub> system, indicating that the nanocrystals of CeO<sub>2</sub> progressively shift to an agglomerated state as a result of densification, resulting in the growth of the titania crystals. However, the TiO<sub>2</sub> crystallite size decreases in the TiO<sub>2</sub>-CuO composites compared to pure inverse opal TiO<sub>2</sub>. This behaviour can be ascribed to the fact that the introduced CuO

nanoparticles (salt precursor added together with titanium isopropoxide before the thermal treatment) inhibit the grain aggregation. In the  $\text{TiO}_2$ - $\text{BiVO}_4$  system, indeed, the crystal size varies progressively with the amount of bismuth vanadate from 25 to 29 nm.

Fig. 5.16 show the XRD patterns of  $\text{TiO}_2$ -N (Fig. 5.16A),  $\text{TiO}_2$ -W (Fig. 5.16B), and  $\text{TiO}_2$ -Hf (Fig. 5.16C) systems. In this case, reasonably due to the low amount of doping agent used (0.2-2 at%), no substantial variations in the crystallite size were observed respect to the un-doped  $\text{TiO}_2$  (Table 5.1). However, a close inspection of the (1 0 1) anatase peak of these samples (Fig. 5.17) reveals that there is a slight shift to lower angles in the presence of N, W and Hf, pointing to the substitution of the  $\text{Ti}^{4+}$  ions of  $\text{TiO}_2$  lattice with N, W or Hf atoms or ions [30, 31].

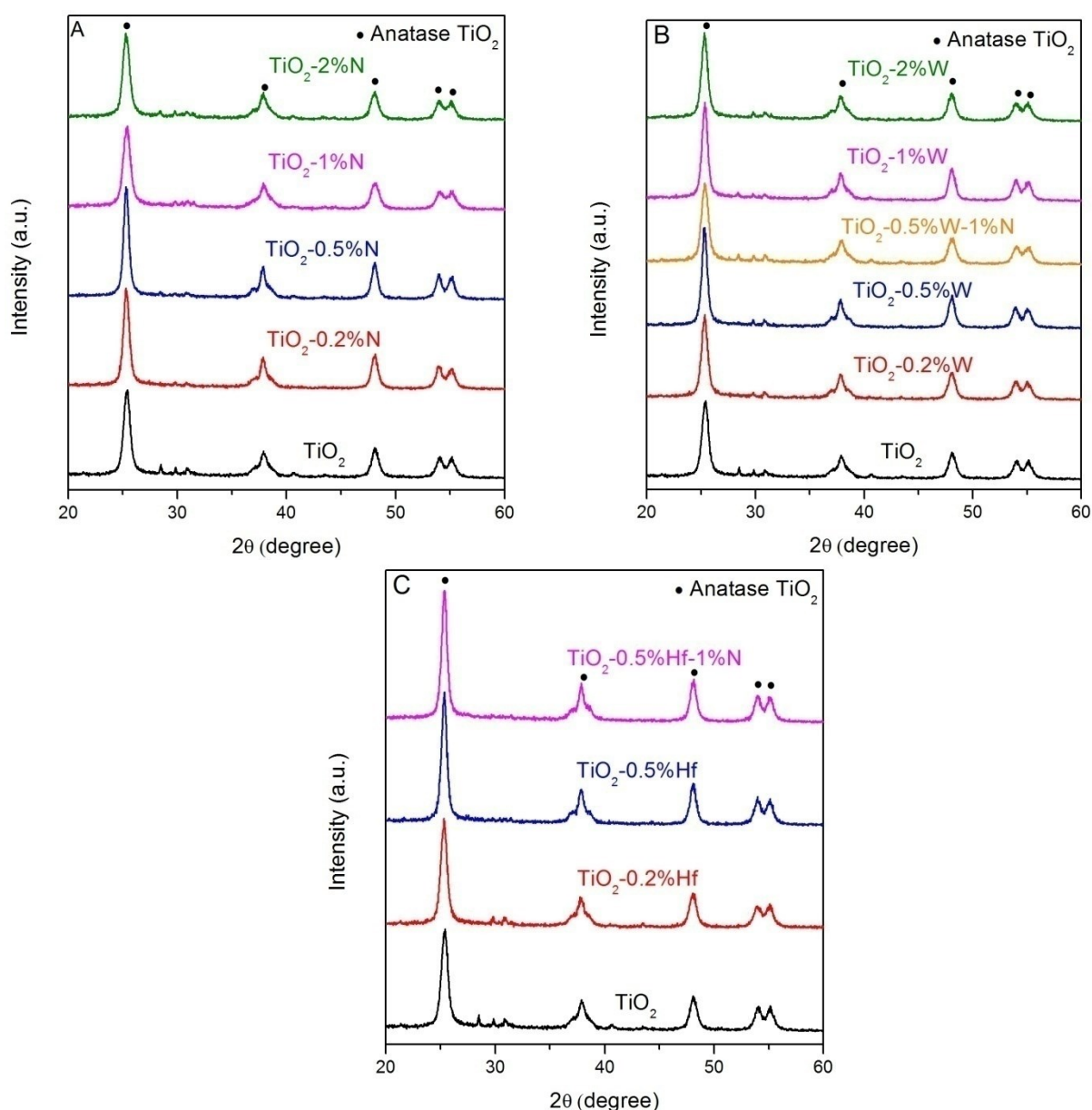
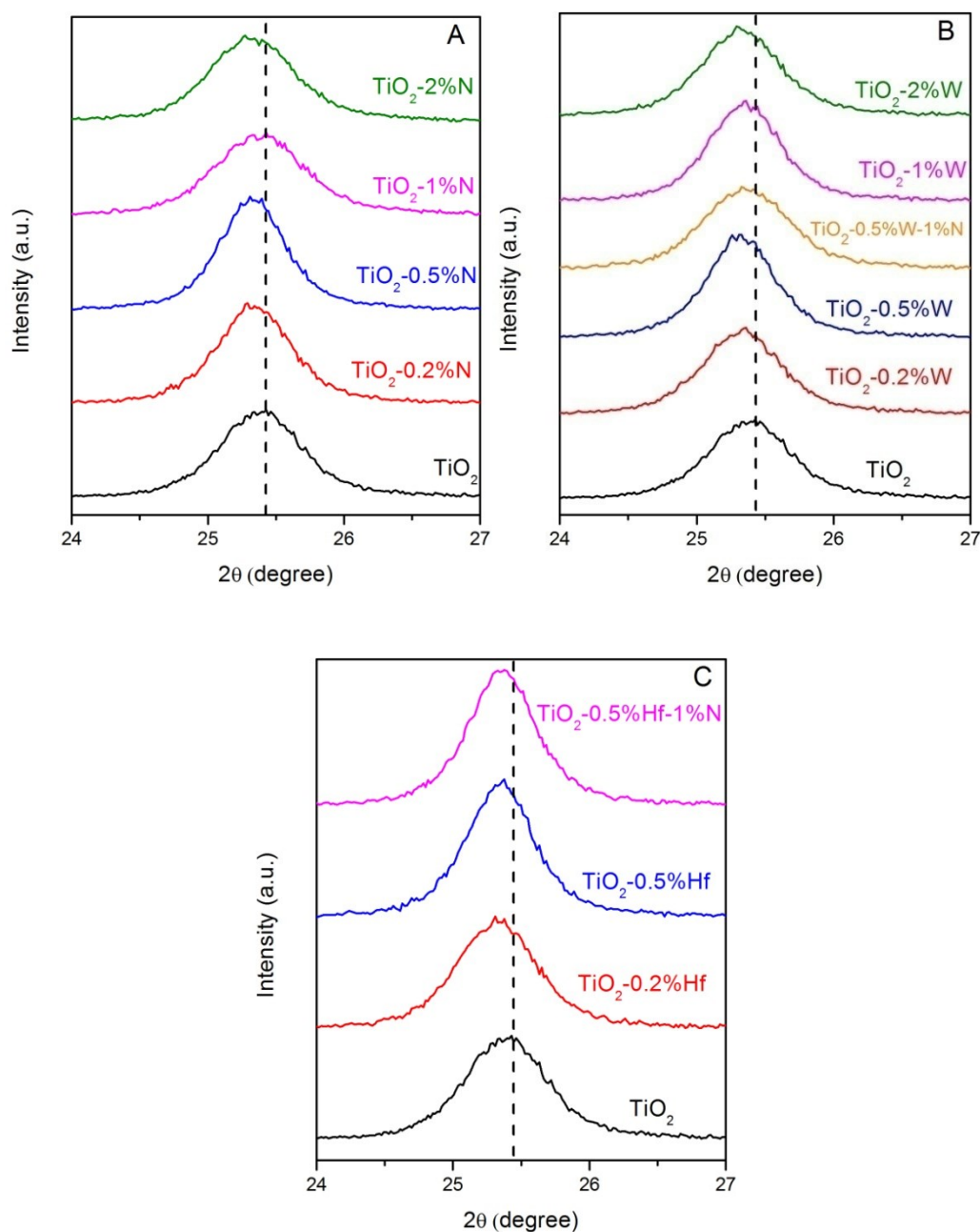
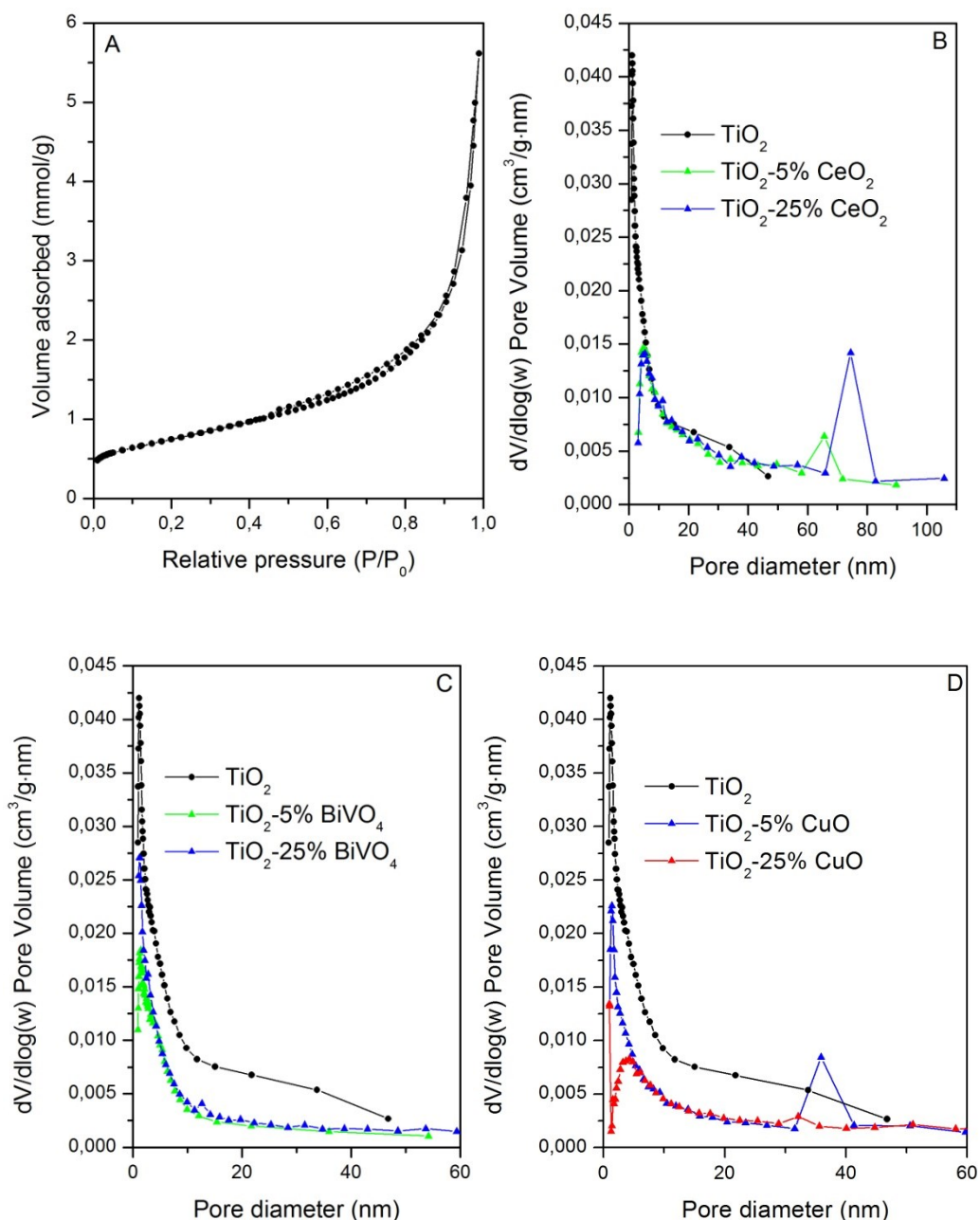


Fig. 5.16 XRD patterns of inverse opal  $\text{TiO}_2$ -N (A); inverse opal  $\text{TiO}_2$ -W (B) and  $\text{TiO}_2$ -Hf (C) systems.



**Fig. 5.17** (1 0 1) Anatase peak of I.O. TiO<sub>2</sub>-N-Metal samples: (A) I.O. TiO<sub>2</sub>-N, (B) I.O. TiO<sub>2</sub>-W, (C) I.O. TiO<sub>2</sub>-Hf.

Fig. 5.18 shows the N<sub>2</sub> adsorption-desorption isotherm (Fig. 5.18A) and the pore size distribution plot (Fig. 5.18B) of the un-doped inverse opal TiO<sub>2</sub> sample, calculated by the Barret-Joyner-Halenda (BJH) method. The isotherm was of type II with a H3 hysteresis loop in the relative pressure (P/P<sub>0</sub>) range of 0.9-1.0 typical of a macroporous structure [32]. The BET surface area was 28 m<sup>2</sup>/g with a narrow pore size distribution centred at 1.5 nm resulting from of the aggregation of TiO<sub>2</sub> nanoparticles. The surface area values of the investigated I.O. TiO<sub>2</sub> modified samples are reported in Table 5.1.



**Fig. 5.18** *N*<sub>2</sub> adsorption-desorption isotherms of I.O. TiO<sub>2</sub> (A); pore size distribution of I.O.TiO<sub>2</sub>, I.O.TiO<sub>2</sub>-5% CeO<sub>2</sub> and I.O.TiO<sub>2</sub>-25% CeO<sub>2</sub> composites (B); pore size distribution of I.O.TiO<sub>2</sub>, I.O.TiO<sub>2</sub>-5% BiVO<sub>4</sub> and I.O.TiO<sub>2</sub>-25% BiVO<sub>4</sub> composites (C) and pore size distribution of I.O.TiO<sub>2</sub>, I.O.TiO<sub>2</sub>-5% CuO and I.O.TiO<sub>2</sub>-25% CuO composites.

In accordance with the above mentioned XRD data, no substantial variations in the textural properties were found for the N-doped or metal doped TiO<sub>2</sub> systems (Table 5.1), whereas for the I.O. TiO<sub>2</sub> composites slight differences in the BET surface area and in the pore size distribution were detected compared to bare inverse opal TiO<sub>2</sub>. In particular, Fig. 5.18B compares the pore size distributions of two samples of the TiO<sub>2</sub>-CeO<sub>2</sub> series having a low (TiO<sub>2</sub>-5%CeO<sub>2</sub>) and a high amount (TiO<sub>2</sub>-25%CeO<sub>2</sub>) of cerium oxide. It is possible to note for both samples the

presence of a macroporous system with pore sizes centered at about 65 and 75 nm for TiO<sub>2</sub>-5%CeO<sub>2</sub> and TiO<sub>2</sub>-25%CeO<sub>2</sub> respectively, attributed to the aggregation of CeO<sub>2</sub> nanoparticles. Interestingly, with an increased amount of CeO<sub>2</sub> nanoparticles, the surface area of the sample decreases, due to the aggregation of CeO<sub>2</sub> nanoparticles and the formation of larger pores (see [Table 5.1](#)).

No changes in the pore sizes distribution were detected adding BiVO<sub>4</sub> ([Fig. 5.18C](#)), on the contrary with the addition of CuO ([Fig. 5.18D](#)), another pore size feature centred at about 36 nm was observed, probably due to the aggregation of copper oxide, aggregation that it is largely reduced in amount on the TiO<sub>2</sub>-25%CuO sample. The progressive introduction of CuO on the TiO<sub>2</sub>-lattice as suggested by XRD measurements, can explain the decrease of pore diameters with the increase of CuO as consequence of the inhibition of the TiO<sub>2</sub> grain aggregation.

The band-gap energies ([Table 5.1](#)) of the catalysts were estimated from the plot of  $(\alpha h\nu)^{1/2}$  versus photon energy ( $h\nu$ ) via the Kubelka-Munk method [[33](#), [34](#)]:  $\alpha h\nu = A(h\nu - E_g)^{1/2}$ , where  $\alpha$ ,  $h$ ,  $\nu$ ,  $E_g$ , and  $A$  are the absorption coefficient, Planck's constant, light frequency, band-gap energy, and constant, respectively. The intercept of the tangents to the x-axis gives a good approximation of the band-gap energy for the materials.

For the TiO<sub>2</sub>-CeO<sub>2</sub> system ([Fig. 5.19A](#)) a slight decrease of band-gap energies was noted when the amount of cerium oxide was increased. This decrease was accompanied by a red-shift to visible region, most evident for the TiO<sub>2</sub>-25%CeO<sub>2</sub> sample. Moreover it is possible to note that the CeO<sub>2</sub> sample had the lowest value of  $E_g$  (2.72 eV). Some authors correlated the decrease in  $E_g$  value of TiO<sub>2</sub>-CeO<sub>2</sub> nanocomposites to the substitution of Ti<sup>4+</sup> cations by Ce<sup>4+</sup>/Ce<sup>3+</sup> cations in the TiO<sub>2</sub> network [[35](#), [36](#)].

The I.O. TiO<sub>2</sub>-BiVO<sub>4</sub> system ([Fig. 5.19B](#)) showed an enhancement of absorption in the visible region by increasing the amount of bismuth vanadate. Consequently a decrease of the band-gap energy was observed ([Table 5.1](#)). It is noteworthy that another absorption feature at about 400 nm was detected in the samples with higher BiVO<sub>4</sub> amounts, more evident for the TiO<sub>2</sub>-25%BiVO<sub>4</sub> catalyst. As it can be seen in the [inset of Fig. 5.19B](#), plotting  $[F(R_\infty) h\nu]^{1/2}$  versus the energy of the exciting light for TiO<sub>2</sub>-25%BiVO<sub>4</sub>, two contributes were found, one at 3.19 eV, due to I.O. TiO<sub>2</sub> and another at 2.40 eV, due to monoclinic BiVO<sub>4</sub> [[37](#), [38](#)]. In accordance with the literature, the presence of these two features suggests the formation of an efficient heterojunction between the I.O. TiO<sub>2</sub> and the BiVO<sub>4</sub> [[39](#)].

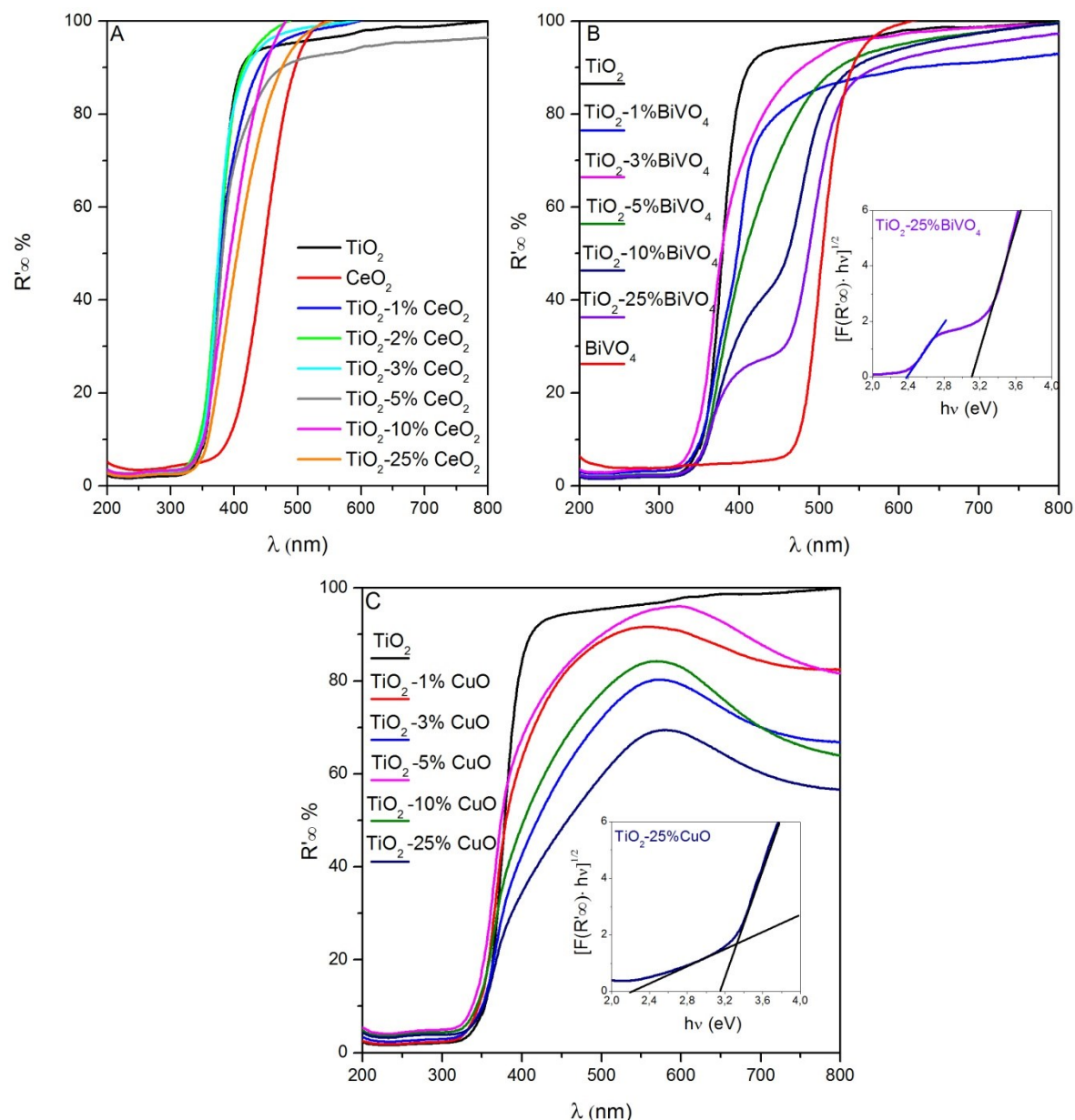


**Fig. 5.19** UV-Vis Diffuse reflectance spectra of (A) Inverse Opal TiO<sub>2</sub>-CeO<sub>2</sub>; (B) Inverse Opal TiO<sub>2</sub>-BiVO<sub>4</sub> and (C) Inverse Opal TiO<sub>2</sub>-CuO composites.

The TiO<sub>2</sub> band edges of the I.O. TiO<sub>2</sub>-CuO samples are all shifted towards the visible region (Fig. 5.19C), indicating that additional energy levels were created by the Cu ions in the band gap of TiO<sub>2</sub> [26, 40], as confirmed by the presence of a mid-gap band located above the valence band in the sample containing high CuO amounts (inset of Fig. 5.19C). Moreover a small decrease (0.05-0.09 eV) in the TiO<sub>2</sub> band-gap energies can be observed (Table 5.1). As reported in the literature, CuO electrons can give excitation from the valence band to the exciton level (< 730 nm), d-d transition of Cu<sup>2+</sup> giving absorption in the 600-800 nm range. These features are ascribed to the CuO nanoparticles, embedded inside the skeleton of TiO<sub>2</sub> [40, 41]. It has been

reported [42] that the presence of Cu(II) causes a shift of the valence band edge towards less positive values, and consequently a decrease of the band gap.

Fig. 5.20 shows the photoluminescence (PL) emission spectra of the I.O. TiO<sub>2</sub>-composites.

It is well known that the PL emission spectra can be used to reveal the efficiency of trapping, transfer and separation of charge carriers, and to investigate their lifetime in the semiconductor. The PL intensity depends on two main factors: a) the recombination of excited electrons and holes as the lower the PL emission intensity, the lower is the recombination property of the sample [43-45] and b) the presence of oxygen vacancies, intensity increasing when the number of vacancies increases. Several emission features can be observed in Fig. 5.20: the peak at 388 nm (UV region) is due to the band to band emission of the TiO<sub>2</sub> [46], the one at 420 nm is attributed to the self-trapped excitons localized on TiO<sub>6</sub> octahedral [47], the two peaks at 485 nm and 525 nm are ascribed to electrons trapped in the defect centres connected with oxygen vacancies [48]. These vacancies trap the excited electrons giving rise to F<sup>+</sup> (with one electron) (Farbe center or color center is a type of crystallographic defect in which an anionic vacancy in a crystal is filled by one or more unpaired electrons) and F center (with two electrons). The shape of the spectra of the I.O. TiO<sub>2</sub>-CeO<sub>2</sub> (Fig. 5.20A) samples was similar to that of bare TiO<sub>2</sub> indicating that the presence of CeO<sub>2</sub> did not originate new PL phenomena, while a decrease of the intensity of some bands was evident, in particular for samples with high amounts of CeO<sub>2</sub>, due to the coverage of the TiO<sub>2</sub> surface with cerium oxide. The bare CeO<sub>2</sub> catalyst shows an emission peak at around 455 nm, due to its band to band emission. A non-linear trend with the CeO<sub>2</sub> percentage was found in the PL spectra of TiO<sub>2</sub>-CeO<sub>2</sub> samples, indicating that during the synthesis process the variation of several parameters (particles size, recombination velocity, presence of defects) occurred at the same time, thus contributing in a different way to the photoluminescence spectra. Excluding the TiO<sub>2</sub>-25%CeO<sub>2</sub> sample (due to the high ceria amount) the lowest PL intensity was found for the TiO<sub>2</sub>-3%CeO<sub>2</sub> catalyst, indicating a lower recombination rate of electrons/holes pairs and a good separation efficiency.

The bare BiVO<sub>4</sub> (red line, Fig. 5.20B), exhibits a broad and strongest emission peak observed at 488 nm ( $E_g = 2.5$  eV) and at 525 nm, corresponding to the near band edge emission (NBE) and defect emission, respectively. The observed NBE emission which is in line with the optical band gap value estimated UV-vis DRS measurements (2.44 eV) and it is also in good agreement with previous reports [49, 50].

It is interesting to note that increasing the amount of BiVO<sub>4</sub> the band at 420 nm decreases in intensity becoming very small on TiO<sub>2</sub>-25% BiVO<sub>4</sub> composites (Fig. 5.20B), thus can mark that the intrinsic radiative recombination between the charge carriers it is reduced. Consequently, the

recombination rate between photogenerated holes and electrons is significantly decreased in the TiO<sub>2</sub>-25% composite. The formation of an efficient heterojunction between BiVO<sub>4</sub> and TiO<sub>2</sub>, favoured increasing the amount of bismuth vanadate, also confirmed by DRS measurements is the key factor to improve the charge transfer typical of photogenerated carriers and to increase the catalytic activity.

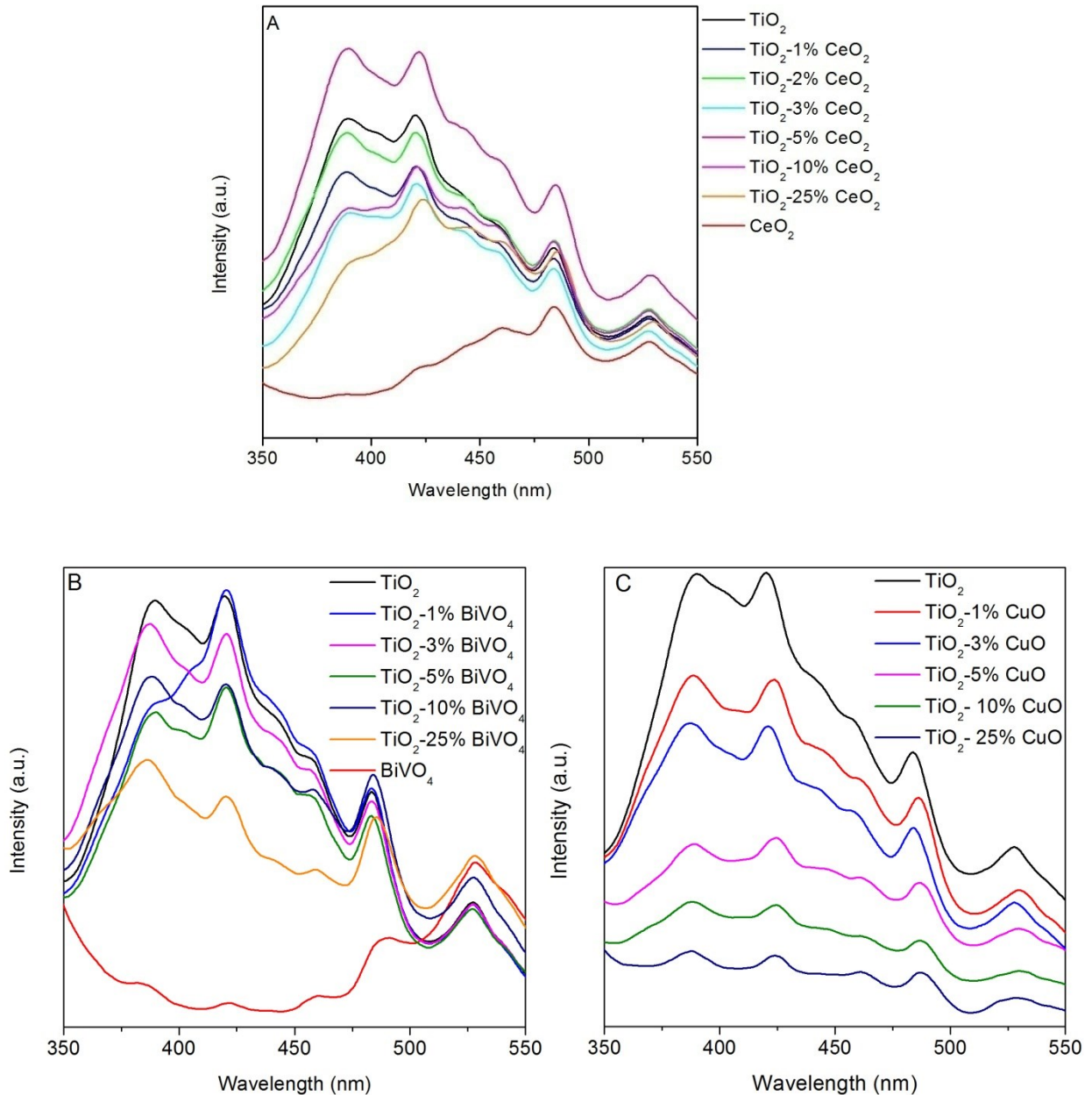


**Fig. 5.20** PL spectra of (A) Inverse Opal TiO<sub>2</sub>-CeO<sub>2</sub>; (B) Inverse Opal TiO<sub>2</sub>-BiVO<sub>4</sub> and (C) Inverse Opal TiO<sub>2</sub>-CuO composites.

For the I.O. TiO<sub>2</sub>-CuO composites (Fig. 5.20C) a strong decrease of the PL bands is detected increasing the amount of copper oxide. In particular the decrease of the intensity of the bands at 420 and 485 nm, more evident for the I.O TiO<sub>2</sub>-5%CuO, I.O TiO<sub>2</sub>-10%CuO and I.O TiO<sub>2</sub>-



25%CuO, can be related to the surface oxygen vacancies and defects of the TiO<sub>2</sub>-CuO photocatalysts. Reasonably in these samples there are a lower recombination rate of photoelectrons and photoholes. The electrons in fact, excited from the valence band to the conduction band of TiO<sub>2</sub> can be easily transfer to CuO clusters, being the Fermi Level of CuO lower of the conduction band of TiO<sub>2</sub>, this transfer prevent the direct recombination of electrons and holes thus resulting in a lower PL intensity [51, 52].

For the I.O. TiO<sub>2</sub>-doped with nitrogen and metallic ions systems, in accordance with the low amount of dopants and with the other characterization measurements no substantial variation were detected compared to the macroporous un-doped TiO<sub>2</sub>, considering both the band-gap values (Table 5.1) and the PL emission spectra.

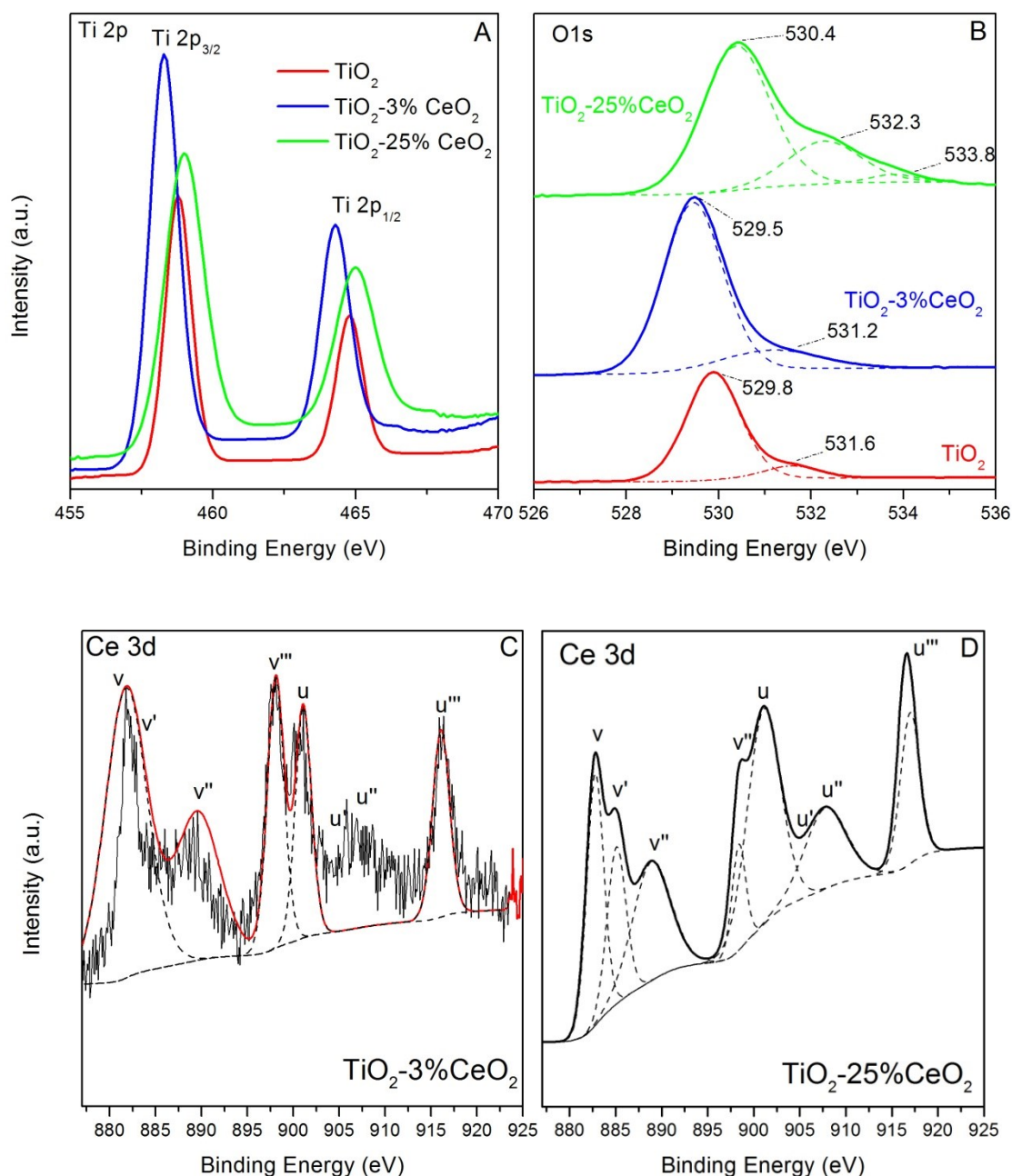
To investigate the oxidation states and the surface composition of involved species, XPS measurements of some samples of the I.O. TiO<sub>2</sub>-modified samples were carried out.

Fig. 5.21A depicts the Ti region of inverse opal TiO<sub>2</sub>, I.O. TiO<sub>2</sub>-3%CeO<sub>2</sub> and I.O. TiO<sub>2</sub>-25%CeO<sub>2</sub>. The two bands with binding energies of 458.8 eV and 464.8 eV on the TiO<sub>2</sub> inverse opal (red line) are assigned to Ti 2p<sub>3/2</sub> and Ti 2p<sub>1/2</sub>, respectively, corresponding to Ti<sup>4+</sup> in a tetragonal structure such as anatase titania [53]. With respect to pure inverse opal TiO<sub>2</sub>, a 0.6 eV shift to lower binding energy in the TiO<sub>2</sub> peak positions (458.2 eV and 464.2 eV) is observed for TiO<sub>2</sub>-3%CeO<sub>2</sub> (blue line), possibly due to a charge or energy transfer occurred after the formation of the heterojunction between CeO<sub>2</sub> and TiO<sub>2</sub>. On the contrary for a higher amount of cerium oxide (TiO<sub>2</sub>-25%CeO<sub>2</sub>, green line), no substantial shift was detected.

The binding energies of O 1s (Fig. 5.21B) for TiO<sub>2</sub> (red line) are located at 529.8 and 531.6 eV. The lowest binding energy is assigned to the lattice oxygen in the metal oxides, whereas the highest one is ascribed to surface oxygen of hydroxyl species and/or weakly adsorbed oxygen species (O<sup>2-</sup>) on the surface [54, 55]. It can be noticed that the TiO<sub>2</sub>-25%CeO<sub>2</sub> catalyst (green line) shows the second component with the largest intensity shifted to higher B.E. (532.3 eV). On the basis of the literature, this is attributed to an increase in the number of chemisorbed oxygen on the surface of macroporous TiO<sub>2</sub> [56]. Moreover another component at 533.8 eV is visible in the TiO<sub>2</sub>-25%CeO<sub>2</sub> sample, assignable to organic oxygen or to surface defects [57, 58]. A shift to lower BE of about 0.4 eV in the oxygen bands was detected in the TiO<sub>2</sub>-3%CeO<sub>2</sub> catalyst compared to bare TiO<sub>2</sub> inverse opal, pointing out a strong interaction between CeO<sub>2</sub> and TiO<sub>2</sub> occurring in this sample.

Figs. 5.21C-D show the four bands of Ce 3d<sub>5/2</sub> corresponding to v, v', v'', and v''' components, respectively, and the features of Ce 3d<sub>3/2</sub> due to u, u', u'', and u''' components, for the TiO<sub>2</sub>-3%CeO<sub>2</sub> and TiO<sub>2</sub>-25%CeO<sub>2</sub>. v' and u' correspond to characteristic signals of Ce<sup>3+</sup> whereas the

signal ( $u'''$ ) at about 917 eV is the fingerprint of  $\text{Ce}^{4+}$  state [59, 60]. As reported in the literature for similar composites, it is possible that a mixture of  $\text{Ce}^{3+}/\text{Ce}^{4+}$  species exists on the surface of  $\text{TiO}_2$ - $\text{CeO}_2$  catalysts [61, 62]. The increase of the amount of cerium oxide leads to an increase in the intensity of the signals at 917 eV, 907 eV and 904 eV ( $u'''$ ,  $u''$  and  $u'$ ) whereas the signals at 899 eV and 901 eV decrease in intensity.



**Fig. 5.21** XPS spectra of I.O.  $\text{TiO}_2$ - $\text{CeO}_2$  samples: (A) Ti 2p region, (B) O 1s region, (C) Ce 3d region for the  $\text{TiO}_2$ -3% $\text{CeO}_2$  sample, (D) Ce 3d region for the  $\text{TiO}_2$ -25% $\text{CeO}_2$  sample.

**Table 5.2** Surface composition of I.O. TiO<sub>2</sub>-CeO<sub>2</sub> samples estimated by XPS.

| Catalysts                              | Ti (at %) | O (at%) | Ce (at%) | Ce <sup>3+</sup> /Ce <sup>4+</sup> ratio |
|--|-----------|---------|----------|--|
| TiO <sub>2</sub>                       | 22.5      | 55.7    | -        | -  |
| TiO <sub>2</sub> - 3%CeO <sub>2</sub>  | 22.9      | 57.1    | 0.6      | 0.46                                     |
| TiO <sub>2</sub> - 25%CeO <sub>2</sub> | 20.2      | 53.1    | 3.4      | 0.15                                     |

These changes in the Ce 3d XPS spectra point out a decrease of Ce<sup>3+</sup> concentration in the TiO<sub>2</sub>-25%CeO<sub>2</sub> catalyst, as evidenced by XPS data in [Table 5.2](#). The presence of Ce<sup>3+</sup> species is attributed to the occurrence of a strong electronic interaction between the TiO<sub>2</sub> support and the CeO<sub>2</sub> nanolayer that causes a charge transfer between the Ti<sup>3+</sup> and Ce<sup>4+</sup> metal cations, resulting in a change of their oxidation states on the surface. On TiO<sub>2</sub>-3%CeO<sub>2</sub> the Ce<sup>3+</sup> concentration was found to increase and consequently the interaction between TiO<sub>2</sub> and CeO<sub>2</sub> should be stronger, as also confirmed by the changes in BE values of Ti 2p and O 1s. On the contrary, with a higher amount of cerium oxide (TiO<sub>2</sub>-25%CeO<sub>2</sub>), the concentration of Ce<sup>3+</sup> species is lower probably due to the increased saturability of supported CeO<sub>2</sub> nanolayers and to the formation of islands or isolated clusters of cerium oxide related to the agglomeration of CeO<sub>2</sub> particles [[56](#), [59](#)], as detected by XRD and N<sub>2</sub> adsorption-desorption measurements.

[Fig. 5.22A](#) shows the two typical bands of Ti 2p region for I.O. TiO<sub>2</sub>, I.O. TiO<sub>2</sub>-3%BiVO<sub>4</sub> and I.O. TiO<sub>2</sub>-25%BiVO<sub>4</sub>. Only the sample with a lower amount of bismuth vanadate showed a slight shift to lower binding energy (458.5 eV and 464.5 eV, compared to bare I.O. TiO<sub>2</sub> which has these bands at 458.8 eV and 464.8 eV). In the O1s zone ([Fig. 5.22B](#)) the I.O. TiO<sub>2</sub>-25%BiVO<sub>4</sub> catalyst exhibited a shift at higher binding energy to about 0.4 eV compared to I.O. TiO<sub>2</sub>, moreover the signal is more intense. In the vanadium zone (V 2p spectrum [Fig. 5.22C](#)) a doublet with peak centred at 517 eV and 524.5 eV for I.O. TiO<sub>2</sub>-25%BiVO<sub>4</sub> and at 516 eV and 523.6 eV for I.O. TiO<sub>2</sub>-3%BiVO<sub>4</sub> were detected. These signals assigned to the V 2p<sub>1/2</sub> and V 2p<sub>3/2</sub> orbit, exhibited binding energy values characteristic of vanadium (V) as reported in the literature [[63](#), [64](#)].

The binding energies of Bi 4f ([Fig. 5.22D](#)) were 159.5 eV (Bi 4f<sub>7/2</sub>) and 164.5 eV (Bi 4f<sub>5/2</sub>), for I.O. TiO<sub>2</sub>-25%BiVO<sub>4</sub>, these are the fingerprint of bismuth in BiVO<sub>4</sub> [[64](#)]. It is possible to note from the [inset of Fig. 5.22D](#)) that for I.O. TiO<sub>2</sub>-3%BiVO<sub>4</sub> the intensity of the bismuth signals are very low. Considering also the low intensity of the vanadium zone detected for this sample the surface composition estimated by XPS ([Table 5.3](#)) and consistent with XRD data, probably the use of a little amount of salts precursors is not sufficient to can form the bismuth vanadate oxide at the interface of TiO<sub>2</sub>.

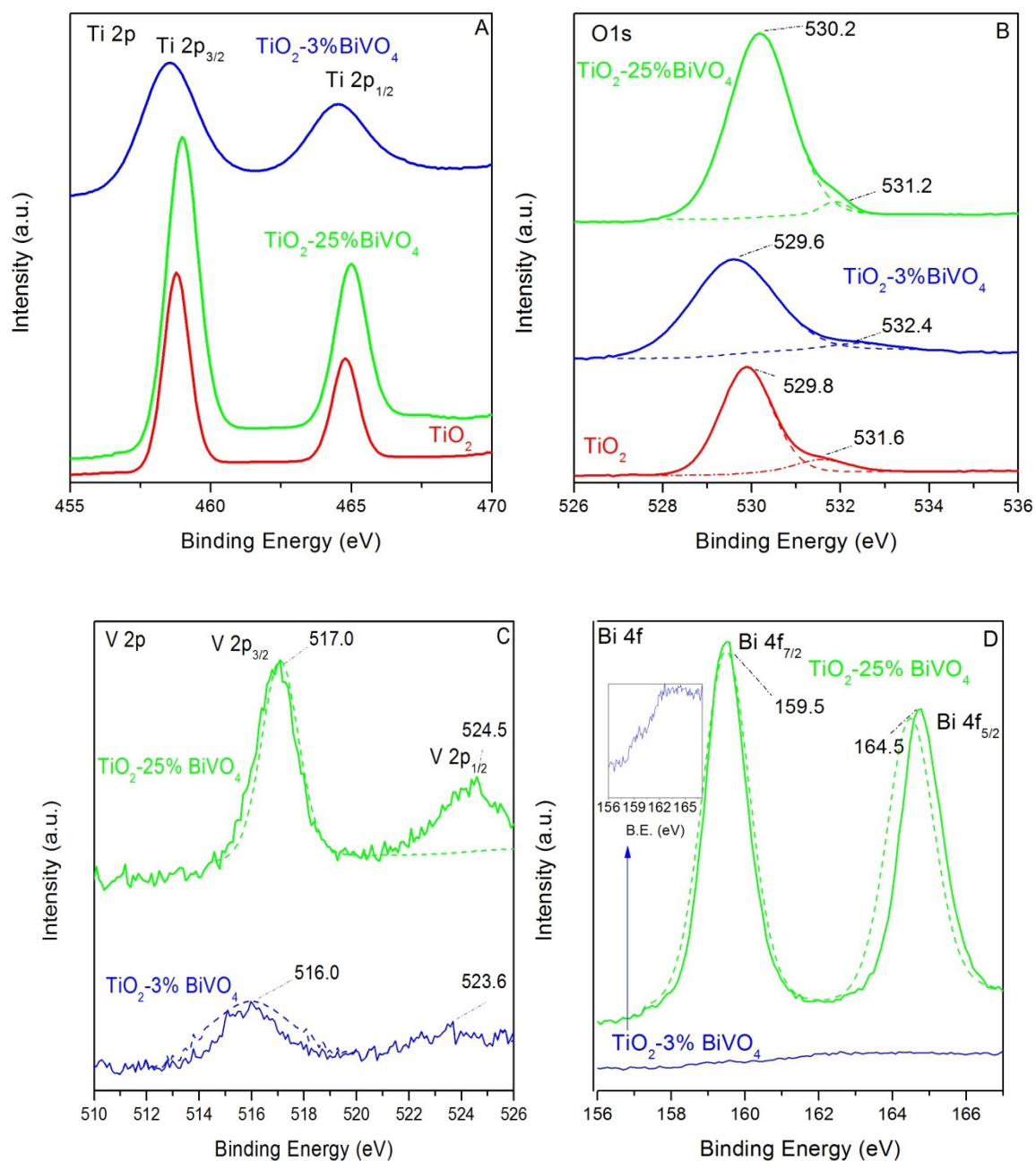


**Fig. 5.22** XPS spectra of I.O. TiO<sub>2</sub>-BiVO<sub>4</sub> samples: (A) Ti 2p region, (B) O 1s region, (C) V 2p region, (D) Bi 4f region.

**Table 5.3** Surface composition of I.O. TiO<sub>2</sub>-BiVO<sub>4</sub> samples estimated by XPS.

| Catalysts                               | Ti (at %) | O (at%) | Bi (at%) | V (at%) |
|---|-----------|---------|----------|---------|
| TiO <sub>2</sub>                        | 30.5      | 55.7    | -        | -       |
| TiO <sub>2</sub> - 3%BiVO <sub>4</sub>  | 32.8      | 58.8    | 0.01     | 0.04    |
| TiO <sub>2</sub> - 25%BiVO <sub>4</sub> | 28.6      | 51.5    | 1.7      | 0.9     |

**Fig.5.23A** reports the Ti 2p zone for the I.O. TiO<sub>2</sub>, I.O. TiO<sub>2</sub>-3%CuO and I.O. TiO<sub>2</sub>-25%CuO catalysts. In this case the sample with a small amount of copper oxide didn't exhibit considerable shifts compared to bare inverse opal TiO<sub>2</sub> whereas the I.O. TiO<sub>2</sub>-25%CuO showed a shift to 0.6

eV at higher binding energy. Also in the O1s zone (Fig. 5.23B) a shift to higher binding energy (1 eV) was present for I.O. TiO<sub>2</sub>-25%CuO compared to I.O. TiO<sub>2</sub>. Furthermore, in the composites with the higher amount of copper oxide, the third component of oxygen zone located at higher binding energy (534 eV) ascribed to surface oxygen species adsorbed in the surface, had a higher intensity compared to I.O. TiO<sub>2</sub>-3%CuO sample.

Fig. 5.23C shows the Cu 2p region of the X-ray photoelectron spectra for the I.O. TiO<sub>2</sub>-3%CuO and I.O. TiO<sub>2</sub>-25%CuO composites. The measured binding energies of Cu 2p<sub>3/2</sub> and Cu 2p<sub>1/2</sub> were equal to 933.2 eV and 953.0 eV and 933.9 and 953.0 eV for I.O. TiO<sub>2</sub>-3%CuO and I.O. TiO<sub>2</sub>-25%CuO respectively. These binding energies indicate that copper are mostly present in the surface of I.O. TiO<sub>2</sub> composites as Cu<sup>2+</sup> [65, 66]. A shake-up line among the binding energies of Cu 2p<sub>3/2</sub> and Cu 2p<sub>1/2</sub> further confirms this oxidation state, which is in a good agreement with the XRD data.

The I.O. TiO<sub>2</sub>-25%CuO sample exhibited a relative stronger Cu 2p peak than those of I.O. TiO<sub>2</sub>-3%CuO sample and considering the surface at % reported in Table 5.4, the amount of copper was about 10 times higher in the I.O. TiO<sub>2</sub>-25%CuO compared to I.O. TiO<sub>2</sub>-3%CuO. Furthermore, the I.O. TiO<sub>2</sub>-25%CuO sample shows a relative high binding energy value for Ti 2p and O1s XPS spectra. Such results should confirm the electrons transfer from TiO<sub>2</sub> to CuO as suggested also by the optical measurements and in accordance with the literature data [40, 67]. The electron transfer was favoured in the I.O. TiO<sub>2</sub>-25% CuO, being the surface concentration of CuO nanoparticles higher compared to I.O. TiO<sub>2</sub>-3%CuO. On the other hand, copper oxide can easily segregate on the surface of TiO<sub>2</sub> [68], and its higher amount can cover in part, the TiO<sub>2</sub> surface active sites, thus explain the progressively decrease of H<sub>2</sub> production both under UV than solar light irradiation measured in the photocatalytic test.

By comparing the atomic percentages of Bi<sup>3+</sup> and Cu<sup>2+</sup>, (Tables 5.3-5.4) it can be seen that BiVO<sub>4</sub> is dispersed within the TiO<sub>2</sub> matrix, whilst CuO is mostly present on the surface.

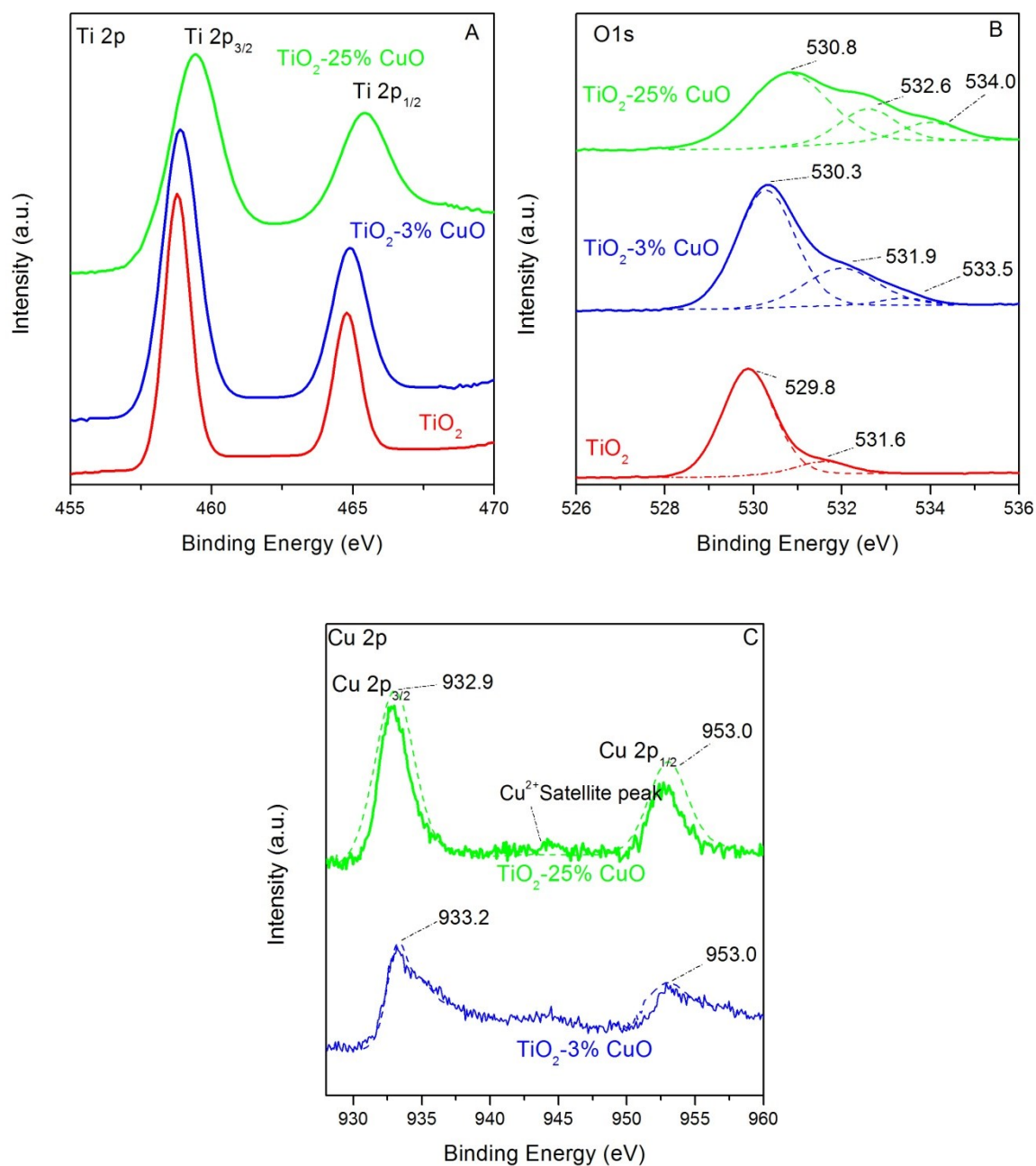


Fig. 5.23 XPS spectra of I.O. TiO<sub>2</sub>-CuO samples: (A) Ti 2p region, (B) O 1s region, (C) Cu 2p region.

Table 5.4 Surface composition of I.O. TiO<sub>2</sub>-BiVO<sub>4</sub> samples estimated by XPS.

| Catalysts                 | Ti (at %) | O (at%) | Cu (at%) |
|---------------------------|-----------|---------|----------|
| TiO <sub>2</sub>          | 30.5      | 55.7    | -        |
| TiO <sub>2</sub> - 3%CuO  | 25.3      | 59.1    | 1.2      |
| TiO <sub>2</sub> - 25%CuO | 27.6      | 52.2    | 9.9      |

Figs. 5.24A- 5.24B display the Ti 2p region and the O 1s of TiO<sub>2</sub> (red line), TiO<sub>2</sub>-0.5% N (blue line), TiO<sub>2</sub>-0.5% Hf (cyan line), TiO<sub>2</sub>-0.5% N (blue line), TiO<sub>2</sub>-0.5% Hf-1% N (orange line) and

TiO<sub>2</sub>-2%N (green line). No substantial variations are revealed compared to un-doped macroporous TiO<sub>2</sub>.

The N 1s zone for TiO<sub>2</sub>-0.5% N, TiO<sub>2</sub>-0.5%Hf-1% N and TiO<sub>2</sub>-2%N is shown in Fig. 5.24C. The binding energy peak of N 1s was at about 400.6 eV for all samples. On the basis of the energy value, the signal can be attributed to a nitrogen atom in the environment O-Ti-N [69, 70]. For the TiO<sub>2</sub>-0.5% N catalyst the intensity of this signal was very low according to the low amount of nitrogen. The band of hafnium (Fig.5.24D) splits in a doublet at 17.79 and 16.49 eV which is typical of Hf<sup>4+</sup> [71-73].

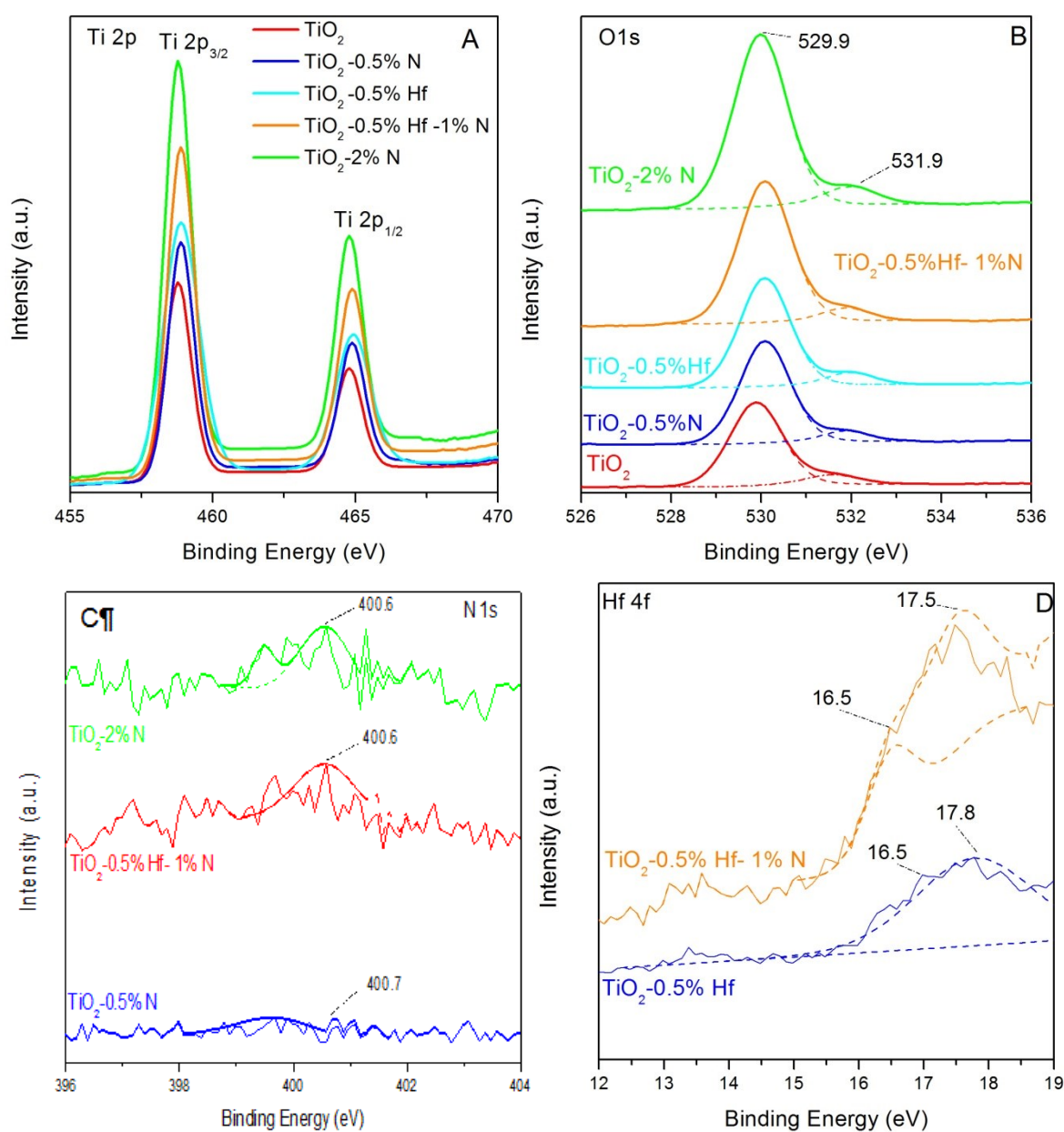


**Fig. 5.24** XPS spectra of I.O. TiO<sub>2</sub>-N-Hf samples: (A) Ti 2p region, (B) O 1s region, (C) N 1s region, (D) Hf 4f region.

**Table 5.5** Surface composition of I.O. TiO<sub>2</sub>-N-Hf samples estimated by XPS.

| Catalysts                     | Ti (at %) | O (at%) | N (at%) | Hf (at%) |
|-------------------------------|-----------|---------|---------|----------|
| TiO <sub>2</sub>              | 22.5      | 55.7    | -       | -        |
| TiO <sub>2</sub> - 0.5%N      | 23.4      | 57.8    | 0.2     | -        |
| TiO <sub>2</sub> - 2%N        | 22.7      | 56.5    | 0.7     | -        |
| TiO <sub>2</sub> - 0.5%Hf     | 29.7      | 51.5    | -       | 0.08     |
| TiO <sub>2</sub> - 0.5%Hf-1%N | 22.4      | 55.9    | 0.3     | 0.07     |

The surface atomic composition of samples, reported in [Table 5.5](#), showed that the higher temperature of synthesis lead to decrease in the amount of nitrogen with respect to the nominal one, due to the desorption of ammonia [[74](#), [75](#)]. The hafnium had the same surface concentration in both samples (TiO<sub>2</sub>-0.5%Hf and TiO<sub>2</sub>-0.5%Hf-1%N) lower of the nominal one (0.1 at.% detected by XPS data vs. 0.5 at.% nominal). This is probably due to a more homogeneous dispersion of hafnium at the surface and inside the pores of TiO<sub>2</sub>, the Hf<sup>4+</sup> ions being able, in fact, to easily replace the Ti<sup>4+</sup> ions with possible formation of Hf<sub>1-x</sub>Ti<sub>x</sub>O<sub>2</sub> composite; moreover the presence of hafnium oxide facilitates the formation of O-H species on the surface and the adsorption of atmospheric oxygen [[71](#), [76](#)].

The Ti 2p zone for the TiO<sub>2</sub>, TiO<sub>2</sub>-0.5%W and TiO<sub>2</sub>-2%W are depicted in [Fig. 5.25A](#). In the case of the sample with higher amount of tungsten it is possible to note a slight shift to lower binding energy (about 0.3 eV) compared to bare TiO<sub>2</sub> and TiO<sub>2</sub>-0.5% W samples. With concern to the O 1s zone ([Fig. 5.25B](#)), as also found for the other doped-TiO<sub>2</sub> systems, the asymmetric peak indicates that also free oxygen species are present. The signals of tungsten ([Fig. 5.25C](#)) at 37.8 eV and 37.5 eV for TiO<sub>2</sub>-2% W and TiO<sub>2</sub>-0.5% W samples are attributed to the formation of WO<sub>3</sub>, whereas the peaks at 35.2 eV and 35.5 eV (obtained by curve fitting of the spectra) are consistent with the W<sup>4+</sup> oxidation state; moreover the shoulder at about 35.4 eV, more evident for the TiO<sub>2</sub>-2%W, can be related to the formation of some non-stoichiometric tungsten oxides [[73](#), [77](#)]. Also in this case, as reported in the literature [[78-80](#)], the stoichiometric ion exchange between W<sup>4+</sup> and Ti<sup>4+</sup> might occur. W<sup>4+</sup> in fact, can substitute Ti<sup>4+</sup> in the lattice of TiO<sub>2</sub> because of the similarity in the ionic radius of W<sup>4+</sup> and Ti<sup>4+</sup>, in the W-O and Ti-O bond lengths and in the crystal structures of WO<sub>2</sub> and TiO<sub>2</sub>. Consequently, non-stoichiometric solid solution of W<sub>x</sub>Ti<sub>1-x</sub>O<sub>2</sub> would form, with a possible production of tungsten impurity energy levels [[78-80](#)]. Interestingly as shown in [Table 5.6](#), the surface of TiO<sub>2</sub>-0.5%W was richer in tungsten (2 at%) compared to the nominal concentration (0.5 at%), whereas for TiO<sub>2</sub>-2%W the nominal concentration is equal to that detected by XPS analysis. Probably a lower amount of tungsten leads to facilitate the ionic exchange between W<sup>4+</sup> and Ti<sup>4+</sup> favouring a surface enrichment of tungsten oxide.



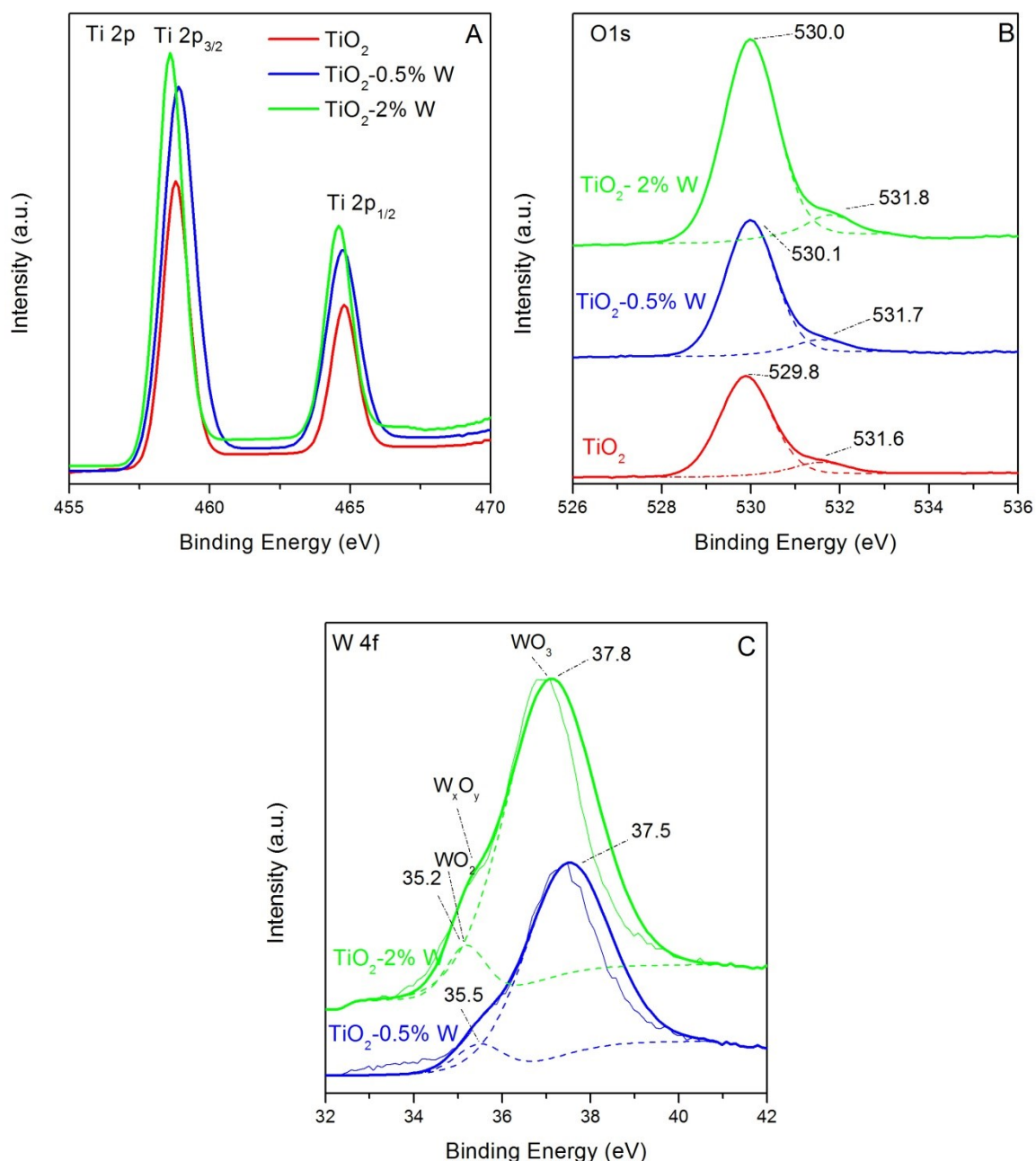


**Fig. 5.25** XPS spectra of I.O. TiO<sub>2</sub>-W samples: (A) Ti 2p region, (B) O 1s region, (C) W 4f region.

**Table 5.6** Surface composition of I.O. TiO<sub>2</sub>-W samples estimated by XPS.

| Catalysts                | Ti (at %) | O (at%) | W (at%) |
|--------------------------|-----------|---------|---------|
| TiO <sub>2</sub>         | 22.5      | 55.7    | -       |
| TiO <sub>2</sub> - 0.5%W | 21.8      | 53.4    | 2.2     |
| TiO <sub>2</sub> - 2%W   | 21.7      | 54.7    | 2.3     |

The degradation of rhodamine B (RhB) under visible light irradiation was carried out as a test reaction for analysing the photocatalytic activity of all the investigated samples. The absorption spectrum of the dye in the range of 500-600 nm at different irradiation times in the presence of

the un-doped porous TiO<sub>2</sub> sample is shown in Fig.5.26. It can be seen that the major absorption peaks of RhB, located at around 554 nm, diminished gradually under visible light irradiation.

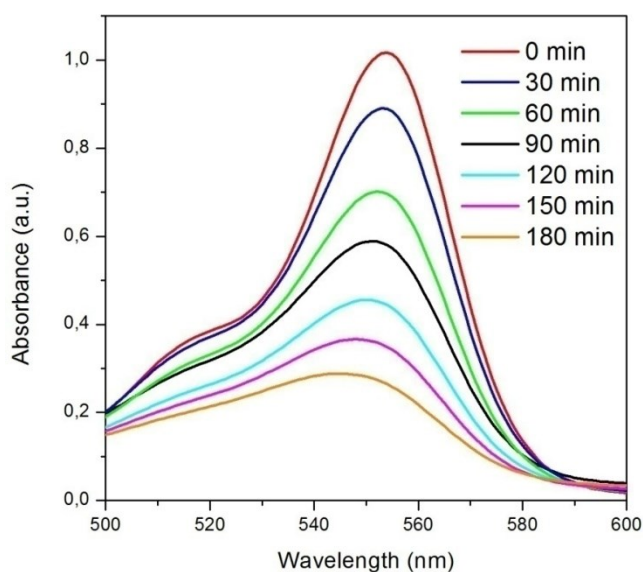


**Fig. 5.26** The temporal evolution of the absorption spectra of the RhB solution in the presence of the macroporous un-doped TiO<sub>2</sub> photocatalyst under visible-light illumination.

The photocatalytic efficiencies ( $C/C_0$ ) of all investigated TiO<sub>2</sub> systems are illustrated in Fig. 5.27. The blank experiment of RhB degradation in the absence of a photocatalyst is reported in all the photocatalyst series (black curve), pointing to a very low degradation rate of RhB, similarly to that reported in the literature [22, 81]. In particular it is possible to note that the un-doped macroporous inverse opal TiO<sub>2</sub> material (red curve, Fig. 5.27A) exhibits a good catalytic performance. Namely 60% of RhB was degraded after 120 minutes of irradiation, a much higher performance than that of the commercial TiO<sub>2</sub> anatase as also confirmed by the six times higher kinetic rate constant (see Table 5.7). This is a quite interesting result considering that the wide band-gap energy of TiO<sub>2</sub> should allow the absorption only in the UV range. Thus theoretically, no degradation of dye molecules by TiO<sub>2</sub> should be expected under visible irradiation.

The photocatalytic performance of inverse opal TiO<sub>2</sub> was further improved on some of the investigated doped systems (Figs. 5.27 B-E). In fact, in the case of for the I.O. TiO<sub>2</sub>-composites only a low amount of cerium oxide (1, 2 and 3 wt.%) had a positive effect, whereas a higher amount and the presence of other components (CuO and BiVO<sub>4</sub>) had a negative effect (Table 5.7).

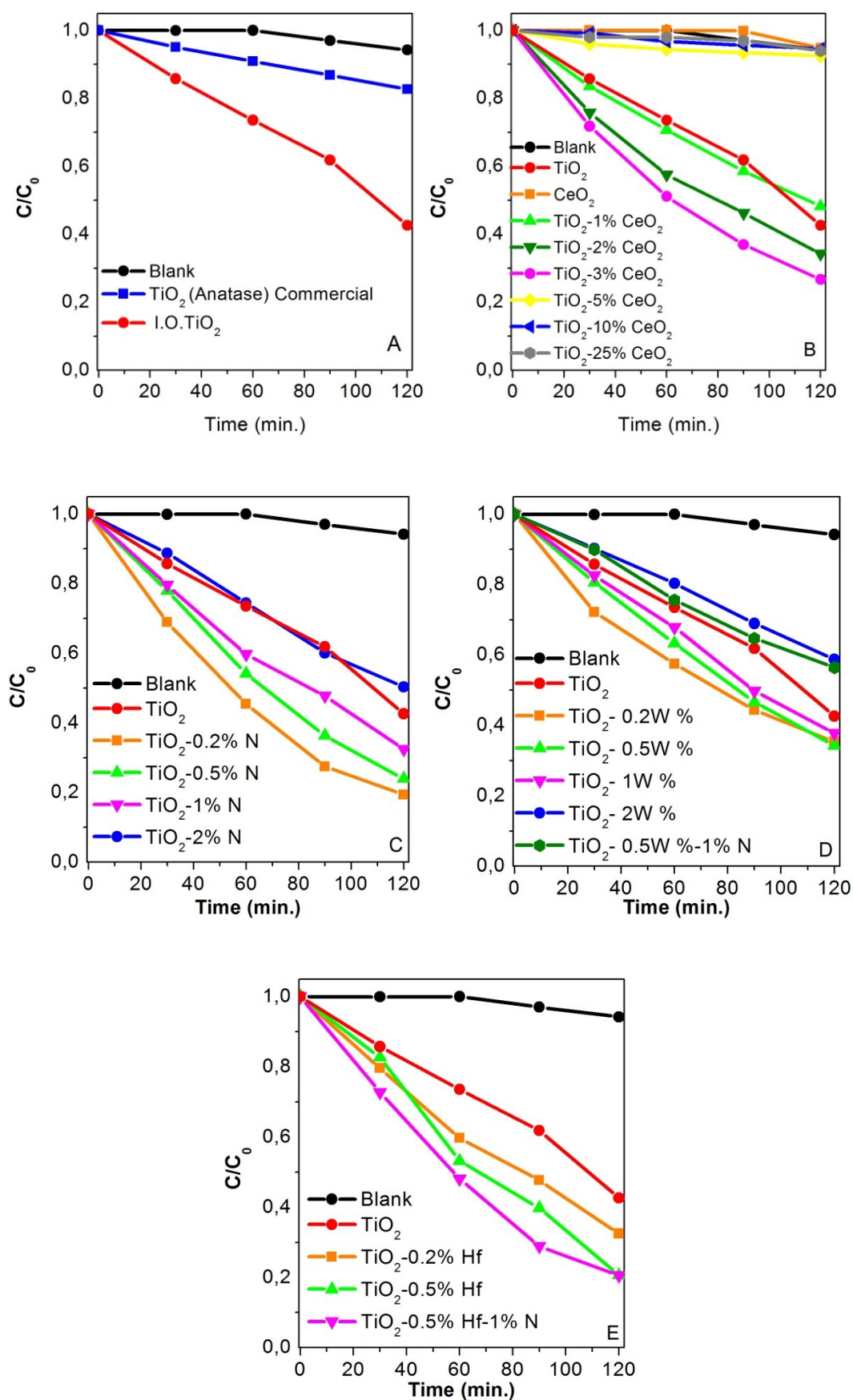


**Fig. 5.27** The variation of RhB concentrations ( $C/C_0$ ) with irradiation time over different photocatalysts series: (A) Different TiO<sub>2</sub>, (B) I.O. TiO<sub>2</sub>-CeO<sub>2</sub>, (C) I.O. TiO<sub>2</sub>-N, (D) I.O. TiO<sub>2</sub>-W, (E) I.O. TiO<sub>2</sub>-Hf.

On the contrary the doping with nitrogen or metal ions lead to improve the photocatalytic activity of macroporous TiO<sub>2</sub>, especially when the doping agent was present at low concentration (0.2, 0.5, 1 at.%). The co-presence of nitrogen and tungsten didn't enhance the TiO<sub>2</sub> performance whereas for the TiO<sub>2</sub>-N-Hf system an increase of photoactivity was detected when both nitrogen and hafnium were present (Figs. 5.27 C-E). It has been reported that the photocatalytic degradation process of RhB follows first-order kinetics [82]. To better compare the effect of TiO<sub>2</sub> dopants the calculated kinetic rate constants for all the investigated systems are reported in Table 5.7.

**Tab. 5.7** Kinetic constants for RhB degradation over investigated I.O. TiO<sub>2</sub>-based samples.

| Catalysts                                | k (min <sup>-1</sup> ) |
|--|------------------------|
| <b>I.O. TiO<sub>2</sub></b>              | <b>0.006</b>           |
| <b>Comm. TiO<sub>2</sub> Anatase</b>     | <b>0.001</b>           |
| TiO <sub>2</sub> -1%CeO <sub>2</sub>     | 0.006                  |
| TiO <sub>2</sub> -2%CeO <sub>2</sub>     | 0.009                  |
| <b>TiO<sub>2</sub>-3%CeO<sub>2</sub></b> | <b>0.011</b>           |
| TiO <sub>2</sub> -5%CeO <sub>2</sub>     | 0.0008                 |
| TiO <sub>2</sub> -10%CeO <sub>2</sub>    | 0.0002                 |
| TiO <sub>2</sub> -25%CeO <sub>2</sub>    | 0.0002                 |
| CeO <sub>2</sub>                         | 0.0001                 |
|  |                        |
| TiO <sub>2</sub> -1%BiVO <sub>4</sub>    | 0.00203                |
| TiO <sub>2</sub> -3%BiVO <sub>4</sub>    | 0.00062                |
| TiO <sub>2</sub> -5%BiVO <sub>4</sub>    | 0.00082                |
| TiO <sub>2</sub> -10%BiVO <sub>4</sub>   | 0.00059                |
| TiO <sub>2</sub> -25%BiVO <sub>4</sub>   | 0.00058                |
| BiVO <sub>4</sub>                        | 0.00167                |
|  |                        |
| TiO <sub>2</sub> -1%CuO                  | 0.00144                |
| TiO <sub>2</sub> -3%CuO                  | 0.00068                |
| TiO <sub>2</sub> -5%CuO                  | 0.00087                |
| TiO <sub>2</sub> -10%CuO                 | 0.00067                |
| TiO <sub>2</sub> -25%CuO                 | 0.00059                |
|  |                        |
| <b>TiO<sub>2</sub>-0.2%N</b>             | <b>0.014</b>           |
| TiO <sub>2</sub> -0.5%N                  | 0.011                  |
| TiO <sub>2</sub> -1%N                    | 0.009                  |
| TiO <sub>2</sub> -2%N                    | 0.006                  |
|  |                        |
| TiO <sub>2</sub> -0.2%W                  | 0.008                  |
| TiO <sub>2</sub> -0.5%W                  | 0.009                  |
| TiO <sub>2</sub> -1%W                    | 0.007                  |
| TiO <sub>2</sub> -2%W                    | 0.004                  |
| TiO <sub>2</sub> -0.5%W-1%N              | 0.005                  |
|  |                        |
| TiO <sub>2</sub> -0.2%Hf                 | 0.007                  |
| TiO <sub>2</sub> -0.5%Hf                 | 0.012                  |
| <b>TiO<sub>2</sub>-0.5%Hf-1%N</b>        | <b>0.013</b>           |

It is possible to infer that the best photocatalysts are TiO<sub>2</sub>-3%CeO<sub>2</sub> and TiO<sub>2</sub>-2%CeO<sub>2</sub> for the TiO<sub>2</sub>-CeO<sub>2</sub> system, whereas for the TiO<sub>2</sub>-N-metal samples, TiO<sub>2</sub>-0.2%N, TiO<sub>2</sub>-0.5%W and TiO<sub>2</sub>-0.5%Hf-1%N exhibit the best performance.

The photoactivity was tested also using the LED reactor (see par. 5.4). Despite the use of a light source with a closer range of emission (430-470 nm) but lower power, 16 W instead of 108 W of Neon reactor, the macroporous TiO<sub>2</sub> photocatalyst maintains good performance; with a kinetic rate constant of 0.005 min<sup>-1</sup> instead of 0.006 min<sup>-1</sup> calculated with Neon reactor. On the contrary all TiO<sub>2</sub>-doped systems showed worse or similar performance compared to single TiO<sub>2</sub>. Probably the use of a closer excitation emission it is sufficient to generate the slow photon effect, but is not enough to activate the effects of the doping agent that become as inert or poisoning agent covering the surface active sites of TiO<sub>2</sub>.

The above reported results showed that the macro-mesoporous inverse opal TiO<sub>2</sub> exhibited a much higher photodegradation activity towards RhB under visible light than the commercial TiO<sub>2</sub>. Moreover the use of chemical agents has been found to affect in different ways the chemico-physical properties and the photocatalytic performance of macro-mesoporous TiO<sub>2</sub>. In order to rationalize these results it must be reminded that the photocatalytic degradation of dyes has been reported to occur [83-86] according to a mechanism which involves, firstly the activation of the TiO<sub>2</sub> particles by photons with wavelengths shorter than 385 nm; successively the electrons at the particles surface are scavenged by the ubiquitously present molecular oxygen to yield the superoxide radical anion, O<sub>2</sub><sup>•-</sup>, which is then protonated to give the HOO<sup>•</sup> radical (Fig. 5.28)

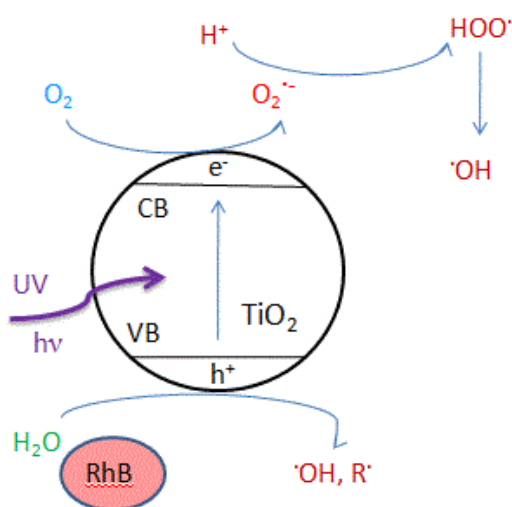
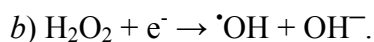
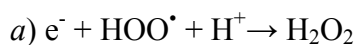


Fig. 5.28 Typical photocatalytic mechanism under UV irradiation.

The valence band holes become trapped as surface-bound  $\cdot\text{OH}$  radicals by oxidation of either the surface  $\text{OH}^-$  groups and/or the surface  $\text{H}_2\text{O}$  molecules. The  $\cdot\text{OH}$  radical can also derive from the trapped electron reacting with the  $\text{HOO}\cdot$  radical by the sequence of reactions *a* and *b*, namely:



According to this mechanism, photo-oxidation of the organic substrate RH (i.e., the RhB dye or the corresponding  $\text{R}\cdot$  radical) can take place through the reaction *c*:



The participation of active oxygen species  $\text{O}_2^{\cdot-}$ ,  $\text{HOO}\cdot$ , or  $\cdot\text{OH}$  radicals in the degradation of various organic substrates has been well acknowledged [83-86].

It is remarkable that  $\text{TiO}_2$  particles cannot be photo activated by visible light. In this case dyes or analogous organic substrates under suitable energetic condition of the conduction band of  $\text{TiO}_2$  and of the excited state of the dye, can act by injecting electrons from the adsorbed dye species to the  $\text{TiO}_2$  conduction band (Fig. 5.29).

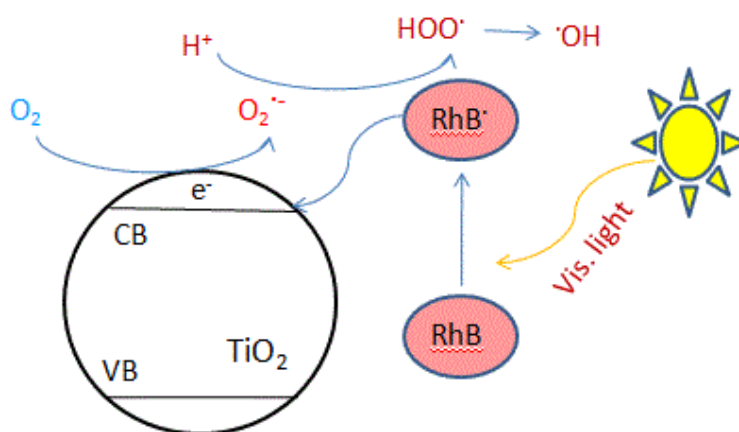


Fig. 5.29 Photosensitization mechanism under visible light irradiation.

The injected electron reacts with the surface-adsorbed  $\text{O}_2$  molecules to yield the  $\text{O}_2^{\cdot-}$  radical anion and then the  $\text{HOO}\cdot$  radical by protonation, in competition with the back electron transfer to the dye $^{+\cdot}$  radical cation. However, the latter option is usually two to three orders of magnitude slower. Subsequently the formation of  $\cdot\text{OH}$  radicals and the degradation mechanism follow the same path described before (reaction *c*). It must be underlined that the presence of  $\text{TiO}_2$  particles has a key role in the above mechanism, acting as electron carriers to electron acceptors adsorbed on the particles [83-86].

In this context the very good performance in the degradation of RhB under visible light exhibited by the inverse opal  $\text{TiO}_2$ , according to the literature [22, 23, 87], can be ascribed to the

photosensitization mechanism (i.e. electronic transfer from the LUMO of RhB to the conduction band of TiO<sub>2</sub>), which also explains the moderate activity of commercial TiO<sub>2</sub> anatase, boosted by the slow photon effect generated by the inverse opal structure. In fact, the peculiar mesoporosity of this structure leads to an enhanced accessibility which increases the mass transfer and allows light waves to easily enter the photocatalyst, increasing the path length of light and enhancing the light absorption of the material, thus resulting in an improved photo-reaction efficiency.

Regarding the effect of the chemical agents, the photocatalytic results pointed out that CeO<sub>2</sub> led to a significant improvement of the performance of inverse opal TiO<sub>2</sub>, only when cerium oxide is present in a low amount (1-3 wt%). The decrease of activity observed with a higher amount of cerium oxide (5-25 wt. %) can be ascribed to the progressive agglomeration of CeO<sub>2</sub> particles, clearly evidenced by XRD and N<sub>2</sub> adsorption-desorption measurements, covering TiO<sub>2</sub> nanoparticles thus hindering the access of the light to TiO<sub>2</sub> active sites. This behaviour agrees with that reported in the literature also for gas-phase reactions [88-90]. Moreover, as detected by XPS, small amounts of cerium oxide favour the presence of Ce<sup>3+</sup> ions, which could have a positive effect for the photoactivity because the occurrence of a mutual influence between the Ti and Ce metal cations is promoted, allowing a more easily change of their oxidation states on the surface. In particular, the redox process of CeO<sub>2</sub> can be favoured and this is beneficial for oxidation reactions [91]. Furthermore the formation of Ce<sup>3+</sup> impurities on the CeO<sub>2</sub> particles could allow the injection of electrons from TiO<sub>2</sub> to the Ce 4f level. This would also contribute to the enhancement of photo-produced hole lifetimes [89], as also confirmed by the photoluminescence data. All these consideration could explain the highest kinetic rate constants of TiO<sub>2</sub>-3%CeO<sub>2</sub> and TiO<sub>2</sub>-2%CeO<sub>2</sub> compared to other I.O. TiO<sub>2</sub>-CeO<sub>2</sub> samples.

The presence of nitrogen, tungsten and hafnium has been found also to promote the photocatalytic activity of the macro-mesoporous inverse opal TiO<sub>2</sub> sample, mainly at the lowest amount of the doping agent (0.2, 0.5 at.%). The positive effect of nitrogen as doping agent of TiO<sub>2</sub> has already been reported in the literature [69, 92-97]. Some authors correlated the positive effect of nitrogen to the location of the doped N species at the interstitial sites of TiO<sub>2</sub>, which leads to narrow the band-gap of TiO<sub>2</sub>, thus extending the range of light absorption towards the visible region and greatly enhancing the adsorption capacity of the dye [69, 93]. Other authors attributed the beneficial effect of N doping for photocatalysis to its influence on the TiO<sub>2</sub> surface defects and/or the loosing of stoichiometry in TiO<sub>2</sub> [94-96]. Cheng *et al.* studied the degradation of RhB under visible light irradiation over TiO<sub>2</sub>-N catalysts prepared by sol-gel. The enhanced photocatalytic activity of the TiO<sub>2</sub>-N doped system was attributed to several effects, namely (i) the formation of smaller size TiO<sub>2</sub> particles, (ii) the presence of a higher amount of hydroxyl

groups on the catalytic surface, (iii) the more efficient light absorption in the visible region and (iv) the higher separation efficiency of the photo-induced charge carriers [97]. Dong *et al.* examined the degradation of methyloange (MO) under UV-Visible light over three-dimensionally ordered macroporous titanium dioxide doped with nitrogen (N-3DOM TiO<sub>2</sub>). They found a better photocatalytic performance of the TiO<sub>2</sub>-N doped system which was attributed to the incorporation of N-atoms into the lattice of TiO<sub>2</sub>, which can induce a band-gap narrowing and cause the red-shift absorption threshold of TiO<sub>2</sub>, in addition to the slow photons effect generated by the 3DOM structure [92].

In our case all N-doped samples showed a higher or similar kinetic rate constant in the degradation of RhB under visible light compared to the bare porous inverse opal TiO<sub>2</sub> (Table 5). The TiO<sub>2</sub>-0.2%N exhibited the best performance among all tested photocatalysts. Considering that, the characterization measurements did not point out any substantial variation of the band-gap energy and other chemico-physical properties of inverse opal TiO<sub>2</sub> due to the presence of nitrogen, according to the literature the enhanced photoactivity can be explained by the incorporation of N-atoms into the lattice of TiO<sub>2</sub>, as indirectly confirmed by XRD. This can be beneficial for the photocatalytic performance because N atoms act as impurity sensitizers, also influencing the TiO<sub>2</sub> surface defects concentration [94-96, 98]. Similar results were found by Sato *et al.* using the wet-method for doping TiO<sub>2</sub> samples with nitrogen [74]. A higher amount of nitrogen as impurities dopants, on the contrary, lead to a decrease of the positive effect towards the photodegradation of dye, in so as the higher concentration of surface defects could also act as photoelectrons traps [99].

Also the presence of tungsten or hafnium at low concentration (0.2, 0.5 and 1 at.%) enhanced the photoactivity of inverse opal TiO<sub>2</sub>. Some authors correlate the positive effect of tungsten to the effects of shift of the light absorption band from near UV to the visible range, due to the presence of tungsten oxides that hinder the recombination rate of excited electrons/holes and to the stoichiometric ion exchange between tungsten and titanium ions [77, 100, 101]. In our case, XPS analysis revealed the presence of different W species (mostly W<sup>6+</sup> and W<sup>4+</sup>). The presence of W<sup>4+</sup> ions could favour the ion exchange with Ti<sup>4+</sup> and the tungsten ions can substitute the titanium ions in the lattice of TiO<sub>2</sub>. Moreover a non-stoichiometric solid solution of W<sub>x</sub>Ti<sub>1-x</sub>O<sub>2</sub> would form on the TiO<sub>2</sub> surface, leading to have tungsten impurity energy level [78-80]. These effects were more pronounced when the concentration of tungsten was low, as shown by XPS data, with a surface enrichment of tungsten oxide species on the surface of TiO<sub>2</sub>. A similar behaviour was also confirmed by XPS in the presence of hafnium, which appears to favour the formation of non-stoichiometric Hf<sub>1-x</sub>Ti<sub>x</sub>O<sub>2</sub> composite on the titanium dioxide surface with



Hf<sup>4+</sup> ions replacing the Ti<sup>4+</sup> ions [71, 76]. Also in this case, this was beneficial for the photocatalytic performance of the TiO<sub>2</sub> based system towards the photodegradation of RhB.

The combination of nitrogen and tungsten as doping agents of macro-mesoporous inverse opal TiO<sub>2</sub> structure did not significantly improve the performance compared to the doping with single atoms (Table 5.7). On the other hand the co-doping with nitrogen and hafnium (TiO<sub>2</sub>-0.5%Hf-1%N sample) enhanced about twice the kinetic rate constant of degradation of RhB compared to the un-doped TiO<sub>2</sub> inverse-opal. *Xu et al.* studied the degradation of methylene blue under visible irradiation on titania inverse opal films co-doped with N and F. They correlated the higher activity of co-doped samples over the slow photon effect to the existence of defects in the titania structure and/or Ti<sup>3+</sup> species [75]. In our case, the combination of the impurity effect due to nitrogen and the presence of hafnium oxide that facilitates the formation of hydroxyl groups on the TiO<sub>2</sub> surface and then the adsorption of atmospheric oxygen [71, 76], could explain the higher activity of the N-Hf co-doped sample. This synergistic effect had a minor effect when tungsten was present instead of hafnium.

Regarding the detrimental effect due to the presence of BiVO<sub>4</sub> and CuO, it is important to highlight that as reported in literature the role of BiVO<sub>4</sub> in the TiO<sub>2</sub> composites was of light sensitizer [22, 102, 103], larger is the amount of bismuth vanadate, greater is the sensitizing effect and better is the charge separation effect [22]. In this case, contrarily to the other systems, also the highest amount of BiVO<sub>4</sub> used (25 wt.%) was not sufficient to activate the sensitizing effect of BiVO<sub>4</sub>. As in fact observed by XPS measurements a low concentration probably didn't allow to formation of BiVO<sub>4</sub> at the TiO<sub>2</sub> surface interface.

The characterisations data pointed to that copper oxide was mostly embedded in the skeleton of TiO<sub>2</sub>. The negative performance of these samples was probably related to the copper oxide present on the surface of TiO<sub>2</sub> that blocked the photocatalytic process by capturing the photo-generated holes.

In summary it is possible to state that a positive effect of chemical agents towards the photocatalytic degradation of RhB under visible light was verified when:

- a) The amount of the chemical agent was low;
- b) The ionic exchange of Ti<sup>4+</sup> ions by host ions was favoured and the substitution of these ions in the crystal lattice of TiO<sub>2</sub> could occur;
- c) The formation of non-stoichiometric Ti-composites on the catalytic surface was favoured.

The photocatalytic performances of the I.O. TiO<sub>2</sub>-based samples were evaluated also for the photo-oxidation of VOC and for the photoreduction of proton from water. In particular the I.O.

TiO<sub>2</sub>-doped samples (I.O.TiO<sub>2</sub>-N, I.O.TiO<sub>2</sub>-W, I.O. TiO<sub>2</sub>-Hf) were tested for the photo-oxidation of ethanol, whereas the I.O. TiO<sub>2</sub>-composites samples (I.O.TiO<sub>2</sub>-CeO<sub>2</sub>, I.O.TiO<sub>2</sub>-CuO, I.O. TiO<sub>2</sub>-BiVO<sub>4</sub>) were tested for the photocatalytic water splitting.

Recently, the use of ethanol as biofuels component has been growing due to its environmental sustainability. However, the combustion in the cars engine leads to a significant increase in formaldehyde and acetaldehyde emissions which are considered carcinogenic and contribute to the formation of tropospheric ozone. Moreover being ethanol a common solvent the removal of its vapours from air is also important for many industries as bakeries, breweries, metal coating, etc.

**Fig.5.30** displays the photocatalytic results in terms of conversion of ethanol, selectivity to acetaldehyde and selectivity to CO<sub>2</sub> under UV irradiation. In accordance with data reported in the literature [104] acetaldehyde is the main gaseous intermediate, and the concentration of other products (formaldehyde, CO, formic acid and acetic acid) in the gas phase was much lower (selectivity < 2%). Also in this case the inverse opal TiO<sub>2</sub> sample exhibited better performance compared to commercial TiO<sub>2</sub> anatase. In particular a higher ethanol conversion (35% of I.O. TiO<sub>2</sub> compared to the 17% of commercial TiO<sub>2</sub>) and a higher selectivity to CO<sub>2</sub> (33% of I.O. TiO<sub>2</sub> compared to the 14% of commercial TiO<sub>2</sub>) were detected. In this reaction an increase of selectivity to CO<sub>2</sub> is a positive feature considering the hazard nature of acetaldehyde. A further increase of ethanol conversion and CO<sub>2</sub> selectivity was verified increasing the amount of nitrogen as doping agent (**Fig.5.30A**) reaching the 54% and the 53% respectively on I.O. TiO<sub>2</sub>-2%N. These results confirm the positive effects due to the presence of nitrogen in the macroporous skeleton of inverse opal TiO<sub>2</sub>. The addition of tungsten (**Fig.5.30B**) leads to have only an increase of acetaldehyde selectivity compared to the bare inverse opal TiO<sub>2</sub>, whereas no substantial change was measured due to the presence of hafnium (**Fig.5.30C**).

**Fig.5.31** shows the H<sub>2</sub> evolution under UV irradiation in the presence of the investigated TiO<sub>2</sub> composites systems. The bare I.O. TiO<sub>2</sub> (red line) showed a higher H<sub>2</sub> production compared to commercial TiO<sub>2</sub> anatase (black curve) (**Fig. 5.31A**). The presence of BiVO<sub>4</sub> (**Fig. 5.31A**) and CeO<sub>2</sub> (**Fig. 5.31C**) led to a moderate increase of H<sub>2</sub> production, which was more relevant for the samples with the highest amount (I.O. TiO<sub>2</sub>-10% BiVO<sub>4</sub> and I.O. TiO<sub>2</sub>-25% BiVO<sub>4</sub>). On the contrary the addition of CuO (**Fig. 5.31B**) had a negative effect on the performance, even at a low copper amount.

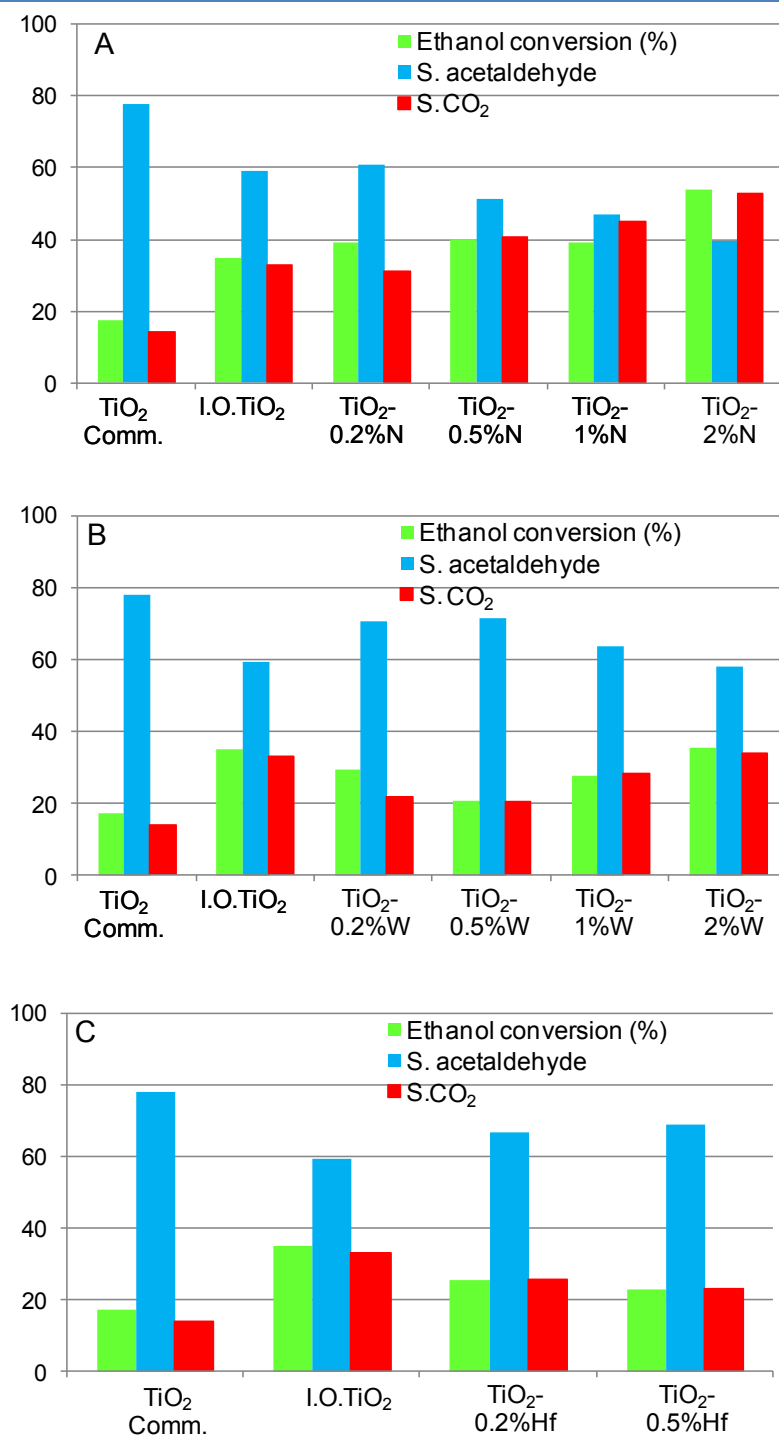


**Fig. 5.30** Results of ethanol photocatalytic oxidation in terms of conversion, selectivity to acetaldehyde and selectivity to CO<sub>2</sub>, under UV irradiation.

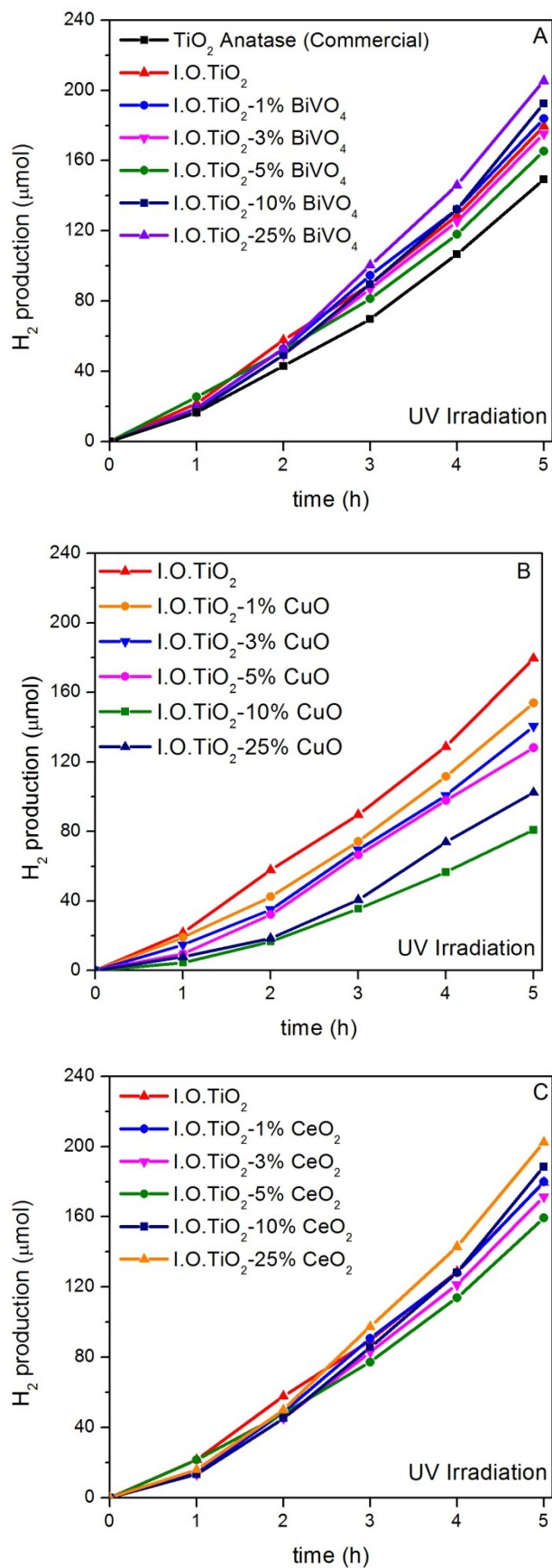


**Fig. 5.31** Photocatalytic  $\text{H}_2$  production at  $30^\circ\text{C}$ : (A) Inverse Opal  $\text{TiO}_2$ - $\text{BiVO}_4$ ; (B) Inverse Opal  $\text{TiO}_2$ - $\text{CuO}$  and (C) Inverse Opal  $\text{TiO}_2$ - $\text{CeO}_2$  composites under UV irradiation.

Under solar light irradiation (Fig. 5.32) the I.O. TiO<sub>2</sub> exhibited a much higher activity (about 5 times) compared to commercial TiO<sub>2</sub>. Also in this case concentrations of BiVO<sub>4</sub> higher than 10 wt.% resulted in a further increase of the hydrogen production, with the I.O. TiO<sub>2</sub>-25% BiVO<sub>4</sub> sample exhibiting the best performance (Fig. 5.32A violet line). Similarly the addition of CeO<sub>2</sub> (Fig. 5.32B) led to increase the activity of I.O. TiO<sub>2</sub> with an increased amount of cerium oxide, however the hydrogen production of I.O. TiO<sub>2</sub>-25% CeO<sub>2</sub> is lower compared to I.O. TiO<sub>2</sub>-25% BiVO<sub>4</sub>. On the contrary for the I.O.TiO<sub>2</sub>-CuO composites (Fig. 5.32C) only the samples with small amounts of CuO (1-3 wt. %) had a better activity with respect to I.O. TiO<sub>2</sub>.

The above reported results confirm that, the presence of a macroporous structure such as that of I.O.TiO<sub>2</sub> largely improves the absorption of photons, increasing the path length and the migration rate of electron-hole pairs towards the surface. Consequently the reduction of H<sup>+</sup> ions on the surface of TiO<sub>2</sub> by the photogenerated electrons is favored [105, 106]. This well agrees with the observed higher photoactivity of I.O. TiO<sub>2</sub> compared to commercial TiO<sub>2</sub>. This photoactivity is further increased in the presence of BiVO<sub>4</sub> and in less extent CeO<sub>2</sub>. The sample with the highest BiVO<sub>4</sub> content, I.O. TiO<sub>2</sub>-25%BiVO<sub>4</sub>, exhibited the best performance both under UV than solar irradiation. Due to the small band-gap of BiVO<sub>4</sub>, the produced high-energy electrons in the bare BiVO<sub>4</sub> relax easily from the conduction (CB) to the valence band (VB) in a remarkably short period, with obvious energy loss, leading to an inefficient charge separation. The coupling of BiVO<sub>4</sub> with TiO<sub>2</sub> leads to an increase of photocatalytic performances. As reported in the literature, in fact, BiVO<sub>4</sub> can be considered as a light sensitizer for TiO<sub>2</sub>. In particular, a generally accepted mechanism considers that under a suitable light irradiation ( $\epsilon_{\text{excitation}} \leq 510\text{-}530$  nm) the electrons of the valence band of BiVO<sub>4</sub> are firstly excited to the conduction band of BiVO<sub>4</sub>, leaving holes behind, and after that these photogenerated electrons are transferred to the CB of TiO<sub>2</sub> [103, 107]. The formation of an efficient heterojunction between TiO<sub>2</sub> and BiVO<sub>4</sub> is a key factor to explain the enhanced photoactivity. On the basis of XRD, XPS and DRS measurements we found that the heterojunction was favoured only for high amount of BiVO<sub>4</sub> (>10 wt%). This is in good agreement with the results of Zalfani *et al.* [23], who investigated the photodegradation of Rhodamine B under visible light irradiation over BiVO<sub>4</sub>-TiO<sub>2</sub> catalysts.

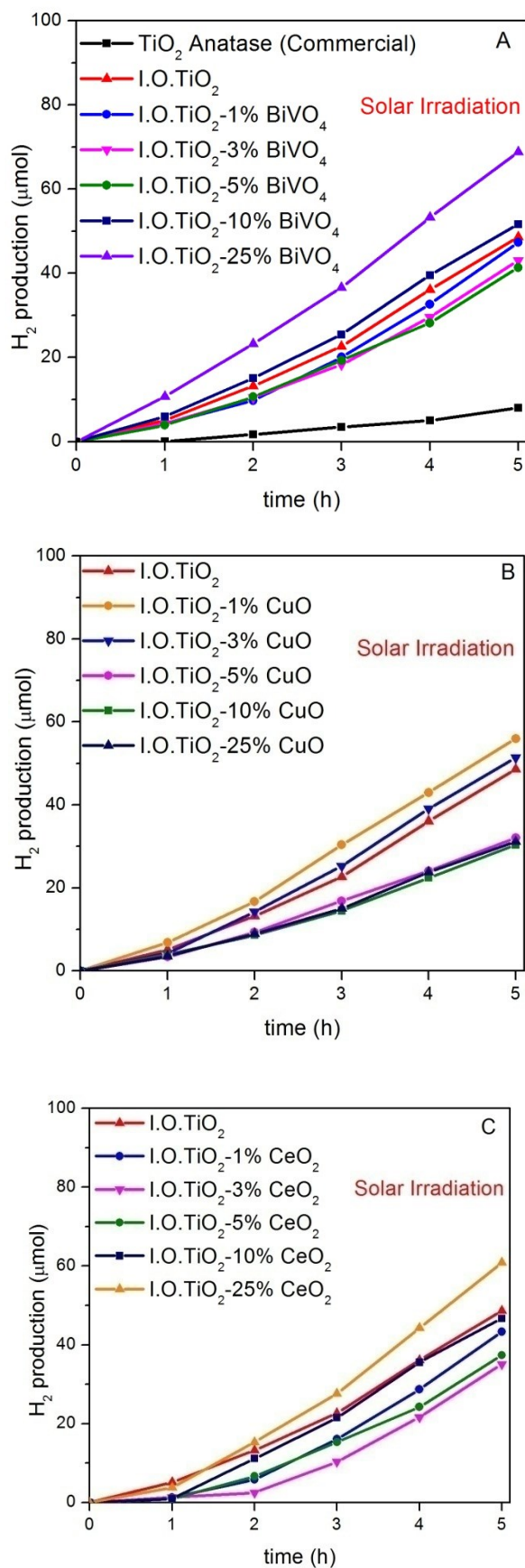


**Fig. 5.32** Photocatalytic  $\text{H}_2$  production at  $30^\circ\text{C}$ : (A) Inverse Opal  $\text{TiO}_2$ - $\text{BiVO}_4$ ; (B) Inverse Opal  $\text{TiO}_2$ - $\text{CuO}$  and (C) Inverse Opal  $\text{TiO}_2$ - $\text{CeO}_2$  composites under solar light irradiation.

Fig. 5.33 depicts the band positions versus the Normal Hydrogen Electrode (NHE) of the different semiconductors according to the literature data [41, 108, 109]. In the TiO<sub>2</sub>-BiVO<sub>4</sub> systems (Fig. 5.33A), electrons can be transferred from BiVO<sub>4</sub> to TiO<sub>2</sub> because the conduction band of BiVO<sub>4</sub> is more negative than that of TiO<sub>2</sub>, whilst holes, due to the more positive valence band of TiO<sub>2</sub>, can move in the opposite direction allowing a very efficient charge separation and an improvement of the photocatalytic activity. A similar mechanism was proposed with the presence of cerium oxide (Fig. 5.33B), moreover as reported in literature [110] the presence of the redox couple Ce<sup>3+</sup>/Ce<sup>4+</sup> led to have a scavenging effect in the TiO<sub>2</sub> conduction band increasing the charge carriers separation, the minor amount of hydrogen detected for the I.O. TiO<sub>2</sub>-CeO<sub>2</sub> system compared to the I.O. TiO<sub>2</sub>-BiVO<sub>4</sub> samples could be related to the major efficiency of BiVO<sub>4</sub> as photosensitizer.

On the contrary, in the TiO<sub>2</sub>-CuO samples (Fig. 5.33C), both holes and electrons will transfer and accumulate on CuO, giving rise also to some extent of recombination, because the conduction band of CuO is more positive than that of TiO<sub>2</sub>, making consequently the junction not very efficient under UV irradiation. Consequently the bare I.O. TiO<sub>2</sub> sample showed to be more active than the TiO<sub>2</sub>-CuO samples. However, from an electrochemical point of view, CuO could favour H<sub>2</sub> formation only if its conduction band edge was more negative than the H<sup>+</sup>/H<sub>2</sub> potential. In accord to Yu *et al.* [41], when the CuO amount is not very high (1 and 3%, in this paper), particle size is small and, due to quantum size effect, the valence and conduction band edges shift toward more positive and more negative values, respectively. In particular the conduction band edge can become more negative than the H<sup>+</sup>/H<sub>2</sub> potential, allowing H<sub>2</sub> evolution. This finding could explain the highest activity of the I.O. TiO<sub>2</sub>-1%CuO and I.O. TiO<sub>2</sub>-3%CuO samples with respect to the other doped samples. In addition, some authors [26, 108, 109] explain the CuO efficiency toward H<sub>2</sub> production by considering that electron excess on CuO under irradiation causes a negative shift of the Fermi level of the oxide, enabling H<sup>+</sup> reduction.

It is worth noting that according to literature [111-113], H<sub>2</sub> formation can derive both from H<sub>2</sub>O splitting and ethanol reforming, while the presence of CO<sub>2</sub> detected during the photocatalytic tests can be related to the mineralization of the organic compound acting as a sacrificial agent.

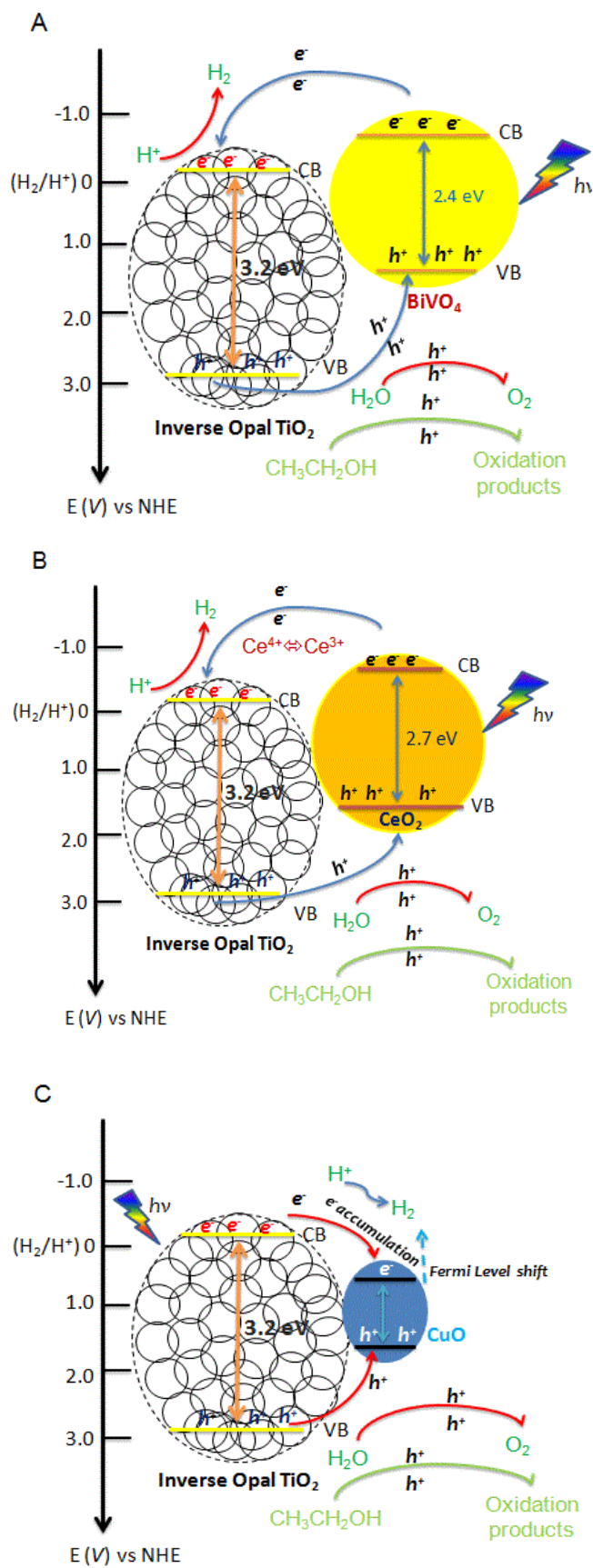


**Fig. 5.33** Possible photocatalytic mechanism of  $\text{H}_2$  generation over (A) Inverse Opal  $\text{TiO}_2$ - $\text{BiVO}_4$ ; (B) Inverse Opal  $\text{TiO}_2$ - $\text{CeO}_2$  and (C) Inverse Opal  $\text{TiO}_2$ - $\text{CuO}$  composites.



Contrarily to what observed under UV irradiation, I.O.TiO<sub>2</sub>-CuO composites with the smallest amounts of CuO (< 5 wt.%) showed to be more photoactive under solar light irradiation with respect to I.O. TiO<sub>2</sub>. It is not easy to explain this apparent contradictory behaviour. A tentative explanation could be provided by considering (i) that only a smaller fraction of efficient UV photons are present in a 300 W lamp simulating solar light (with respect to the high number of photons deriving from a 100 W UV lamp which could give rise to a levelling effect in the accumulation/recombination of pairs), (ii) that a beneficial effect could be due to the presence of CuO which can absorb in the visible range with the occurrence of d-d transition in Cu<sup>2+</sup> species (as detected by DRS measurements), thus favouring the accumulation of electrons in the CB of CuO [41, 109].

XRD and DRS results suggest that the incorporation of small amounts of CuO in the inverse opal TiO<sub>2</sub> allowed the occurrence of a charge tunneling through the interface barrier between the two oxides. CuO could act as a co-catalyst, offering the reduction sites for H<sub>2</sub> production (Fig. 5.33C). The presence of a high CuO loading appeared to be detrimental because the oxide acted as a recombination site between the charge carriers and the unfavorable band position due to the particle size increase. Moreover, high amount of CuO segregated on the TiO<sub>2</sub> surface (see XPS results) thus inhibiting the light absorption of TiO<sub>2</sub> [68, 114].

### 5.6 Conclusions and future perspectives

Macroporous inverse opal TiO<sub>2</sub> systems have been successfully synthesized, characterized and tested in the photocatalytic degradation of Rhodamine B in water, in the photo-oxidation of VOC and in the photocatalytic water splitting under both UV and solar light irradiation. In particular the influence of difference chemical agents (BiVO<sub>4</sub>, CeO<sub>2</sub>, CuO, N, W and Hf) was evaluated both in terms of chemico-physical properties and photocatalytic activity. Compared to commercial TiO<sub>2</sub> the inverse opal TiO<sub>2</sub> exhibited much better photocatalytic performance both under UV than solar light irradiation. This was related to the peculiar structure of the inverse opal TiO<sub>2</sub> which provides more active surface area and increased mass transfer because of its highly accessible porosity. According to the photocatalytic performance and the characterization data a positive effect of chemical agents, in terms of increased photocatalytic activity for the photo-oxidation reaction, was verified when the amount of the dopants (N, W, Hf) or cerium oxide was low. In fact, at low amounts of chemical agents, the ionic exchange of Ti<sup>4+</sup> ions by doping ions with the substitution of the Ti ions in the crystal lattice of TiO<sub>2</sub> was favored and/or the formation of non-stoichiometric Ti-composites on the TiO<sub>2</sub> surface was promoted.

Improvement in terms of H<sub>2</sub> production was indeed verified in the inverse opal TiO<sub>2</sub> composites (I.O. TiO<sub>2</sub>-CeO<sub>2</sub>, I.O. TiO<sub>2</sub>-BiVO<sub>4</sub>, I.O. TiO<sub>2</sub>-CuO) through the addition of an increasing amount of BiVO<sub>4</sub> or CeO<sub>2</sub>. On the contrary, for the I.O. TiO<sub>2</sub>-CuO composites, small copper oxide content was found to be optimal. In fact, due to surface segregation of copper, a higher amount of CuO can decrease the absorption of photon energy on TiO<sub>2</sub> surface due to the coverage of the TiO<sub>2</sub> active sites.

The good photocatalytic performances of inverse opal TiO<sub>2</sub> based photocatalysts encourage further investigation on the use of these systems in other attractive green reactions, such as the CO<sub>2</sub> photoreduction in the framework of a more efficient use of the visible light and of a more sustainable chemistry. As discussed in the introduction in fact, the greenhouse gas effect is considered to be a factor for anthropogenic climate change, and therefore the steady rise in the CO<sub>2</sub> level is a great cause for concern. Mitigating the effect of increasing CO<sub>2</sub> emissions through its sequestration has been studied intensively. However, the process generally requires a substantial input of energy and careful prevention of leakage of CO<sub>2</sub> back into the atmosphere [115]. In this context, the use of solar energy to chemically reduce CO<sub>2</sub> to higher energy compounds such methanol or methane offers a way to address this problem.

For example water can be photocatalytically split and the produced hydrogen is used to catalytically hydrogenate CO<sub>2</sub> to produce useful chemicals for use in further synthesis or as fuels. This approach takes advantage of the recent developments in the photocatalytic generation of H<sub>2</sub> and avoids problems associated with hydrogen storage.

## References

- [1] J. D. Joannopoulos, S. G. Johnson, J. N. Winn, R. D. Meade Photonic Crystals: Molding the Flow of Light , second ed., Princeton University Press, Princeton, New Jersey, 2008.
- [2] J. D. Joannopoulos, P.R. Villeneuve, S. Fan. Nature, 386 (1997), 143-149.
- [3] J. E. G. J. Wijnhoven, W. L. Vos. Science, 281 (1998), 802-804.
- [4] M. Wu, J. Liu, J. Jin, C. Wang, S. Huang, Z. Deng, Y. Li, B.L. Su, , Appl. Catal. B Environ. 150-151 (2014), 411-420.
- [5] I. I. Tarhan, G. H. Watson Phys. Rev. Lett. 76(1996) 315-318.
- [6] L. M. Goldenberg, J. Wagner, J. Stumpe, B. R. Paulke, E. Gornitz, Langmuir 18(2002) 3319-3323.
- [7] S. L. Kuai, X. F. Hu, A. Hach\_e, V. V. Truong, J. Cryst. Growth 267(2004) 317-324.
- [8] J. S. King, E. Graugnard, C. J. Summers, Adv. Mater. 17(2005) 1010-1013.
- [9] Y. Li, T. Kunitake, S. Fujikawa J. Phys. Chem. B 110(2006) 13000-13004.
- [10] S. John, Phys. Rev. Lett. 58 (1987) 2486-2489.
- [11] N. Perez, A. Huls, D. Puente, W. Gonzalezvinas, E. Castano, S. M. Olaizola Sensor Actuat B Chem 126 (2007) 86-90.
- [12] E. Yablonovitch, J. Mod. Opt. 41(1994) 173-194.
- [13] J. I. L. Chen, G. von Freymann, S. Y. Choi, V. Kitaev, G. A. Ozin, Adv. Mater. (2006) 18, 1915-1919.
- [14] X.Y. Li, L.H. Chen, Y. Li, J.C. Rooke, C. Wang, Y. Lu, A. Krief, X.Y. Yang, B.L. Su, J. Colloid Interface Sci. 368 (2012) 128-138.
- [15] Y. Li, Z.Y. Fu, B.L. Su, Adv. Funct. Mater. 22 (2012) 4634-4667
- [16] S. Meng, D.Z. Li, X. Zhang, J. Wang, J. Chen, J.L. Fang, S. Yu, X.Z. Fu, J. Mater. Chem. A (2013) 2744-2747.
- [17] Y. Lu, H.T. Yu, S. Chen, X. Quan, H.M. Zhao, Environ. Sci. Tech. 46 (2012) 1724-1730.
- [18] M. Wu, A.M. Zheng, F. Deng, B.L. Su, Appl. Catal. B: Environ. 138-139 (2013) 213-219.
- [19] J.I.L. Chen, G. von Freymann, V. Kitaev, G.A. Ozin, J. Am. Chem. Soc. 129 (2007) 1196-1202.
- [20] F. Sordello, C. Duca, V. Maurino, C. Minero, Chem. Commun. 47 (2011) 6147-6149
- [21] J. Liu, M. Li, J. Wang, Y. Song, L. Jiang, T. Murakami, A. Fujishima, Environ. Sci. Technol. 43 (2009) 9425-9431
- [22] M. Zalfani, B. van der Schueren, Z.-Y. Hu, J.C. Rooke, R. Bourguiga, M. Wu, Y. Li, G.V. Tendeloo, B.-L. Su, J. Mater. Chem. A. 3 (2015) 21244-21256.
- [23] M. Zalfani, Z.Y. Hu, W. Yu, M. Mahdouani, R. Bourguiga, M. Wu, Y. Li, B. van G. Van Tendeloo, Y. Djaoued, B.L. Su, Appl. Catal. B Environ. 205 (2017) 121-132.
- [24] G. Marci, V. Augugliaro, M.J. López-Muñoz, C. Martín, L. Palmisano, V. Rives, M. Schiavello, R.J.D. Tilley, A.M. Venezia, J. Phys. Chem. B. 105 (2001) 1026-1032.
- [25] Z.N. Kayani, M. Umer, S. Riaz, S. Naseem, J. Electron. Mater. 44 (2015) 3704-3709.
- [26] J. Bandara, C.P.K. Udawatta, C.S.K. Rajapakse, Photochem. Photobiol. Sci. 4(2005) 857-861.
- [27] Z.N. Kayani, M. Umer, S. Riaz, S. Naseem, J. Electron. Mater. 44 (2015) 3704-3709.
- [28] A.K. Bhattacharya, K.K. Mallick, A. Hartridge, Mater. Lett. 30 (1997) 7-13.
- [29] C.-M. Huang, G.-T. Pan, P.-Y. Peng, T.C.-K. Yang, J. Mol. Catal. A: Chem. 327 (2010) 38-44.
- [30] J. Zhu, Z. Deng, F. Chen, J. Zhang, H. Chen, M. Anpo, J. Huang, L. Zhang, Appl. Catal. B: Environ. 62 (2006) 329-335.
- [31] A. Sarkar, G. G. Khan, A. Chaudhuri, A. Das, K. Mandal, Appl. Phys. Lett. 108 (3) (2016) 33112.
- [32] H. Yan, C.F. Blanford, B.T. Holland, W.H. Smyrl, A. Stein, Chem. Mater. 12 (2000) 1134-1141.
- [33] Y. Q. Wu, G. X. Lu, S. B. Li, J. Phys. Chem. C 113 (2009) 9950-9955.
- [34] L. D. Zhang, C. M. Mo, Nanostruct. Mater. 6 (1995) 831-834.
- [35] S. Ameen, M.S. Akhtar, H.K. Seo, H.S. Shin, Chem. Eng. J. 247 (2014) 193-198.
- [36] F. Galindo, R. Gómez, M. Aguilar, J. Mol. Catal. A: Chem. 281 (2008) 119-125.
- [37] A. Kudo, K. Omori, H. Kato, J. Am. Chem. Soc. 121 (1999) 11459-11467.
- [38] Y. Hu, D. Li, Y. Zheng, W. Chen, Y. He, Y. Shao, X. Fu, G. Xiao, Appl. Catal. B: Environ. 104 (2011) 30-36.
- [39] S. Umrao, S. Abraham, F. Theil, S. Pandey, V. Ciobota, P. K. Shukla, C. J Rupp, S. Chakraborty, R. Ahuja, J. Popp, B. Dietzek, A. Srivastava, RSC Adv. 4 (2014) 59890-59901
- [40] R. Yang, L. Yang, T. Tao, F. Ma, M. Xu, Z. Zhang Appl. Surf. Sci. 288 (2014) 363- 368.

- [41] J. Yu, Y. Hai, M. Jaroniec, *J. Colloid Inter. Sci.* 357 (2011) 223-228.
- [42] A. Di Paola, E. García-López, G. Marci, C. Martín, L. Palmisano, V. Rives, A.M. Venezia, *Appl. Catal. B* 48 (2004) 223-233.
- [43] F.B. Li, X.Z. Li, *Appl. Catal. A: Gen.* 228 (2002) 15-27.
- [44] J.C. Yu, J.G. Yu, W.K. Ho, Z.T. Jiang, L.Z. Zhang, *Chem. Mater.* 14 (2002) 3808-3816.
- [45] J.G. Yu, L. Yue, S.W. Liu, B.B. Huang, X.Y. Zhang, *J. Colloid Interface Sci.* 334 (2009) 58-64.
- [46] N. Serpone, D. Lawless, R. Khairutdinov, *J. Phys. Chem.* 99 (1995) 16646-16654.
- [47] J. Liqiang, Q. Yichun, W. Baiqi, L. Shudan, J. Baojiang, Y. Libin, F. Wei, F. Honggang, S. Jiazhong, *Sol. Energ. Mat. Sol. C* 90 (2006) 1773-1787.
- [48] Y. Lei, L.D. Zhang, G.W. Meng, G.H. Li, X.Y. Zhang, C.H. Liang, W. Chen, S.X. Wang, *Appl. Phys. Lett.* 19 (2001) 1125-1127.
- [49] X.C. Karunakaran, S. Kalaivani, P. Vinayagamorthy, S. Dash, *Mater. Sci. Semicond. Process.* 21 (2014) 122-131.
- [50] L. Chen, S.F. Yin, R. Huang, Q. Zhang, S.L. Luo, C.T. Au, *CrystEngComm* 14 (2012) 4217-4222.
- [51] N. Singhal, A. Ali, A. Vorontsov, C. Pendemd, U. Kumar, *Appl. Catal. A Gen.* 523 (2016) 107-117.
- [52] H. Inoue, H. Moriwaki, K. Maeda, H. Yoneyama, *J. Photochem. Photobiol. A:Chem.* 86 (1995) 191-196.
- [53] Z.F. Bian, J. Zhu, S.H. Wang, Y. Cao, X.F. Qian, H.X. Li, *J. Phys. Chem. C*, 112 (2008) 6258-6262.
- [54] J. Zhu, J. Yang, Z. Bian, J. Ren, Y. Liu, Y. Cao, H. Li, H. He, K. Fan, *Appl. Catal. B: Environ.* 76 (2007) 82-91.
- [55] Y. Liu, H. Dai, J. Deng, L. Zhang, B. Gao, Y. Wang, X. Li, S. Xie, G. Guo, *Appl. Catal. B: Environ.* 140-141 (2013) 317-326.
- [56] J. Jiao, Y. Wei, Z. Zhao, J. Liu, J. Li, A. Duan, G. Jiang, *Ind. Eng. Chem. Res.* 53 (2014) 17345-17354.
- [57] A.C. Ferreira, A.M. Ferraria, A.M.B. do Rego, A.P. Gonçalves, A.V. Girão, R. Correia, T.A. Gasche, J.B. Branco, *J. Mol. Catal. A: Chem.* 320 (2010) 47-55.
- [58] L. Ilieva, G. Pantaleo, I. Ivanov, A.M. Venezia, D. Andreeva, *Appl. Catal. B: Environ.* 65 (2006) 101-109.
- [59] S. Watanabe, X. Ma, C. Song, *J. Phys. Chem. C* 113 (2009) 14249-14257.
- [60] E. Beche, P. Charvin, D. Perarnau, S. Abanades, G. Flamant, *Surf. Interface Anal.* 40 (2008) 264-267.
- [61] J. Fang, X. Bi, D. Si, Z. Jiang, W. Huang, *Appl. Surf. Sci.* 253 (2007) 8952-8961.
- [62] X. Gao, Y. Jiang, Y. Zhong, Z. Luo, K. Cen, *J. Hazard. Mater.* 174 (2010) 734-739.
- [63] Z. O.K.-Ataklı, Y. Yurum, *J. Chem. Eng.* 225 (2013), 625-635.
- [64] L. Dong, S. Guo, S. Zhu, D. Xu, L. Zhang, M. Huo, X. Yang, *Catal. Commun.*, 16 (2011), 250-254.
- [65] H. Yu, H. Irie, K. Hashimoto, *J. Am. Chem. Soc.* 132 (2010) 6898-6899.
- [66] H. Irie, K. Kamiya, T. Shibamura, S. Miura, D.A. Tryk, T. Yokoyama, K. Hashimoto, *J. Chem. Phys. C* 113 (2009) 10761-10766.
- [67] B.f. Xin, P. Wang, D.D. Ding, J. Liu, Z.Y. Ren, H.G. Fu, *Appl. Surf. Sci.* 254 (2008) 2569-2574.
- [68] L. Delannoy, G. Thrimurthulu, P. S. Reddy, C. Me' thivier, J. Nelayah, B. M. Reddy, C. Ricolleaudand, C. Louisa, *Phys.Chem.Chem.Phys.* 16 (2014) 26514-26527.
- [69] M. Bellardita, M. Addamo, A. Di Paola, L. Palmisano, A.M. Venezia, *Phys. Chem. Chem. Phys.*, 11 (2009) 4084-4093.
- [70] X. Chen, C. Burda, *J. Phys. Chem B* 108 (2004) 15446-15449.
- [71] .W. Zhang, G. Hea, L. Zhou, H.S. Chen, X.S. Chen, X.F. Chen, B. Deng, J.G. Lv, Z.Q. Sun, *J. Alloy Compd.* 611 (2014) 253-259.
- [72] Q. Fang, J.-Y. Zhang, Z.M. Wang, J.X. Wu, B.J. O'Sullivan, P.K. Hurley, T.L. Leedham, H.Davies, M.A.Audier, C.Jimenez, J.-P. Senateur, Ian W.Boyd, *Thin Solid Films* 428 (2003) 263-268.
- [73] J. F Moulder, W. F. Stickle, P. E. Sobol, K. D. Bomben, *Handbook of X-ray Photoelectron Spectroscopy*, Perkin-Elmer Corporation, Eden Prairie, Minnesota, 1993.
- [74] S. Sato, R. Nakamura, S. Abe, *Appl. Catal. A: Gen.* 284 (2005) 131-137.
- [75] J. Xu, B. Yang, M. Wu, Z. Fu, Y. Lv, Y. Zhao, *J. Phys. Chem. C* 114 (2010), 15251-15259.
- [76] F. Liu, G. Meyer, *Inorg. Chem.* 44, (2005) 9305- 9313.
- [77] X.Z. Li, F.B. Li, C.L. Yang, W.K. Ge, *J. Photochem. Photobio. A* 141 (2001) 209-217.
- [78] A. Scholz, B. Schnyder, A. Wokaun, *J. Mol. Catal. A:Chem.* 138 (1999) 249-261.
- [79] L.Y. Su, Z. Lu, *J. Phys. Chem. Solids* 59 (1998) 1175-1180.
- [80] D.C. Vermaire, P.C. van Berge, *J. Catal.* 116 (1989) 309-317.

- [81] X. Zheng, S. Meng, J. Chen, J. Wang, J. Xian, Y. Shao, X. Fu, D. Li, *J. Phys. Chem. C* 177 (2013), 21263-21273.
- [82] J. Cao, B. Luo, H. Lin, B. Xu, S. Chen, *Appl. Catal. B: Environ.* 111–112 (2012) 288–296.
- [83] A. Bianco Prevot, C. Baiocchi, M. C. Brussino, E. Pramauro, P. Savarino, V. Augugliaro, G. Marci, L. Palmisano, *Environ. Sci. Technol.* 35 (5) (2001) 971-976.
- [84] G. Marci, V. Augugliaro, A. Bianco Prevot, C. Baiocchi, E. García-López, V. Loddo, L. Palmisano, E. Pramauro, M. Schiavello, *Ann. Chim.- Rome* 93 (7-8) (2003) 639-648.
- [85] T. Wu, G. Liu, J. Zhao, H. Hidaka, N. Serpone, *J. Phys. Chem. B*, 102 (30) (1998) 5845-5851.
- [86] V. Augugliaro, C. Baiocchi, A. B. Prevot, E. García-López, V. Loddo, S. Malato, G. Marci, L. Palmisano, M. Pazzi, E. Pramauro, *Chemosphere* 49 (2002) 1223-1230.
- [87] J. I. L. Chen, E. Loso, N. Ebrahim, G. A. Ozin, *J. Am. Chem. Soc.*, 130 (2008) 5420-5421.
- [88] A. Di Paola, G. Marci, L. Palmisano, M. Schiavello, K. Uosaki, S. Ikeda, B. Ohtani *J. Phys. Chem. B* 106 (2002) 637-645.
- [89] M. Meksi, H. Kochkar, G. Berhault, C. Guillard *J. Mol. Catal. A: Chem.* 409 (2015) 162-170.
- [90] C. Belver, J. Bedia, M.A. Álvarez-Montero, J.J. Rodríguez, *Catal Today* 266 (2016) 36-45.
- [91] M. Zeng, Y. Li, M. Mao, J. Bai, L. Ren, X. Zhao, *ACS Catal.* 5 (2015) 3278-3286.
- [92] Y. Dong, Y. Wang, T. Cai, L. Kou, G. Yang, Z. Yan, *Ceram. Int.* 40 (2014) 11213-11219.
- [93] J. Fang, F. Wang, K. Qian, H. Bao, Z. Jiang, W. Huang, *J. Phys. Chem. C* 112, (2008) 18150-18156.
- [94] H. Kishimoto, K. Takahama, N. Hashimoto, Y. Aoi, S. Deki, *J. Mater. Chem.* 8 (1998) 2019-2024.
- [95] Y. X. Zhao, X. F. Qiu, C. Burda, *Chem. Mater.* 20 (2008) 2629-2636.
- [96] J. G. Yu, H. G. Yu, B. Cheng, X. J. Zhao, J. C. Yu, W. K. Ho, *J. Phys. Chem. B* 107 (2003) 13871-13879.
- [97] X. Cheng, X. Yu, Z. Xing, *Appl. Surf. Sci.* 268 (2013) 204-208.
- [98] H.P. Maruska, A.K. Ghosh, *Solar Energy* 20 (1978) 443-458.
- [99] J. Yan, G. Wu, N. Guan, L. Li, Z. Li, X. Cao, *Phys. Chem. Chem. Phys.* 15 (2013) 10978-10988.
- [100] A. Di Paola, E. Garcia-López, S. Ikeda, G. Marci, B. Ohtani, L. Palmisano *Catal. Today* 75 (2002) 87-93.
- [101] K. Nagaveni, M. S. Hegde, G. Madras *J. Phys. Chem. B* 108 (2004), 20204-20212.
- [102] L. Zhang, G. Tan, S. Wei, H. Ren, A. Xia and Y. Luo, *Ceram. Int.*, 39 (2013), 8597-8604.
- [103] M. Xie, X. Fu, L. Jing, P. Luan, Y. Feng and H. Fu, *Adv. Energy Mater.*, 4 (2014), 130095.
- [104] A. V. Vorontsov, V. P. Dubovitskaya, *J. Catal.* 221 (2004) 102-109.
- [105] H. Xu, X. Chen, S.X. Ouyang, T. Kako, J.H. Ye, *J. Phys. Chem. C* 116 (2012) 3833-3839.
- [106] J.I.L. Chen, E. Loso, N. Ebrahim, G.A. Ozin, *J. Am. Chem. Soc.* 130 (2008) 5420-5421.
- [107] J. Sun, X. Li, Q. Zhao, M.O. Tade, S. Liu *J. Mater. Chem. A* 3 (2015) 21655-21663
- [108] H. Hou, M. Shang, F. Gao, L. Wang, Q. Liu, J. Zheng, Z. Yang, W. Yang *ACS Appl. Mater. Interfaces* 8 (2016) 20128-20137.
- [109] S. Xu, J. Ng, A. J. Du, J. Liu, D. D. Sun, *Int. J. Hydrog. Energy* 36 (2011) 6538-6545.
- [110] G. R. Bamwenda, H. Arakawa, *Sol. Energy Mater. Sol. Cells* 70 (2001) 1-14.
- [111] A. Patsoura, D.I. Kondarides, X.E. Verykios, *Catal. Today* 124 (2007) 94-112.
- [112] C.R. López, E. Pulido Melián, J.A. Ortega Méndez, D.E. Santiago, J.M. Doña Rodríguez, O. González Díaz, *J. Photochem. Photobiol. A* 312 (2015) 45-54.
- [113] T. Puangpetch, T. Sreethawong, S. Yoshikawa, S. Chavadej, *J. Mol. Catal. A: Chem.* 312 (2009) 97-106.
- [114] S. Xu, D.D. Sun, *Int. J. Hydrog. Energy* 34 (2009) 6096-6104.
- [115] L. Schmidt-Mende, J. K. Stolarczyk, S. N. Habisreutinger *Angew. Chem. Int. Ed.* 52 (2013) 7372-7408.

## CONCLUSIONS

The rapid development of a global economy and the associated industrialization over the past century has brought about serious concerns regarding global resource consumption. The depletion of fossil fuel resources and the rapid consumption of carbon-based fossil fuel energy sources has led to global warming and climate change concerns. Despite these problems, fossil fuels still remain the major energy source used in people's daily lives. This has motivated an urgent research for renewable sources of clean energy.

The discovery of photocatalysis in 1972 on hydrogen production by water splitting attracted immediate research interest sowing to the following two energy crises, 1973 oil crisis and 1979 energy crisis. With more than four-decade development, photodegradation of either aqueous or gaseous pollutants, and production of solar fuels by photocatalytic either water splitting or CO<sub>2</sub> conversion, have been the hottest topics in photocatalysis. In the next future commercial photocatalysis would become both technically and economically competitive to counterpart technologies, as for example hydrogen production from hydrocarbon reforming, CO<sub>2</sub> conversion by dry reforming and chemical synthesis, water treatment by adsorption, biological treatment or advanced oxidation processes (AOPs). Furthermore, compared to above industrial processes, air purification especially indoor air purification appears to be a promising field in which photocatalysis could potentially act as a commercialized technology, integrating with particulate matter removal technologies.

Since its commercial production in the early twentieth century, titanium dioxide (TiO<sub>2</sub>) has been widely used as pigment and in sunscreens, paints, ointments, toothpaste, etc. Moreover after its first application in water splitting by Fujishima and Honda in 1972, TiO<sub>2</sub> has been heavily investigated in photocatalysis, solar cells, lithium ion battery electrodes, biomedical devices and intelligent coatings. However, there are still some intrinsic drawbacks that have limited the wide application of TiO<sub>2</sub> in its many multidimensional nanostructure forms. Withal wide band gap, TiO<sub>2</sub> (anatase: 3.2 eV, rutile: 3.0 eV) has a low utilization of the solar light spectrum. Furthermore, a fast recombination of photo-generated electron-hole pairs and a large over potential for water splitting leads to low photocatalytic efficiency. Therefore, in these years in order to improve the TiO<sub>2</sub> photoefficiency, more efforts have been devoted to enlarging the effective photocatalytic surface, forming Schottky junctions or heterojunctions, and engineering the band structure to match particular energy levels with structural or chemical modifications.

In this work three different approaches were used to modify the chemico-physical properties of  $\text{TiO}_2$  investigating the effects of these changes on the photocatalytic performance both in the photo-oxidation and photo reduction reactions either under UV than solar light irradiation.

The first strategy was to add at the commercial  $\text{TiO}_2$  another oxide as  $\text{CeO}_2$  and noble metals as gold or silver to exploit their surface Plasmon resonance effect. In particular the  $\text{Au}/\text{TiO}_2\text{-CeO}_2$  catalyst has showed good performance both in the photocatalytic water splitting than in the photo-oxidation of 2-propanol in the gas-phase. The enhanced charge carrier separation due to the presence of gold and the redox properties of cerium oxide were the key factors to increase the photoactivity of  $\text{TiO}_2$ .

The second approach was a structural modification of  $\text{TiO}_2$  with the introduction of  $\text{Ti}^{3+}$  and oxygen vacancies through laser irradiation. The remarkable increase of hydrogen production by photocatalytic water splitting was related to the presence of defects inside the crystalline structure of  $\text{TiO}_2$ .

The combination (third approach) of a  $\text{TiO}_2$  structural modification as the synthesis of inverse opal materials, and chemical modifications as the addition of a host component as  $\text{BiVO}_4$ ,  $\text{CeO}_2$ ,  $\text{CuO}$  or doping agent as N, W or Hf can be a promising strategy to enhance the titania photoactivity under solar light irradiation (Fig. C.1). The high performance of these catalysts was due to the peculiar porous backbone of inverse opal  $\text{TiO}_2$  that led to have a high light absorption inside the material and to exploit the photonic effects. Moreover, the presence of a photosensitizer as  $\text{BiVO}_4$  or the introduction of defects, eased by the presence of doping agents, further enhances the light absorption and the electron-hole charge separation of  $\text{TiO}_2$ .

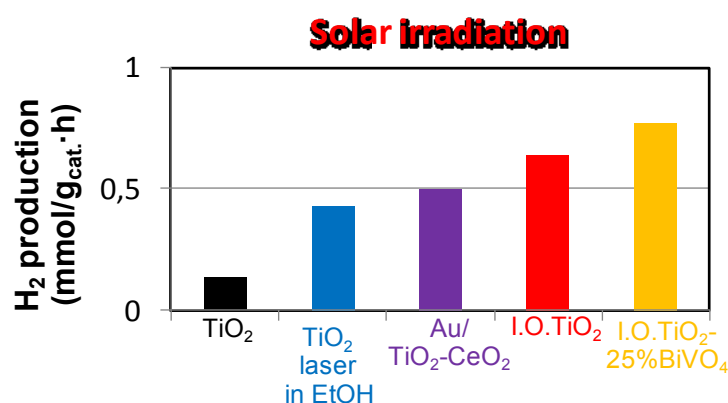


Fig. C.1  $\text{H}_2$  production by photocatalytic water splitting under solar light irradiation over some catalysts synthesized in this work.

## *CONCLUSIONS*

---

The contemporaneous presence of structural and chemical modifications of TiO<sub>2</sub> could be a promising approach to achieve an efficient use of solar energy applied to the TiO<sub>2</sub>-based photocatalysis for energy production and environmental protection.



## Appendix A: Characterization techniques used in this work

- *X-ray powder diffraction (XRD)*: X-ray diffraction (XRD) is an effective method for determining the crystal structure of materials. It detects crystalline materials having crystal domains greater than 3-5 nm. It is used to characterize bulk crystal structure and chemical phase composition. XRD analysis is based on constructive interference of monochromatic X-rays and a crystalline sample: The X-rays are generated by a cathode ray tube, filtered to produce monochromatic radiation, collimated to concentrate, and directed toward the sample. The interaction of the incident rays with the sample produces constructive interference (and a diffracted ray) when conditions satisfy Bragg's Law ( $n\lambda=2d \sin \theta$ ). This law relates the wavelength of electromagnetic radiation to the diffraction angle and the lattice spacing in a crystalline sample.
- *N<sub>2</sub> adsorption-desorption measurements*: The specific surface area of a powder is determined by physical adsorption of a gas, usually N<sub>2</sub>, on the surface of the solid and by calculating the amount of adsorbate gas corresponding to a monomolecular layer on the surface. Physical adsorption results from relatively weak forces (van der Waals forces) between the adsorbate gas molecules and the adsorbent surface area of the test powder. The determination is usually carried out at the temperature of liquid nitrogen. The amount of gas adsorbed can be measured by a volumetric or continuous flow procedure. The Brunauer-Emmett-Teller (BET) theory aims to explain the physical adsorption of gas molecules on a solid surface and serves as the basis for the measurement of the specific surface area of a material. Surface area determinations involve creating the conditions required to adsorb an average monolayer of molecules onto a sample. By extending this process so that the gas is allowed to condense in the pores, the sample's fine pore structure can be evaluated. As pressure increases, the gas condenses first in the pores with the smallest dimensions. The pressure is increased until saturation is reached, at which time all pores are filled with liquid. The adsorptive gas pressure then is reduced incrementally, evaporating the condensed gas from the system. Evaluation of the adsorption and desorption branches of these isotherms and the hysteresis between them reveals information about the size, volume, and area of pores. The BJH (Barrett, Joyner, and Halenda) or the DH (Dollimore and Heal) methods are typical procedure for

calculating pore size distributions from experimental isotherms using the Kelvin model of pore filling. It applies only to the mesopore and small macropore size range.

- *Scanning Electron Microscopy (SEM)*: This technique provides detailed high resolution images of the sample by rastering a focussed electron beam across the surface and detecting secondary or backscattered electron signal. An *Energy Dispersive X-Ray Analyser (EDX or EDA)* is also used to provide elemental identification and quantitative compositional information. EDX relies on an interaction of some source of X-ray excitation and a sample. Its characterization capabilities are due in large part to the fundamental principle that each element has a unique atomic structure allowing unique set of peaks on its X-ray emission spectrum.
- *Transmission Electron Microscopy (TEM)*: A transmission electron microscope utilizes energetic electrons to provide morphologic, compositional and crystallographic information on samples. At a maximum potential magnification of 1 nanometer, TEMs are the most powerful microscopes. TEMs produce high-resolution, two-dimensional images, allowing for a wide range of educational, science and industry applications. A transmission electron microscope produces a high-resolution, black and white image from the interaction that takes place between prepared samples and energetic electrons in the vacuum chamber. Air needs to be pumped out of the vacuum chamber, creating a space where electrons are able to move. The electrons then pass through multiple electromagnetic lenses. These solenoids are tubes with coil wrapped around them. The beam passes through the solenoids, down the column, makes contact with the screen where the electrons are converted to light and form an image. The image can be manipulated by adjusting the voltage of the gun to accelerate or decrease the speed of electrons as well as changing the electromagnetic wavelength via the solenoids. The coils focus images onto a screen or photographic plate. During transmission, the speed of electrons directly correlates to electron wavelength; the faster electrons move, the shorter wavelength and the greater the quality and detail of the image. The lighter areas of the image represent the places where a greater number of electrons were able to pass through the sample and the darker areas reflect the dense areas of the object. These differences provide information on the structure, texture, shape and size of the sample. To obtain a TEM analysis, samples need to have certain properties. They need to be sliced thin enough for electrons to pass through, a property known as electron transparency. Samples

need to be able to withstand the vacuum chamber and often require special preparation before viewing. Types of preparation include dehydration, sputter coating of non-conductive materials, cryofixation, sectioning and staining.

- *X-ray photoelectron spectroscopy (XPS)*: X-ray photoelectron spectroscopy is a surface characterization technique that can analyze a sample to a depth of 2 to 5 nanometers (nm). XPS is conducted in ultrahigh vacuum (UHV) conditions, around 10<sup>-9</sup> millibar (mbar). Irradiating a sample with x-rays of sufficient energy results in electrons in specific bound states to be excited. In a typical XPS experiment, sufficient energy is input to break the photoelectron away from the nuclear attraction force of an element. Two key features are derived from XPS data. The first is that even photo-ejected electrons from core levels have slight shifts depending on the outer valence configuration of the material examined. The second is that the specific energy of an elemental core level transition occurs at a specific binding energy that can uniquely identify (and in favorable cases quantify) the element. In a typical XPS spectrum some of the photo-ejected electrons inelastically scatter through the sample enroute to the surface, while others undergo prompt emission and suffer no energy loss in escaping the surface and into the surrounding vacuum. Once these photo-ejected electrons are in the vacuum, they are collected by an electron analyzer that measures their kinetic energy. An electron energy analyzer produces an energy spectrum of intensity (number of photo-ejected electrons versus time) versus binding energy (the energy the electrons had before they left the atom). Each prominent energy peak on the spectrum corresponds to a specific element. Besides identifying elements in the specimen, the intensity of the peaks can also tell how much of each element is in the sample. Each peak area is proportional to the number of atoms present in each element. The specific chemical composition is obtained by calculating the respective contribution of each peak area. By applying relative sensitivity factors and appropriately integrating peak areas, it can be determined that the sample below is 25 percent oxygen and 75 percent carbon.
- *Raman Spectroscopy*: Raman is a spectroscopic technique used to observe vibrational, rotational, and other low-frequency modes in a system. It relies on inelastic scattering, or Raman scattering, of monochromatic light, usually from a laser in the visible, near infrared, or near ultraviolet range. The laser light interacts with molecular vibrations, phonons or other excitations in the system, resulting in the energy of the laser photons

being shifted up or down. The shift in energy gives information about the vibrational modes in the system.

- *UV-Vis Diffuse Reflectance Spectroscopy (UV-Vis-DRS)*: Reflectance spectroscopy is very closely related to UV/Vis spectroscopy, in that both of these techniques use UV or visible light to excite valence electrons to empty orbitals. The difference in these techniques is that in UV/Vis spectroscopy one measures the relative change of transmittance of light as it passes through a solution, whereas in diffuse reflectance, one measures the relative change in the amount of reflected light off of a surface. A solution that is completely clear and colorless has essentially 100% transmission of all visible wavelengths of light, which means that it does not contain any dissolved components that have (allowed) electronic transitions over that energy range. By the same line of reasoning, a white powder effectively reflects 100% of all visible wavelengths of light that interacts with it. However, if the material has electronic energy levels that are separated by an energy in the visible region, then it may absorb some of light energy to move electrons from the filled energy level (valence band) into this empty level (conduction band). This causes an relative decrease in the amount of light at that particular energy, relative to a reference source. In other words, the % transmission/reflectance will decrease. This techniques permit to estimate the band gap values of materials. Kubelka-Munk (KM) theory provides the theoretical descriptions of DRS. When the powdered sample is radiated with light, a portion is regularly reflected at a powder surface and the remaining enters the powder and diffuse. As light of particular length is absorbed by the sample, the measurement of the diffuse reflected light at different wavelengths yields a spectrum called diffuse reflectance spectrum. The intensity of diffused reflectance spectrum in the limiting case of infinitely thick sample is expressed by Kubelka-Munk equation:

$$\frac{k}{s} = \frac{(1 - R_{\infty})^2}{2R_I} = f(R_I)$$

where  $R_I$  is the absolute diffuse reflectance (Kubelka-Munk function),  $k$  the absorption coefficient and  $s$  the scattering coefficient which varies with particle size and packing. In practice the measure of the relative diffuse reflectance ( $R$ ) is the ratio of the reflection from the sample to the intensity of reflection from a standard sample (usually  $\text{BaSO}_4$ ).

A plot with  $h\nu$  along x-axis and  $\left[\frac{k}{s} h\nu\right]^2$  along y-axis led to estimate the value of band gap of the material extrapolating the straight line in the graph at  $k=0$ .

- *Photoluminescence (PL) spectroscopy*: The Photoluminescence (abbreviated as PL) is light emission from any form of matter after the absorption of photons (electromagnetic radiation). It is one of many forms of luminescence (light emission) and is initiated by photoexcitation (excitation by photons). Following excitation various relaxation processes typically occur in which other photons are re-radiated. Time periods between absorption and emission may vary: ranging from short femtosecond-regime for emission involving free-carrier plasma in inorganic semiconductors up to milliseconds for phosphorescent processes in molecular systems; and under special circumstances delay of emission may even span to minutes or hours. Observation of photoluminescence at a certain energy can be viewed as indication that excitation populated an excited state associated with this transition energy. While this is generally true in atoms and similar systems, correlations and other more complex phenomena also act as sources for photoluminescence in many-body systems such as semiconductors. Photoluminescence (PL) spectroscopy is then a powerful technique for investigating the electronic structure, both intrinsic and extrinsic, of semiconducting and semi-insulating materials. When collected at liquid helium temperatures, a PL spectrum gives an excellent picture of overall crystal quality and purity. It can also be helpful in determining impurity concentrations, identifying defect complexes, and measuring the band gap of semiconductors. When performed at room temperature with a tightly focused laser beam, PL mapping can be used to measure micrometer-scale variations in crystal quality or, in the case of alloys and super lattices, chemical composition. The information obtainable from PL overlaps with that obtained by absorption spectroscopy, the latter technique being somewhat more difficult to perform for several reasons. First, absorption spectroscopy requires a broadband excitation source, such as a tungsten-halogen lamp, while PL can be performed with any above-band-gap laser source. Second, for thin-film samples absorption spectroscopy requires that the substrate be etched away to permit transmission of light through the sample. Third, for bulk samples the transmitted light may be quite weak, creating signal-to-noise ratio difficulties. On the other hand, absorption spectroscopy has the advantage of probing the entire sample volume, while PL is limited to the penetration depth of the above-band-gap excitation source, typically on the order of a micrometer. The areas of application of PL also overlap somewhat with

Raman spectroscopy, but the latter is much harder to perform because of the inherent weakness of nonlinear scattering processes and because of its sensitivity to crystallographic orientation.

## Appendix B: Gas Chromatography

Gas Chromatography (GC or GLC) is a commonly used analytic technique in many research and industrial laboratories for quality control as well as identification and quantification of compounds in a mixture. GC is also a frequently used technique in many environmental and forensic laboratories because it allows for the detection of very small quantities. A broad variety of samples can be analyzed as long as the compounds are sufficiently thermally stable and reasonably volatile. Like for all other chromatographic techniques, a mobile and a stationary phase are required for this technique. The mobile phase (=carrier gas) is comprised of an inert gas i.e., helium, argon, or nitrogen. The stationary phase consists of a packed column in which the packing or solid support itself acts as stationary phase, or is coated with the liquid stationary phase (=high boiling polymer).

The sample is injected into the inlet where it is volatilized and a representative portion is carried onto the column by the carrier gas. The sample components are separated by differential partitioning in the stationary and mobile phases. The separated sample component elute from the column into the detector where some physicochemical parameter is detected and a signal produced (Fig. A.b1). This signal is then amplified and sent to the data system where the chromatogram is electronically constructed.

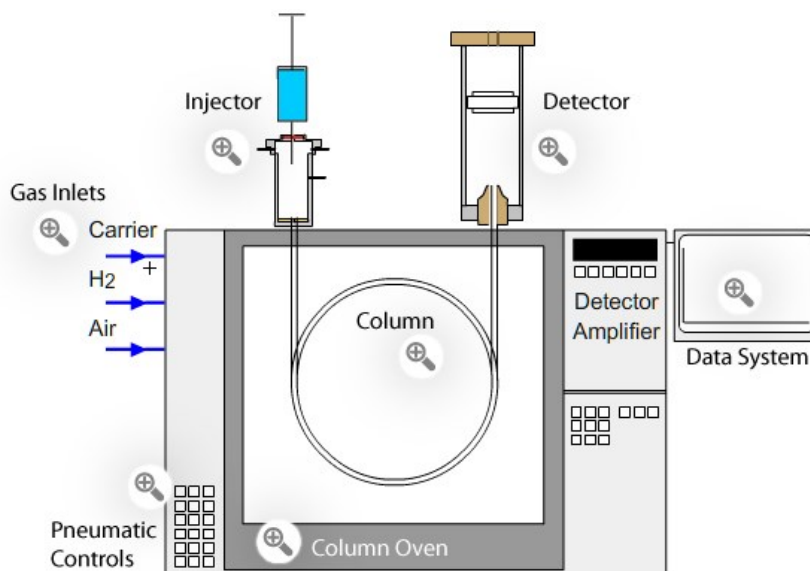


Fig. A.b1 GC instrumentation.

Most analytical gas chromatographs use capillary columns, where the stationary phase coats the walls of a small-diameter tube directly. The separation of compounds is based on the different

strengths of interaction of the compounds with the stationary phase. The stronger the interaction is, the longer the compound interacts with the stationary phase, and the more time it takes to migrate through the column (=longer retention time). The boiling point of a compound is often related to its polarity. The lower the boiling point is, the higher the vapor pressure of the compound and the shorter retention time usually is because the compound will spend more time in the gas phase. That is one of the main reasons why low boiling solvents (i.e., diethyl ether, dichloromethane) are used as solvents to dissolve the sample. The temperature of the column does not have to be above the boiling point because every compound has a non-zero vapor pressure at any given temperature, even solids. If the polarity of the stationary phase and compound are similar, the retention time increases because the compound interacts stronger with the stationary phase. As a result, polar compounds have long retention times on polar stationary phases and shorter retention times on non-polar columns using the same temperature. Chiral stationary phases that are based on amino acid derivatives, cyclodextrins and chiral silanes are capable of separating enantiomers because one enantiomer interacts slightly stronger than the other one with the stationary phase, often due to steric effects or other very specific interactions. A excessively high column temperature results in very short retention time but also in a very poor separation because all components mainly stay in the gas phase. However, in order for the separation to occur the components need to be able to interact with the stationary phase. If the compound does not interact with the stationary phase, the retention time will decrease. At the same time, the quality of the separation deteriorates, because the differences in retention times are not as pronounced anymore. The best separations are usually observed for temperature gradients, because the differences in polarity and in boiling points are used here. A high flow rate reduces retention times, but a poor separation would be observed as well. Like above, the components have very little time to interact with the stationary phase and are just being pushed through the column. A longer column generally improves the separation. The trade-off is that the retention time increases proportionally to the column length and a significant peak broadening will be observed as well because of increased longitudinal diffusion inside the column. One has to keep in mind that the gas molecules are not only traveling in one direction but also sideways and backwards. This broadening is inversely proportional to the flow rate. Broadening is also observed because of the finite rate of mass transfer between the phases and because the molecules are taking different paths through the column. Ideally, the peaks in the chromatogram display a symmetric shape (Gaussian curve). If too much of the sample is injected, the peaks show a significant tailing, which causes a poorer separation. Most detectors are relatively sensitive and do not need a lot of material in order to produce a detectable signal. Strictly



speaking, under standard conditions only 1-2 % of the compound injected into the injection port passes through the column because most GC instruments are operated in split-mode to prevent overloading of the column and the detector. The splitless mode will only be used if the sample is extremely low in concentration in terms of the analyte.

Many GC instruments are coupled with a mass spectrometer, which is a very good combination. The GC separates the compounds from each other, while the mass spectrometer helps to identify them based on their fragmentation pattern. The Flame Ionization Detector (FID) is very sensitive towards organic molecules but relative insensitive for a few small molecules i.e., N<sub>2</sub>, NO<sub>x</sub>, H<sub>2</sub>S, CO, CO<sub>2</sub>, H<sub>2</sub>O. If proper amounts of hydrogen/air are mixed, the combustion does not afford any or very few ions resulting in a low background signal. If other carbon containing components, are introduced to this stream, cations will be produced in the effluent stream. The more carbon atoms are in the molecule, the more fragments are formed and the more sensitive the detector is for this compound. Unfortunately, there is no direct relationship between the number of carbon atoms and the size of the signal. As a result, the individual response factors for each compound have to be experimentally determined for each instrument. Due to the fact that the sample is burnt (pyrolysis), this technique is not suitable for preparative GC. In addition, several gases are usually required to operate a FID: hydrogen, oxygen (or compressed air), and a carrier gas. The Thermal Conductivity Detector (TCD) is less sensitive than the FID, but is well suited for preparative applications, because the sample is not destroyed. The detection is based on the comparison of two gas streams, one containing only the carrier gas, the other one containing the carrier gas and the compound. Naturally, a carrier gas with a high thermal conductivity i.e., helium or hydrogen is used in order to maximize the temperature difference (and therefore the difference in resistance) between two filaments (= thin tungsten wires). The large surface-to-mass ratio permits a fast equilibration to a steady state. The temperature difference between the reference and the sample cell filaments is monitored by a Wheatstone bridge circuit.

## Appendix C: Hydrogen Economy

One of the task of this work was that to investigate new and green way to produce hydrogen a promising non-carbon future fuel. In this appendix a brief summary of other aspect of the hydrogen energy (i.e. the hydrogen purification for the use in the fuel cell and the hydrogen production on-demand) was outlined being another topic of my PhD research project.

The term "hydrogen economy" refers to the vision of using hydrogen as a low-carbon energy source replacing, for example, gasoline as a transport fuel or natural gas as a heating fuel. Hydrogen is attractive because whether it is burned to produce heat or reacted with air in a fuel cell to produce electricity, the only byproduct is water.

Hydrogen is not found in pure form on Earth, however, so it must be produced from other compounds such as natural gas, biomass, alcohols or water. In all cases it takes energy to convert these into pure hydrogen. For that reason, hydrogen is really an energy carrier or storage medium rather than an energy source in itself and the climate change impact of using it depends on the carbon footprint of the energy used to produce it. One of the most potentially useful ways to use hydrogen is in electric cars or buses in conjunction with a fuel cell which converts the hydrogen into electricity. Fuel cells are attractive because they're far more efficient than the internal combustion engines they can replace though the latter can still be used with hydrogen fuels if desired. At the moment, hydrogen is most commonly produced from natural gas. In this situation, a typical fuel cell car generates 70-80 g CO<sub>2</sub> for each kilometer driven similar to a modern gasoline hybrid or to a battery electric vehicle. These emissions can be reduced towards zero if the hydrogen is produced using low-carbon electricity sources such as renewables, nuclear or to electrolyze water, thus would allow to close the cycle of renewable hydrogen (Fig. A.c1). The downside is that in this situation only around half as much electricity comes out of the fuel cell as was put in to produce the hydrogen in the first place. The rest is lost as heat. Partly for this reason, and partly due to concerns over the commercial readiness of hydrogen fuel cell cars, battery-based electric cars have received more attention in recent years than hydrogen cars. However, hydrogen vehicles retain a number of important advantages: they can be rapidly refuelled in just a couple of minutes and have a range of many hundreds of kilometers. So the best technology depends on the final cost, carbon mitigation potential, and consumer needs in each case, moreover in the last years new methods were investigated to produce hydrogen without the use of electricity as the reforming of biomass or the photocatalytic water splitting.

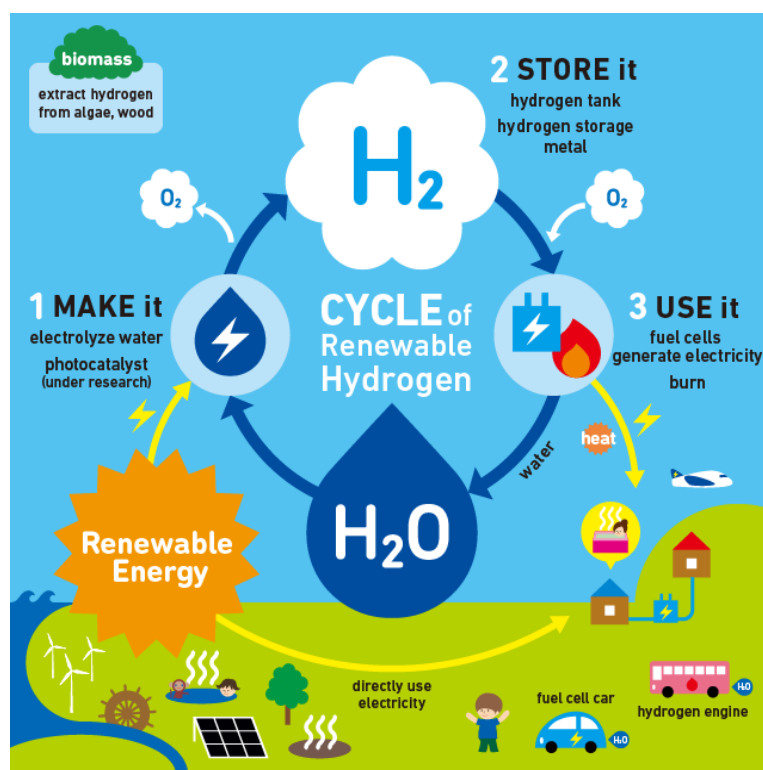


Fig. A.c1 Cycle of renewable Hydrogen.

In addition to transport, hydrogen may also be useful as a way to store renewable energy from intermittent sources for example, when the wind is blowing but there is not high demand for electricity. In this context, it's an alternative to large-scale batteries or other storage systems. Another possibility is to use hydrogen as a heating fuel in our homes and buildings, either blended with natural gas or neat. It is the flexibility that hydrogen offers that makes it so potentially useful within future low-carbon energy systems. It can be produced from a wide variety of resources and can be used in a wide range of applications, such as power generation, as a transport fuel for low carbon vehicles, for the chemical industry, and for low carbon heating. Moreover, hydrogen is already used extensively in the chemical industry so industry is familiar with its production, handling and distribution on a large scale. For all these reasons, many experts see hydrogen as a key enabler of the lowest-cost low-carbon energy system.

While hydrogen can help to decarbonise our energy system, however, it is important to be specific about where and when hydrogen can help. In that sense, it might be better to think about 'hydrogen in the economy' rather than 'a hydrogen economy' as such.

In this contest during my PhD I studied two correlated aspect of the hydrogen economy: the hydrogen purification through the Preferential Oxidation of CO (PROX reaction) for the use in the fuel cell and the production of hydrogen by hydrolysis of boro hydrides (hydrogen on demand system).

Low-temperature proton exchange membrane fuel cells (PEMFC) promise to be a cleaner and more efficient alternative to fuel combustion for power generation in stationary and mobile applications. This technology has been extensively studied during the last two decades due to low operation temperature (around 80°C), high efficiency and environmentally benign nature. The H<sub>2</sub> used in the PEMFC is usually obtained by steam reforming or partial oxidation of hydrocarbons followed by the water gas shift (WGS) reaction. However, the H<sub>2</sub>-rich stream coming from the WGS still exhibits 1-2 vol% of CO, not tolerated by the PEMFC anode. Therefore it is necessary to reduce the CO content in the hydrogen stream with the minimum H<sub>2</sub> consumption. For this purpose, several methods have been reported, selective oxidation of CO (known as PROX reaction, PReferential OXidation) being one of the most promising.

Gold based catalysts for PROX reaction still attracts the attention of researchers. In fact, compared to other systems, as Pt-based or CuO/CeO<sub>2</sub>, gold catalysts are more active in the low temperature range, matching the PEMFC operating temperature. It is well established that the catalytic performances of supported gold catalysts strongly depend on the preparation method, gold particles size and metal-support interaction. In the last years CeO<sub>2</sub> has been largely employed as support in oxidation reactions due its high oxygen storage capacity (OSC), namely the ability to take up oxygen under oxidizing conditions and releasing it under reducing ones. In particular gold supported on ceria has been reported among the most active systems for volatile organic compounds combustion, low temperature WGS reaction and PROX.

Gold performance can be improved by alloying gold with another metal.

We have investigated<sup>1,2</sup> CeO<sub>2</sub> supported Au-based bimetallic catalysts for both VOC combustion and PROX, pointing out a positive role of small amounts of the second metal (Fig. A.c2). In particular we found that the bimetallic Au-Ag/CeO<sub>2</sub> with an Au/Ag ratio of 1wt%/1wt% was the most efficient and stable system for the PROX reaction at low temperature (<100°C) compared to all other investigated mono and bimetallic catalysts (Au-Cu, Au-Pd and Au-Ru). Over Au-Ag/CeO<sub>2</sub> the order of deposition did not affect the catalytic performance whereas a higher amount of silver had a negative effect. Characterization data pointed to the occurrence of a strong Au-Ag interaction, favored mainly when the Au/Ag ratio was 1wt%/1wt%. This interaction caused an enhancement of surface ceria oxygens mobility, which positively affects the preferential oxidation of CO, which occurs through a Mars-van Krevelen mechanism. The better performance of Au-Ag/CeO<sub>2</sub> endorses this bimetallic catalysts as a good candidate for the purification of H<sub>2</sub> in PEMFC technologies.

---

<sup>1</sup>R.Fiorenza, C. Crisafulli, G. G. Condorelli, F. Lupo, S. Scirè, Catal. Lett. 145 (2015) 1691-1702.

<sup>2</sup>R. Fiorenza, C. Crisafulli, S. Scirè, Int. J. of Hydrogen Energ. 41 (2016) 19390-19398.

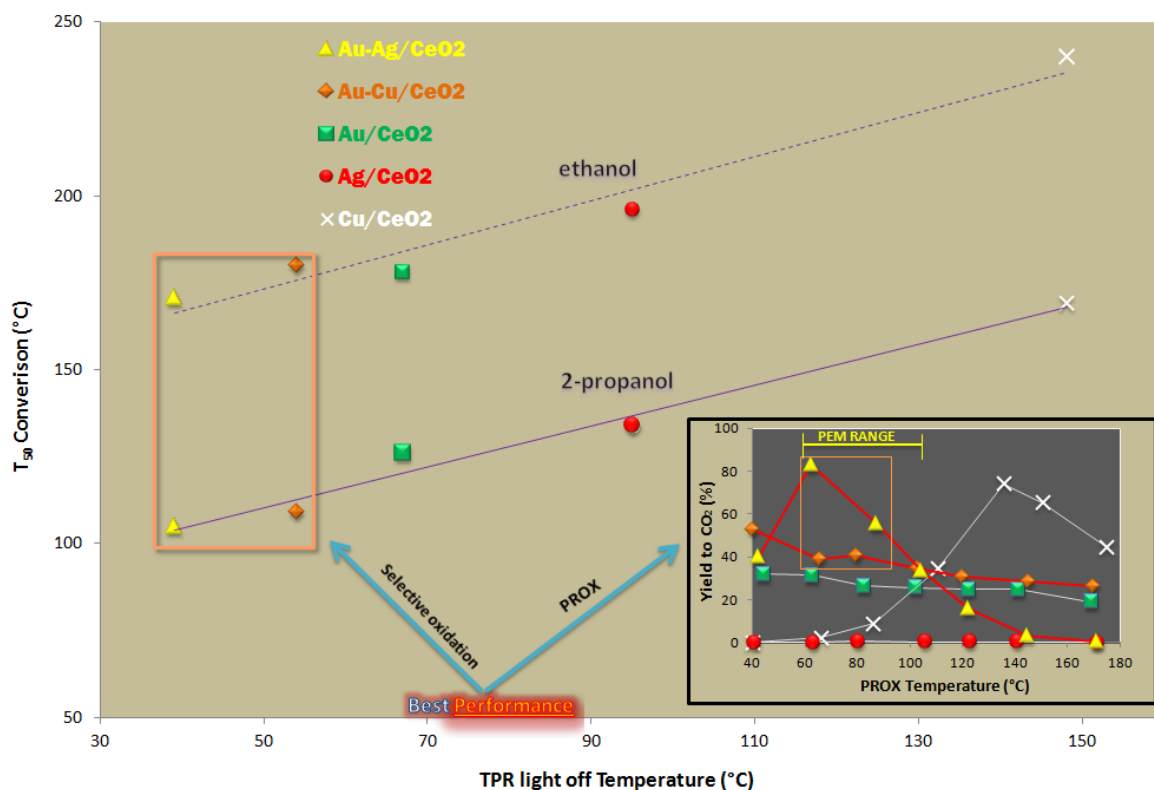
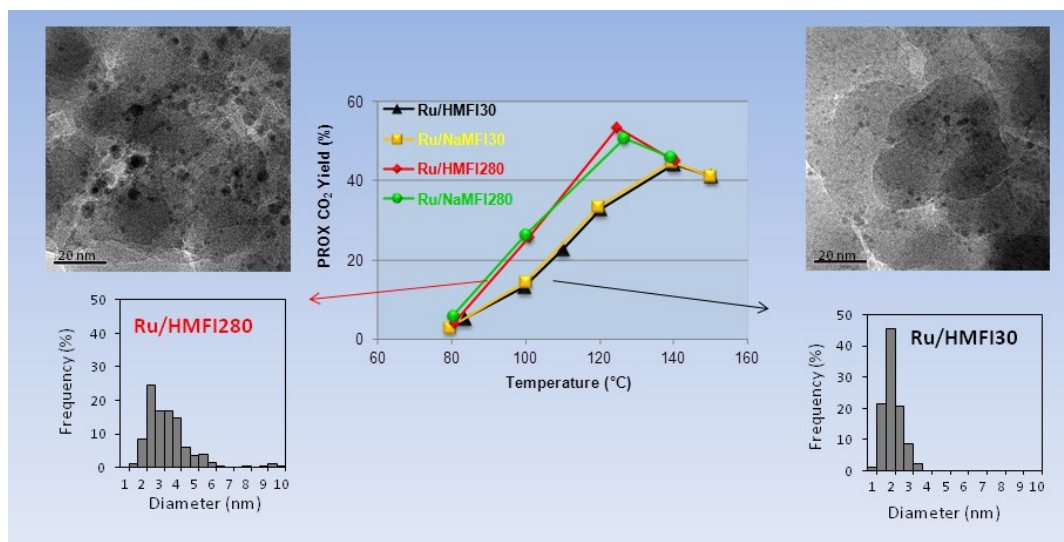


Fig. A.c2 Performance of gold based catalysts supported on  $\text{CeO}_2$ .

Another study was linked to the catalytic performance of Ru supported on ZSM5 (MFI) zeolite, investigating in detail the effect that different silica/alumina ratios (30 and 280) and forms of the zeolite (H- or Na-) play on the performance of these catalysts towards the selective removal of CO in excess of  $\text{H}_2$ <sup>3</sup>. Ru/ZSM5 was found to be more efficient system for PROX reaction compared to other investigated supporter catalysts (Ru/ $\text{Al}_2\text{O}_3$ , Ru/ $\text{SiO}_2$  and Ru/ $\text{CeO}_2$ ). The performance of Ru/ZSM5 catalysts in the PROX reaction were related to the size of Ru nanoparticles and/or the Lewis acidity of the zeolite (Fig. A.c3),  $\text{CO}_2$  yields being the highest over the Ru/HMFI280 catalyst, which is that one with the lowest number of Lewis acid sites and the biggest Ru particles. This behavior was explained considering a reaction mechanism involving both reactants, CO and  $\text{O}_2$ , activated on adjacent Ru sites. The good stability of Ru/HMFI280 in the presence of water encourages also for this system further investigation on the use of this catalytic system in the  $\text{H}_2$  purification by PROX in fuel cell technologies.

<sup>3</sup>S. Scirè, R. Fiorenza, A. Gulino, D.A. Cristaldi, P. M. Riccobene, Appl. Catal. A: Gen. 520 (2016) 82-91.



**Fig. A.c3** Performance of ruthenium catalysts supported on ZMS5 zeolite.

One of drawbacks of hydrogen is the production, the purification, the storing and the distribution. In particular hydrogen storage represents both a scientific and a technological challenge.

Among H<sub>2</sub> storage materials, as carbon nanostructures, metal-organic frameworks (MOFs), alcohols, formic acid, chemical hydrides attracted special attention because of their high gravimetric/volumetric H<sub>2</sub> storage capacities, being also an ideal source of pure hydrogen for PEM fuel cell technology, mainly for portable applications, like computers and cellular phones.

Chemical hydrides are able to produce hydrogen through a simple hydrolysis reaction and, generally, exhibit good stability during long periods of storage without usage. Among different hydrides, sodium borohydride (NaBH<sub>4</sub>, thereafter denoted SB) has been up to now regarded as the most promising, due to its good hydrogen storage capacity (10.9 wt%), high stability in alkaline solution and non-flammability. The NaBH<sub>4</sub> hydrolysis for hydrogen production (NaBH<sub>4</sub> + 2H<sub>2</sub>O ↔ NaBO<sub>2</sub> + 4H<sub>2</sub>) is an exothermic reaction occurring even at 0°C, releasing a non-toxic by-product such as sodium metaborate (NaBO<sub>2</sub>). At pH > 13 NaBH<sub>4</sub> is very stable and hydrogen release takes place only in the presence of suitable catalysts, such as Ru, Co, Pt, Ni or Pd, leading to “hydrogen on demand“ systems (HOD).

More recently, ammonia borane (NH<sub>3</sub>BH<sub>3</sub>, denoted AB) has been reported as an interesting alternative to SB, exhibiting higher H<sub>2</sub> capacity (19.6 wt%) together with a low toxicity and a high stability under ambient conditions. The stability of AB at pH 7 is of great practical interest as it allows the use of a larger number of supports, as silica, ceria and zeolites, not suitable under the strongly basic pH conditions of the SB solution. Several catalysts have been found effective

in accelerating  $\text{NH}_3\text{BH}_3$  hydrolysis ( $\text{NH}_3\text{BH}_3 + 2\text{H}_2\text{O} \rightarrow \text{NH}_4\text{BO}_2 + 3\text{H}_2$ ), namely noble metals, non-noble metals and B-containing nanocomposites.

For both SB and AB hydrolysis precious metal catalysts (Pt, Rh, and Ru) exhibited significantly higher activities than non-noble metal ones. Among precious metals, Ru-based catalysts remain the preferred choice for both SB and AB hydrolysis as Ru is sensibly less expensive than Pt and Rh.

We have investigated<sup>4</sup> both the  $\text{NaBH}_4$  and the  $\text{NH}_3\text{BH}_3$  hydrolysis over mono and bimetallic Ru-Co/activated carbon catalysts with the aim to get a better insight on the mechanism of these reactions and on the role of ruthenium and cobalt species in affecting the catalytic performance of this system.

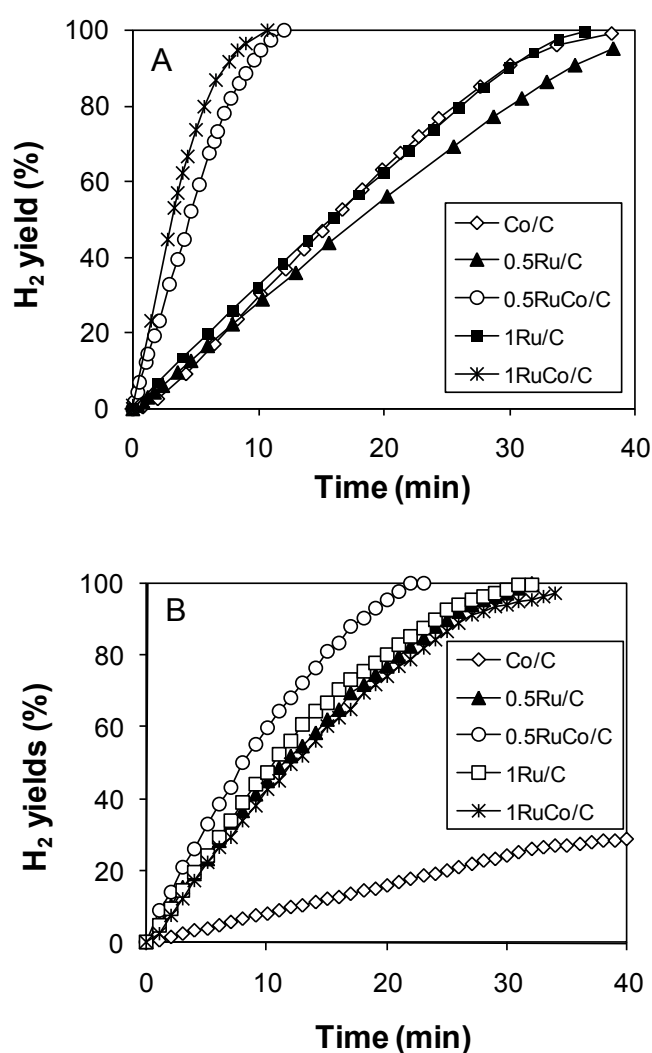


**Fig. A.c4**  $\text{H}_2$  yields in (A)  $\text{NaBH}_4$  and  $\text{NH}_3\text{BH}_3$  hydrolysis ( $T=35^\circ\text{C}$ ) as a function of reaction time over Ru based catalysts supported on activated carbon.

<sup>4</sup>R. Fiorenza, S. Scirè, A.M. Venezia, Int. J. Energ. Res. (2017) 1-13, In press, DOI: 10.1002/er.3918 .

We pointed out that the addition of small amount of Ru strongly enhances the catalytic performance of activated carbon supported Co catalysts towards the  $\text{NaBH}_4$  hydrolysis (Fig. A.c4A). The activity of the bimetallic Ru-Co/carbon samples is indeed much higher than the sum of the activities of corresponding monometallic samples. The characterization data pointed out a mutual interaction between ruthenium and cobalt oxide causing a decrease in the particle size of Ru and Co oxide nanoparticles. It was proposed that  $\text{Ru}^\circ$ , formed first during the reduction step of the Ru-Co samples, favors the  $\text{H}_2$  activation and the subsequent reduction of cobalt and ruthenium species, facilitated in the hydride reaction medium, enhances the reduction degree of the cobalt salt to  $\text{Co}^{2+}$  and the number of cobalt oxide species nucleation centers. The enhancement of catalytic activity of the Ru-Co system was much less evident in the case of the  $\text{NH}_3\text{BH}_3$  hydrolysis reaction (Fig. A.c4B) and this was attributed to the much lower reactivity of Co species compared to Ru ones towards the hydrolysis of  $\text{NH}_3\text{BH}_3$ .



## References:

- R.A. Lemons, J. Power Sources 29 (1990) 251-264.
- M. Twigg, Catalysts Handbook, Wolfe Publishers, London (UK), 1989 (Chapters 4-7).
- O. Korotkikh, R. Farrauto, Catal. Today 62 (2000) 249-254.
- T.V. Choudary, D.W. Goodman, Catal. Today 77 (2002) 65-78.
- S.H. Oh, R.M. Sinkevitch, J. Catal. 142(1993) 254-262.
- A. Manasilp, E. Gulari, Appl. Catal. B: Environmental 37 (2002) 17-25.
- M.J. Kahlich, H.A. Gasteiger, R.J. Behm, J. Catal. 171 (1997) 93-105.
- H. Igarashi, H. Uchida, M. Suzuki, Y. Sasaki, M. Watanabe, Appl. Catal. A: Gen. 159 (1997) 159-169.
- P.V. Snytnikov, V.A. Sobyenin, V.D. Belyaev, P.G. Tsyrlunikov, N.B. Shitova, S.A. Shlyapin, Appl. Catal. A: Gen. 239 (2003) 149-156.
- F. Marino, C. Descorme, D. Duprez, Appl. Catal. B: Environ. 54 (2004) 59-66.
- H. Tanaka, S. Ito, S. Kameoka, K. Tomishige, K. Kunimori, Appl. Catal. A: Gen. 250 (2003) 255-263.
- G.K. Bethke, H.H. Kung, Appl. Catal. A: Gen. 194 (2000) 43-53.
- R.J.H. Griesel, B.E. Nieuwenhuys, J. Catal. 199 (2001) 48-59.
- H.S. Oh, J.H. Yang, C.K. Costello, Y.M. Wang, S.R. Bare, H.H. Kung, M.C. Kung, J. Catal. 210 (2002) 375-386.
- S. Scirè, C. Crisafulli, P.M. Riccobene, G. Patanè, A. Pistone Appl. Catal. A: Gen. 417-418 (2012) 66-75.
- N.A.A. Rusman, M. Dahari, Int. J. Hydrogen Energy 41 (2016) 12108-12126.
- W. Grochala, P.P. Edwards, Chem. Rev. 104 (2004) 1283-1316.
- L. Schlapbach, A. Züttel, Nature 414 (2001) 353-358.
- U. B. Demirci, Int. J. Hydrogen Energy 40 (2015) 2673-2691.
- J.H. Kim, H. Lee, S.C. Han, H.S. Kim, M.S. Song, J.Y. Lee, Int. J. Hydrogen Energy 29 (2004) 263-267.
- C. Crisafulli, S. Scirè, M. Salanitri R. Zito, S. Calamia, Int. J. Hydrogen Energy 36 (2011) 3817-3826
- S. Peng, X. Fan, J. Zhang, F. Wang, Appl. Catal. B: Environ. 140-141 (2013) 115-124.
- Y. Li, X. Zhang, Q. Zhang, J. Zheng, N. Zhang, B.H. Chen, K.J. Smith, RSC Adv. 6 (2016) 29371-29377.
- S.C. Amendola, S.L. Sharp-Goldman, M.S. Janjua, N.C. Spencer, M.T. Kelly, P.J. Petillo, M. Binder, Int. J. Hydrogen Energy 25 (2000) 969-975.
- U.B. Demirci, P. Miele Energy Environ. Sci. 2 (2009) 627-637.
- N.A.A. Rusman, M. Dahari, Int. J. Hydrogen Energy 41 (2016) 12108-12126.
- M. Rakap, S. Ozkar, Int. J. Hydrogen Energy 35 (2010) 1305-1312.
- J. A. Sullivan, R. Herron, A. D. Phillips, Appl. Catal. B: Environ. 201 (2017) 182-188.
- O. Song-Il, J.-M. Yan, H.-Li Wang, Z.-Li Wang, Q. Jiang Int. J. Hydrogen Energy 39 (2014) 3755-3761.
- S. Akbayrak, S. Tanyıldızı, I. Morkan, S. Ozkar, Int. J. Hydrogen Energy 39 (2014) 9628-9637.
- R. Fernandes, N. Patel, R. Edla, N. Bazzanella, D.C. Kothari, A. Miotello, Appl. Catal. A: Gen. 495 (2015) 23-29.
- M. Zahmakiran, S. Özkar, Appl. Catal. B: Environ. 89 (2009) 104-110.
- C. Crisafulli, S. Scirè, R. Zito, C. Bongiorno, Catal. Lett. 142 (2012) 882-888.

## **Curriculum vitae**

Roberto Fiorenza was born in November 6, 1989 in Paternò (Catania). He attained his Master Degree in Materials Chemistry with full marks (110/110 cum laude) at the University of Catania in 2014 and in the same university in 2012, he achieved the Bachelor Degree in Industrial Chemistry. In November 2014, he started the PhD course in Chemical Science at the University of Catania where he worked in the laboratory of Environmental and Industrial Catalysis under the supervision of Prof. Salvatore Sciré. He spent part of his PhD course (6 months) at University of Namur (Namur, Belgium), with an Erasmus grant, under the supervision of Prof. Bao-Lian Su.



The main scientific interests are focused on some environmental (VOCs oxidation) and industrial (H<sub>2</sub> production and purification) applications of heterogeneous catalysis with particular concern on TiO<sub>2</sub>-based materials for photocatalysis.

During the PhD course he presented the results of his research activity, giving both oral and poster contributions, at several international conferences and he attended different catalysis schools. He won the Young Scientist Award at Symposium F: “Photocatalytic material for energy and environment “of the E-MRS (European Materials Research Society) Spring Meeting 2017 in Strasbourg (France).

Roberto Fiorenza is author or co-author of several articles, published in international referred scientific journals. He is a member of RSC (Royal Society of Chemistry) and SCI (Italian Chemistry Society). He was reviewer of some international journals dealing with catalysis as Applied Catalysis A and Catalysis Today.

## List of publications

- S. Filice, G. Compagnini, **R. Fiorenza**, S. Scirè, L. D'Urso, M. E. Fragalà, P. Russo, E. Fazio, S. Scalese  
*"Laser processing of TiO<sub>2</sub> colloids for an enhanced photocatalytic water splitting activity"*  
Journal of Colloid and Interface Science 489 (2017) 131-137.
- **R. Fiorenza**, M. Bellardita, L. Palmisano, S. Scirè  
*"A comparison between photocatalytic and catalytic oxidation of 2-Propanol over Au/TiO<sub>2</sub>-CeO<sub>2</sub> catalysts"*  
Journal of Molecular Catalysis A: Chemical 415 (2016) 56-64.
- **R. Fiorenza**, M. Bellardita, L. D'Urso, G. Compagnini, L. Palmisano, S. Scirè  
*"Au/TiO<sub>2</sub>-CeO<sub>2</sub> Catalysts for Photocatalytic Water Splitting and VOCs Oxidation Reactions"*  
Catalysts 6 (2016) 121.
- G. Ognibene, D. A. Cristaldi, **R. Fiorenza**, I. Blanco, G. Cicala, S. Scirè, M. E. Fragalà  
*"Photoactivity of hierarchically nanostructured ZnO-PES fibre mats for water treatments"*  
RSC Advances 6 (2016) 42778-42785.
- **R. Fiorenza**, C. Crisafulli, S. Scirè  
*"H<sub>2</sub> purification through preferential oxidation of CO over ceria supported bimetallic Au-based catalysts"*  
International Journal of Hydrogen Energy 41 (2016) 19390-19398.
- S. Scirè, **R. Fiorenza**, A. Gulino, A. Cristaldi, P. M. Riccobene  
*"Selective oxidation of CO in H<sub>2</sub>-rich stream over ZSM5 zeolites supported Ru catalysts: An investigation on the role of the support and the Ru particle size"*  
Applied Catalysis A: General 520 (2016) 82-91
- **R. Fiorenza**, C. Crisafulli, G.G. Condorelli, F. Lupo, S. Scirè  
*"Au-Ag/CeO<sub>2</sub> and Au-Cu/CeO<sub>2</sub> catalysts for volatile organic compounds oxidation and CO preferential oxidation"*  
Catalysis Letters 145 (2015) 1691-1702.
- A. Paternò, **R. Fiorenza**, S. Marullo, G. Musumarra, S. Scirè  
*"Prediction of ionic liquid's heat capacity by means of their in silico principal properties"*  
RSC Advances 6 (2016) 36085-36089.

- **R. Fiorenza**, S. Sciré, A. M. Venezia  
“Carbon supported bimetallic Ru-Co catalysts for  $H_2$  production through  $NaBH_4$  and  $NH_3BH_3$  hydrolysis”  
International Journal of Energy Research (2017); 1-13 *In press*, DOI: 10.1002/er.3918
- **R. Fiorenza**, M. Bellardita, T. Barakat, S. Scirè, L. Palmisano  
“Visible light photocatalytic activity of macro-mesoporous  $TiO_2$ - $CeO_2$  inverse opals”  
Journal of Photochemistry and Photobiology A: Chemistry (2017) *In press*,  
DOI: .org/10.1016/j.jphotochem.2017.10.052.
- **R. Fiorenza**, M. Bellardita, S. Scirè, L. Palmisano  
“Photocatalytic  $H_2$  production over inverse opal  $TiO_2$  catalysts”  
Catalysis Today (2017) *Submitted*.
- G. Compagnini, C. La Rosa, L. D’Urso, S. Scirè, **R. Fiorenza**, S. Filice, S. Scalese  
“Laser induced synthesis and processing of nanoparticles in the liquid phase for biosensing and catalysis”  
Chapter Springer book: "Laser micro-nano-nanomanufacturing and 3D microprinting"  
(2017), *Submitted*.

**List of Communications:**

**Oral communications:**

- **R.Fiorenza**, S. Scirè, C. Crisafulli  
*“Au-Ag/CeO<sub>2</sub> and Au-Cu/CeO<sub>2</sub> catalysts for CO preferential oxidation and VOC combustion”*  
Meeting of Italian Chemical Society, sections: Sicily and Calabria.  
Palermo (IT) 1-2/12/2014
- **R.Fiorenza**, S. Scirè, C. Crisafulli  
*“Au-Ag/CeO<sub>2</sub> and Au-Cu/CeO<sub>2</sub> catalysts for CO preferential oxidation”*  
HYPOTHESIS XI Hydrogen Power Theoretical and Engineering Solutions -  
International Symposium.  
Toledo (ES) 6-9/09/2015
- **R.Fiorenza**, S. Scirè, M. Bellardita, L. Palmisano  
*“TiO<sub>2</sub>-CeO<sub>2</sub> based catalysts for photocatalytic oxidation of VOC and water splitting reactions”*  
GIC 2016: XIX Congresso del Gruppo Interdivisionale di Catalisi della Società Chimica Italiana  
Bressanone (IT) 11-14/09/2016
- **R.Fiorenza**, S. Scirè, M. Bellardita, L. Palmisano, Bao-Lian Su  
*“Inverse Opal TiO<sub>2</sub> as visible-light-driven photocatalysts”*  
Meeting of Italian Chemical Society, sections: Sicily and Calabria.  
Messina (IT) 9-10/02/2017
- **R.Fiorenza**, S. Scirè, M. Bellardita, L. Palmisano, Bao-Lian Su  
*“Inverse Opal TiO<sub>2</sub> photocatalysts for energy production and environmental protection”*  
CIRCC XIV PhD Day and CO<sub>2</sub> RUCADI Meeting.  
Bari (IT) 30-31/03/2017
- **R. Fiorenza**, S. Filice, G. Compagnini, S. Scirè, S. Scalese  
*“Influence of laser treatment on TiO<sub>2</sub> based nanoparticles for photocatalytic water splitting”*  
E-MRS Spring Meeting 2017 Symposium F: *“Photocatalytic materials for energy and environment”*.  
Strasbourg (FR) 22-26/05/2017

- **R.Fiorenza**, S. Sciré, M. Bellardita, L. Palmisano  
“*Photocatalytic water splitting over Inverse Opal TiO<sub>2</sub>*”  
E-MRS Spring Meeting 2017 Symposium F: “*Photocatalytic materials for energy and environment*”.  
Strasbourg (FR) 22-26/05/2017
- **R.Fiorenza**, M. Bellardita, S. Sciré, L. Palmisano, Bao-Lian Su  
“*Inverse Opal TiO<sub>2</sub> photocatalysts for environmental applications*”  
EUROPACAT 2017, 13<sup>th</sup> European Congress on Catalysis  
Firenze (IT) 27-31/08/2017

**Poster communications:**

- **R.Fiorenza**, S. Scirè, A.F. Lombardo  
“*Ammonia borane hydrolysis over Ru/MFI zeolites for H<sub>2</sub> production for PEM fuel cells*”  
6th Czech-Italian-Spanish conference on Molecular Sieves and Catalysis joint with GIC 2015 Congress (XVIII National Congress of Catalysis) and AIZ 2015 Congress (XII National Congress of Zeolites Science and Technology).  
Amantea (IT) 14-17/06/2015
- **R.Fiorenza**, S. Scirè, M. Bellardita, L.Palmisano  
“*Catalytic and Photocatalytic oxidation of 2-Propanol by (Au) TiO<sub>2</sub>-CeO<sub>2</sub> Composites*”  
Catalysis Fundamentals and Practice summer school, University of Liverpool.  
Liverpool (UK) 20-24/07/2015
- **R. Fiorenza**, S. Sciré, G. Compagnini, L. D’Urso, M. E. Fragalà, S. Filice  
“*The effect of doping and laser irradiation on the photocatalytic water splitting over TiO<sub>2</sub> nanoparticles*”  
Faraday Discussion: Designing New Heterogeneous Catalysts  
London (UK) 4-6/04/2016
- **R.Fiorenza**, M. Bellardita, L.Palmisano, S. Scirè,  
“*Photocatalytic and Catalytic Oxidation of 2-Propanol over Au/TiO<sub>2</sub>-CeO<sub>2</sub> Catalysts*”  
SPEA 9:9th European Meeting on Solar Chemistry and Photocatalysis: Environmental Applications.  
Strasbourg (FR) 13-17/06/2016

## **Courses and Schools**

- 2nd SINCHEM Winter School: The European Doctoral Programme on Sustainable Industrial Chemistry, University of Bologna, Department of Industrial Chemistry *Toso Montari*.  
Bologna (IT) 16-17/02/2015
- Catalysis Fundamentals and Practice summer school, University of Liverpool.  
Liverpool (UK) 20-24/07/2015
- Elitecat 2017 Catalysis School, Université Claude Bernard Lyon.  
Lyon (FR) 3-7/07/2017.

### **Acknowledgements**

I want to thank my tutor professor Salvatore Sciré for his very useful guide during these years, dr.ssa Marianna Bellardita and professor Leonardo Palmisano of University of Palermo for their fundamental help and for sharing with me their enormous knowledge in the field of photocatalysis, the research group of prof. G. Compagnini (Simona Filice and dott.ssa Luisa D'Urso) of University of Catania for their advantageous collaboration and miss Isabel Virlet and prof. Bao-Lian Su of University of Namur (Belgium) to give me the opportunity to work in another country and in another laboratory.

Last but not least my family, my friends, and Enrica, to have supported me (as a catalyst) during this very exciting “way”.